# TU

## Technische Universität Wien

# DISSERTATION

# ENHANCEMENT OF CREEP RESISTANCE BY PARTICLE REINFORCEMENT

ausgeführt zum Zwecke der Erlangung des akademischen Grades eines Doktors der technischen Wissenschaften unter der Leitung von

O.UNIV.PROF. DIPL.-ING. DR.TECHN. HANS PETER DEGISCHER

E 308

INSTITUT FÜR WERKSTOFFWISSENSCHAFT UND WERKSTOFFTECHNOLOGIE

eingereicht an der Technischen Universität Wien
Fakultät für Maschinenwesen und Betriebswissenschaften

von

DIPL.-ING. BERND BAUER

99 26 2 86

WIEN

WIEN, AM 19.3.2009

# Acknowledgments

# Kurzfassung

Sowohl eine 2124 (AlCu) Al-Legierung  als auch eine 6061 (AlMgSi) Al-Legierung wurden mit und ohne SiC Partikelverstärkung mittels Pulvermetallurgie (PM) hergestellt und stranggepresst. Diese Legierungen wurden herangezogen, um die damit erzielten Kriechergebnisse mit schon existierenden Ergebnissen von konventionell hergestellten unverstärkten Legierungen zu vergleichen.

Verschiedene partikelverstärkte Materialien (PRMs) verstärkt mit SiC von 3 verschiedenen Größen <5µm, <10µm und <20µm und einem Volumenanteil von 25vol% wurden mittels PM erzeugt. Auf der einen Seite wurde das Pulver durch ein hochenergetisches Kugelmühlverfahren (BM) gemischt und auf der anderen Seite wurde ein Mischen in einer Flüssigkeit vorgenommen, genannt wet blending (WB). Beide Mischverfahren, sowie auch die entstandenen Gefügeunterschiede werden erläutert.

Mit diesen PRMs, sowie mit den unverstärkten Matrizen wird die Abhängigkeit des Kriechverhaltens von der Größe der Verstärkungspartikeln und Dispersoide, sowie der Einfluss der ausgeführten Herstellmethoden, untersucht. Der Einfluss der Herstellmethode wird durch den Vergleich der hier erhaltenen Ergebnisse mit jenen aus früheren Studien sichtbar.

Die PRMs sowie auch die unverstärkten Matrixlegierungen wurden vom Autor pulvermetallurgisch in CENIM (Centro Nacional de Investigaciones Metalúrgicas) in Madrid, Spanien, im Rahmen eines bilateralen Projektes „Acciones Integradas", hergestellt. Metallographisch charakterisiert wurden die Materialien mit Hilfe von Lichtmikroskopie, FEG-SEM und TEM kombiniert mit energiedispersiver Analyse. Das Kugelmühlverfahren sorgt für eine feine Verteilung gebrochener SiC Partikeln unabhängig von der Größenverteilung des zugesetzen Pulvers. Diese extreme Reduktion der Partikelgröße tritt beim Mischen in Flüssigkeit nicht auf. Der erhöhte Gehalt an Dispersoiden (<0.5µm) in BM Materialien gegenüber der WB Herstellung wird beschrieben. Diese Untersuchungen wurden sowohl durch E-Modul Messungen mittels DMA als auch durch Warmzugversuche vervollständigt. Parallel dazu wurden Messungen der Makrohärte vor dem Kriechen und nach einer bestimmten Kriechdauer durchgeführt. Um die Nanohärte ermitteln zu können wurde Nano indentation durchgeführt. Die Kriechtests wurden an der TU-Wien unter konstanter

Temperatur von 300°C und in Luftatmosphäre bei Zugspannungen von 15MPa bis 70MPa ausgeführt.

Die unverstärkte Matrix, welche mit BM präpariert wurde, zeigt eine niedrigere Kriechrate als jene Matrix die nicht mit BM gemischt wurde. Diese Steigerung der Kriechbeständigkeit entsteht durch die Oxide, welche durch das BM vom Matrix Pulver entstehen. Die Kriechrate aller Komposite, die mit BM hergestellt wurden, ist erheblich geringer als jene von den WB Kompositen bei allen getesteten Zugspannungen. Dieser deutliche Anstieg der Kriechbeständigkeit der BM Materialien wird durch die Partikel <0.5μm erzielt. Unter all den BM Kompositen mit verschiedenen ursprünglichen Partikelgrößen konnte kein Unterschied der Kriecheigenschaft festgestellt werden. Hingegen zeigen jene WB Komposite mit größeren SiC Partikeln eine deutliche Verminderung der Kriechbeständigkeit, was der Tatsache zugesprochen werden kann, dass je größer die Partikel sind, desto eher wirken sie als Versetzungsquellen.

Zusammenfassend kann gesagt werden, dass die Kriechbeständigkeit von pulvermetallurgisch hergestellten Al-Legierungen durch das Zumischen steifer Verstärkungspartikel (<0.5μm), so wie es durch den Einsatz von Kugelmühlverfahren zur Pulveraufbereitung erzielt wird, erheblich gesteigert wird, jedoch durch Partikel >5μm signifikant verschlechtert wird.

# Abstract

A 2124 (AlCu4) Al-alloy as well as a 6061 (AlMgSi) Al-alloy with and without SiC particle reinforcement were produced by powder metallurgy (PM) and subsequently extruded. Those alloy systems were investigated to compare the obtained creep results with already existing results from conventional produced alloys.

Particle reinforced materials (PRMs) with 3 different sizes of SiC reinforcing particles <5µm, <10µm and <20µm and with a volume fraction of 25vol% were produced by means of PM. On the one hand the powder was mixed by means of a high energy ball mill (BM) device and on the other hand a low energy wet blending (WB) technique was conducted. Both mixing techniques as well as the resulting differences in the microstructure are explained.

The dependence of the creep behavior on the size of the reinforcing particles and dispersoids as well as the effect of the conducted processing methods are investigated on these unreinforced and particle reinforced materials. The effect of the mixing technique can be seen by comparing the present results with those from previous studies.

The PRMs as well as the unreinforced matrix alloys were produced by PM routes by the author himself in CENIM (Centro Nacional de Investigaciones Metalúrgicas) in Madrid, Spain as a framework of a bilateral project called „Acciones Integradas". The metallographic investigations were carried out by means of light microscopy, FEG-SEM and TEM combined with energy dispersive analysis. Due to the BM the SiC particles are fractured and very fine spread independently of their initial size. This extreme reduction of the SiC particles is not observed during mixing within a liquid. The increased content of dispersoids (<0.5µm) present in the BM materials compared with the WB materials is investigated. The conducted investigations were completed by conducting Young´s Modulus measurements by means of a DMA device as well as high temperature tensile tests. Measurements of the macro hardness prior to creep and after a certain creep exposure time were carried out. In order to evaluate the nano hardness the nano indentation was conducted. The creep tests were done at constant temperature of 300°C in air atmosphere and for loads ranging from 15MPa to 70MPa at the Vienna University of Technology.

The unreinforced matrix alloy produced by BM shows a lower creep rate than the matrix produced without BM. This increase in creep resistance can be explained by the higher oxide fraction which results during the BM of the matrix powder. The creep rate of all the composites produced by BM is significantly lower than those of the WB composites at all the applied tensile loads. This sharp increase of the creep resistance of the BM materials can be attributed to the particles <0.5µm. Among all the BM composites with different initial particle sizes no difference of the creep behavior was found. Those WB PRMs reinforced with the bigger SiC particles show a clear decrease of the creep resistance what can be attributed to the fact that the bigger particles act as dislocation sources.

It is concluded that the creep resistance of Al-alloys produced by powder metallurgy can be significantly increased by adding a stiff reinforcing phase <0.5µm as it is obtained by means of BM, whereas by adding particles >5µm the creep resistance is dramatically reduced.

# Content

# 1  Introduction

Metal matrix composites (MMCs) have been subject of scientific investigation and applied research for about three decades but only in the past few years these advanced materials became realistic candidates in engineering components, such as electronic heat sinks, automotive drive shafts, ground vehicle brake rotors, jet fighter aircraft fins or combustion engine components. Their greatest potential is the large variety in combining matrix and reinforcement enabling tailor-made material properties [1].

The term metal matrix composites encompasses a wide range of scales and microstructures. Common to them all is a continuous metallic matrix. MMCs are obtained when a continuous metallic matrix is reinforced by means of a second stiffer phase, usually a ceramic. The reinforcement of metals can have many different objectives such as an increase in mechanical strength, creep resistance, fatigue strength, Young's modulus, or reduction of thermal expansion, etc. [2]. Accordingly, the requirements for the reinforcement phases are, for instance, low density, chemical compatibility, thermal stability, high strength, and high Young's modulus. The MMCs can be sorted into four broad classes based on the type or the reinforcement: particle reinforced metals (PRM), short fibre reinforced metals (SFRM), continuous fibre reinforced metals (CFRM) and monofilament reinforced metals (MFRM) [3].

In the present work, different PRMs prepared by different routes of powder metallurgy (PM) were studied regarding their creep resistance. In fact PM is a very ancient method to produce metallic objects. The earliest techniques date from 3000 B.C. when the Egyptians heated iron oxide in a charcoal and crushed shell fire, which was intensified by air blasts from below to reduce the oxide to a spongy metallic iron. The resulting hot sponge was then hammered to weld the particles together. Final shapes were obtained by simple forging procedures [4].

The first commercial application of PM occurred when carbon, and later osmium, zirconium, vanadium, tantalum, and tungsten, were used for incandescent lamp

filaments. Methods were developed from 1878 to 1898 for making carbon filaments by the extrusion and subsequent sintering of carbonaceous materials [4].

Infiltration techniques, porous materials, iron powder cores, PM permanent magnets, and tungsten-copper-nickel-heavy metal compositions were developed during the period between 1900 and the late 1920`s. The automobile has been the basis for most industrial applications of PM. The first commercial application of a PM product, the self-lubricating bearing, was used in automobiles in 1927 [4].

The creep behaviour of PRMs has been studied during the last decades and there is still some discrepancy regarding the determination of the dominating creep mechanisms. Controversal explanations were published by several scientists since the 1990s [5 - 15] regarding the influence of the addition of ceramic particles on the creep behaviour of Al-based PRMs. The reinforcing mechanisms of particles (>1µm) are different from those achieved by small particles (<1µm), called dispersoids.

For both dispersion hardening and precipitation hardening, the basis of the strengthening mechanism is to impede dislocation motion by small particles. This is achieved by the incorporation of either fine particles or non-shearable precipitates within a metallic matrix. Of prime importance is the minimisation of the spacing between the inclusions. Creep is effectively suppressed because the dislocations must climb over the dispersoids by diffusive processes and this result in creep rates decreasing with increasing dispersoid volume fraction [16].

Processing of MMC by PM overcomes the non wetability of the reinforcement with the liquid matrix and avoids chemical reaction of the constituents. In the present study, the dependence of the creep resistance on the reinforcing particle size is investigated on Al-based PRMs produced by PM using different blending methods. Two Al alloy powders were used as matrices, 2124 (AlCu4) and 6061 (AlMg1SiCu). The reinforcement used was powder of SiC with three initially different particles sizes (<5µm, <10µm, <20µm).

Chapter 2 reviews the relevant definitions regarding PRMs as well as the state of the art of PM techniques including the physics of ball milling and hot extrusion. Additionally, an introduction to the physics of creep can be found. All the materials studied during this work, their chemical compositions, the type and volume fraction of the reinforcement phase, the blending routes, the extrusion details, the heat

treatment and all the conducted experimental testing procedures are described in chapter 3. This leads to chapter 4 where all the results of the experimental procedures are given. All the creep curves with the corresponding creep rate curves as well as micrographs of all the materials are given in the appendix. These results are interpreted in chapter 5 and finally discussed in chapter 6. Conclusions and summaries are given in chapter 7.

# 2 State of the Art for PRMs and PM

## 2.1 Metal Matrix Composites (MMCs)

MMCs have found application in some high tech components for quite some time. Substantial progress in the development of light metal matrix composites has been achieved in recent decades, so that they were introduced into important engineering applications such as the automotive and the electronic industry [1].

The possibility of combining various materials (metal – ceramic – organic) gives the opportunity of several variations. Figure 2.1 shows the allocation of the composite materials as a combination of different material groups [2].

MMC consist of at least two chemically and physically distinct pre existent phases, suitably distributed to provide properties not obtainable with either of the individual phases. There are generally two phases, a rigid ceramic phase, distributed in a metallic matrix [1, 17].

This group of engineering materials becomes interesting for structural and functional applications, if the properties profile of conventional materials do not reach the increased requirements of specific demands.
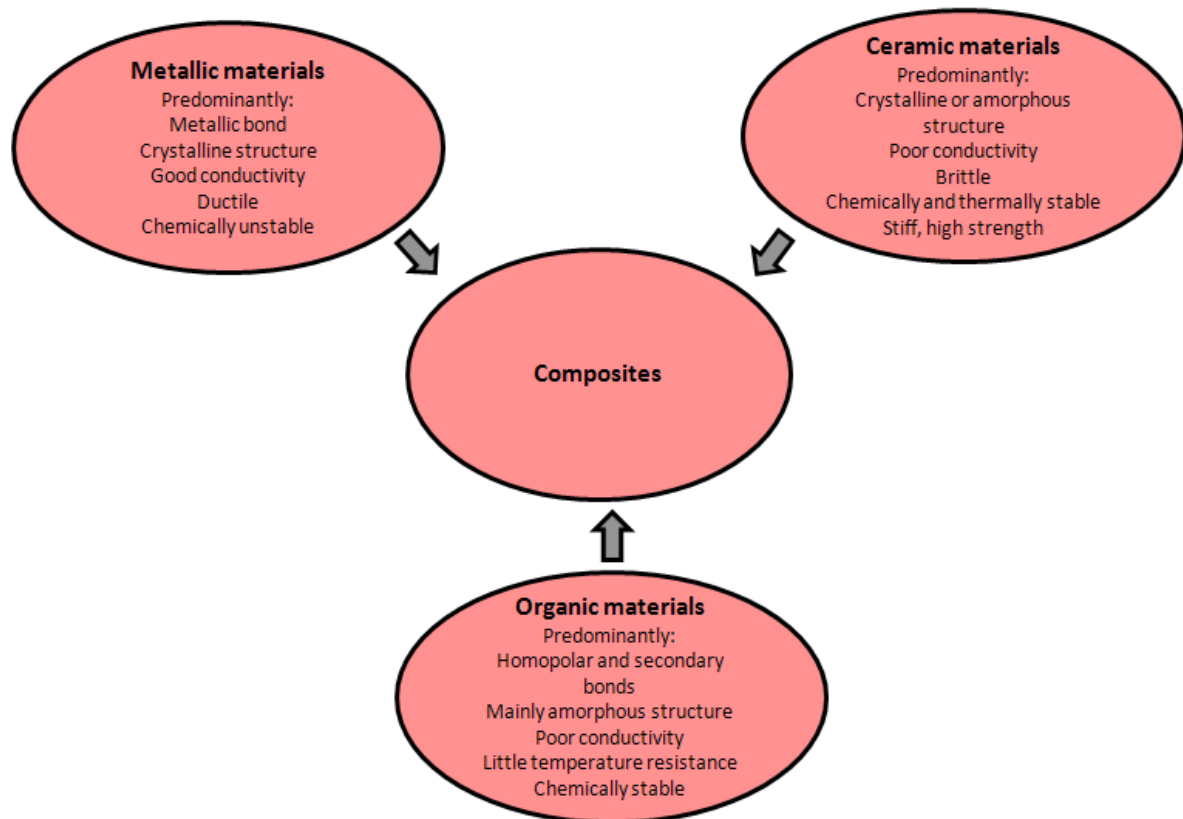
**Figure 2.1** Allocation of the ingredients of composite materials (modified from [2]).

According to the reinforcement phase utilized to build up a composite we obtain [1]:

- PRM: Particle Reinforced Metals
- SFRM: Short Fibre Reinforced Metals
- CFRM: Continuous Fibre Reinforced Metals (fibres usually supplied in bundles)
- MFRM: Monofilament Reinforced Metals (essentially endless reinforcement as continuous fibres, handled as individual fibres with diameters typically greater than 100 µm)
- WRM: Whisker Reinforced Metals (similar to short fibres, but smaller and monocrystals; health hazard due to sub-µm particles)

9

### 2.1.1 Fabrication of Metal Matrix Composites

Several processes have been and are being developed for the manufacture of MMCs. These may be divided into primary material production and secondary consolidation or forming operations. A further important distinction can be drawn for the primary processes depending on whether the matrix becomes liquid at any stage. Each technique has its limitations in terms of component size and shape, and imposes certain microstructural features on the product [16].

#### 2.1.1.1 Primary Liquid Phase Processing

- Stir casting [18]
- Slurry casting (rheo casting) [16]
- Pressureless infiltration [19]
- Gas pressure Infiltration [20]
- Squeeze infiltration (high pressure infiltration) [20]
- Spray deposition [21]
- Reactive processing [16, 22]

#### 2.1.1.2 Primary Solid Phase Processing

- Powder blending and pressing (see section 2.2) [4]
- Diffusion bonding (fibre/foil, fibre/fibre) [16]
- Physical vapour deposition [23]

### 2.1.2 Strengthening Mechanisms of Particle Reinforced Metals (PRMs)

#### 2.1.2.1 Dislocation strengthening

This strengthening mechanism is important for room temperature applications. Dislocations can be formed either as a result of applied plastic straining or built up of residual stresses due to thermal mismatch. Assuming cube-shaped particles embedded in a metallic matrix Miller and Humphreys [24] obtained the following equation to predict the change in dislocation density $\Delta\rho$ after a temperature drop $\Delta T$:

$$\Delta\rho = 12\frac{\Delta\alpha\Delta Tf}{bd}$$

where d is the particle size, ΔαΔT is the thermal misfit strain, b the Burgers vector and f is the reinforcement volume fraction. This model predicts that the dislocation density increases with decreasing particle size at constant volume fraction. This is predicted to be especially marked for particle sizes below about 1µm.

In order to predict the influence of dislocation density on matrix strength, a relation of the type [2]:

$$\Delta\sigma_\alpha = kGb\sqrt{\rho}$$

can be used, where $\Delta\sigma_\alpha$ is the yield strength contribution due to geometrical necessary dislocations and inner tension, k is a constant (values 0.5-1), G is the shear modulus, b the Burger´s vector and ρ is the dislocation density.

### 2.1.2.2 Strengthening from grain size refinement

This strengthening mechanism again is important at room temperature. Discontinuously reinforced PRMs typically have a grain size smaller than that of their unreinforced matrices. It is assumed that each particle nucleates a single grain. The contribution to the yield stress of this refinement can then be estimated using the Hall-Petch relation, which relates yield stress enhancement to grain size d [2]:

$$\Delta\sigma_{YM} = \beta d^{-\frac{1}{2}}$$

The value of β depends on a number of factors but is typically around 0.1 MPa $\sqrt{m}$. Given that d might be decreased to around 1µm for fine reinforcements, this suggests that grain refinement can have a large strengthening effect [2].

Chapter: State of the Art for PRMs and PM

### *2.1.2.3 Precipitate and dispersion strengthening*

This strengthening mechanism is important for room and for high temperature applications.

If an impurity (e.g. Cu) is dissolved in a metal (e.g. Al) at a high temperature, and the alloy is cooled to room temperature, the impurity may precipitate as small particles. An alloy of Al containing 4% Cu treated in this way gives very small closely spaced precipitates of the hard compound $Al_2Cu$. As long as they are coherent, they can be cut by dislocations. Small particles can be introduced into metals or ceramics in other ways. The most obvious is to mix non shearable dispersoids into a powdered metal and then compact and sinter the mixed powders. Either approach distributes small, hard particles in the path of a moving dislocation. Figure 2.2 shows how they obstruct its motion. The stress $\tau$ has to push the dislocation between the obstacles. Once a large enough bulge is formed it can easily expand further. The critical configuration is the semicircular one (see Figure 2.2 c)): here the force $\tau$ bL on one segment is just balanced by the force 2T due to the line tension, acting on either side of the bulge. The dislocation escapes when [25]

$$\tau = \frac{2T}{bL}$$

The obstacles thus exert a resistance of $f_0 = 2T/L$. Obviously the greatest hardening is produced by strong, closely spaced precipitates or dispersoids.

b) Approach situation
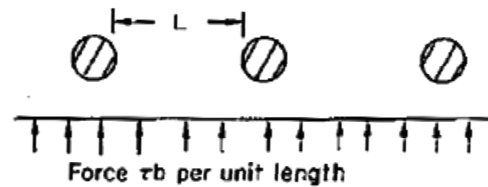
c) Sub-critical situation
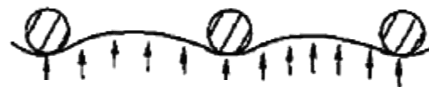
d) Critical situation
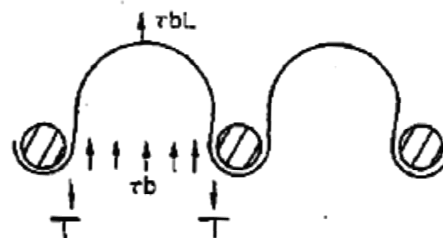
a) Escape situation
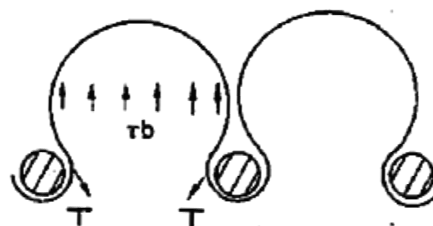
**Figure 2.2** How dispersed non shearable precipitates prevent the movement of dislocations and help prevent plastic flow of materials [25]

### 2.1.2.4 Solid solution strengthening

A good way of hardening a metal is simply by alloying. Foreign elements go into solution in a solid metal just as sugar dissolves in tea. A good sample is the addition of zinc to copper to make the alloy called brass. The zinc atoms replace copper atoms to form a random substitutional solid solution. At room temperature Cu will dissolve up to 30% Zn in this way. The Zn atoms are bigger than the Cu atoms, and, in squeezing into the Cu structure, generate stresses. These stresses roughen the

slip plane, making it harder for dislocations to move. They increase the resistance and thereby increase the yield strength.

In a solid solution of concentration c, the spacing of dissolved atoms on the slip plane varies as $c^{-1/2}$. The smaller the spacing, the rougher is the slip plane. As a result $\tau$ increase with solute concentration (see Figure 2.3) [25].
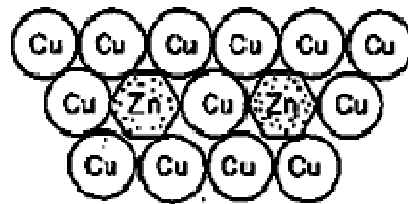


**Figure 2.3** Substitutional solid solution hardening [25]

## 2.2 Powder Metallurgy

Metal powder production has always been influenced greatly by cost and quality requirements of powder consolidation techniques and applications. This interrelationship has led to the development of many powder-producing processes. Manufacturing methods must be cost effective with respect to the properties achieved. Powders must possess the required physical and chemical characteristics for use in the various PM consolidation processes and applications. Generally, powders in current use are cleaner, more uniform in size, and may be produced within narrower specification ranges than in former times. Microprocessor control can be used to achieve refined manufacturing methods and improved final product performance. Improved and more complete powder characterization is certain to become more important.

High degree of consolidation is of prime importance for the production of structural parts by pressing and sintering or by powder forging or extrusion to achieve full density as good as possible. Powder purity has become equally important for the achievement of increased dynamic properties [4].

### 2.2.1 Blending and Premixing

According to [4] blending of powders is defined as the thorough intermingling of powders of different size classes of the same nominal composition, while premixing is the preparation of a uniform mixture of two or more components. Many properties of powders and sintered parts – such as powder flow, apparent density, ejection stress, delubrication behaviour, dimensional change, and mechanical strength – are quite sensitive to even small changes in particle size distribution and to fluctuations in the concentrations of components within a powder mixture. Lubricated, single-component metal powders comprise the most important systems in powder metallurgy. Important three- and four-component systems include iron-carbon-lubricant, copper-tin-lubricant, iron-copper-carbon-lubricant, and copper-tin-carbon-lubricant. The widespread use of powder mixtures rather than prealloyed powders is attributable to

both economic and technical factors: powder mixtures often are less expensive, have better compacting properties, and sometimes permit shorter sintering times.

The degree of blending and premixing should be related to the intended use of the product. As the degree of blending increases toward the theoretically perfect blend, required energy will also increase. Accordingly, equipment operating maintenance, as well as analytical, and other associated costs, will be higher. Thus, the economic importance of defining the degree of uniformity or blending needed for each particular application is obvious. Control over mixing time becomes more important when using higher velocity mixing devices, in which particle fragmentation can introduce severe changes in particle behaviour and a tendency toward segregation. Although the determination of minimum or optimum blending is usually done by measuring specific technological powder properties as a function of blending time, a general method based on measuring the uniformity of a blend or mixture follows.

The blending of a powder mixture improves as the number of contacts between the different components of the mixture increases. Figure 2.4 schematically illustrates various powder dispersions. A truly ordered particle arrangement is a theoretical standard. The agglomerated and the demixed or segregated arrangements represent extreme and undesirable particle dispersions. From a practical point of view, a homogeneous distribution of the components represents the optimum degree of mixing. This doesn´t necessarily mean that a homogeneous distribution is best or even attainable for a given application, but it provides a reference mark against which the actual distribution can be measured.
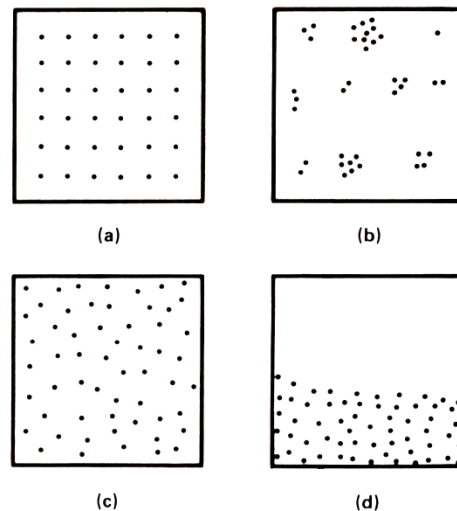
**Figure 2.4** Various powder dispersions: a) a truly ordered particle arrangement, b) agglomerated, c) demixed and d) segregated arrangement

### 2.2.1.1 *Compressibility of Metal Powders* [4]

Compressibility of a powder is a major factor in the design of pressing tools, the part density attainable, and the size of the press needed to press to that density. Powders of high apparent density are preferred because tooling can be made shorter and thus stronger.

The compressibility of a powder is influenced by the following factors:

- Inherent ductility of the metal or alloy

  Some metals tend to work harden to a greater extent than others. Since considerable deformation of a powder takes place during pressing, its work hardening characteristics have a strong influence on compressibility.

- Particle shape

  In general, the more irregular a powder is, the lower is its compressibility.

- Internal porosity

  Fine internal porosity in a powder tends to become not interconnected during pressing, thus trapping air within particles. Although air is highly compressible, it takes up volume and contributes little to weight. Non-porous powders have the highest compressibility.

- Particle size distribution

  Powders of a uniform size exhibit relatively poor compressibility. Mixtures of particle sizes designed to occupy the most space have better compressibility.

- Presence of non-metallic elements/compounds

  Non-metallic elements/compounds such as unreduced oxides reduce compressibility because of their hardness and low specific gravity.

- Use of solid lubricants

  Solid lubricants added to aid the pressing of metal powder increase compressibility (5 to 7%). Some lubricants perform better than others at pressing pressures.

- Addition of alloying elements

  Alloying additions such as graphite and sulphur generally degrade compressibility.

### 2.2.1.2  Milling of Brittle and Ductile Materials [4]

The objectives of milling include:

- Particle size reduction
- Particle size growth
- Shape change (flaking)
- Agglomeration
- Mixing or blending of two or more materials or mixed phases
- Solid-state blending (incomplete alloying)
- Solid-state alloying (mechanical alloying)
- Modifying or changing properties of a material

The milling operation fractures, deforms (cold works) or cold welds the impacted particles. The specific effect that milling has on the powder depends on the physical and chemical properties of the powder, the vacuum, gaseous, or liquid environment in which the operation is conducted and milling conditions.

During milling, four types of forces act on a particulate material: impact, attrition, shear, and compression.

Impact is the instantaneous striking of one object by another. Both objects may be moving or one may be stationary. Attrition is the production of wear depris or particles created by the rubbing action between two bodies. Shear consists of cutting or cleaving of particles and usually is combined with other types of force. Shear contributes to fracture by breaking particles into individual pieces. Compression is the slow application of compressive forces to a body (crushing or squeezing of particulate material).

*Principles of milling [4]:*

Figure 2.5 represents the moment of collision at which particles are trapped between two colliding balls. The number of particles trapped between two balls on impact in loose powder mass should increase as the ratio of the ball diameter (D) to the particle diameter (d) increases. At the high ratios of D/d encountered in milling of fine particles the trapped volume consists of particles within the micro volume BB´BB´ (Figure 2.5). Outside this incremental volume the apparent density of the powder sharply decreases to the density of the agitated loose powder.
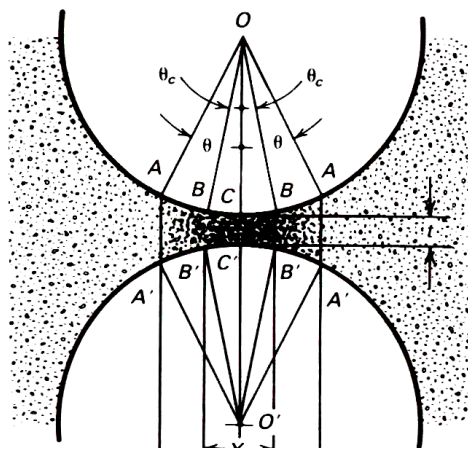


**Figure 2.5** Moment of collision at which particles are trapped between colliding balls volume BB'-BB'

Figure 2.6 a) presents a certain volume of agitated powder which is trapped between two impacting balls. If impacting force is sufficient, the trapped incremental volume of powder is compacted to form an agglomerate particle or pellet, as it is shown in Figure 2.6 b). This agglomerate is released when elastic energy impels the balls apart, as Figure 2.6 c) shows. If bonding by welding or adhesion occurs between contacting surfaces of the particles and bonding forces are sufficient the agglomerate does not break apart. Similarly, particles may bond to the surfaces of the balls which may become coated with the powder.
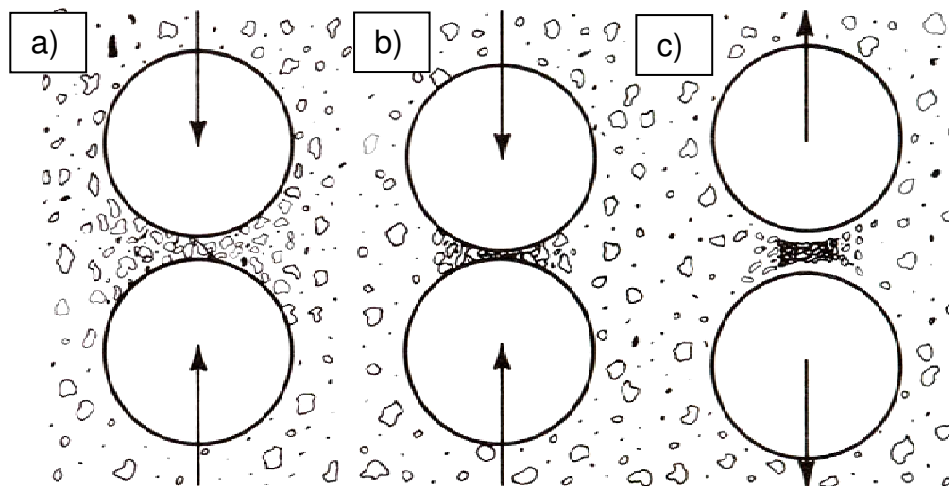


**Figure 2.6** Powder trapped between impacting balls: a) volume of agitated powder trapped between two balls, b) compacted to form an agglomerate, c) agglomerate is released

The first stage of compaction consists of rearrangement and restacking of particles. Particles slide past one another with a minimum of deformation and fracture, producing some fines – especially from brittle, irregularly shaped particles. During this stage flowability is reduced and void spaces are partially filled with fine particles. Particle shape plays an important role during this stage. Spherical particles having the greatest flowability and least friction are almost totally ejected from between colliding balls. Flake particles having the least flowability and greatest frictional resistance to flow tend to be retained between ball surfaces. Particles with irregular surfaces also tend to mechanically bond together to form agglomerates.

The second stage of compaction involves elastic and plastic deformation of particles. Elastic deformation plays a relatively minor role, whereas plastic deformation and cold welding have major effects. During this stage cold welding occurs between metal particles. Most metals work harden during the second stage of compaction which increases deformation resistance. The third stage of compaction, involving particle fracture, results in further deformation or fragmentation of the particles. Densification of brittle ceramic and metallic particulate materials in the microbed occurs when small pores are filled with fragmented particles.

Changes in powder particle morphology that occur during milling of metal powders are produced by the following processes:

1.  Microforging
    The initial and predominant process during milling is compression shape forming of ductile metal particles by impact from the milling medium. Individual particles or a cluster of particles are impacted repeatedly by the milling medium so that they deform (flatten) with little or no change in individual mass.

2.  Fracture
    After a period of milling individual particles deform to the extent that cracks initiate, propagate, and ultimately fracture the particles. Cracks, defects and inclusions in particles facilitate fracturing. Particles formed from irregular or spongy particles contain fissures and cracks that facilitate compression, fatigue failure and fragmentation compared to smooth and nonporous spheroidal particles.

3.  Agglomeration
    Agglomeration of particles may occur by welding, mechanical interlocking of spongy or rough surfaces, or adhesion. Adhesion is the molecular interaction of particles among themselves, characterised by van der Waals forces. Deagglomeration is a process that breaks up agglomerates formed without further disintegration of the individual powder particles.

*Dispersion of Oxide Films:*

The strengthening effect produced by ultrafine oxide particles through solid-state or mechanical alloying is an important factor affecting final equilibrium particle size and the time required to reach equilibrium particle size. Oxide particles, derived from oxide films originally present on the particle surface and/or from oxygen in the chamber environment become entrapped between cold welded surfaces by kneading. The strengthening effect of the dispersoid, cold working and the composite structure greatly increase toughness, strength and fracture resistance of individual particles [4].

The most advantageous size of the oxides to produce dispersion strengthening should be less than 100nm and the subgrain size of the matrix alloy should not exceed 1µm [26].

### 2.2.1.3 Mechanical Fundamentals of Consolidation

Consolidation of a metal powder into useful product forms generally begins by transfer of the powder into a container. Density of the powder transferred into the container depends on the properties of the powder and on the method of transfer, which may include tapping and vibrating.

- Packing of metal powders

  Considerable research has been done on the density of packed powders [27, 28]. When powders of spherical particle shape and uniform size are poured into a container, the density is lower than if the particles were arranged in a regular face centered cubic or hexagonal close-packed array. Densities can be increased by vibration or by adding the powder in small quantities with intermediate tapping.

- Pressure-Density Relationship in Powder Compacts

  The relationship which has been widely used was developed by Balshin [29]:

$$\ln P = -AV + B$$

  in which ln P is the natural logarithm of the applied pressure; V is the relative powder volume (the ratio of the volume of the powder compact and the volume

of solid metal of the same mass); and A and B are constants. This relationship is only valid for certain powders and even for these powders only within a narrow pressure range.

A second relationship was developed by Heckel [30]:

$$P = \frac{1}{K}\left( \ln\frac{1}{1-\rho^*} + B \right)$$

where $\rho^*$ is the relative density of the compact (ratio of green density to solid density); P is the applied pressure; and K and B are constants. Experimental results reveal that for a number of powders the relationship applies reasonably well for pressures between 150 and 700MPa.

- Overview of Methods of Compacting Powders to higher Density:

*Sintering*

Sintering is the consolidation of ingredient materials at elevated temperatures without application of pressure [1].

*Hot Isostatic Pressing (HIP)*

HIP means the diffusion bonding of ingredient materials with application of hydrostatic pressure by means of a gas, at temperatures high enough to effect concurrent sintering of the matrix, which for metal matrices is generally above the matrix recrystallisation temperature [1].

*Die Barrel Rotation*

Rotating the die barrel while the powder is being pressed was reported by Hammond and Schwartz [31]. Compaction with a stationary and a rotating die barrel were compared. In static compression, 20% of the applied stress was

consumed in the wall friction, while only 2% of the stress was consumed when the die barrel was rotated.

*Triaxial compression by simultaneous isostatic and uniaxial compression*

This is obtained by applying pressure to the circumference of a cylindrical specimen confined in a flexible envelope, while an axial load is superimposed by a vertical piston. With this method, the level of pressure necessary to obtain a given density is less than with isostatic or uniaxial compression alone. The principles involved in this method of compaction have been reviewed by Broese van Groenou [32].

*High-Energy-Rate Compacting*

The effects of the rate of pressure application in compacting was studied by Davies and Elwakil [33]. They found that higher densities can be obtained for a given pressure and for a given energy input when compacts from iron powder are pressed in high speed presses using explosives.

Rusnak [34] showed that the density of copper powder is not so much a function of projectile velocity but depends primarily on the kinetic energy of the projectile. He used compressed gas to actuate the projectile.

*Vibratory Compacting of Powders*

Vibrating and simultaneous compacting of powders to obtain higher densities has been studied primarily by Soviet scientists [35]. The relative densities of powders vibrated under carefully controlled conditions are much higher than those obtained by simply pouring the powder into the container. Therefore, much lower compaction pressures are required to reach a given density for a vibrated than for a poured powder.

*Compacting in Rigid Dies at High Pressures*

Pressures in the order of 3000MPa which are approximately four times those customarily used for compacting in rigid dies have been suggested. Gutmanas [36], developer of this technique, terms it "cold sintering". Useful products can

be produced either without subsequent sintering or by sintering at much lower temperatures than those ordinarily used. According to Gutmanas clean surfaces that provide extensive atomic contact between powder particles at room temperature are freshly formed through plastic deformation at high pressures.

### 2.2.1.4 Hot Extrusion

Hot extrusion combines hot compacting and hot mechanical working, yielding a fully dense product [37]. In extrusion, large hydrostatic compressive forces occur and a unidirectional force component makes the compact flow through the die. Frictional forces produce a shear component which results in a characteristic shear pattern in the extruded material. The total amount of deformation in extrusion is much larger than in any other single metalworking step. Thus, the oxide skin on the powder particles is fractured and friction welding is promoted.

3 methods of hot extrusion are generally used:

1. Loose powder is placed without preheating into the heated extrusion container and extruded directly through the die. This method has been developed for the extrusion of certain magnesium alloy powders [38, 39]. No atmospheric protection is provided and the heat of the container is used to raise the temperature of the powder sufficiently to allow extrusion.

2. In the second method, which is used for hot extrusion of aluminium alloy powder billets, the powder is cold compacted and then hot pressed [40]. The hot pressed compact is extruded by techniques used for extruding cast aluminium alloy billets.

3. The mostly used method is placing the powders into a metallic can, heating and extruding with the can. In hot extrusion, a metal powder compact may be canned or cold pressed into the metal can under moderate pressure. To prevent turbulent flow during extrusion the end of the can is conical and fits into an extrusion die with a conical opening. The "filled billet" technique [41], a method of producing extruded structural shapes from superalloy powder was developed by Gorecki and Friedman. An enlarged replica of the desired shape

is produced within a round extrusion billet. The ratio of the dimensions in the filled billet and in the final extrusion is determined by the extrusion ratio. The cavity is filled with a powder of the superalloy composition to be produced. The machined filler is placed in a carbon steel can. Superalloy powder is poured into the cavity and the billet is sealed, evacuated and heated for extrusion. The billet is extruded through a round orifice conical approach die. The filler is then dissolved leaving the desired shape 100% dense.

## 2.3  Isothermal Tensile Creep

Time scales of parts used for gas turbines vary from working lives of hours for rockets to lives measured in decades for electricity generation plants. Direct testing of the long-term creep properties of materials which will be in use for more than 30.000 hours is not practical. Reliable methods for extrapolating the results of accelerated creep tests carried out at temperatures and stresses higher than those which will be encountered in service are necessary. The operating creep mechanism must be known to restrict extrapolations within the same creep mechanism.

Tensile creep tests can be carried out at constant load or at constant stress. The use of a constant load implies an increasing stress as the cross-section of the sample decreases during the creep tests.

The isothermal tensile creep tests in the present study are conducted at a constant load. Therefore, this section will be focussed on the typical creep curve resulting from a constant load test, as it is shown in Figure 2.7.
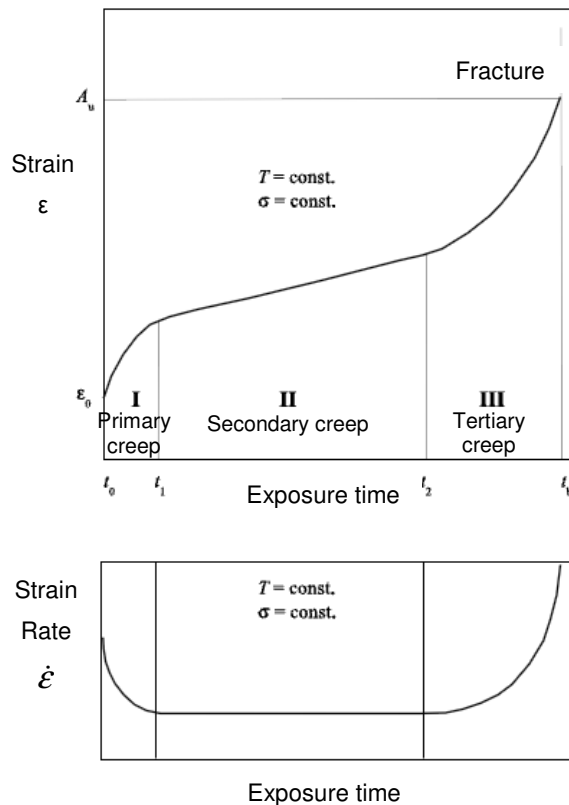
**Figure 2.7** Isothermal tensile creep test and creep curve

The constant load curve exhibits an instantaneous elongation which is made up of elastic, anelastic and plastic components as occurring in tensile tests at the first loading below the yield strength. A period of decelerating creep strain follows, called primary creep. Secondary creep is characterized by a more or less steady-state creep rate. Then accelerated creep until fracture is called tertiary creep.

Elastic strains are instantaneous and reversible. Anelastic strains are delayed and slowly reverse themselves when the stress is removed while plastic strains can be reversed only by the application of a reverse stress comparable in magnitude to the original forward stress. Both anelastic and plastic strains usually involve the glide of dislocations. Thermally activated plastic deformation occurs by diffusion of vacancies or of single atoms [42, 43].

Creep is a time-dependent deformation under a constant load. Creep is a thermally activated deformation process and for most metals, it is expected to become significant only at elevated temperatures ($T \geq 0.3\text{-}0.4 T_{Melt}$[K]). Typically, the

deformation history of a specimen during creep has the form shown in Figure 2.7. The extent of each regime and the mechanisms responsible for the deformation may differ. Broadly, primary creep represents the setting up of some kind of microstructural balance, which is then maintained during the quasi-steady state of secondary creep before breakdown begins as the tertiary regime is entered [24]. Generally, as temperature increases the creep strain rate goes up due to the increasing activation of the structural elements, e.g. increase of the mobility of dislocations or mobility of the atoms. If the temperature of the creep test is relatively low, $T<0.4T_{melt}$[K], the predominance of the slip type creep mechanism characteristic for the primary creep, is observed. Increasing the temperature to $0.4T_{melt}<T<0.5T_{melt}$[K] rises the thermal activity of the dislocations in the crystalline lattice structure. Hence, the dislocations can overcome the natural glide resistance of the crystal and other obstacles to move through the lattice. The dislocation creep mechanism diminishes the strain hardening effect in the material, although the cross slip mechanism, which mainly characterizes the primary creep, still predominates. The higher temperature, $0.5T_{melt}<T<0.6T_{melt}$[K], causes the dislocation creep to equilibrate the hardening mechanism and hence, the secondary creep phase may occur [44]. Pure metals would mainly deform by power law creep following the equation

$$\dot{\varepsilon}_{stat} = A * \sigma_A^n$$

where $\dot{\varepsilon}_{stat}$ is the strain rate, A is a constant, $\sigma_A$ is the applied stress and n is the creep exponent.

By scaling the results of the creep tests by $\dot{\varepsilon}_{stat}$ vs. $\sigma_A$ the resulting creep exponent, n, identifies the dominating creep mechanism for a certain range of $\sigma_A$. There are four main creep mechanisms identified by the different values of the creep exponent, n: 1) n=1 for diffusion creep, 2) n=2 for grain boundary sliding, 3) n=3 for viscous drag and 4) n=5 for dislocation climb. When creep takes place it is somehow difficult to determine the actual creep mechanism since there are always combinations of the mentioned mechanisms. The creep exponent gives information about the dominating creep mechanism occurring during the deformation process.

### 2.3.1 The creep mechanisms

#### *2.3.1.1 Dislocation creep giving power-law creep*

The stress required to deform plastically a crystalline material is that needed to make dislocations move. Their movement is resisted by a) the intrinsic lattice resistance and b) the obstructing effect of obstacles, like dissolved solute atoms, precipitates, dispersoids or other dislocations. Diffusion of atoms can unlock dislocations from obstacles in their path and the movement of these unlocked dislocations under the applied stress is what leads to dislocation creep.

*Dislocation climb*

Figure 2.8 shows a dislocation which cannot glide because a precipitate blocks its path. The glide force $\tau$b per unit length is balanced by the reaction $f_0$ from the precipitate. The component $\tau$b tanθ tries to push the dislocation out of its slip plane. The dislocation can move upwards if atoms at the bottom of the half plane are able to diffuse away, as it is shown in Figure 2.9. A mechanical force can do exactly the same thing and this is what leads to the diffusion of atoms away from the loaded dislocation, eating away its extra half-plane of atoms until it can clear the precipitate. The process is called climb, and since it requires diffusion, it can occur only when the temperature is above $0.3T_{melt}$. Climb unlocks dislocations from the precipitates which pin them and further slip can take place again (see Figure 2.10). Similar behaviour takes place for pinning by solute and by other dislocations. After a little glide the unlocked dislocations bump into the next obstacles and the whole cycle repeats itself. The dependence of the creep rate on applied stress $\sigma_A$ is due to the climb force: the higher $\sigma_A$, the higher the climb force $\tau$b tanθ, the more dislocations become unlocked per second, the more dislocations glide per second, and the higher is the strain rate [25]. The associated stress exponent is around 5 [22, 45].
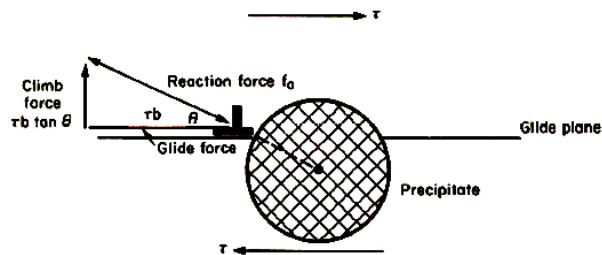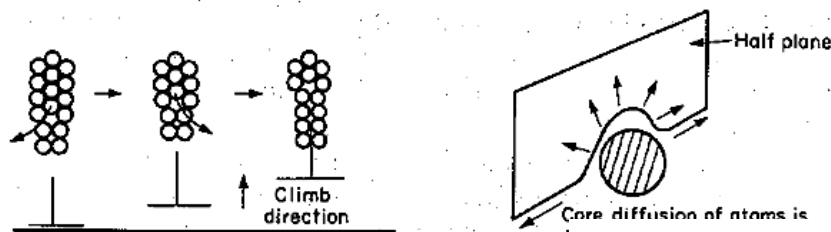
**Figure 2.8** The climb force on a dislocation [25]



**Figure 2.9** How diffusion leads to climb of an edge dislocation over a dispersoid [25]



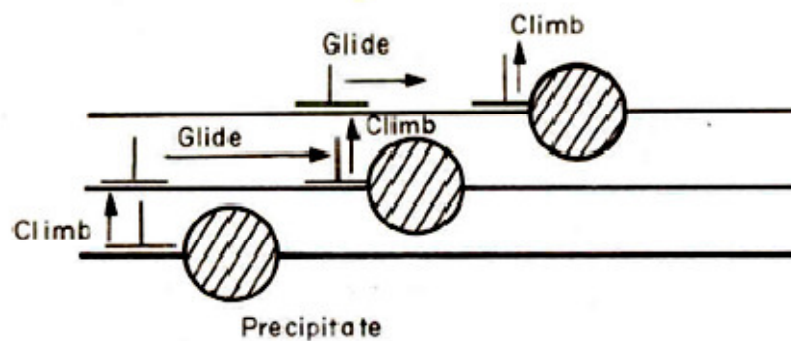**Figure 2.10** How the climb-glide sequence leads to creep [25]

## *Viscous Drag*

As reported by Mohamed et al. [46] the dislocations are attached to dissolved alloying atoms in the lattice. As temperature rises diffusion takes place and as a result of the applied stress the solute atoms are able to drag the dislocation through the lattice. The resulting stress exponent is stated to be n=3 [46].

### 2.3.1.2 Diffusion Creep

According to Figure 2.11 there are two mechanisms of diffusion creep: 1) the grain boundary diffusion or Coble creep and 2) the bulk diffusion or Nabarro Herring creep. As the stress is reduced, the rate of power-law creep falls quickly. But creep does not stop, instead, an alternative mechanism takes over. As Figure 2.11 shows, a polycrystal can extend in response to the applied stress σ by grain elongation, here, σ acts again as a mechanical driving force but, this time atoms diffuse from one set of the grain faces to the other and dislocations are not involved.

At high $T/T_{melt}$ this diffusion takes place through the crystal itself, that is, by bulk diffusion called Nabarro-Herring creep. The rate of creep is then obviously proportional to the diffusion coefficient D and to the stress σ and the creep rate varies as $1/d^2$ where d is the grain size. When d gets larger, atoms have to diffuse further. Assembling these facts leads to the equation

$$\dot{\varepsilon}_{stat} = \frac{C' \sigma e^{\frac{-Q}{RT}}}{d^2}$$

where C' is a constant, Q is the activation energy for creep, R is the universal gas constant and T is the absolute temperature.

At lower $T/T_{melt,}$ when bulk diffusion is slow, grain boundary diffusion takes over, but the creep rate is still proportional to σ. In order to that holes do not open up between the grains leading to the equation

$$\dot{\varepsilon}_{stat} = \frac{C'_{gb} \sigma e^{\frac{-Q_{gb}}{RT}}}{d^3}$$

where the bulk self diffusion coefficient C' must be replaced by the grain boundary self diffusion coefficient $C_{gb}$', which has roughly half the activation energy of self diffusion through the bulk.
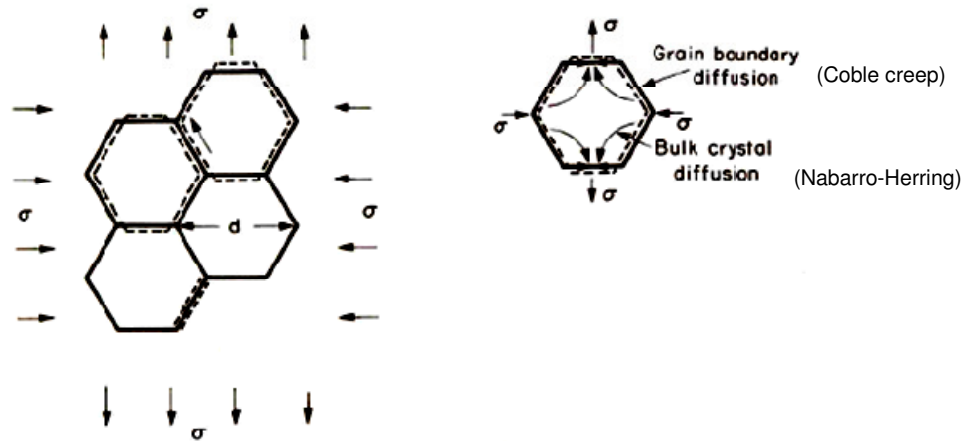
**Figure 2.11** How creep takes place by diffusion

### 2.3.1.3 Grain boundary sliding

Grain boundary sliding during creep of polycrystals is considered to be an independent deformation mechanism which follows specific relations involving stress, temperature, strain rate and grain size. Such mechanism will be rate controlling if it is more easily accomplished than diffusional creep or diffusion-controlled dislocation creep.

The stress, grain size and temperature dependences for grain boundary sliding are quite well established [47]. When grain boundary diffusion is rate controlling, White [48] showed that

$$\dot{\varepsilon}_{gbs} = \frac{C_{gb} D_{gb} b}{d^3} \left( \frac{\sigma}{E} \right)^2$$

whereas $C_{gb}$ is a constant, $D_{gb}$ is the grain boundary self diffusion coefficient, b is the burgers vector, d is the grain size, σ is the flow stress, E is the Young´s Modulus and $\dot{\varepsilon}_{gbs}$ is the creep rate when grain boundary diffusion is rate controlling (n=2).

They also showed that when lattice diffusion is rate controlling the creep rate is given by

$$\dot{\varepsilon}_{gbs} = \frac{C_L D_L}{d^2} \left( \frac{\sigma}{E} \right)^2$$

where $C_L$ is a constant and $D_L$ is the lattice self diffusion coefficient.

The equations of grain boundary sliding exhibit considerable similarity to the equations describing diffusional creep. Thus, Coble creep and grain boundary diffusion is rate controlled grain boundary sliding are dependent on the same temperature and grain size variables $\left( \dot{\varepsilon}_{stat} = \frac{D_{gb}}{d^3} \right)$. Similarly, both Nabarro Herring and lattice diffusion controlled grain boundary sliding are also dependent on the same temperature and grain size variables $\left( \dot{\varepsilon}_{stat} = \frac{D_L}{d^2} \right)$.

### 2.3.1.4  Overview of creep mechanisms using deformation maps

In Figure 2.12 the deformation map for pure nickel given by normalized shear stress vs. homologous temperature shows the most considerable creep mechanisms. It illustrates seven mechanism regions: a dislocation creep region (above $\tau/G > 3 \times 10^{-3}$), two diffusion controlled dislocation creep regions (low temperature and high temperature), two diffusional creep regions (Coble and Nabarro-Herring) and two grain boundary sliding regions (grain boundary controlled and lattice diffusion controlled).

The red line indicates the possible appearing creep mechanisms for a certain homologous temperature of 0.4 depending on the applied stress. In the lower stresses area mainly diffusional creep will dominate. Increasing the applied stress leads to grain boundary sliding and dislocation creep mechanisms (indicated as power law creep) and finally to conservative dislocation glide [47].
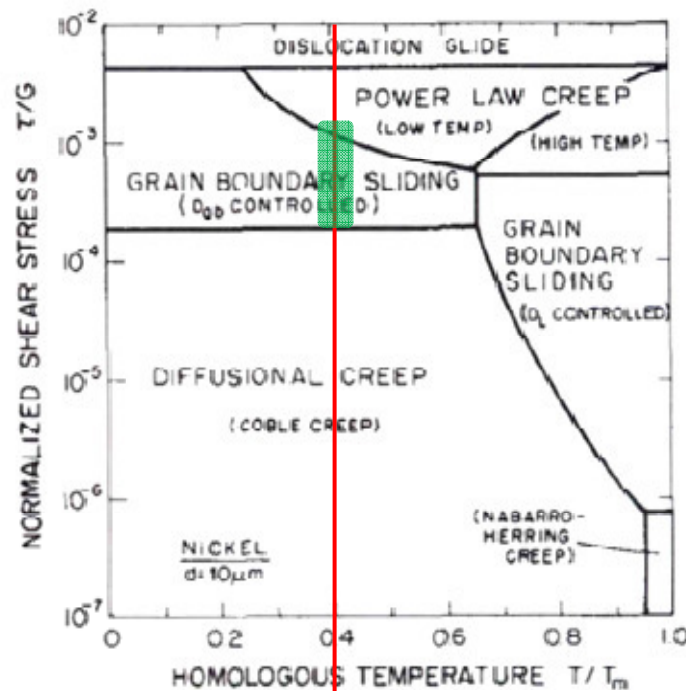
Chapter: State of the Art for PRMs and PM

**Figure 2.12** Ashby deformation map – normalized shear stress vs. homologous temperature (derived for Nickel in [47]). The range of creep tests reported here.

At high values of the applied stress, there is a transition from climb-controlled creep to glide-controlled creep. This leads to an observed exponential dependency of strain rate on the applied stress [49].

Power law break down means that the Norton equation is not valid anymore, because thermally activated deformation is increasingly superimposed to conservative dislocation movement with growing stress [50].

### 2.3.2  Creep of Dispersion Strengthened Metals

It is well established that the presence of dispersion of fine (~100nm) insoluble particles in a metal can raise the creep resistance substantially. This arises during power law creep primarily by the opposition to dislocation glide offered by the stable obstacles on the slip plane.

The pinning of a dislocation is associated with the concept of a threshold stress $\sigma_0$ below which there is essentially no climb. Under these circumstances, the strain rate is given by

$$\dot{\varepsilon}_s = A' \left( \frac{\sigma_A - \sigma_0}{G} \right)^n e^{\frac{-Q}{RT}}$$

where A' is a constant, Q is the activation energy, R is the gas constant and T is the absolute temperature, $\sigma_A$ is the applied stress and G is the shear modulus [51].

In practice, the threshold stress may be less than the Orowan stress, because climb processes can assist by-pass, particularly at higher temperatures. A further important point about dislocation creep in dispersion strengthened metals is that the presence of the particles tends to stabilize the dislocation substructure. It is clear that this stabilisation reduces dislocation creep.

One consequence of the reduced mobility of dislocations is, that the dispersion strengthened metals often creep by a diffusional mechanism at stresses and temperatures, where the corresponding pure metals would deform by power law creep ($\dot{\varepsilon}_{stat} = A^* \sigma^n$) [24].

In the case of extensively studied Ni based superalloys full or partial coalescence exists between γ' precipitation and the matrix. In PRM, there is a completely incoherent interface similar to a grain boundary [42].

### 2.3.3 Creep of PRMs

#### *2.3.3.1 The creep curve*

In [52] the isothermal tensile creep behaviour of an aluminium alloy unreinforced and reinforced with 10% $Al_2O_3$ particles [$6061/Al_2O_3/10_p$] was tested.

According to these studies the resulting creep curves show the well known three stages, whereas the secondary creep stage decreases when particles are added to the Al alloy. The largest part of the creep curve is occupied by the tertiary creep stage. These results are also found by other studies [53, 54].

#### *2.3.3.2 The secondary creep stage*

According to the results found in [52] the creep exponent of the $AlMg1SiCu/Al_2O_3/10_p$ at 300 °C in T6 condition is almost the same as it is for the unreinforced $AlMg_1SiCu$ matrix ($n \approx 5$). A 100% increase of the $Al_2O_3$ volume fraction results only in a small change of the creep rate curve. This means, that the amount of reinforcing phase seems to have a secondary influence on the creep behaviour. Whereas a T6S (S=>stabilisation) heat treatment leads to an increase of the strain rate of about two orders of magnitude. Amount and distribution of precipitates within the matrix alloy seem to have much more influence on the creep behaviour than the bigger particles. In T6S condition the creep exponent increases up to $n \approx 12$.

These results are verified by the findings for the PM produced AlMg4 alloy reinforced with SiC particles. Although this matrix has no hardening behaviour by precipitates it shows a quite high creep resistance. It is mentioned that due to the powder metallurgical route the oxide content increases what makes the creep resistance also increasing.

The influence of the temperature was found to be very important. Temperatures below 300 °C do not create big differences in the resulting creep curves of the different mentioned studies. Increasing creep temperature results in the development of large gaps between different studies. This comes from the different heating- and cooling rates, for instance. Precipitation produces different materials if the heating phase takes one hour or only half an hour.

Chapter: State of the Art for PRMs and PM

With temperature the creep exponent decreases for the unreinforced matrix as well as for the PRM [52]. All the measured results can be connected by a straight line. This means, that there is no obvious change in the deformation mechanisms within the tested load and temperature range.

The creep behaviour from both, the unreinforced matrix and the PRM, in [52] are compared by utilizing two different creep temperatures. Temperatures of the creep tests ranging from 250°C to 300°C yield strain rates which are two orders of magnitude higher for the unreinforced matrix than for with the PRM. This means that the presence of the particles reduces the creep resistance. At 250°C a reduplication of the amount of added particles leads only to a slight reduction of the creep resistance. At 300°C the opposite can be obtained. Again with these results the weak influence of the present amount of the reinforcing particles can be seen.

### 2.3.3.3 Effect of particle size on creep resistance

There are controversial findings regarding the effect of the bigger particles introduced to an aluminum alloy on the creep resistance resulting from different studies. In ranges of low strain rate ($\dot{\varepsilon}_{stat} \leq 10^{-6} s^{-1}$) it was reported [52, 55, 56] that the introduction of particles leads to a reduction of the creep resistance. On the other hand it is reported [57, 58, 59, 60] that there is an increase of the creep resistance obtained by adding particles, whereas [57, 58] observed an inversion of this effect at higher strain rates.

Qin et al [61] investigated the effect of particle shape on ductility of SiCp reinforced 6061 Al matrix composites with the result that there is a localisation of deformation due to the pointed corners of reinforcing particles compared to more spherical particles. According to their studies there is a much larger residual plastic strain in this area than the area of the matrix near a plane interface. When these pointed particles are elongated along the tensile direction after extrusion, tensile ductility of the composite will be reduced owing to the cooperative effect of serious in situ plastic deformations near the pointed corners. They found that the distribution of thermal residual stress in the particle also varies with the particle shape. There is a serious stress concentration in the pointed particle corner which increases rapidly with

decreasing pointed corner degree of particle. After SiC particles were blunted, eliminating the pointed particle corners the plastic strain concentration in the matrix around the pointed particle corners decrease and the possibility of the particle corner fracturing so that ductility of BM PRMs is improved [61, 62]. Spowart et al [63] linked these localized stresses to void nucleation in the matrix adjacent to the particles during tensile loading. The incorporation of a less-angular reinforcement phase is, therefore, seen as a potential route to improve the ductility of discontinuously reinforced PRMs, by reducing the propensity for tensile failure by the commonly-observed void growth and coalescence mechanism.

### 2.3.3.4 Generation of Dislocations

<u>Dislocations by Frank-Read Sources</u>

The first model proposed by Frank and Read resembles the model proposed to account for the role of dislocations in crystal growth. In an irregular array some dislocations lie partly in their slip planes and partly in other planes. This is illustrated in Figure 2.13 a). The length BC of the edge dislocation ABC lies in the slip plane CEF and can move freely in this plane. The length AB is not in the slip plane and is sessile. Thus BC will be anchored at one end and can move by rotating about B. The dislocation will tend to wind up into a spiral as illustrated in Figure 2.13 b). Two things are noted about this mechanism: 1) each revolution around B produces a displacement of the crystal above the slip plane by one atom spacing b. The progress is regenerative since the progress can repeat itself so that n revolutions will produce a displacement nb. A large slip step will be produced at the surface of the crystal. 2) The spiralling around B results in an increase in the total length of dislocation line.

The well known Frank-Read source is an extension of the above mechanism to a dislocation line held at each end and is illustrated in Figure 2.14. The dislocation line DD' lies in a slip plane represented by the plane of the paper. It is held at both ends by an unspecified barrier which may be dislocation intersections or nodes, composite jogs, precipitates or reinforcement phases. An applied stress $\tau$ tends to make the dislocation bow out and the radius of curvature R depends on the stress. As the dislocation bows out under an increasing stress a minimum value of R is reached at

the position in Figure 2.14 b). The radius of curvature will be L/2, where L is the length of DD'. The dislocation will continue to expand under a decreasing stress. The subsequent events are shown in Figure 2.14 c)-e). The dislocation forms a large kidney-shaped loop and when the segments at m and n meet they will annihilate each other to form a large loop and a new dislocation DD'. At sites k and l (Figure 2.14 c)) as well as at m and n (Figure 2.14 d)) the dislocation will be in positive and negative edge orientation and since, they have a mutual attraction, they will combine and annihilate at this point. The process is regenerative and a series of loops can be produced [64].



(a)                    (b)
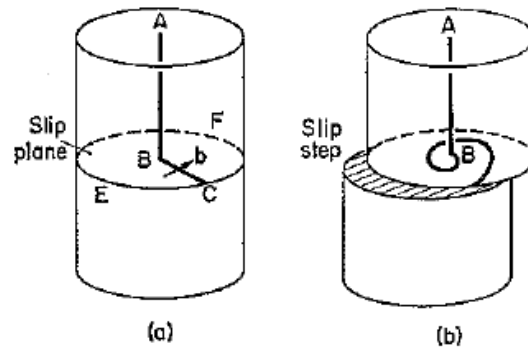
**Figure 2.13** Single ended Frank-Read source. a) Dislocation lying partly in the slip plane CEF. b) Formation of a slip step and spiral dislocation by rotation of BC about B [64]
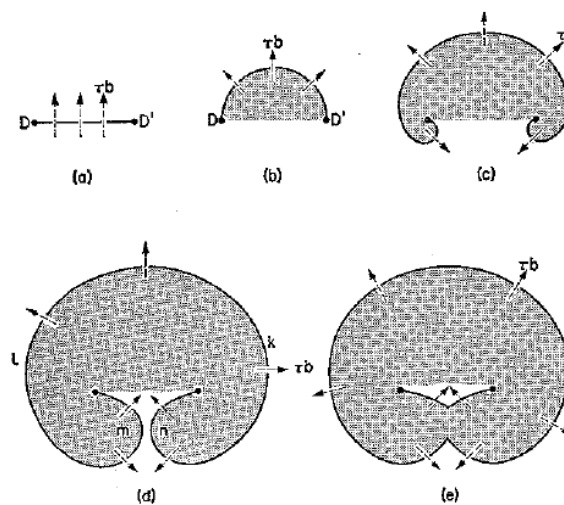


**Figure 2.14** Representation of the dislocation movement in the Frank-Read source. Unit slip has occurred in the shaded area [64]

*Influence of the Particle size*

There are various mechanisms to generate dislocations. The most likely case in the present study is the thermal misfit. In the most commonly used dislocation-based model, misfitting spherical particles of radius $r_p$ fully relax through the emission of prismatic dislocation loops of radius $r_p \sqrt{2}$, generating a dislocation density

$$\rho_g \leq \frac{12}{\sqrt{2}} \frac{\Delta\alpha\Delta T}{r_p b} \frac{f}{(1-f)}$$

where f is the volume fraction of the particles, b is the Burgers vector, $\Delta\alpha$ is the difference of CTE and $\Delta T$ is the temperature difference [22].

A composite system consisting of a matrix with embedded assumed spherical particles as in the present study is considered. The particles have an isotropic coefficient of thermal expansion (CTE), $\alpha_p$, different from that of the matrix, $\alpha_m$. When the system is subjected to temperature fluctuation $\Delta T$, the constrained strain mismatch, $\Delta\varepsilon^c$, is given by the following equation [65]:

$$\Delta\varepsilon^c = \frac{3K_p \Delta T(\alpha_m - \alpha_p)}{3K_p + 4G_m}$$

where $G_m$ is the shear modulus of the matrix and $K_p$ the bulk modulus of the particle. The dislocation generation mechanism map (seen in Figure 2.15) shows how the dislocation generation and instability conditions change with mismatch strain, applied load and particle size. The horizontal axis represents the applied axial load $\sigma/G_m$, while the left vertical axis represents the mismatch strain $\Delta\varepsilon^c$, and the right one the temperature change $\Delta T$. Line G represents the lower bound of dislocation generation. Line I remarks the instability line whereas line W identifies the upper bound for theoretical strength. Lines G and I meet at point M and continue in the horizontal part MN with increasing stress. Four regions in the map can be identified: 1) the inactive zone: in this region the mismatch strain or applied load, is insufficient to generate dislocations. 2) The loop segment zone: In this region the mismatch strain, or load

level, is sufficient to generate a dislocation loop segment from the interface. 3) The emission zone: In this region, the mismatch or load level is so high that dislocations are emitted and 4) the maximum strain and temperature difference out of normal experimental conditions and therefore not described. The shape of the map change when the particle sizes change. Figure 2.16 shows the mechanism map for three different particle sizes. The map demonstrates the substantial effect of particle size on dislocation generation and emission conditions. The lower generation bound move left-downwards with increasing particle size. Such size dependence indicates that for a given particle volume fraction and morphology, mismatch enhanced plasticity can be switched off, if the particle size is sufficiently reduced.

Each point defect produces a stress field in the surrounding lattice and will therefore interact with dislocations. Additional work will be required to separate the defect and the dislocation and the crystal will be stronger. The hydrostatic compressive stresses around an atom will be relaxed if the atom is situated in the dilated region below the extra half plane of the edge dislocation and therefore the atom will be attracted to the dilated region and repelled from the compressed region.

The stress component $\tau_{xz}$ in the matrix around the particle consist of two contributions:

$$\tau_{xz} = \tau_{xz}^{m} + \tau_{xz}^{a}$$

where
$$\tau_{xz}^{m} = \frac{6\mu a_{p}^{3} xz}{r^{5}} \Delta \varepsilon^{c} \qquad \text{for } r \geq a_{p}$$

where $a_p$ is the particle radius and $r^2 = x^2 + y^2 + z^2$,

and
$$\tau_{xz}^{a} = \sigma \overline{\tau}_{xz}^{a}(r)$$

where the dimensionless stress distribution function, $\overline{\tau}_{xz}^{a}$, is obtained by a numerical procedure.

*Very finely Dispersed Particles*

The wavelength of the internal stress field $\Omega$ is very small and for individual atoms is $b/c^{1/3}$ where b is the interatomic spacing and the concentration c. The local stress fields are not sufficient to bend the dislocation round each individual particle and

$$\Omega \ll R$$

where R is the maximum bending. The dislocation therefore over-rides partially the strain field of the particles, but since it is flexible it takes up, under a given shear stress, a position where there is a net positive interaction energy.

*Large, Widely separated Particles*

The mean distance between particles is much larger than the limiting radius of the dislocation, thus

$$\Omega \gg R$$

The crystal is soft and the dislocation can bow out between the particles. The flow stress is that required to bend the dislocations to a radius $\frac{1}{2}\Omega$, i.e.

$$\tau \cong \frac{Gb}{\Omega}$$

As each dislocation bows round the precipitate it will leave a loop of dislocation. This will result in an increase in flow stress with increasing strain, due to the back stress resulting from the dislocation rings around the precipitate.
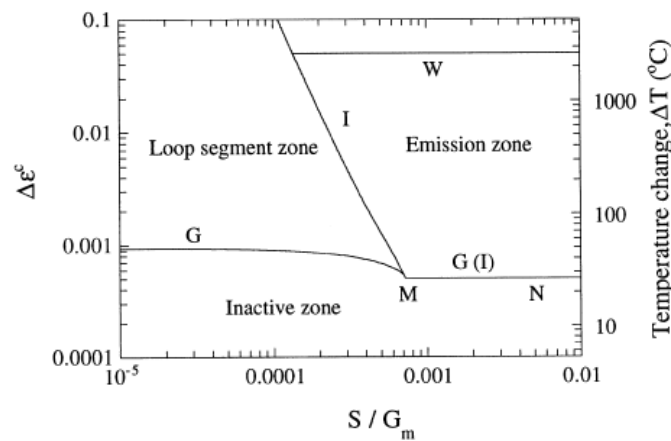


**Figure 2.15** Dislocation generation mechanism map for particle size $a_p/b=3.6\times10^3$ [65] assuming $\Delta\alpha=19\times10^{-6}/°C$ typical for Al-SiC composites
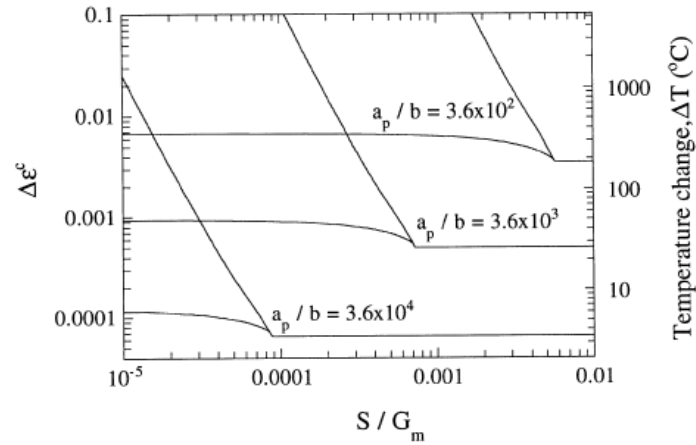
**Figure 2.16** Dislocation generation mechanism map for various particle sizes [65] assuming $\Delta\alpha=19\times10^{-6}/°C$ typical for Al-SiC composites

### 2.3.4  Threshold stress creep behaviour

As reported, dispersion strengthened materials show very high values of apparent stress exponent. This fact suggests that the creep behaviour of such composites may be explained in terms of the existence of a threshold stress for creep, although the origin and the characteristics of the threshold stress are still controversial [9, 66, 67, 68, 100]. During the last decades several researchers investigated the creep behaviour of discontinuously-reinforced aluminium-based composites. It is well-established that the presence of a dispersion of fine (~100nm or less) insoluble particles in a metal can raise the creep resistance substantially, even when constituting only a small overall volume fraction (<1vol%). This arises during power law creep primarily through the opposition to dislocation glide offered by the stable obstacles on the slip plane. Orowan bowing is necessary for dislocations to by-pass the particles by glide, requiring an applied stress given approximately by

$$\sigma_{Orow} \approx \frac{G*b}{L}$$

where G is the shear modulus, b is the Burgers vector and L is the particle separation [16].

There is considerable evidence for the presence of a threshold stress in the high temperature creep of metal matrix composites [10, 16, 69, 70, 71], where the threshold stress is defined as a lower limiting stress below which no measurable strain rate can be achieved. When a threshold stress is present, the steady-state creep rate, $\dot{\varepsilon}_{stat}$, is expressed by a relationship of the form

$$\dot{\varepsilon}_{stat} = \frac{ADGb}{kT}\left(\frac{\sigma - \sigma_0}{G}\right)^n$$

where D is the appropriate diffusion coefficient [D=$D_0$ exp(-Q/RT), where $D_0$ is a frequency factor, Q is the activation energy, R is the gas constant and T is the absolute temperature], G is the shear modulus, b is the Burgers vector, k is Boltzmann´s constant, $\sigma$ is the applied stress, $\sigma_0$ is the threshold stress, n is the stress exponent and A is a dimensionless constant.

In practice, creep tests are conducted under conditions where the value of $\sigma_0$ is not known and it is a standard procedure to plot the experimental data in logarithmic coordinates as $\dot{\varepsilon}$ versus $\sigma$. When $\sigma_0$=0, all of the data points lie along a line with a slope which defines the true stress exponent, n. However when $\sigma_0$ is a reasonable fraction of the applied stress, the data points fall along a line having a slope which continuously increases with decreasing applied stress, so that a small change in the applied stress in the low strain rate region leads to a very significant change in the measured strain rate. The approximate slope of this curve defines the apparent stress exponent, $n_a$ [72].

In the presence of a threshold stress, it is possible to estimate the magnitude of $\sigma_0$ by plotting linear axes as $\dot{\varepsilon}^{\frac{1}{n}}$ against $\sigma$ and extrapolating linearly to zero strain rate [72]. However, a plot of this type requires a judicious selection of the appropriate value of the true stress exponent, n. Analyses are generally undertaken using values of n of n=1 for diffusion creep, n=2 for grain boundary sliding, n=3 for viscous drag and n=5 for dislocation climb, respectively.

Numerous attempts have been made to identify the appropriate value of n by preparing separate plots for each of these values of n and then selecting the plot

where all of the data fall most closely onto a straight, rather than a curved, line. However it has been noted in several investigations that the experimental data extend over a rather limited range of strain rates so that a linear relationship can be achieved with at least two different values of n [71]. As a result, Cadek and Sustek [71] proposed that it was necessary to obtain experimental data over not less than five orders of magnitude of strain rate while the same creep mechanism should be dominant.

### 2.3.4.1 The nature of the threshold stress

The threshold stress is defined as the applied stress to which zero creep strain rate corresponds [73, 71].

The threshold stress increases with volume fraction of SiC particulates as it was found by Pandey et al [5]. They suggested the load transfer as a possible origin of the threshold creep behaviour of SiCp-Al composites. The values for threshold stress in oxide dispersion strengthened Al-30SiCp are higher by factor of about 3.5 than those in the Al-30SiCp composite, as it was shown by Cadek et al [73].

The documented creep behaviour for Al 2024PM alloy in [69] is very similar to that reported for the 6061PM alloy [74, 75] as well as to that reported for the 2124PM alloy [76, 75]. In these studies [69, 74, 76] the threshold stress was attributed to the interaction between mobile dislocations and the fine incoherent oxide particles which are introduced during the PM processing. This behaviour is also similar to several dispersion strengthened alloys where the threshold stress is associated with the presence of a fine dispersion of stable incoherent particles. It is appropriate to consider the three possible mechanisms that are used to explain the origin and magnitude of the threshold stress in dispersion strengthened alloys:

- First, the threshold stress may be equal to the Orowan stress, $\sigma_0$, which is required to bow the dislocations between the particles.
- Second, the threshold stress may be associated with a back stress, $\sigma_b$, which is needed to create the additional dislocation segment as the dislocation surmounts the obstacle by local climb.

- Third, the threshold stress may represent the detachment stress, $\sigma_d$, associated with detaching a dislocation from an attractive particle.

### 2.3.4.2 Calculation of the threshold stress

Having acknowledged that the experimentally observed threshold stress could not be explained by a simple Orowan mechanism between dislocations and the reinforcement particles, it was suggested that the cause of the threshold stress must be dislocation interactions with the fine oxide dispersion in the matrix, resulting from the powder processing route. Using a thermal detachment stress model, they obtained fairly good agreement between their predictions and the experimental threshold stresses.

Pandey et al. reported that the threshold stress is dependent on the reinforcement volume fraction [77]. Winand also observed a reinforcement volume fraction dependence for the threshold stress at 3µm particle sizes [78]. However, it is clear that the available explanations for the existence of a threshold stress in discontinuously reinforced MMCs do not provide an accurate picture of the processes that are actually occurring.

In alloys where the creep exponent increases reaching values bigger than 10, the existence of a threshold stress, $\sigma_{th}$, is suggested.

The calculation of the threshold stress, $\sigma_{th}$, for a certain load range always needs the assumption of the dominating dislocation creep mechanisms either viscous drag (n=3) or dislocation climbing (n=5). Scaling by $\dot{\varepsilon}^{\frac{1}{n}}{}_{stat}$ vs. the applied stress, $\sigma_A$, and calculating the correlation coefficient, R, leads to the result of the actually predominating creep mechanism by choosing that creep mechanism with the best linear fit [22]. Extrapolation to zero gives the result of the threshold stress for creep. Figure 2.17 illustrates the procedure of calculating the threshold stress by means of the example of unreinforced BM 2124 alloy. In this case n=5 is suggested since it obtains the best linear fitting of the rescaled data points as the value of R indicates.

In the present study the data of the high stress region were calculated by assuming n=3 and n=5 by a scale $\dot{\varepsilon}^{\frac{1}{n}}{}_{stat}$, vs. the applied stress, $\sigma_A$. It was found that the value

for the correlation coefficient gives the best fitting by assuming the dominating creep mechanism for this region is dislocation climb with a corresponding n=5. The resulting threshold stress $\sigma_{th}$=26+/-4MPa depends on the reinforcing phase and decreases with increasing SiC particles. The result for n=3 of 30+/-3MPa is not far off, but threshold stress for viscous drag is less probable.

Since the true stress exponent selected for the calculation of the threshold stress contains assumptions about the dominant creep mechanism that is operating, it is essential to check the validity of this choice by checking for a linear fit of the plot.

If the interparticle spacing is larger than the subgrain spacing, then it is unlikely that structure invariant creep is occurring, in which case, it would be appropriate to select 5 as the true stress exponent.
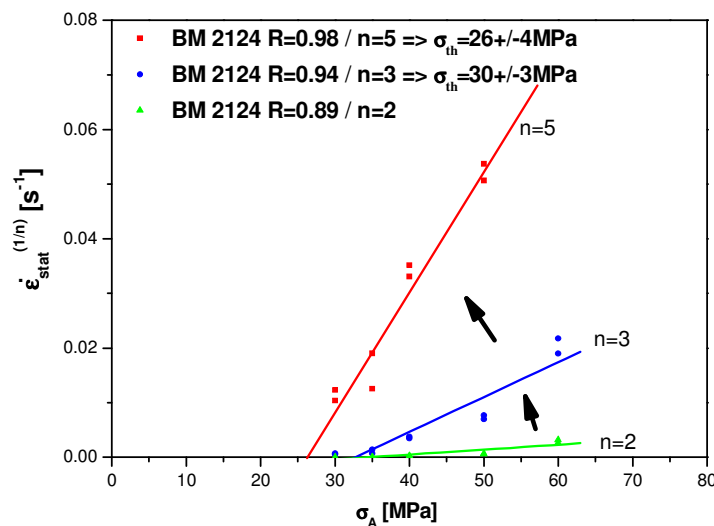


**Figure 2.17** Illustration of the calculation of the different values for the creep exponent n

# 3 Experimental

The creep behaviour of two different Al-based matrices reinforced with SiC particulates as well as the unreinforced matrices was investigated in the present work. The introduced reinforcing SiC particles are of different initial sizes in order to describe the dependence of the creep resistance on the particle size.

The powders of the matrices and the SiC particulates were mixed using two different routes with subsequent extrusion. On the one hand, the mix was done by means of a high energy ball milling technique, designated as BM, and on the other hand, it was done using a low energy wet blending technique further designated WB.

In this chapter the materials, the blending routes, the resulting differences as well as the experimental procedures are described.

## 3.1 Description of the Materials investigated

### 3.1.1 The Unreinforced Alloys

There are two different powders of aluminium alloys utilised each as matrix material for the composites: AA 2124 (AlCu4) and AA 6061 (AlMg1SiCu).

2xxx or aluminium-copper alloys are precipitation hardening alloys and usually complex because of the many additives used for strength, corrosion resistance, or grain structure control.

6xxx or aluminium-magnesium-silicon alloys are also age hardening alloys based on the $Mg_2Si$ precipitation [79]. The chemical composition of these alloys is shown in Table 3.1.

The 2124 as well as the 6061 alloy powders were produced by Alpoco, Aluminium Powder Company, United Kingdom and provided by CENIM-Madrid.

Both Al alloys were produced by means of PM with powder particle sizes of <75µm. In case of the 2124 alloy, the as-produced powder was extruded without any further treatment as well as after 4 hours BM. In this way the effect of 4 hours BM on the

resulting material can be determined regarding the microstructure as well as the resulting mechanical properties. The 6061 alloy was extruded after 4 hours BM.

| Alloy | Si [wt%] | Fe [wt%] | Cu [wt%] | Mn [wt%] | Mg [wt%] | Cr [wt%] | Ni [wt%] | Zn [wt%] | Ti [wt%] |
|---|---|---|---|---|---|---|---|---|---|
| AA 2124[80] | 0.03 | 0.07 | 3.93 | 0.6 | 1.46 | ≤0.01 | ≤0.01 | ≤0.01 | ≤0.01 |
| BM 2124[80] | 0.03 | 0.08 | 3.9 | 0.6 | 1.45 | ≤0.01 | ≤0.01 | ≤0.01 | ≤0.01 |
| Limits AA2124 [79] | 0.2 max. | 0.3 max. | 3.8-4.9 | 0.3-0.9 | 1.2-1.8 | 0.1 max. | - | 0.25 max. | 0.15 max. |
| AA 6061[81] | 0.45 | 0.15 | 0.27 | ≤0.01 | 0.96 | 0.16 | - | - | - |
| Limits AA6061 [79] | 0.4-0.8 | 0.7 max. | 0.15-0.4 | 0.15 max. | 0.8-1.2 | 0.04-0.35 | | 0.25 max. | 0.15 max. |

**Table 3.1** Chemical composition of the alloys used as matrix material

### 3.1.2  The Silicon Carbide Particles

Silicon carbide (SiC) is a ceramic compound. SiC in particulate form has been available for a long time. Particulate SiC is processed by reacting silica in the form of sand and carbon in the form of coke at 2400°C in an electric furnace. The SiC produced in the form of large granulates is subsequently processed to the desired size by ESK [17]. The shape of the utilized SiC particles is irregular and sharp etched.

The above mentioned Al-alloys, 2124 and 6061, were reinforced with SiC-particles of different initial sizes in order to investigate the influence of the reinforcing particle size on the creep resistance. The initial SiC-particle sizes used can be seen in Table 3.2 [82]. Hereby, the designations F360, F600 and F1000 correspond to the particle sizes <20µm, <10µm and <5µm, respectively (see Figure 3.1). Three values in order to characterize the powders are given: 1) the P97-value is the 97% percentile what

means that 97% of the particle number is below this value, 2) the median what indicates that 50% of the particle number is above and 50% is below this value and 3) the P6-value what indicates that 6% of the particle number is below this value.

| Grit designation | P97-value-max. [µm] | Median grain size $d_{s50}$-value [µm] | P6-value-min. [µm] |
|---|---|---|---|
| F 360 | 40 | 22.8 ± 1.5 | 12 |
| F 600 | 19 | 9.3 ± 1.0 | 3 |
| F1000 | 10 | 4.5 ± 0.8 | 1 |

**Table 3.2** Initial SiC-particle sizes used to reinforce the aluminium alloys by creating PRMs
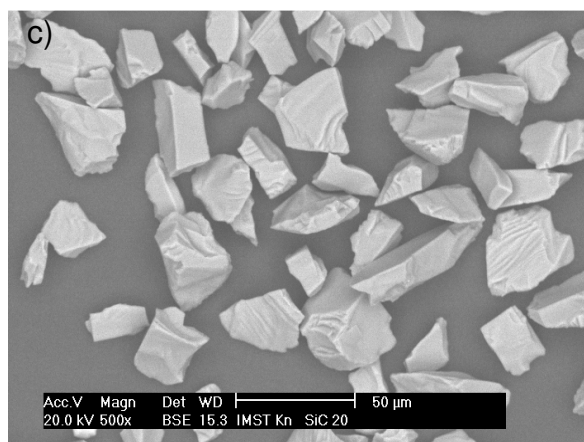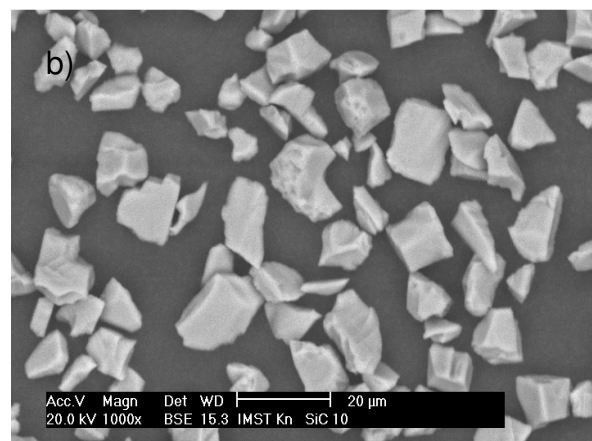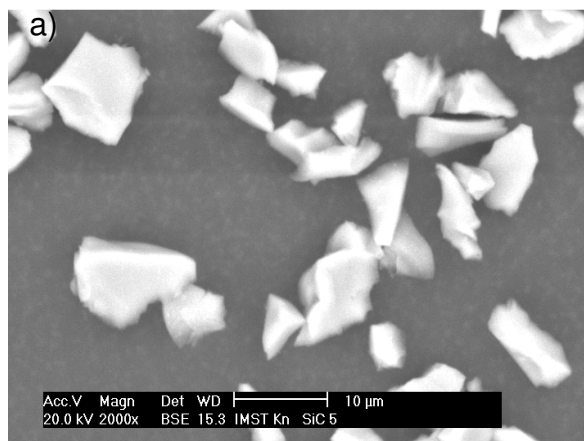


**Figure 3.1** Images of the SiC particles a) <5µm (F1000), b) <10µm (F600) and c) <20µm (F360)

SiC is resistant to acids and alkalis and it resists heating to around 1500 °C in air. It decomposes in liquid Al with less than 7wt% Si into Si and $Al_4C_3$. Therefore the investigated compositions can only be produced by PM. Its properties can be seen in Table 3.3 [82]. As SiC is conventionally used as grinding material due to the below mentioned properties, the workability of the PRMs reinforced with SiC decreases considerably, what makes it necessary to use hard metal or diamond tools to process these materials.

| Chemical formula | | SiC |
|---|---|---|
| Relative molar mass | [g/mol] | 40.097 |
| Chemical composition | [%] | Si 70.05 / C 29.95 |
| Density | [g/cm³] | 3,21 |
| Young´s Modulus | [GPa] | 200 - 300 |
| Hardness -Mohs | | 9.5 - 9.75 |
| Melting point | [°C] | >2300 |
| Heat capacity 20°C / 1000°C | [J/g * K] | 0.67 / 1.27 |
| Thermal conductivity 20°C / 1400°C | [kJ/m * h *K] | 150 / 54 |
| Linear thermal expansion 20-1400 °C | $[K^{-1}]$ | $4.7 * 10^{-6}$ |
| Entropy S° $_{25°C}$ | [J/mol * K] | 16.50 ±0.13 |
| Specific electrical resistivity | [Ω * cm] | $0.1 - 1*10^{12}$ |

**Table 3.3** Properties of the SiC particles used typically to reinforce Al alloys

### 3.1.3  Conducted Mixing and Blending Techniques

Two different routes to mix the alloys and the SiC powders were used to produce the PRMs at CENIM-Madrid.

The low energy mixing technique was carried out using different initial size of alloy powder and of the SiC particles. This blending was done within cyclohexane for a period of 24 hours and subsequent evaporating the liquid. Cyclohexane is a cycloalkane with the molecular formula $C_6H_{12}$. Cyclohexane is used as a nonpolar solvent for the chemical industry, and also as a raw material for industrial production. This process is called wet blending (WB). During WB the particles are neither

deformed nor fractured. The blending time of 24 hours was chosen because of the relatively high size ratio between the matrix powder particles and the SiC-particles. The smaller the ratio is the better is the blending [17]. In this case the ratio is 15 and 3.75 for the 2124 as well as the 6061 matrix powder and the <5µm and <20µm SiC-particles, respectively (75/5 and 75/20). As these values are constant, the blending time and the blended amount of powder was determined by doing some blending experiments. It was found experimentally that the optimal amount of blended powder is 100g and 200g for the <5µm and the <20µm SiC-particles, respectively. After blending the cyclohexane was evaporated and the powder was dried and cold compacted within Al-tubes and subsequently extruded.

High energy BM was the other blending technique which was carried out to produce the metal matrix composites with 2124 matrix alloy and SiC particles of initial sizes <5µm, <10µm and <20µm. BM was done for a period of 4 hours as it was determined experimentally by microscopic investigations after testing 2, 4, 6, 8 and 10 hours respectively. A planetary milling device with 4 containers, see Figure 3.2, was used to obtain the PRMs. The rotating velocity of the containers was 200 rpm.
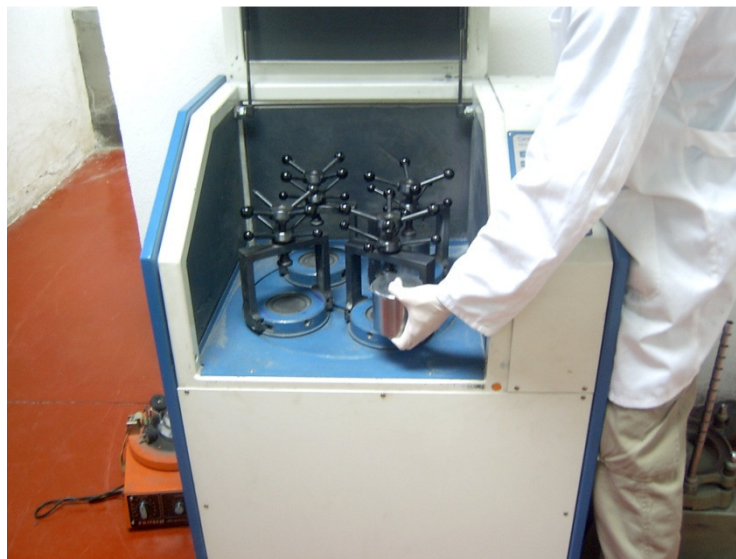


**Figure 3.2** Planetary ball milling device with four containers used to mix the powders with a duration of 4 hours

An amount of 60g of powder mixture of matrix and SiC was blended in each of the container. 12 steel balls with a diameter of 14.4mm and 31g weight each were placed in each container to blend the alloy and the SiC powder. The powder particles are deformed, fractured and cold welded during ball milling [4, 83]. The blended powder was cold compacted within Al-tubes and subsequently extruded.

### 3.1.4 Hot Extrusion

After blending the powder was cold compacted and hot extruded. Hot extrusion is the process of forcing a heated billet of 40mm diameter to flow through a shaped die opening. The temperature at which extrusion is performed depends on the material being extruded. Billet temperatures for aluminium alloys generally range from 300 to 595°C. Hot extrusion is used to produce long, straight metal products of constant cross section, such as bars, solid and hollow sections, tubes, wires, strips, from materials that cannot be formed by cold extrusion. In the present study the type of forward non lubricated extrusion was conducted [79].

Hot extrusion combines hot compacting and hot mechanical working, yielding a fully dense product. Large hydrostatic compressive forces occur, and a unidirectional force component makes the compact flow through the die [4].

In the present case a die with a diameter 11.8mm was used and the hot extrusion was carried out at 450°C in order to obtain the bars, see Figure 3.3. The achieved deformation ratio (billet/bar) is 3.4.
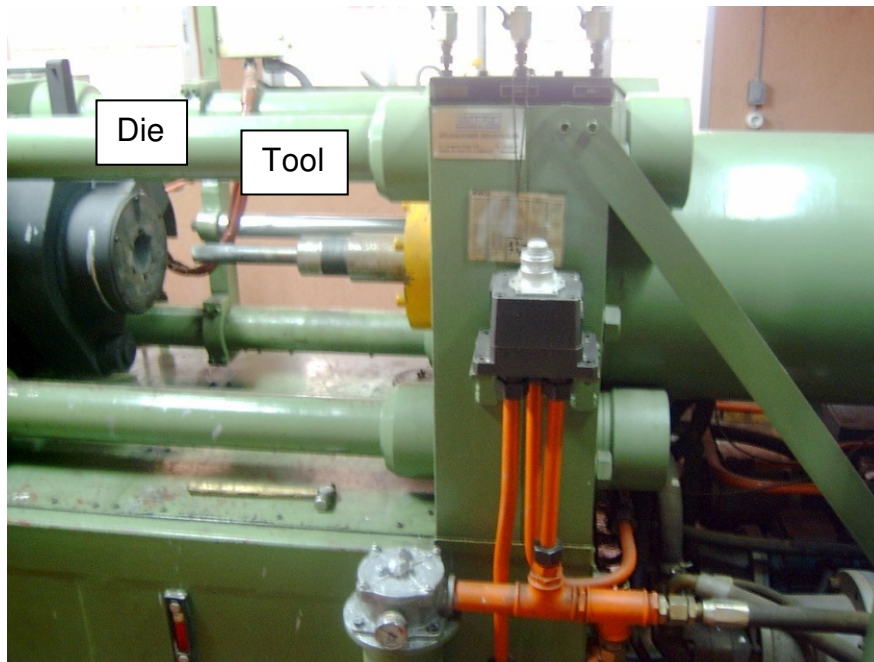
**Figure 3.3** Extrusion device used to fabricate the introduced materials at 450°C and a diameter of 11.8mm

### 3.1.5  The Particle Reinforced Composites

There are two matrices reinforced with SiC particles of different sizes produced to investigate and to compare each other as well as to compare with the corresponding unreinforced matrices. The matrices in the present study are AA2124 (AlCu4) and AA6061 (AlMg1SiCu), respectively, as mentioned in section 3.1.1.

Different SiC particle sizes were utilised to reinforce the matrices all with the same volume fraction of 25vol%. The initial SiC particle sizes were <5µm, <10µm and <20µm in order to investigate the effect of reinforcement particle size on materials properties, see section 3.1.2.

The microstructural differences between the BM and WB PRMs can be clearly seen in Figure 3.4. The SiC particles are fractured during BM causing the formation of sub-µm particles according to Chapter 2, section 1.2.1.2. This results in a multimodal particle size distribution for the BM composites (see Figure 3.4 a)).

On the other hand, the WB materials show a monomodal particle size distribution due to the absence of the fractured sub-μm particles (see Figure 3.4b)). The SiC particles of the WB material have sharper edges than those of the BM PRMs.

All the images exhibit some elongated particle free zones which result from the hot extrusion process of matrix grains. An alignment of the SiC particles in direction of extrusion is evident in the materials mixed by WB. This alignment is hardly observed in the materials prepared by BM due to the more spherical shape of the fractured particles.

The chemical composition of the BM and WB PRMs can be found in Table 3.4. The corresponding measurements were carried out by means of ICP-analysis of AMAG rolling GmbH. The Si content is increased only slightly (SiC is not desintegrated) and the Fe content insignificantly. Results of conducted measurements of the oxygen contents carried out by means of LECO system done by Institute of Chemical Technologies and Analytics are compared and given in Table 3.5. The BM material contains about 2-3 times more oxygen (i.e. oxides) than the WB material or mixed powder compacts.

| Matrix Alloy | Si [wt%] | Fe [wt%] | Cu [wt%] | Mn [wt%] | Mg [wt%] | Cr, Ni, Zn, Ti |
|---|---|---|---|---|---|---|
| BM 2124/SiC/25p<5μm[80] | 0.25 | 0.09 | 3.7 | 0.58 | 1.39 | ≤ 0.01 |
| WB 2124/SiC/25p<5μm[80] | 0.20 | 0.09 | 3.8 | 0.59 | 1.43 | ≤ 0.01 |

**Table 3.4** Chemical composition of the BM and WB PRMs

| Material | Oxygen-Fraction [wt%] | Ratio (BM/without BM) |
|---|---|---|
| Unreinforced 2124 without BM T4S | 0.05 ± 0.01% | (0.17/0.05)=3.4 |
| Unreinforced 6061 without BM T4S | 0.18 ± 0.02% | |
| Unreinforced 2124 with BM T4S | 0.17 ± 0.06% | (0.4/0.18)=2.2 |
| Unreinforced 6061 with BM T4S | 0.4 ± 0.1% | |
| WB 2124/SiC/25p<5μm T4S | 0.19 ± 0.02% | (0.54/0.19)=2.8 |
| BM 2124/SiC/25p<5μm T4S | 0.54 ± 0.07% | (0.39/0.19)=2 |
| BM 2124/SiC/25p<20μm T4S | 0.39 ± 0.04% | |

**Table 3.5** Oxygen fraction of the unreinforced 2124 without BM, unreinforced 2124 with BM, WB 2124/SiC/25p<5μm, BM 2124/SiC/25p<5μm, BM 2124/SiC/25p<20μm

Chapter: Experimental
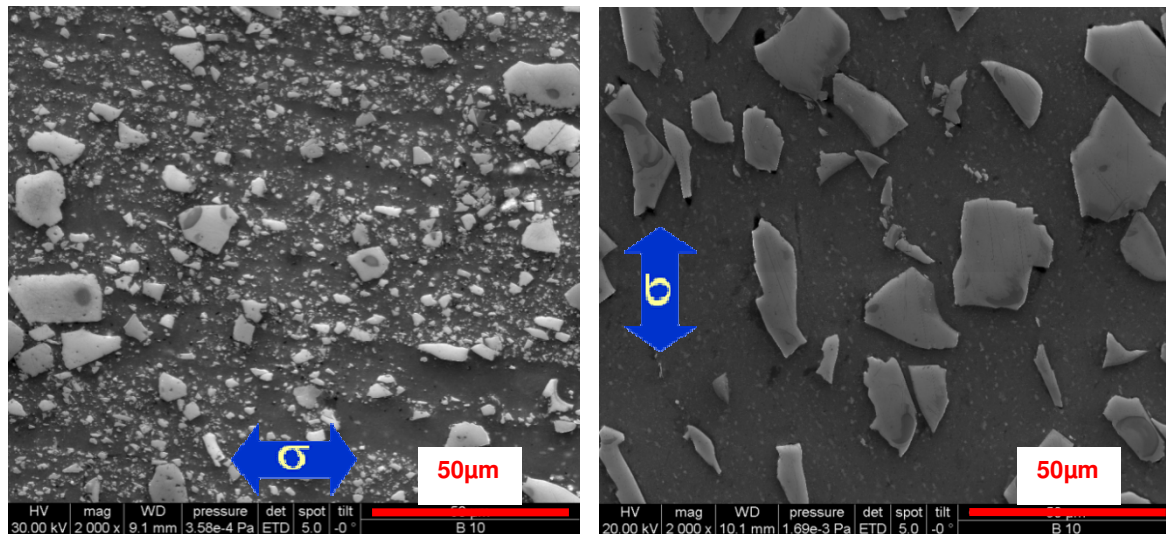
**Figure 3.4** Microstructure of a) BM 2124/SiC/25p<20µm and b) WB 2124/SiC/25p<20µm

### 3.1.6   Heat treatment

Prior to testing all the materials were heat treated at 495°C for 20 minutes with subsequent water quenching and over aged at 300°C for 1 hour in order to stabilize the precipitates by overaging (see Figure 3.5). This treatment is designated as T4S where S means stabilisation.
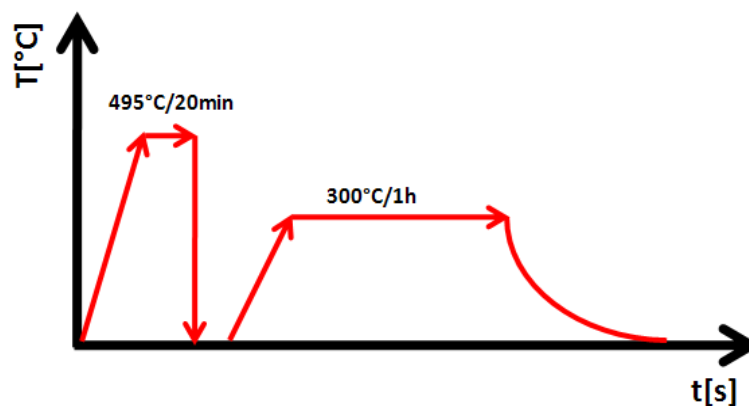


**Figure 3.5** Conducted heat treatment for all the materials prior to testing – T4S

### 3.1.7 Designation of the Materials

Two extrusion bars with a diameter 11.8mm and about 1.5m in length were produced for each material. Each bar is designated with a different number. Therefore, only this number was used for most of the conducted experiments to identify the materials. All the extrusion numbers are shown in Table 3.6.

"BM" or "WB" gives the blending technique used according to chapter 3.1.3. Subsequently, the matrix alloy is mentioned (2124 or 6061). SiC means the reinforcing phase and 25p informs about the volume fraction (25vol%) and "p" means particle. Afterwards the initial size of the added particles is pointed out.

All the datasheets of the extrusions of the material are found in Appendix.

| Extrusion number | Material |
|---|---|
| 566 | BM 2124/SiC/25p<5µm |
| 567 | BM 2124/SiC/25p<10µm |
| 568 | BM 2124/SiC/25p<20µm |
| 570 | 2124 Matrix without BM |
| 571 | 2124 Matrix without BM |
| 572 | BM 2124/SiC/25p<5µm |
| 573 | BM 2124/SiC/25p<10µm |
| 574 | BM 2124/SiC/25p<20µm |
| 576 | BM 2124 Matrix |
| 577 | BM 2124 Matrix |
| 632 | WB 6061/SiC/25p<20µm |
| 633 | WB 2124/SiC/25p<20µm |
| 636 | WB 6061/SiC/25p<20µm |
| 637 | BM 6061 Matrix |
| 638 | WB 6061/SiC/25p<5µm |
| 639 | WB 2124/SiC/25p<5µm |
| 640 | BM 6061 Matrix |
| 641 | WB 6061 /SiC/25p<5µm |
| 642 | WB 2124/SiC/25p<20µm |
| 643 | WB 2124/SiC/25p<5µm |

**Table 3.6** Numbers of extrusion to identify the materials

## 3.2  Metallography

### 3.2.1  Sample preparation

All the specimens for microscopic characterization were cut by means of an Accutom-5 device provided by Struers using SiC discs (459 CA) for the unreinforced Al alloys and diamond discs (452 CA) for the SiC-particle reinforced composites. The presence of SiC embedded in the Al matrix requires diamond tools to cut the materials. Subsequently, the samples were embedded either by cold or hot mounting. A mixture of Araldit resin (AY 103) and Araldit hardener (HY 956) with a ratio of 100:17 was used for cold embedding. Hot mounting was carried out by means of a Predopress provided by Struers.

The samples were polished using Pedemax-2 provided by Struers. The applied polishing program is shown in Table 3.7.

| Process | Plate | Roughness | Pressure | Time |
|---|---|---|---|---|
| Grinding 300rpm | Grinding plate | 220 piano | 1 ≈ 30N | Until plane |
| Polishing 150rpm | Largo | 15µm | 2 ≈ 65N | 1 hour |
| | DP Pan | 15µm | 1 ≈ 30N | 30 minutes |
| | DP Dur | 6µm | 1 ≈ 30N | 30 minutes |
| | DP Mol | 3µm | 1 ≈ 30N | 10 minutes |
| | OP Chem | OPS | 1 ≈ 30N | 5 minutes |

**Table 3.7** Program for metallographic polishing of the samples

### 3.2.2 Microscopy

Images taken using a light optical microscope (LOM) (see Figure 3.6 a)) were analysed by means of the software Axio Vision in order to determine the distribution of the SiC particles and to observe pores. The samples were cut and embedded to study both the longitudinal "L" and perpendicular "P" directions to extrusion of the sample (see Figure 3.6 b)). The samples were grinded stepwise and mechanically polished with diamond paste according to section 3.2.1.

Only the amount and distribution of SiC particles bigger than 1µm were analysed by LOM because of the limited resolution of this device. The existence of much smaller ones can be clearly seen but not analysed in terms of distribution and size. Therefore, FEG-SEM was conducted to analyse the particles of sizes <1µm as described in section 3.2.3.

a)

b) **Direction of Extrusion**
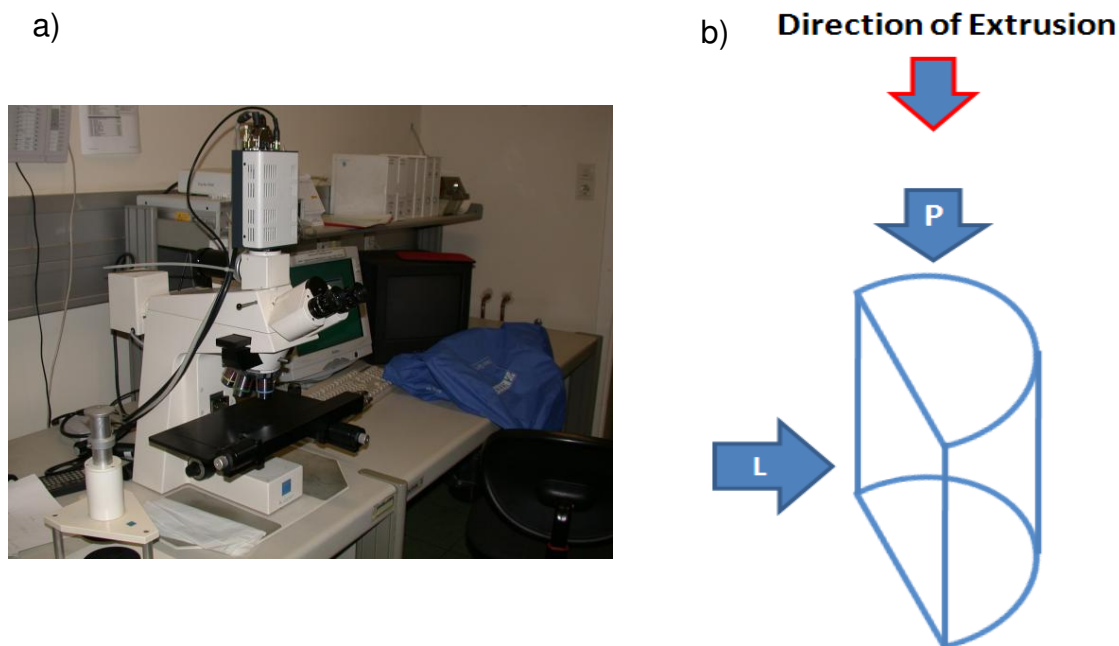


**Figure 3.6** a) LOM to analyse the microstructure and b) longitudinal (L) and perpendicular (P) direction of sample preparation for microscopic analyses

### 3.2.3 Field Emission Gun – Scanning Electron Microscopy (FEG-SEM)

FEG-SEM was utilized to analyse the sub-µm particles which were seen in conventional LOM but could not be counted and analysed by LOM. The comparison of images taken by two different FEG-SEM devices is shown in Figure 3.7 and Figure 3.8. Images taken by FEG-SEM in CENIM Madrid were used to analyse the SiC particles >1µm of the BM material. The device was a FEG-SEM with detectors for secondary electrons as well as backscattered electrons and microanalysis by energy dispersion system with a resolution of 1.5 nm (15kV), 5nm (1kV). As the BSE contrast of the SiC particles and the surrounding Al matrix was quite poor it was necessary to paint each particle in black colour in order to separate them clearly from the matrix (see Figure 3.7). According to Figure 3.8 FEG-SEM analyses was conducted by means of FEI QUANTA 200 FEGSEM device provided by USTEM at TU Vienna [84] in order to investigate the SiC particles <1µm from SEI.

Only small differences between the longitudinal and the perpendicular directions were found. In longitudinal direction the particles tend to be bigger due to the extrusion process. Therefore only the images taken in longitudinal direction were further evaluated.

The preparation of the samples for FEG-SEM was done according to section 3.2.1. A modified polishing program was necessary to avoid SiC particles sticking out the surface causing shadows next to them. The modified program for preparation can be seen in Table 3.8. Nevertheless it was not possible to avoid completely having shadows around the SiC particles.

The designation of the SiC particle distribution resulting from the image analysis is shown in Figure 3.9 with the resulting percentiles 6, 25, 75, 95, 97 and 99 as well as the median and the mean value of the distribution.
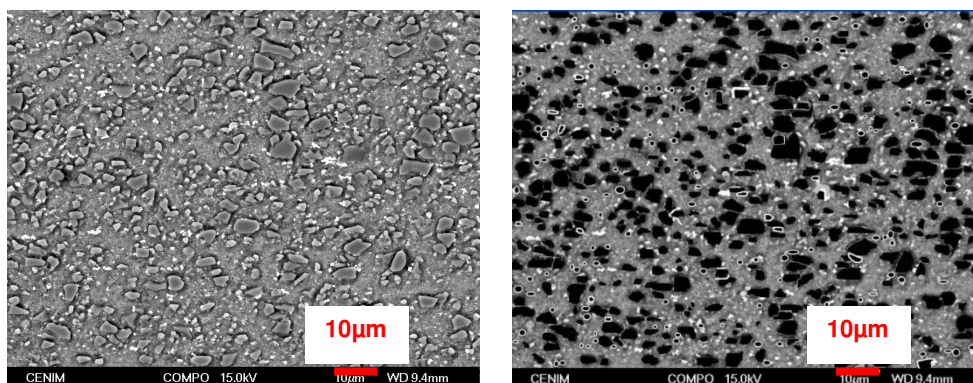
**Figure 3.7** FEG-SEM images of BM 2124/SiC/25p<5µm taken at CENIM Madrid with separated black SiC particles (BSE)
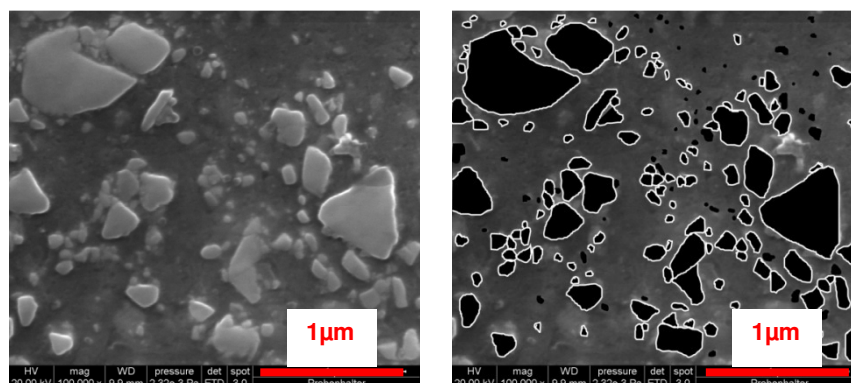


**Figure 3.8** FEG-SEM images of BM 2124/SiC/25p<5µm taken at USTEM Vienna with separated black SiC particles (SEI)
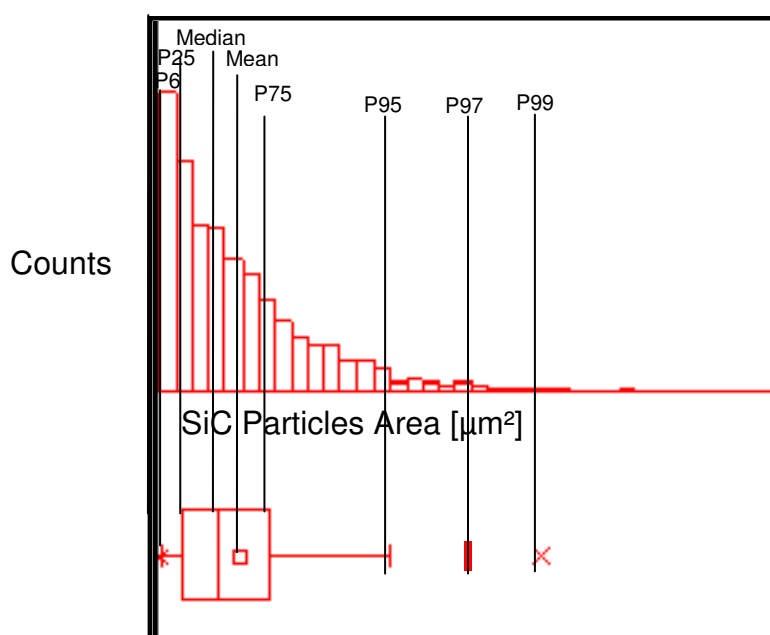


**Figure 3.9** Designation of the resulting distribution of the image analysis

| Process | Plate | Roughness | Pressure | Time |
|---|---|---|---|---|
| Grinding 300rpm | Grinding plate | 220 piano | 1 ≈ 30N | Until plane |
| Polishing 150rpm | Largo | 15µm | 2 ≈ 65N | 30 minutes |
| | DP Pan | 15µm | 1 ≈ 30N | 30 minutes |
| | DP Dur | 6µm | 1 ≈ 30N | 1 hour |
| | DP Mol | 3µm | 1 ≈ 30N | 1 hour |
| | OP Chem | OPS | 1 ≈ 30N | 30 minutes |

**Table 3.8** Modified program for polishing the samples for FEG-SEM

### 3.2.4 Transmission Electron Microscopy (TEM)

The composition of the sub-µm particles was analysed by energy dispersive X-ray spectroscopy (EDX) in a TEM.

The samples for TEM were prepared by electro polishing in the case of the unreinforced matrices and by ion milling in the case of the WB material. The electro polishing was carried out using a TenuPol-5 provided by Struers (see Figure 3.10). The ion milling was done by means of a Precision Ion Polishing System (PIPS – see Figure 3.11). The material for TEM investigations was studied in T4S condition in order to have stabilized precipitates and after a long period of creep exposure at 300 °C (WB material <5µm: 30h – 4% strain – 30MPa; BM material <5µm: 8000h – 0.2% strain – after a load sequence 40=>50=>60MPa).

TEM investigations as well as the sample preparation were conducted by USTEM at Vienna University of Technology [84].

**Figure 3.10** TenuPol-5 provided by Struers



**Figure 3.11** Precision Ion Polishing System (PIPS)

### 3.2.5 Electron Backscatter Diffraction Technique (EBSD)

Optical microscopy and scanning electron microscopy are both used to examine the microstructure of the materials. Techniques of polishing and etching help to reveal the position of grains and grain boundaries but the information obtained may not be absolute. Electron backscatter diffraction (EBSD) is a technique for obtaining crystallographic information as well as the orientation of individual grains from samples in the scanning electron microscope. A stationary electron beam strikes a tilted (70°) crystalline sample and the diffracted electrons form a pattern characteristic of the crystal structure and orientation of the sample region from which it was generated. When the beam is scanned in a grid across a polycrystalline sample and the crystal orientation measured at each point, the resulting map will reveal the constituent grain morphology, orientations, and boundaries.

EBSD measurements were carried out in all the materials investigated in order to obtain the initial grain size of the materials. Due to the problems mentioned in 3.2.3

the specimens were prepared according to the route in Table 3.9. Because of the very small grains in the BM material it was not possible to analyse the grains precisely but the obtained images help to get at least an overview on the distribution of the grains.

| Process | Plate | Roughness | Pressure | Time |
|---|---|---|---|---|
| Grinding  300rpm | Grinding plate | 220 piano | 1 ≈ 30N | Until plane |
| Polishing 150rpm | Largo | 15µm | 2 ≈ 65N | 1 hour |
| | DP Pan | 15µm | 1 ≈ 30N | 1 hour |
| | DP Dur | 6µm | 1 ≈ 30N | 1 hour |
| | DP Mol | 3µm | 1 ≈ 30N | 2 hours |
| | OP Chem | OPS | 1 ≈ 30N | 2 hours |

**Table 3.9** Modified program for polishing the samples for EBSD

## 3.3 Brinell Hardness Measurements

Brinell hardness measurements were conducted by means of an EMCO TEST hardness tester model M1C010/100 for WB 2124/25p/<5µm, BM 2124/25p/<5µm as well as for the unreinforced 2124 and 6061 matrices in T4S condition and after different creep exposure times. These measurements were done in order to determine the aging effect on the creep behaviour and to find out about the hardening effects of the particles in the matrices. Tests were carried out using Brinell HB1 and load grade 10 (98.1N) with a holding time of 10s. The measurements were carried out in the longitudinal direction of extrusion by 5 measuring points at each surface.

Directly below the indentation the density of particles is increased locally, compared to the regions away from the depression. This is schematically shown in Figure 3.12. As the indenter moves downwards during the test, the pressure is accommodated by the non-uniform matrix flow along with the localized increase of particle concentration, which tends to increase the resistance of deformation. Consequently, the hardness value increases due to the local increase in particle concentration and thus strain hardening of the matrix is associated with indentation. This was illustrated by micromechanical modelling using the finite element method in [10]. Under indentation the material system with discrete particles exhibits a higher resistance to deformation than the homogenized system having exactly the same overall stress-strain behaviour. These findings are true even when the particle size is much smaller than the indenter size [104]. This affects the influenced zone and leads to a different result from that of the matrix. Therefore increasing the number of measured points per area of interest is necessary to get a statistic result.
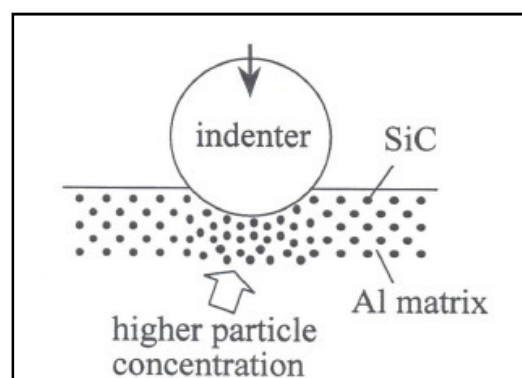


**Figure 3.12** Locally concentrated particles due to indentation

## 3.4 Nano Hardness Measurements

Indentation tests are perhaps the most commonly applied means of testing the mechanical properties of materials. The technique has its origins in the Mohs scale of mineral hardness, in which materials are ranked according to what they can scratch and are, in turn, scratched by. The characterization of solids in this way takes place on an essentially discrete scale, so much effort has been expended in order to develop techniques for evaluating material hardness over a continuous range. More recently (in 1975), the nano indentation technique has been established as the primary tool for investigating the hardness of small volumes of material [85].

Nano hardness measurements were conducted by means of Nano Indenter XP for the unreinforced matrix 2124 with and without BM, BM 2124/SiC/25p<5µm, BM 2124/SiC/25p<10µm, BM 2124/SiC/25p<20µm, WB 2124/SiC/25p<5µm and WB 2124/SiC/25p<20µm in order to determine the effect of the sub-µm particles and the precipitates on the hardness of the matrix.

The nano hardness was measured in longitudinal and perpendicular direction of extrusion by 25 measured points at each surface and with a fixed displacement at maximum depth and maximum load of 700nm. This was necessary due to the scattering introduced by the SiC particles. The problem with hardness measurements of PRMs is that it could be possible to measure the matrix but with a reinforcement particle near the surface at the measured point. During a hardness test severe plastic flow is concentrated in the localized region directly below the indentation, outside of which the material still behaves elastically. Due to the evident scattering of the results the most scattered measured points were not taken into account for the analysis (see Figure 3.13) in order not to falsify the results too much. Curve number 1 in Figure 3.13 was not taken into the calculation of the mean since the displacement was exceeded due to an error of the measurement. Curves number 2, 3, 4 and 5 were deleted due to the convexity of the loading curve what indicates not measuring only the matrix. Curve 6 was eliminated since it doubles (32mN) the curve with the minimum load (16mN) and therefore producing too large scattering. The hardness of the matrix should be represented by the lower load curves bundle since in the upper load regions SiC particles are supposed to increase those hardness values.

In nano indentation small loads and tip sizes are used, so the indentation area may only be a few square micrometers or even nanometers. This presents problems in determining the hardness, as the contact area is not easily found. Atomic force microscopy or scanning electron microscopy techniques may be utilized to image the indentation, but can be quite cumbersome. Instead, an indenter with a geometry known to high precision is employed. During the course of the instrumented indentation process, a record of the depth of penetration is made, and then the area of the indent is determined using the known geometry of the indentation tip [85].

Nano-Indentation technology is a high precision technique for the determination of the nano mechanical properties of thin films, coatings and matrix particle interfaces. By means of nano-indentation one can quickly determine properties such as hardness and Young's modulus on almost any type of material - soft, hard, brittle or ductile [86].
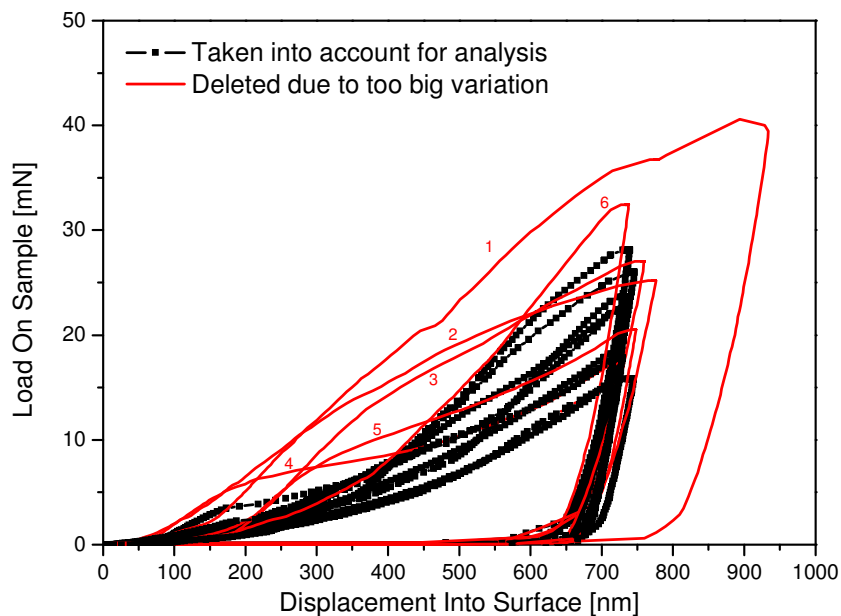


**Figure 3.13** Illustration of the hardness curves of nano indentation

## 3.5  Dynamical Mechanical Analysis

The Youngs Modulus of all the investigated materials was measured by means of Dynamical Mechanical Analysis (DMA) in order to evaluate the quality of the produced materials. DMA delivers information on the elastic behaviour of a material under small, sinusoidal modulated dynamic loads in dependence of temperature, time and frequency. The investigations were conducted with TA Instrument DMA 2980 equipment within air atmosphere with a frequency of 1Hz, amplitude of 40µm and in a temperature range from room temperature up to 300°C.

The DMA were carried out using the 3-point-bending clamp which is shown in Figure 3.14. The samples for all the 3-point-bending-tests had a geometry of 55 x 4 x 2 (Length x Width x Thickness [mm³]), grinded and parallel surfaces and the bearing clearance was 50mm.
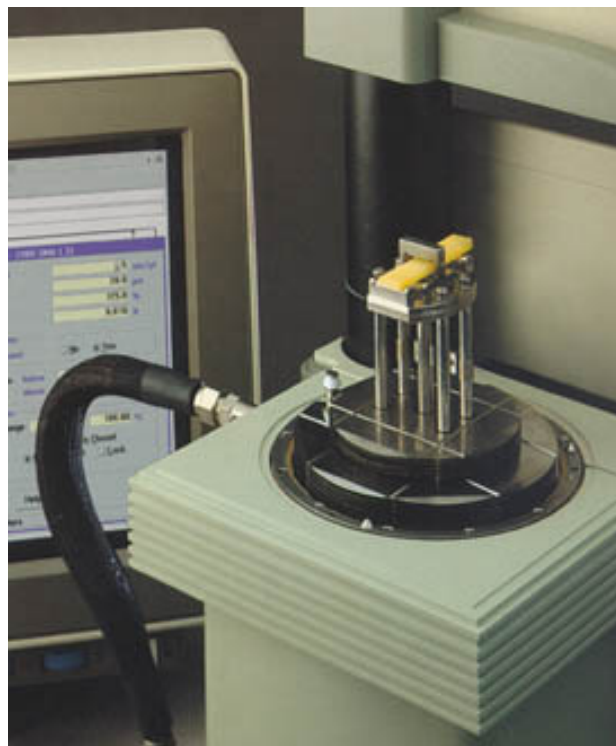


**Figure 3.14** DMA device for 3-point-bending clamp in order to obtain the Young´s Modulus

## 3.6  Hot Tensile Tests

Hot tensile tests were carried out for all the unreinforced matrices as well as for all the composites. The device used for hot tensile tests is Zwick Z250 (see Figure 3.15) which can be used for tensile, compression and bending tests with a maximum load of 250kN.

There is a special heating chamber to be adapted what enables tensile tests at elevated temperatures. The tensile tests for the present study were conducted in air atmosphere at a temperature of 300 °C. The temperature was measured using 2 thermocouples – one on the upper end of the sample and another on the lower end of the sample. The time to heat up to test temperature was 30 minutes whereas the holding time at this temperature was about 20 minutes and the time to carry out the tests also was about 20 minutes. The sample geometry used had the same geometry as for the isothermal tensile creep tests, according to 3.7. All the samples were subjected to T4S heat treatment prior to testing, according to 3.1.6. The gauge length was 25mm and the testing velocity was chosen to be 2mm/min.



**Figure 3.15** Zwick Z250 used for hot tensile tests

Chapter: Experimental

## 3.7  Isothermal Tensile Creep Experiments

### 3.7.1  Experimental Equipment

Isothermal tensile creep tests were carried out in order to investigate the creep behaviour of the described discontinuously reinforced aluminium alloys and the corresponding unreinforced matrices. The devices used for the tensile creep tests were initially built in 1957 and were modified by integrating a new digital acquisition system, inductive displacement transducers and a digital temperature control system. This creep rig offers nowadays the possibility to carry out simultaneously 10 tensile creep tests at elevated temperatures Figure 3.16 a) [87].

a)
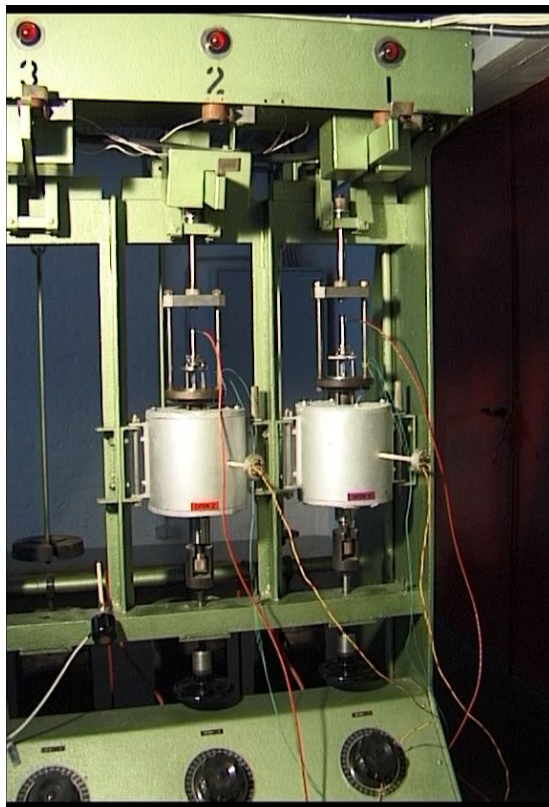
b)
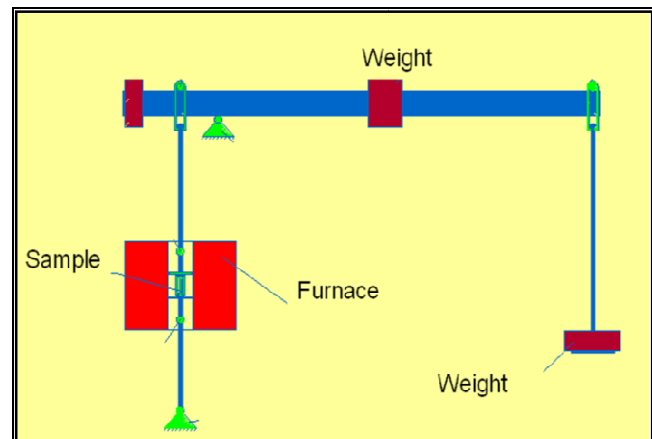


**Figure 3.16** a) Arrangement of the furnaces for the isothermal tensile creep tests; b) tensile creep test shown schematically

The load can be changed by placing weights in form of plates ranging from 200g up to 5kg at the backside of the device. The temperature of the sample during testing was measured using two thermocouples one at the bottom and another at the top of the sample. As the temperature measured by the thermocouple placed at the bottom of the sample showed the most stable behaviour this was decided to control the temperature of the furnace. The strain during the tests was measured using linear variable displacement transducers (LVDT) provided by Micro-Epsilon [88] with a sensitivity of 56mV/V and a resolution of 0.01µm. The measured signals were then amplified and recorded using a data acquisition system made up of a PC and external amplifiers model Spider8 provided by Hottinger Baldwin Meßtechnik G.m.b.H. [89]

### 3.7.2  Tensile Creep Samples

Tensile specimens were tested with geometry of 36mm gauge length and 6mm in diameter. The specimens were cut along the axis coinciding with the direction of extrusion (0°). Figure 3.17 shows the geometry of the samples used for the isothermal tensile creep tests. The design was done according to the requirements of the standard DIN EN 10291. All the samples were manufactured by Fa. Gerhard Rauch GmbH, Eitnergasse 9, 1230 Vienna [90] since it was necessary to use diamond tools in order to produce the samples because of the SiC particles introduced.

Figure 3.18 a) shows an image of one sample with the fixations for the thermocouples on each side. In Figure 3.18 b) this can be seen already joined and ready for the creep furnace.
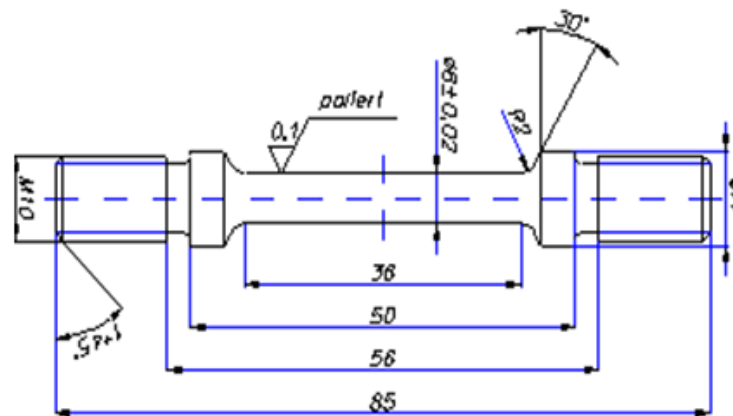
**Figure 3.17** Geometry of tensile creep samples used to study the creep behaviour
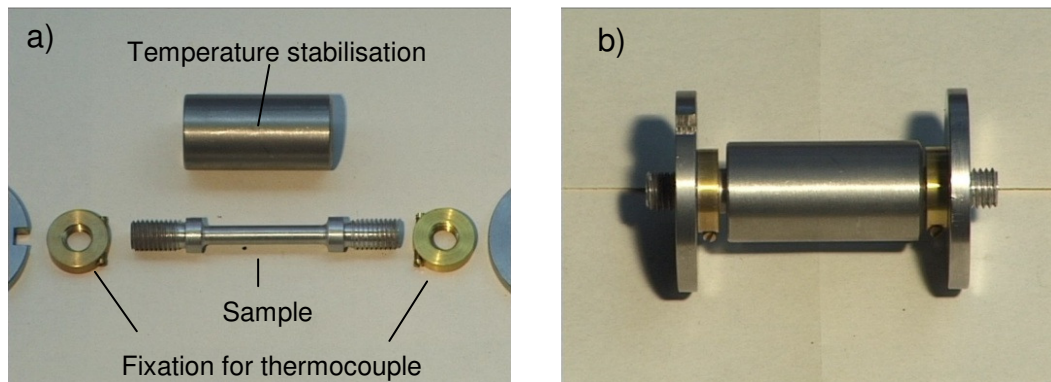


**Figure 3.18** a) Tensile creep sample with fixation for thermocouples and the temperature stabilisation cylinder before mounting and b) joined

### 3.7.3 Test Procedure

A preload of $\sigma=10$MPa for 1 hour was imposed before the creep test load in order to stabilise the microstructure.

The tensile creep tests were carried out in air atmosphere at 300°C. The creep investigations were done at constant load with loads ranging from 15MPa to 70MPa.

Once the steady-state creep rate was reached for one load, the load was increased and held until the new steady-state creep rate was reached. Not all the conducted creep tests led to creep fracture of the sample but were stopped when steady-state creep occurred.

# 4  Results

The following sections present all the results obtained during the investigation. The micrographs of the materials as well as all the strain ε vs. time t and strain rate $\dot{\varepsilon}$ vs. time t creep curves are collected in the appendix at the end of the thesis.

## 4.1  Microscopy

The distribution of the SiC particles were analysed with the images given in the Appendix.

The quantitative analysis of the SiC particles was separated in two parts: 1) SiC particles with diameter ≥ 1μm (≥  0.8μm² if round particles are supposed), analysed by means of FEG-SEM for the BM PRMs (Figure 4.1 a)-c)) and by means of LOM for the WB PRMs (Figure 4.2) and 2) SiC particles with diameter ≤ 1μm (≤ 0.8μm² if round particles are supposed), analysed by means of FEG-SEM due to the higher resolution achieved by this technique (Figure 4.1 d) and e)). In order to distinguish between the <1μm SiC and the precipitates those images were also taken in BSE mode to analyse the <1μm SiC particles (see Figure 4.1 e)). Samples perpendicular and longitudinal to the extrusion direction were investigated. Since only small differences between both directions were obtained the further investigations of the particles were carried out using the images in longitudinal direction due to the slight alignment of the particles because of the extrusion process. An equivalent circle was assumed in order to calculate the corresponding diameter of the calculated areas. The quantitative analyses were conducted using the Axio Vision Software. Some of the images of all the studied PRMs used to analyse the particles are given in the appendix.

There is a wide range of SiC particle sizes in the PRMs especially in the BM PRMs for which SiC particles smaller than 1μm can be observed.
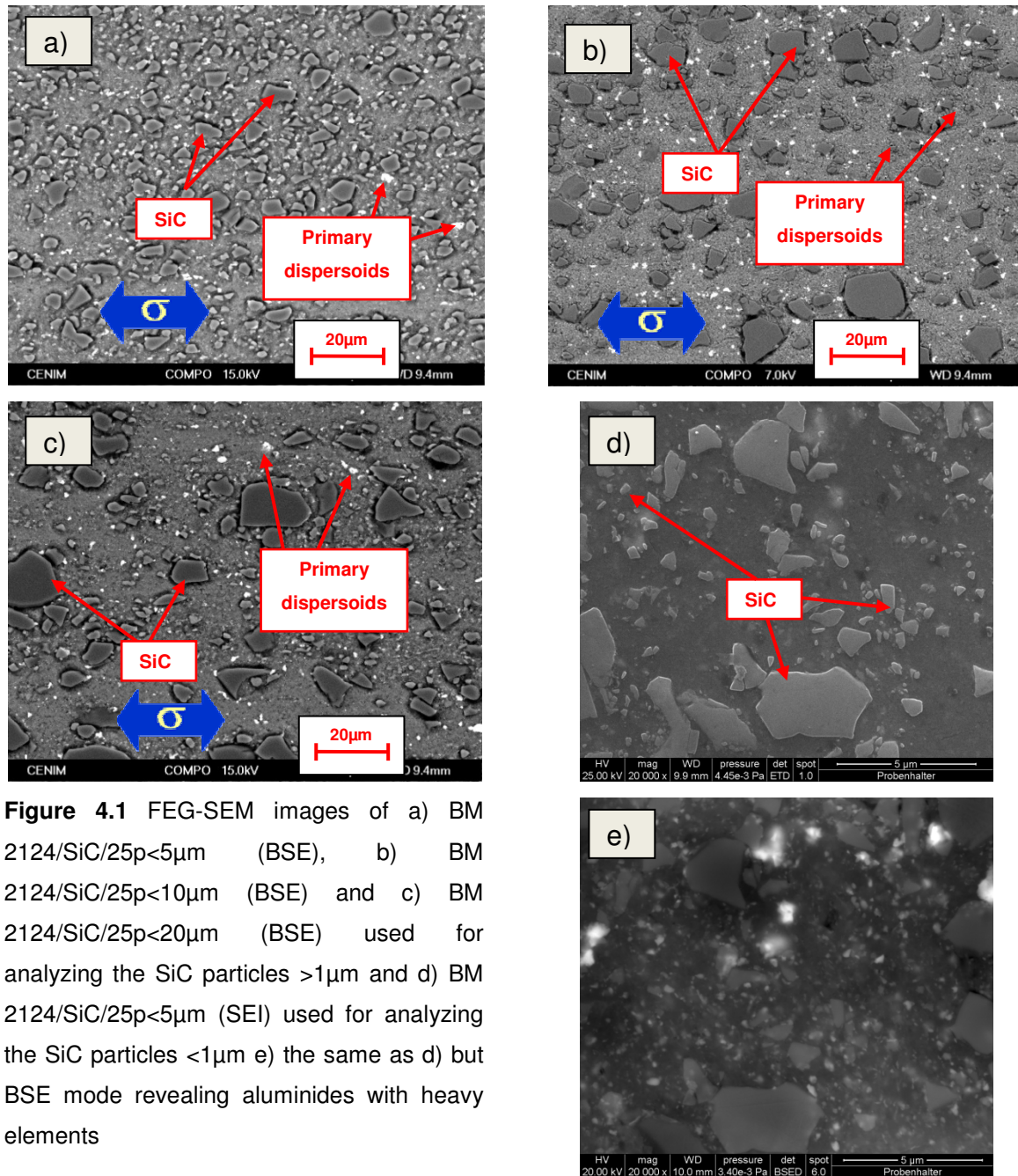
**Figure 4.1** FEG-SEM images of a) BM 2124/SiC/25p<5µm (BSE), b) BM 2124/SiC/25p<10µm (BSE) and c) BM 2124/SiC/25p<20µm (BSE) used for analyzing the SiC particles >1µm and d) BM 2124/SiC/25p<5µm (SEI) used for analyzing the SiC particles <1µm e) the same as d) but BSE mode revealing aluminides with heavy elements
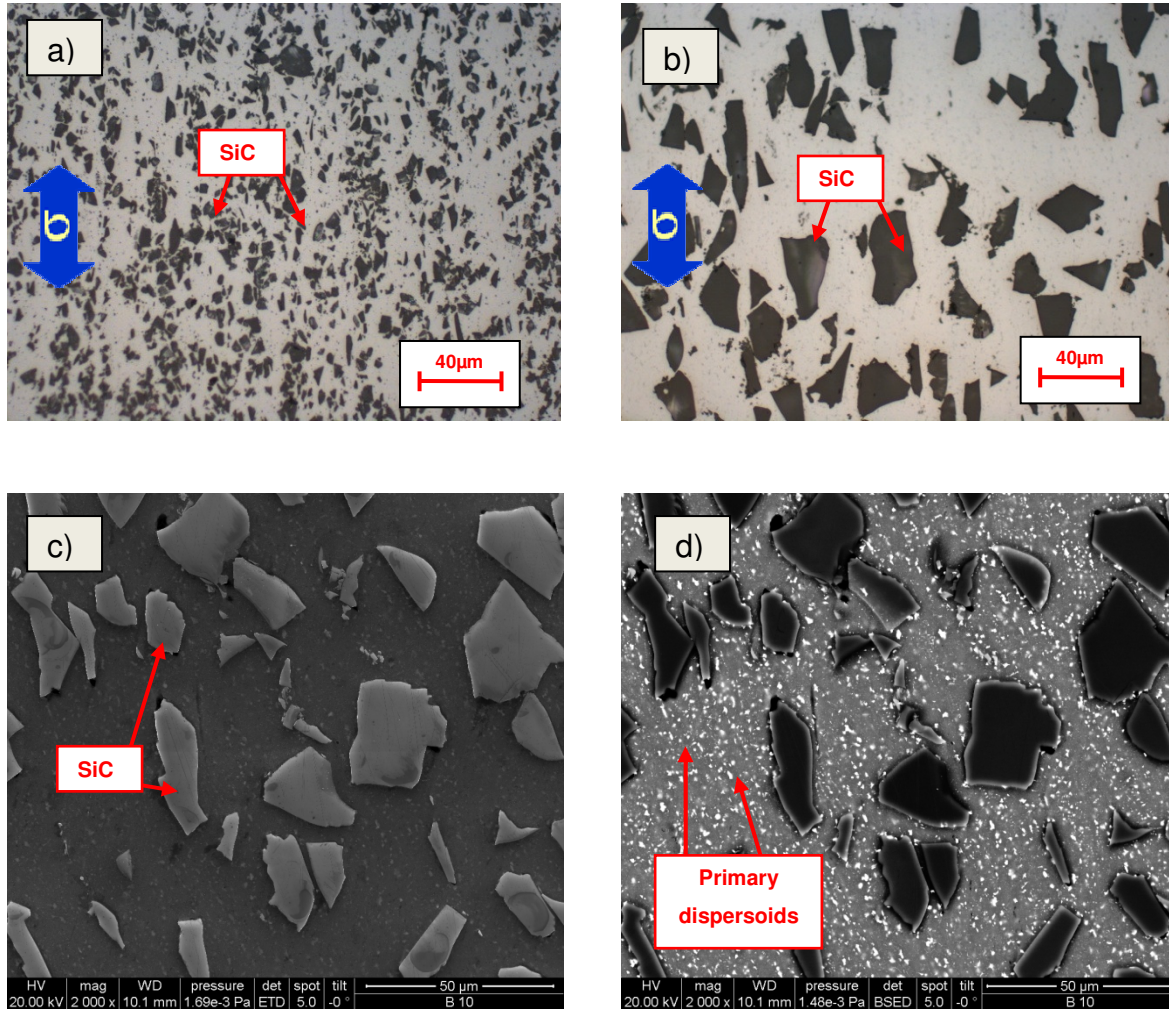
**Figure 4.2** LOM images of a) WB 2124/SiC/25p<5µm and b) WB 2124/SiC/25p<20µm used for analyzing the SiC particles >1µm and FEG-SEM of WB 2124/SiC/25p<20µm in c) SE and d) BSE mode showing Fe/Mn/Cu rich inclusions

### 4.1.1 Analyses of the SiC Particles >1µm in the PRM

In order to analyse the distribution of the SiC particles of the BM PRMs all the FEG-SEM images had to be adapted to increase the accuracy of the results since the gray SiC particles have white boundaries surrounded by black shadows. Therefore, each single particle had to be redrawn with black colour and separated one from the other as it was shown in chapter experimental. Then all the black areas were calculated.

The SiC particles taken by LOM of all the WB material do appear in black colour and therefore in this case it was only necessary to separate the particles one from another and not to redraw each single one.

The distributions of the SiC particles in longitudinal and perpendicular direction to extrusion are shown in Figure 4.3 for the BM PRMs and in Figure 4.4 for the WB PRMs (see explanation of the box chart in Figure 3.9). It can be seen that there are no significant differences between these two directions except for the 2124 WB PRMs <20µm, for which the longitudinal direction results show larger particle sizes than for the perpendicular direction. All the micrographs were analysed in order to get the distribution of the gray SiC particles larger than 0.8µm² area which corresponds to a equivalent diameter of 1µm of the round particles.

The results for the longitudinal direction are summarized in Table 4.1. Here, the median of the area, the P25 and the P75 percentiles as well as the fraction of particles larger than 5µm in equivalent diameter (area >19.6µm² for round particles) are shown for all the investigated materials. These results reveal considerable differences between the WB PRMs with particles <5µm and the WB PRMs with particles <20µm. The WB PRMs <5µm contain about 4vol% of particles bigger than 19.6µm² while in the WB PRMs <20µm remain about 9.5vol% of SiC particles >19.6µm². These aspects are not observed in the BM materials with various initial particle sizes. The median of the particle size is markedly reduced for the case of the BM composites with respect to WB: <1/2 for <5µm and ≈1/5 for <20µm. The volume fraction of particles larger than 5µm remains below 2vol% for all BM composites. This volume fraction is larger for the WB PRMs reaching about 4vol% for the <5µm WB PRMs and about 9vol% for the <20µm WB PRMs.

In Figure 4.5 the statistical calculation of the SiC particles area of all the studied PRMs is shown. Due to the SiC particles being broken during the BM the range for the P25 and P75 percentiles is much decreased compared to the WB PRMs. The median for the WB materials also is much bigger than for all the BM PRMs. The median of the SiC in the BM PRMs decreases slightly with increasing input particle size.
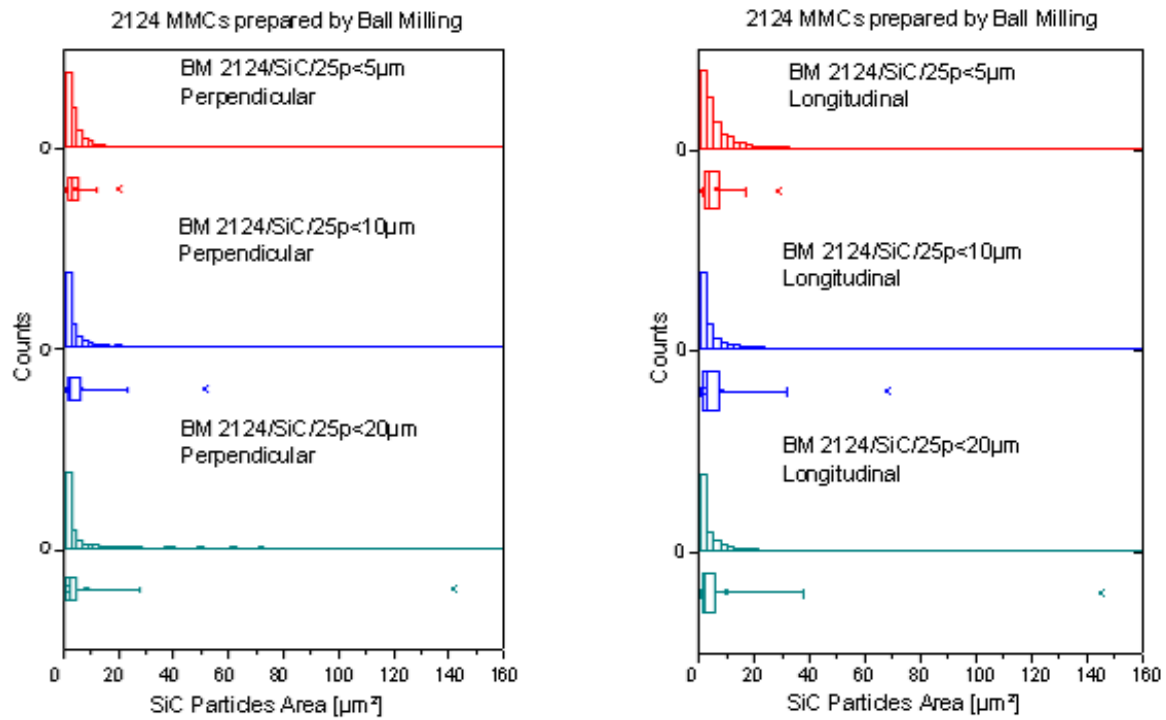
**Figure 4.3** Histograms and box charts of SiC particles with an area >0.8µm² for BM PRMs a) perpendicular and b) longitudinal to extrusion
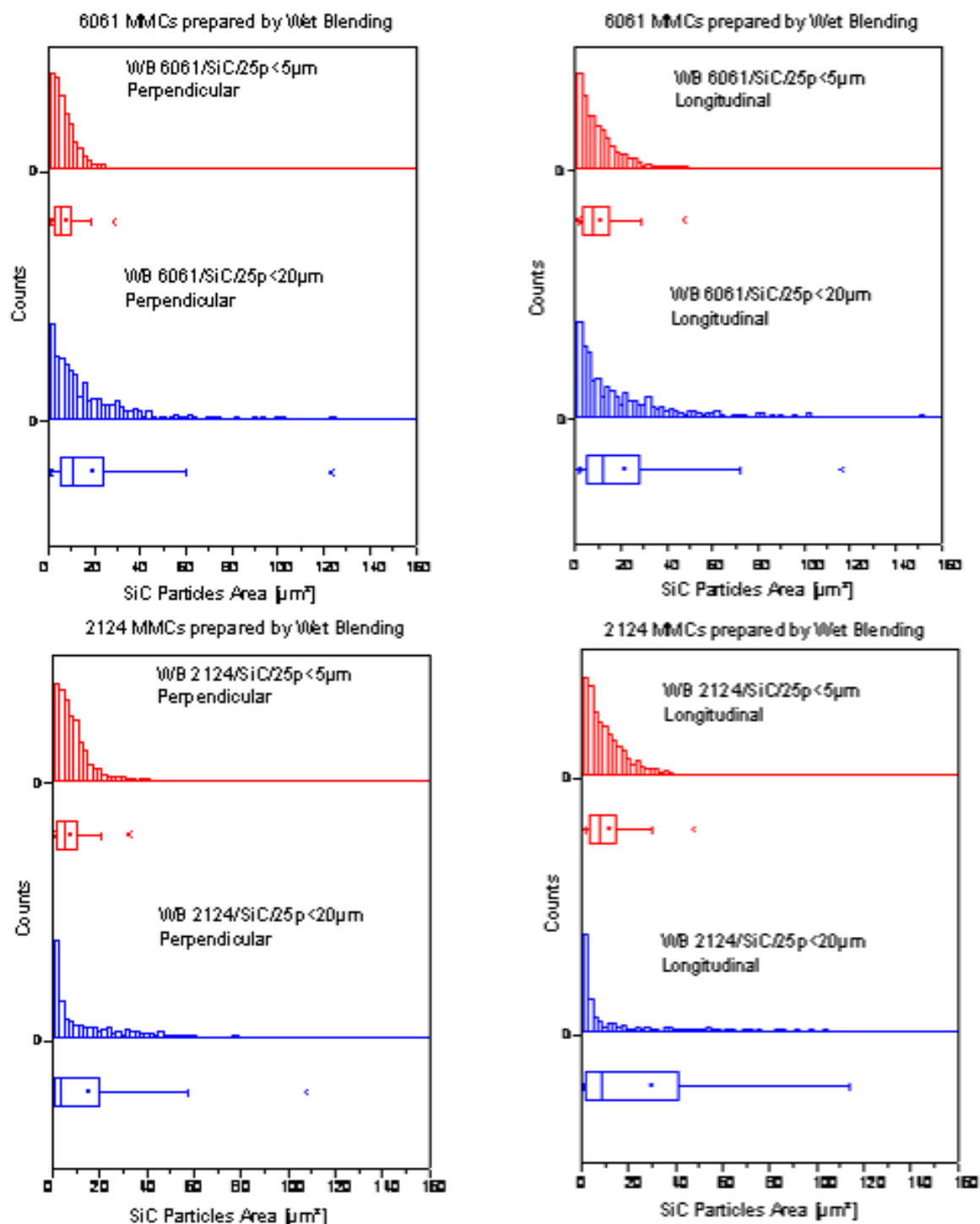
**Figure 4.4** Histograms and box charts of SiC particles with an area >0.8µm² for a) WB 6061 PRMs in the direction perpendicular to extrusion, b) WB 6061 PRMs in the direction longitudinal to extrusion, c) WB 2124 PRMs in the direction perpendicular to extrusion and d) WB 2124 PRMs in the direction longitudinal to extrusion

| Material | P5 percentiles [µm] | Median of diameter [µm] | P25-P75 percentiles [µm] | P97 percentiles [µm] | Vol.fraction [%] of particles in PRM >5µm |
|---|---|---|---|---|---|
| BM: | | | | | |
| 2124/SiC/25p<5µm | 1.1 | 2.1 | 1.6 - 2.9 | 5.0 | 0.6 |
| 2124/SiC/25p<10µm | 1.1 | 1.9 | 1.3 - 2.9 | 8.0 | 2.0 |
| 2124/SiC/25p<20µm | 1.1 | 1.7 | 1.3 - 2.6 | 11.0 | 2.0 |
| | | | | | |
| WB: | | | | | |
| 2124/SiC/25p<5µm | 1.8 | 3.2 | 2.2 - 4.4 | 7.0 | 4.0 |
| 2124/SiC/25p<20µm | 1.2 | 3.4 | 1.6 - 7.3 | 14.0 | 9.7 |
| 6061/SiC/25p<5µm | 1.3 | 3.2 | 2.1 - 4.3 | 7.0 | 3.8 |
| 6061/SiC/25p<20µm | 1.3 | 3.9 | 2.4 - 6.0 | 11.0 | 9.1 |

**Table 4.1** Results of the analysed SiC particles >0.8µm² in longitudinal direction for all the studied PRMs
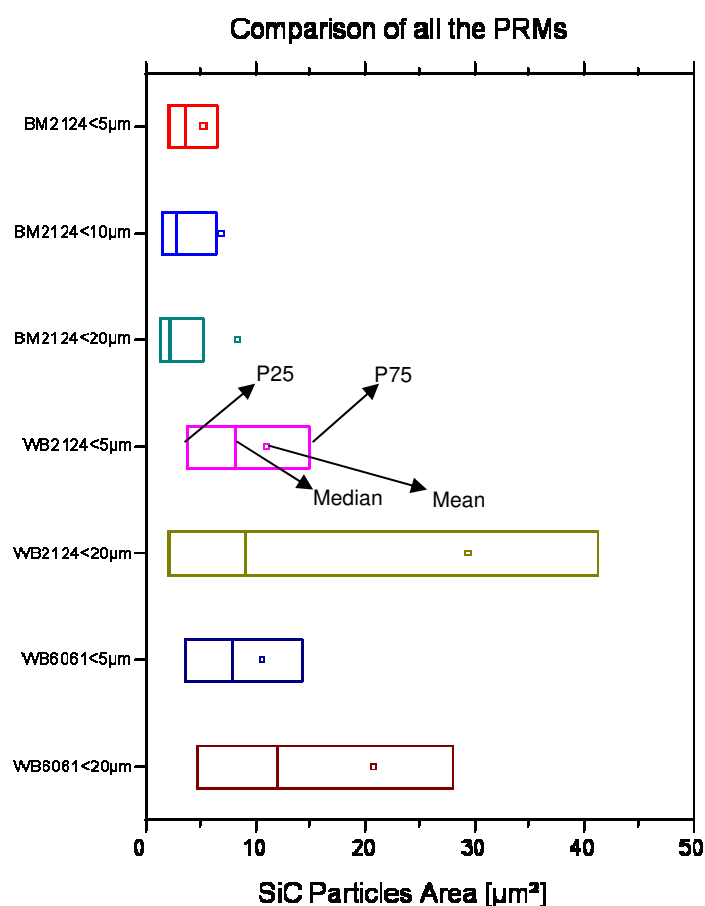


**Figure 4.5** Statistical graphs of the SiC particles area of all the studied PRMs

### 4.1.2 Analyses of the SiC Particles <1µm in the PRM

No sub-µm SiC particles were observed in the WB materials. The comparison of the micrographs in SE mode with those in BSE mode taken by FEG-SEM reveal various sub-µm particles that do not correspond to SiC particles. These others are not taken into account in this chapter and are analysed by TEM in section 4.1.3.

In order to study the SiC particles <1µm the images taken by FEG-SEM were taken into account. Since there is only weak contrast between the SiC particles and the surrounding matrix the images also needed to be redrawn by painting each single particle separating them from each other.

The distribution of the gray SiC particles in SE <1µm of both BM 2124/SiC/25p<5µm as well as for BM 2124/SiC/25p<20µm was found to be very close to each other (see Figure 4.6 and Table 4.2) but with a considerable high systematic error.
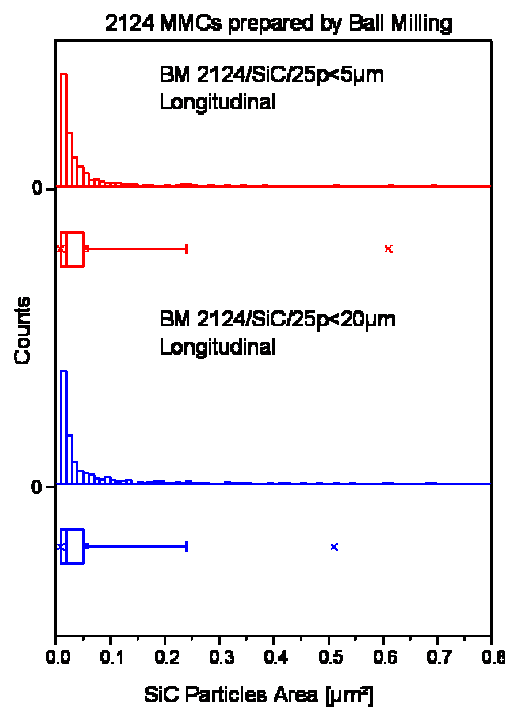


**Figure 4.6** Histogram and box chart of SiC particles with an area <0.8µm² for the BM 2124 PRMs

| Material | Median of diameter [µm] | P25-P75 percentiles [µm] |
|---|---|---|
| BM: | | |
| 2124/SiC/25p<5µm | 0.16 | 0.1-0.3 |
| 2124/SiC/25p<20µm | 0.16 | 0.1-0.3 |
| WB: | | |
| No SiC Particles <1µm present at all | | |

**Table 4.2** Results of the analysed SiC particles <1µm in longitudinal direction

### 4.1.3  Transmission Electron Microscopy (TEM)

Images taken by FEG-SEM showed the presence of sub-µm particles which can act as dispersoids. TEM investigations from both the 2124 BM and WB PRMs were carried out to study these particles. EDX analyses were done by line scan and also by spot analysis as it is designated in the images in order to distinguish the different inclusions. This aluminium alloy system contains various inclusions and precipitates. According to [79] the 2024 alloy, which is very close to the 2124 alloy composition, has a multiphase structure consisting of $(Mn,Fe)_3SiAl_{12}$, $Mg_2Si$, $CuAl_2$, $Al_2CuMg$ and occasionally $(Fe,Mn)Al_3$ or $(Mn,Fe)Al_6$. Heating to 300 °C dissolves much of the copper and magnesium leaving some $Al_2CuMg$ and perhaps $CuAl_2$ precipitates. Most of the iron containing phase undergo transformation to $Al_7Cu_2Fe$. Simultaneously, manganese is precipitated from solid solution as $Cu_2Mn_3Al_{20}$ dispersoid. According to this, the normal wrought 2024-T4 product shows rounded $Al_2CuMg$ as an undissolved excess phase, irregularly shaped particles of unreacted $(Mn,Fe)_3SiAl_{12}$ and reaction product $Al_7Cu_2Fe$, along with fine dispersoids of $Cu_2Mn_3Al_{20}$.

All the results of the conducted EDX measurements presented in this section underlie a certain measurement inaccuracy due to different reasons. The Cu peaks could be slightly higher in the results since the sample holder also contains Cu and it is possible to overlap the Cu peak from the sample with those from the sample holder. Regarding the Al precipitations inaccuracies can occur since the matrix alloys are also Al containing and therefore the Al fraction in the analysed precipitations is raised to a very high peak. Also problems occurred at analysing the SiC and the oxides

since C and O are very lightweight elements and in combination with a more heavy element they are hard to determine.

### 4.1.3.1 The unreinforced 2124 matrix with and without BM

In order to see the effect of BM route on the microstructure TEM images of the unreinforced 2124 alloy with and without BM are compared in T4S condition. Figure 4.7 shows the microstructure of the 2124 alloy without BM with the corresponding EDX of point 1 in Figure 4.8 which reveals a $Al_2CuMg$ precipitation as it is expected. A TEM image of the same alloy prepared by means of BM is given in Figure 4.9. Here 4 different points were analysed by conducting EDX analysis. The results of point "1", "2", "3" and "4" are presented in Figure 4.10, Figure 4.11, Figure 4.12 and Figure 4.13, respectively. Point 1 (Figure 4.10) reveals a precipitation of Al, Mn and Cu, probably $Cu_2Mn_3Al_{20}$ as it is expected for this alloy system. Point 2 (Figure 4.11) seems to be a Mg-rich $Al_2Cu$ precipitate whereas point 3 (Figure 4.12) indicates also an $Al_2Cu$. Point 4 (Figure 4.13) is a mixture of Al, Mg, Cu, Mn, Fe, O as it is a very typical result of the BM process.
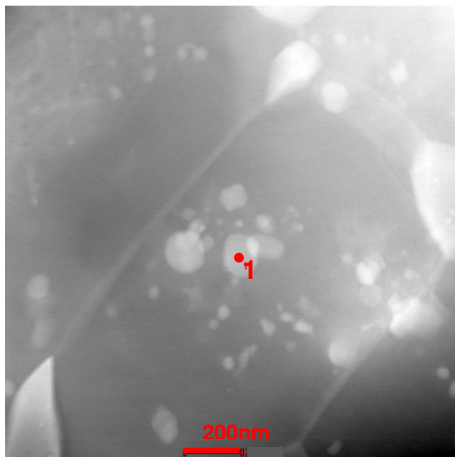


**Figure 4.7** TEM image of an unreinforced 2124 matrix alloy without BM with positions of spot analysis "1" (**Figure 4.8**)
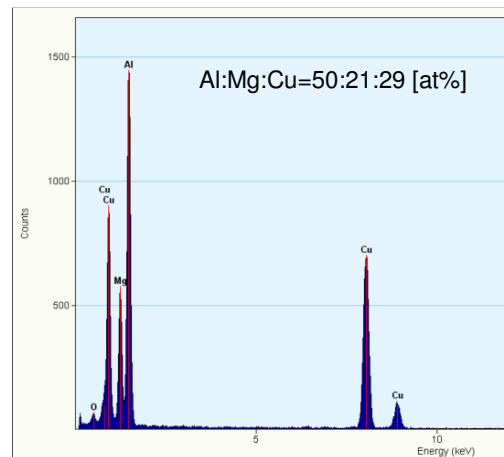


**Figure 4.8** Corresponding EDX of point 1 in **Figure 4.7**
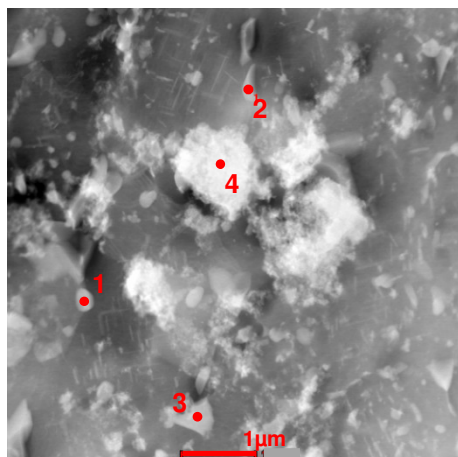
**Figure 4.9** TEM image of an unreinforced BM 2124 matrix alloy with positions of spot analysis "1" (**Figure 4.10**), "2" (**Figure 4.11**), "3" (**Figure 4.12**) and "4" (**Figure 4.13**)



Al:Mn:Cu=86:9:5 [at%]
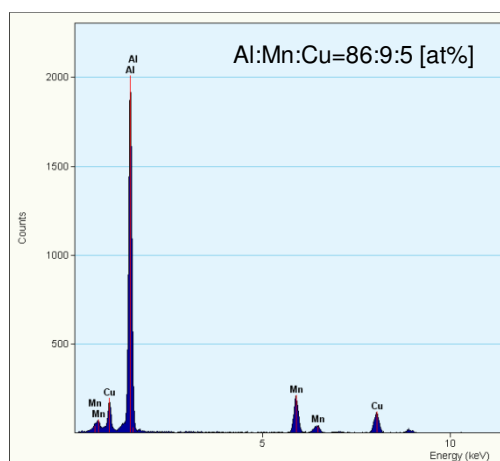
**Figure 4.10** Corresponding EDX of point 1 in **Figure 4.9**



Al:Mg:Cu=82:10:8[at%]
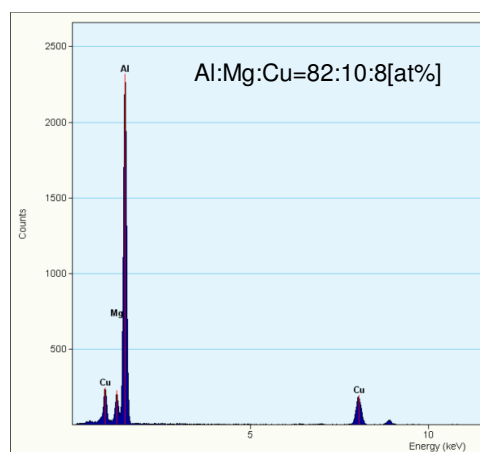
**Figure 4.11** Corresponding EDX of point 2 in **Figure 4.9**



Al:Cu=73:27[at%]
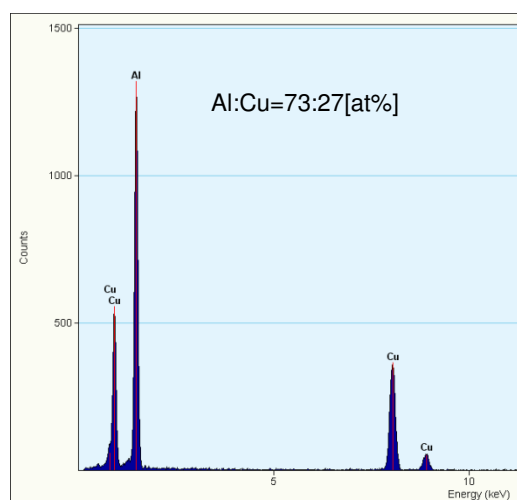
**Figure 4.12** Corresponding EDX of point 3 in **Figure 4.9** – Al$_2$Cu



Al:Mg:Cu:Mn:Fe:O= 64:19:8:5:3:1[at%]
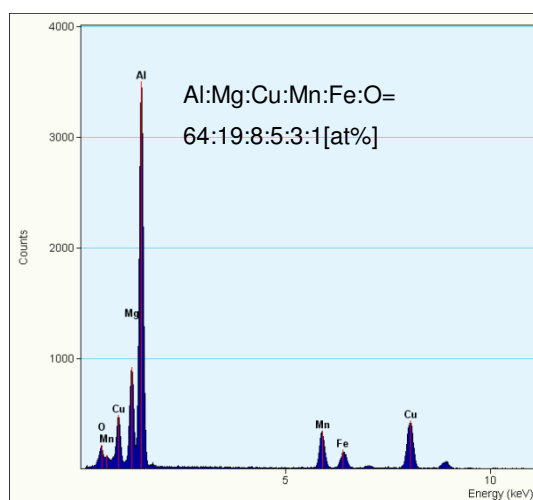
**Figure 4.13** Corresponding EDX of point 4 in **Figure 4.9**

### 4.1.3.2 The unreinforced BM 6061 matrix analysed by TEM

The 6061 alloy system is formulated to make use of the solubility of $Mg_2Si$ and thereby utilize precipitation hardening. If there is no manganese present, the iron-rich phases are $Fe_3SiAl_{12}$, $Fe_2Si_2Al_9$, or a mixture of the two, depending on the proportions of silicon and iron. Manganese and chromium stabilize $(Fe,Mn,Cr)_3SiAl_{12}$. 6061 generally has an excess of $Mg_2Si$ at the solutionizing temperature and, if slowly cooled, precipitates occur [79].

Figure 4.14 reveals a Si and O- rich $Mg_2Si$ precipitate. $Mg_2Si$ precipitation systems are aspired for this alloy system. The corresponding EDX is given in Figure 4.15. The precipitate in Figure 4.16 could possibly identify a Cr-containing $Fe_2Si_2Al_9$ particle as it is reported in the literature [4]. Considerable Si-rich Al-oxides developed during the extrusion were found which are bigger than 1µm as Figure 4.18 reveals. The corresponding analyse including the composition of the precipitate is given in Figure 4.19.
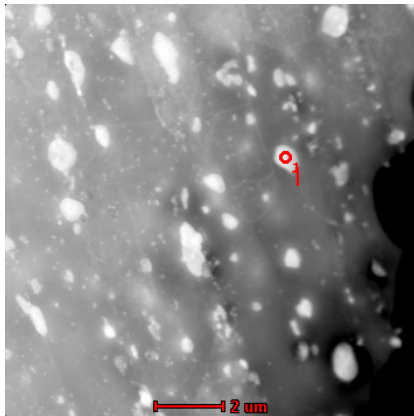


**Figure 4.14** a) TEM image of unreinforced BM 6061



O:Mg:Al:Si=31:5:45:19[at%]
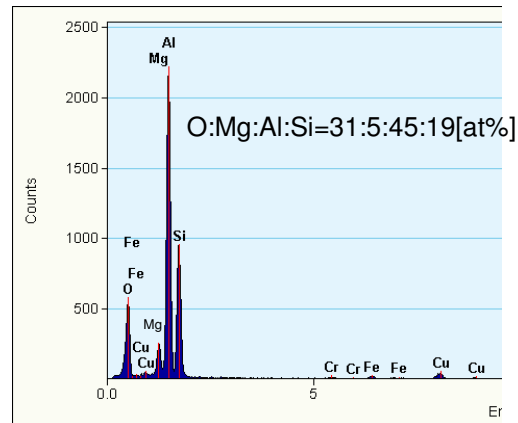
**Figure 4.15** Corresponding EDX of point 1 in **Figure 4.14**
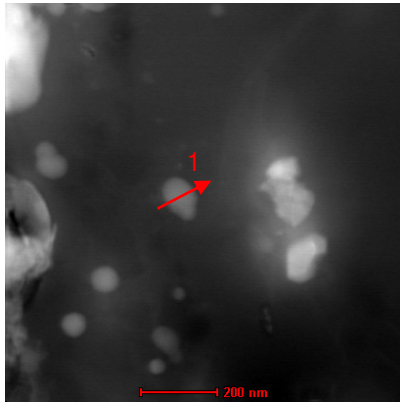
**Figure 4.16** a) TEM image of unreinforced BM 6061
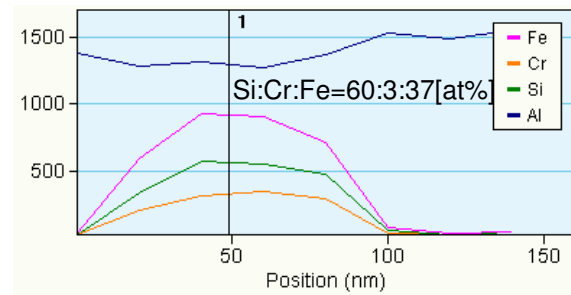


**Figure 4.17** Corresponding EDX of line 1 in **Figure 4.16**
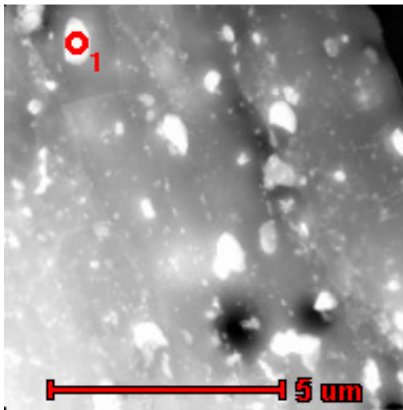


**Figure 4.18** a) TEM image of unreinforced BM 6061
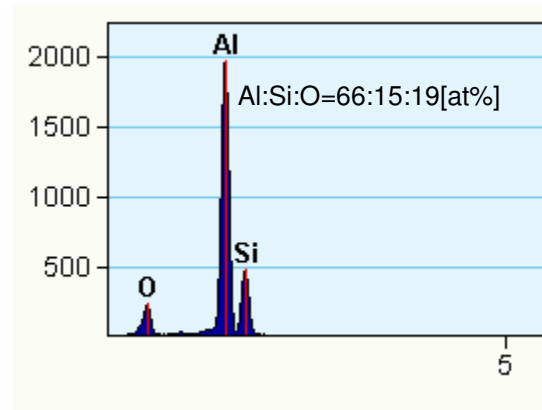


**Figure 4.19** Corresponding EDX of point 1 in **Figure 4.18**

### *4.1.3.3  The BM 2124/SiC/25p<5µm PRM analysed by TEM*

Figure 4.20 to Figure 4.33 show TEM images of the BM 2124/SiC/25p<5µm PRM. Figure 4.20 reveals the presence of different kinds of sub-µm particles in the size range of 0.05µm-0.3µm. Figure 4.21 shows the results of the line scan 1 from Figure 4.20 b) going from a SiC particle to the matrix alloy. Mg-rich Oxides appear at the SiC-particle-matrix interface. Figure 4.22 identifies three particles, two of them are CuMn-rich particles, probably $Cu_2Mn_3Al_{20}$. The third one is a Cu-rich particle, probably $Al_2Cu$. Oxide structures located at the SiC particle interfaces are shown connecting SiC particles in Figure 4.30. The corresponding line scan 1 of these

structures can be observed in Figure 4.31. These kind of multiphase structures with oxides are a distinctive characteristic of the studied BM PRMs.

Images of the <1µm SiC particles present in the BM materials are shown in Figure 4.23 a) and c) and the corresponding analyses are given in b) and d).

Figure 4.24 shows the presence of different sub-µm particles. Three spot analysis and two line scans were performed in this region. Figure 4.25 shows the result of EDX analyses of dot 1 which reveals a SiC particle whereas Figure 4.26 and Figure 4.27 gives the results of EDX analyses of dots 2 and 3 which show possible oxide particles. In Figure 4.28 the result of the line scan 1 in Figure 4.24 is presented with oxides on one side shows an increase in Si as well as an increase in C what refers to a SiC particle. The result given in Figure 4.29 for line scan 2 shows a Cu-rich particle that may correspond to an $Al_2Cu$ precipitate in between oxides. Figure 4.32 shows a sequence of the same material but prepared by electro polishing. According to Figure 4.33 it can be concluded that in this image some structures of oxides similar to the structures observed in Figure 4.20 near the SiC particles were observed on a SiC particle. Neither the shape nor the absorption contrast enables to distinguish the sub-µm particles by TEM.

Figure 4.43 in the next chapter shows TEM images of a BM 2124/SiC/25p<5µm a) in T4S condition with 1 hour overaging and b) after 8000 hours of creep exposure time. These images reveal that there is a change in the shape of the precipitates after certain overaging but in spite of this there is no affect on the materials since the hardness does not change.
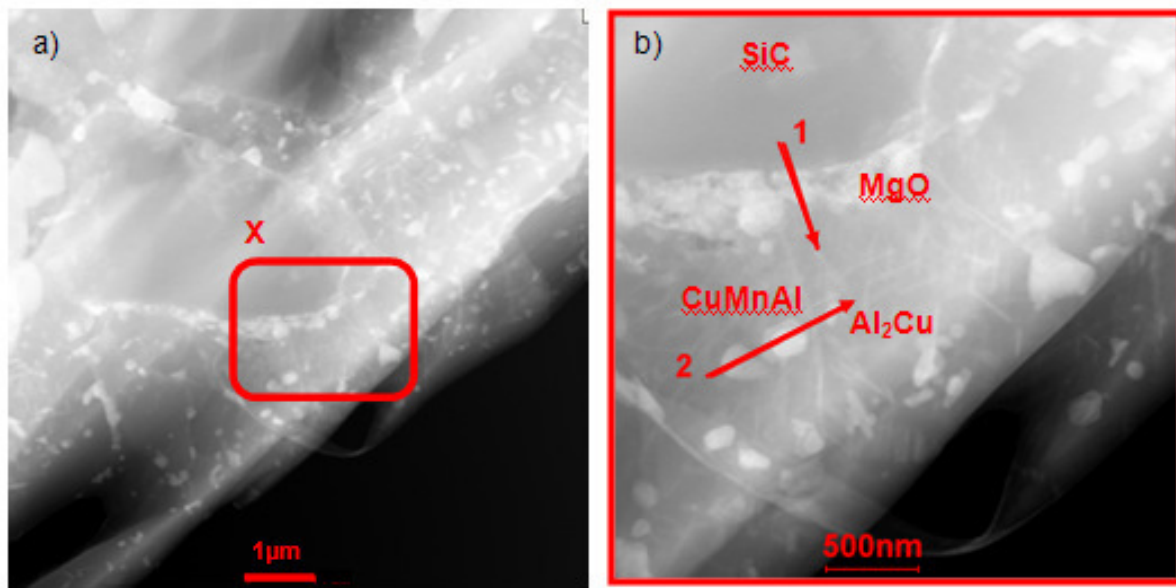
**Figure 4.20** TEM image of a BM 2124/SiC/25p<5µm sample prepared by ion milling a) overview and b) detail X and the lines "1" and "2" where the EDX analysis was performed
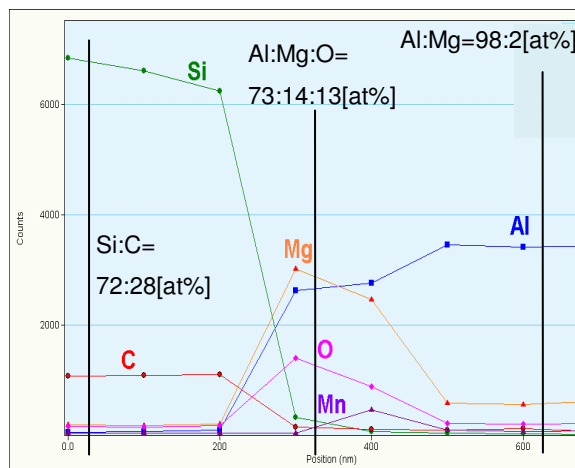


**Figure 4.21** Corresponding EDX counts of line scan 1 in **Figure** 4.20
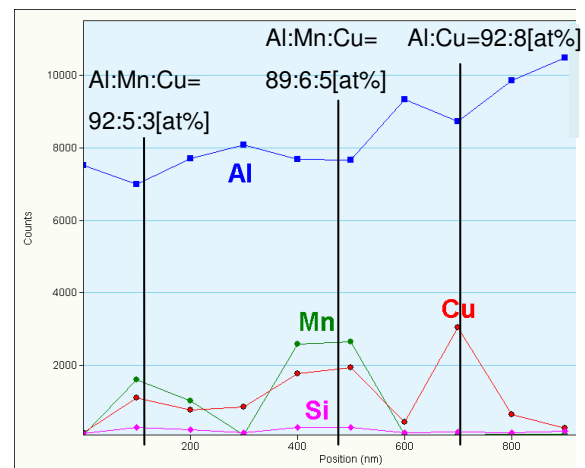


**Figure 4.22** Corresponding EDX counts along line scan 2 in **Figure** 4.20
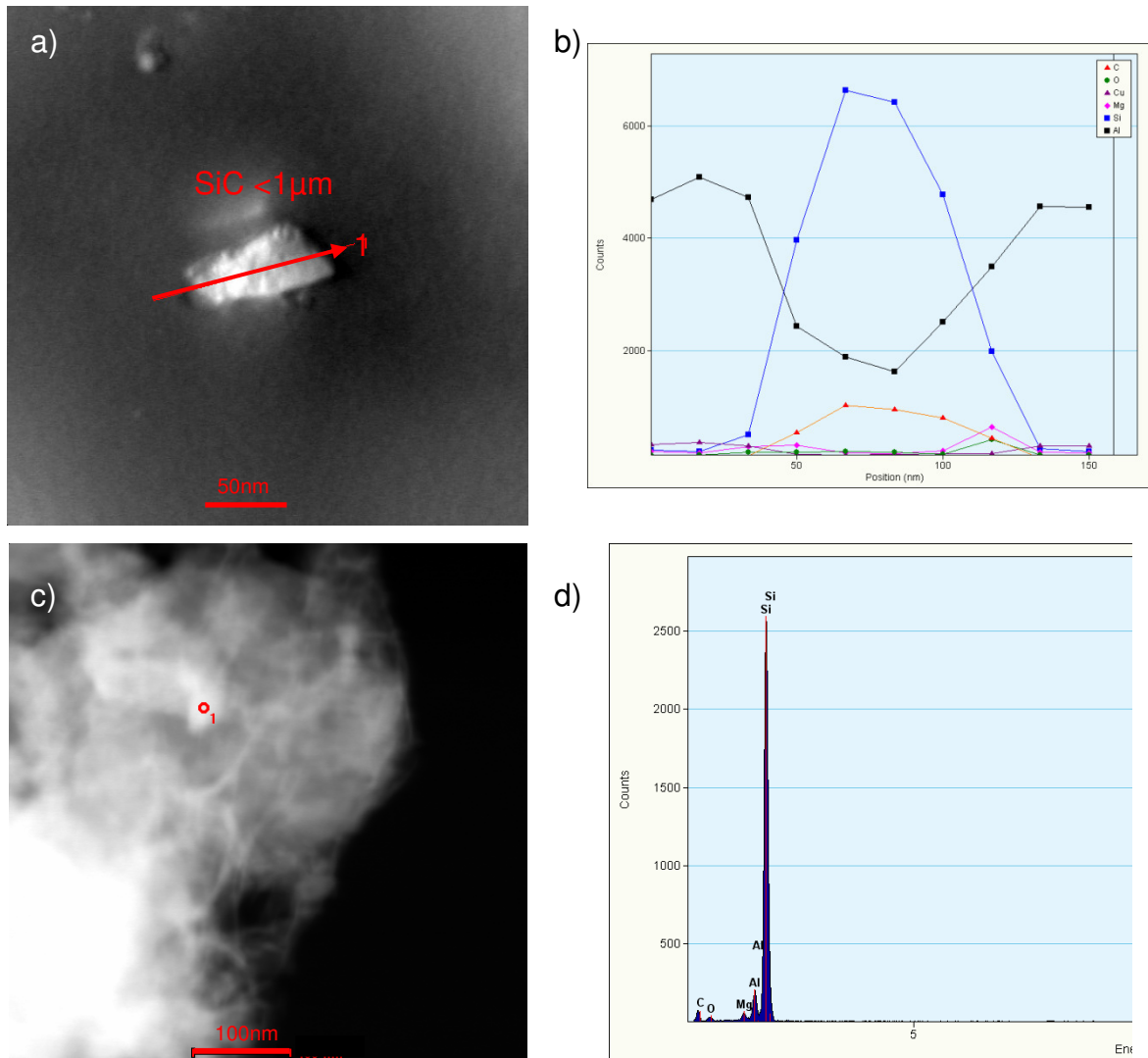
**Figure 4.23** TEM images of BM 2124/SiC/25p<5µm (a) and c)) in order to analyse the <1µm SiC particles with b) corresponding line scan 1 and d) corresponding spot scan 1
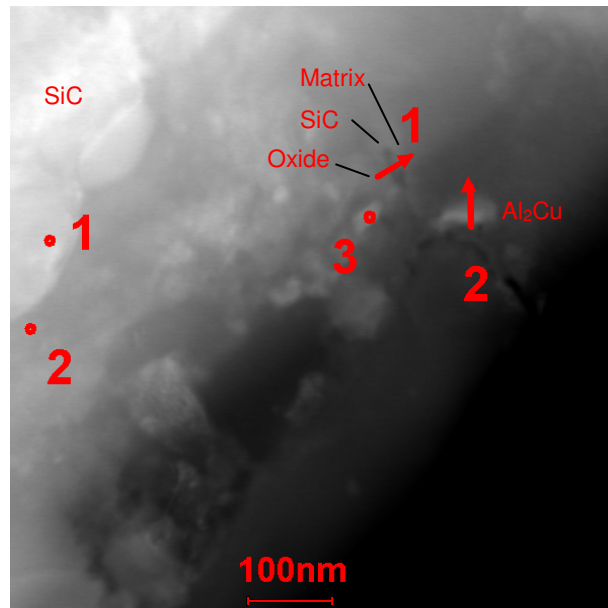
**Figure 4.24** TEM image of a BM 2124/SiC/25p<5µm sample prepared by ion milling with positions of spot analysis "1" (**Figure 4.25**) "2" (**Figure 4.26**) "3" (**Figure 4.27**) and line scans"1" (**Figure 4.28**) "2" (**Figure 4.29**)



Si:C=66:34[at%]



Mg:O=57:43[at%]



Mg:O=58:42[at%]
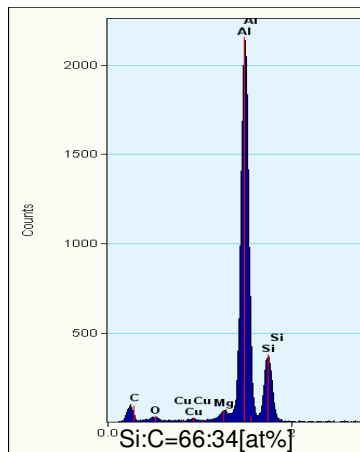
Al:Mg:O=76:16:8[at%]

**Figure 4.25** Corresponding EDX of point 1 in **Figure 4.24** – mainly SiC
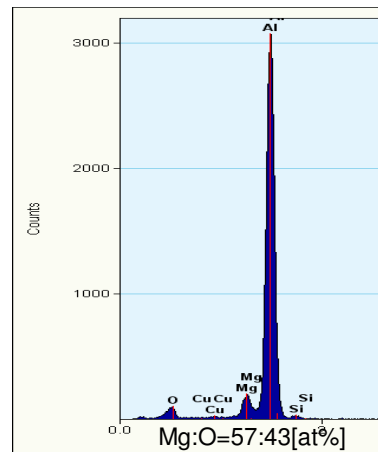
**Figure 4.26** Corresponding EDX of point 2 in **Figure 4.24** – mainly oxide
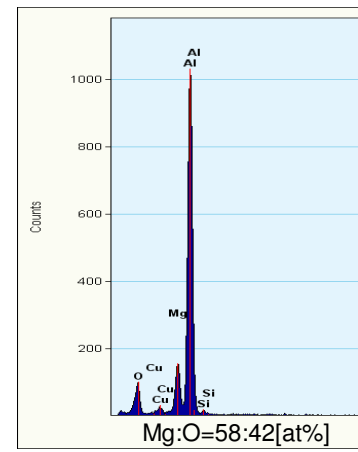
**Figure 4.27** Corresponding EDX of point 3 in **Figure 4.24** – mainly oxide
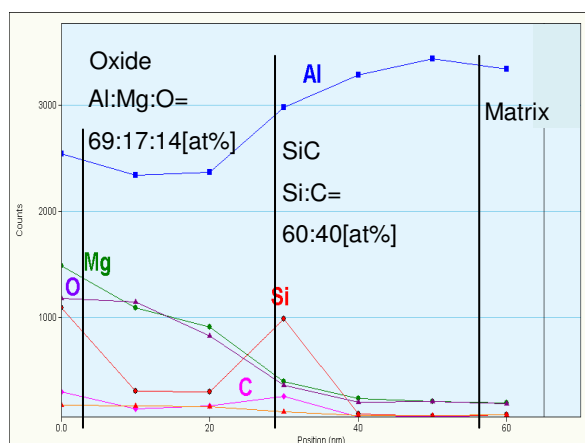
**Figure 4.28** Corresponding line scan 1in **Figure 4.24**
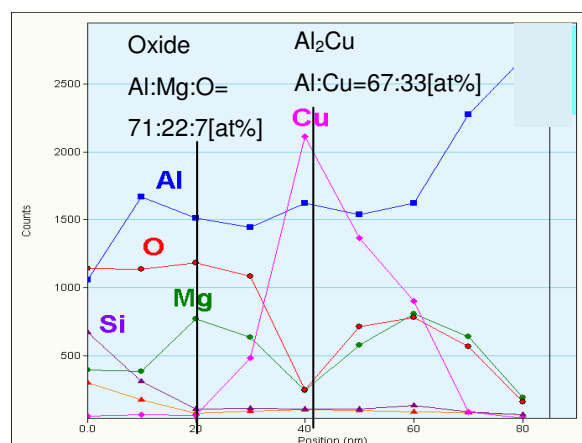


**Figure 4.29** Corresponding line scan 2 in **Figure 4.24**
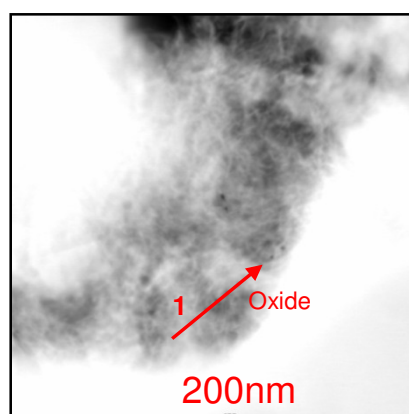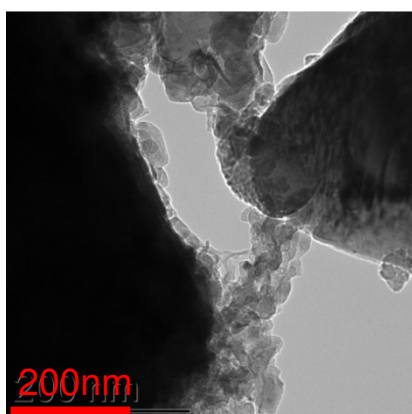


**Figure 4.30** Oxide structures in the BM PRMs with line "1" where EDX analysis were taken
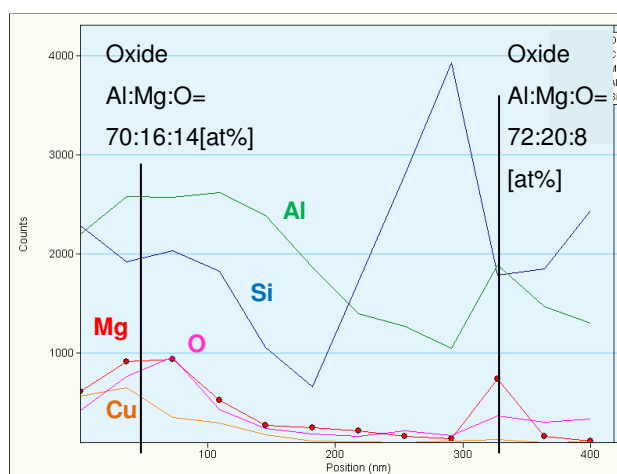


**Figure 4.31** Corresponding EDX line scan 1 in **Figure 4.30**
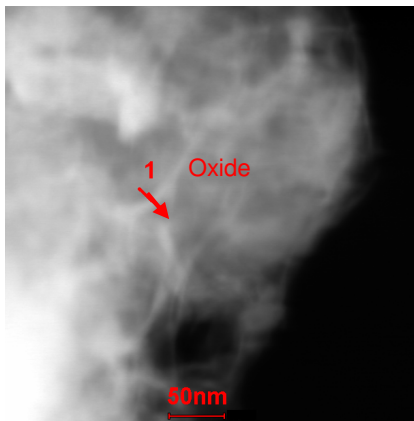
**Figure 4.32** TEM image of a BM 2124/SiC/25p<5µm sample prepared by electro polishing with indicated line for **Figure 4.33**
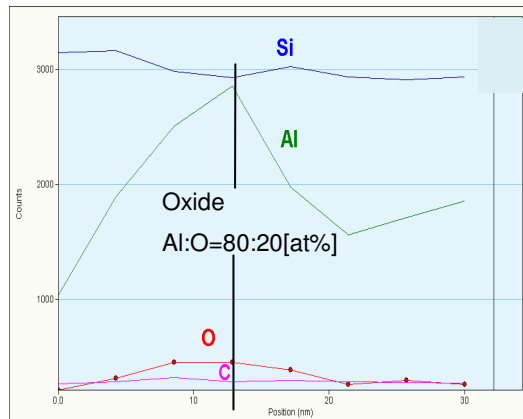
**Figure 4.33** Corresponding EDX line scan 1 in **Figure 4.32** – SiC particles with oxide

### 4.1.3.4  The WB 2124/SiC/25p<5µm PRM analysed by TEM

Figure 4.34 to Figure 4.42 show TEM images and EDX analyses of the WB 2124/SiC/25p<5µm PRM.

It can be seen in Figure 4.34 that a smaller amount of sub-µm particles is present in the WB material resulting in a "cleaner" microstructure than for the BM material. Figure 4.35 shows a detail of the region of Figure 4.34. The results of line scan 1, spot analysis 1 to 5 (see Figure 4.36, Figure 4.37 to Figure 4.41, respectively) show the different kinds of precipitates. Analyses of spot 2 and spot 3 (see Figure 4.38 and Figure 4.39, respectively) compare the spot analysis of an $Al_2Cu$ precipitate with that of the matrix as it was also observed in the BM material according to Figure 4.22. Spot 4 and 6 seem to be the same kind of $Al_2Cu$ particles. As Figure 4.40 and Figure 4.42 reveal these particles are $Al_2Cu$ precipitations. Mainly $Al_2Cu$ platelets of 0.1-0.3µm diameter were identified.

Figure 4.44 presents images of a a) WB 2124/SiC/25p<5µm in T4S condition with 1 hour overaging and b) WB 2124/SiC/25p<20µm after 30 hours of creep exposure time. Here also the shapes of the precipitates become round during creep without affecting the hardness of the material.
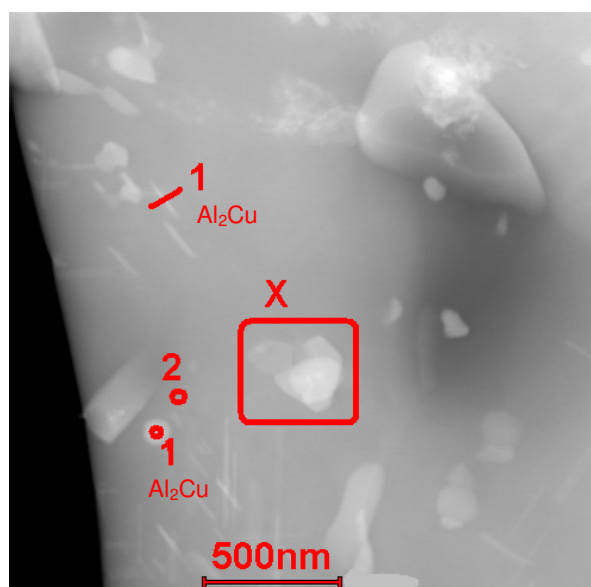
**Figure 4.34** TEM image of WB 2124/SiC/25p<5µm prepared by electro polishing
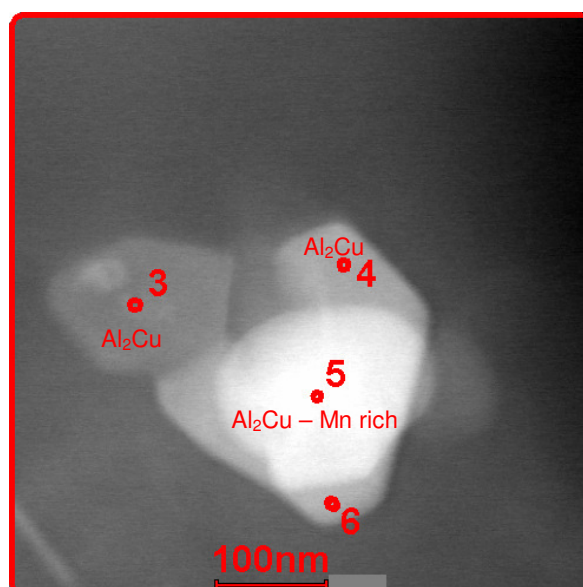


**Figure 4.35** Detail X of WB 2124/SiC/25p<5µm in **Figure 4.34**
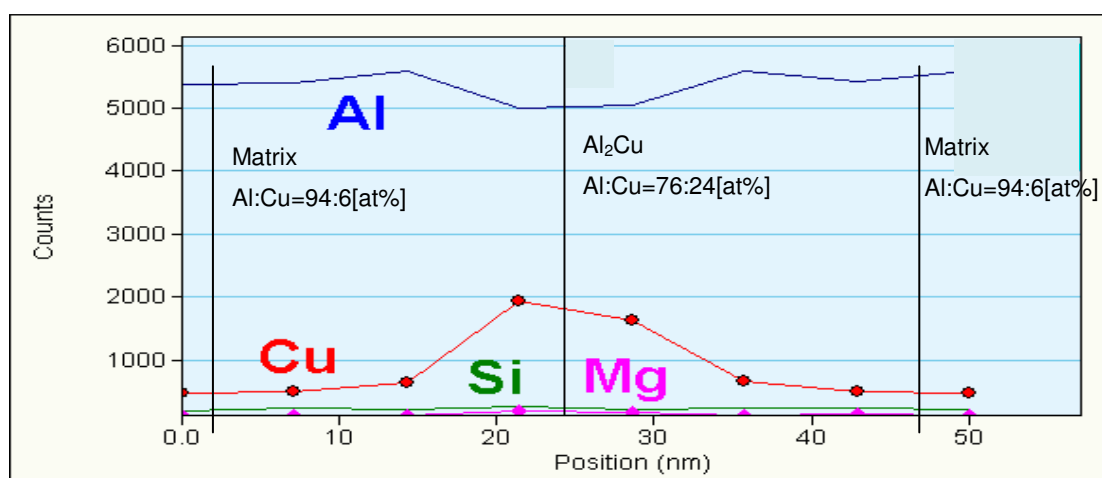


**Figure 4.36** Corresponding line scan 1 in **Figure 4.34**
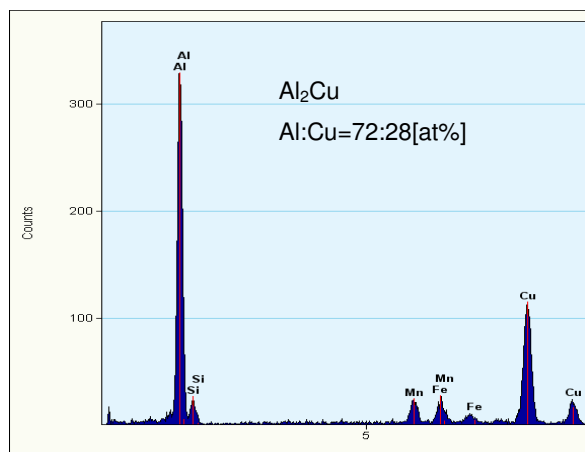
**Figure 4.37** Corresponding EDX of point 1 in **Figure 4.34** – Al$_2$Cu
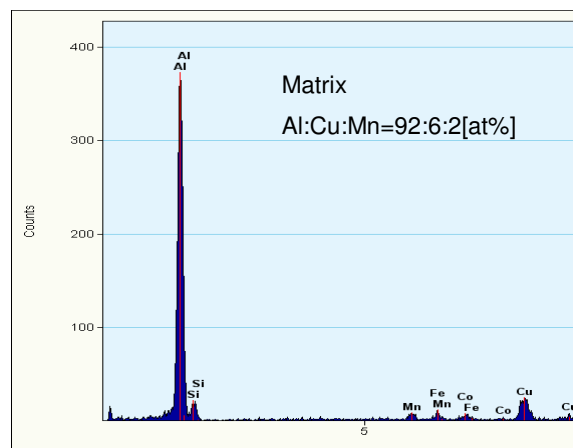


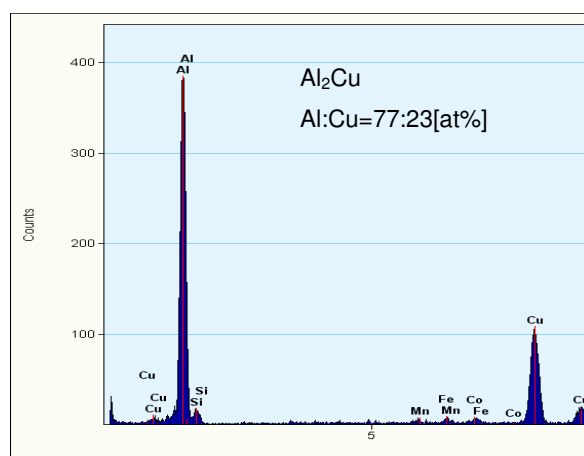**Figure 4.38** Corresponding EDX of point 2 in **Figure 4.34** - matrix
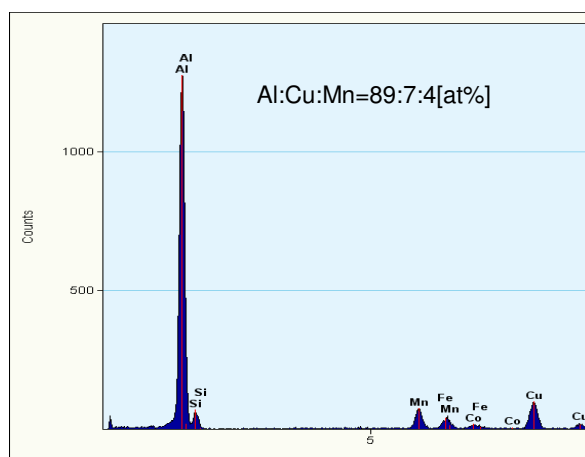


**Figure 4.39** Corresponding EDX of point 3 in **Figure 4.35**
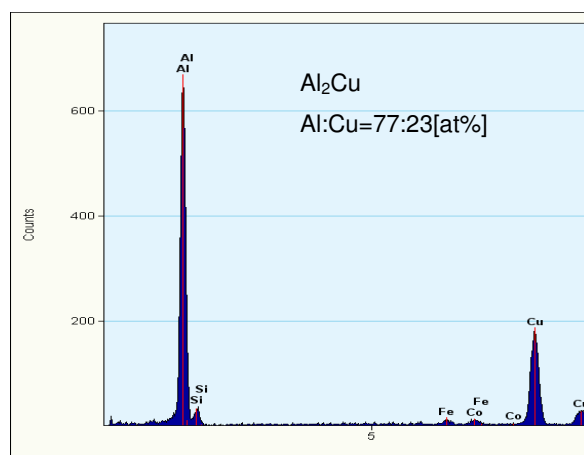


**Figure 4.40** Corresponding EDX of point 4 in **Figure 4.35** – Al$_2$Cu
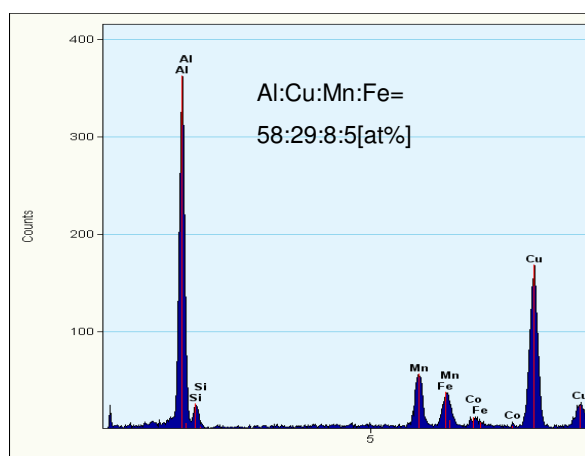


**Figure 4.41** Corresponding EDX of point 5 in **Figure 4.35**



**Figure 4.42** Corresponding EDX of point 6 in **Figure 4.35** – Al$_2$Cu
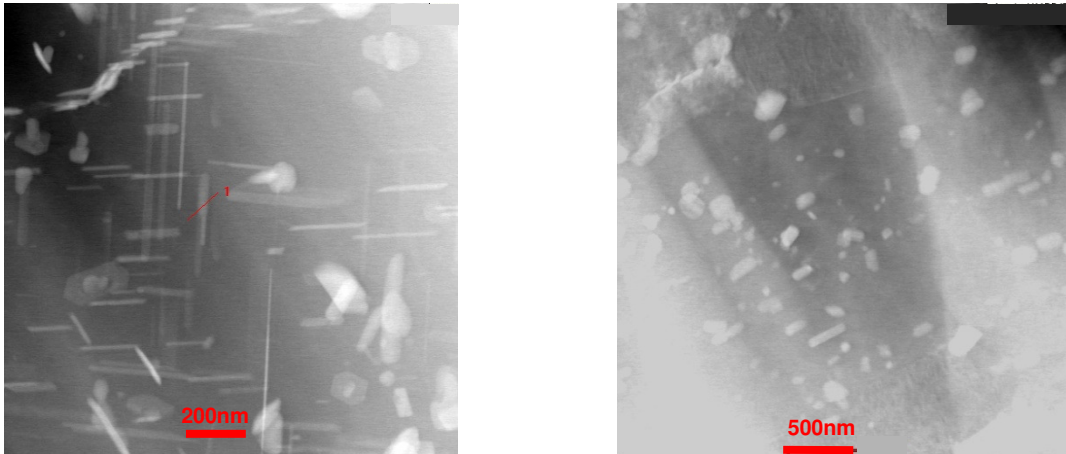
**Figure 4.43** BM 2124/SiC/25p<5µm a) in T4S condition with 1 hour overaging and b) after 8000 hours of creep exposure time
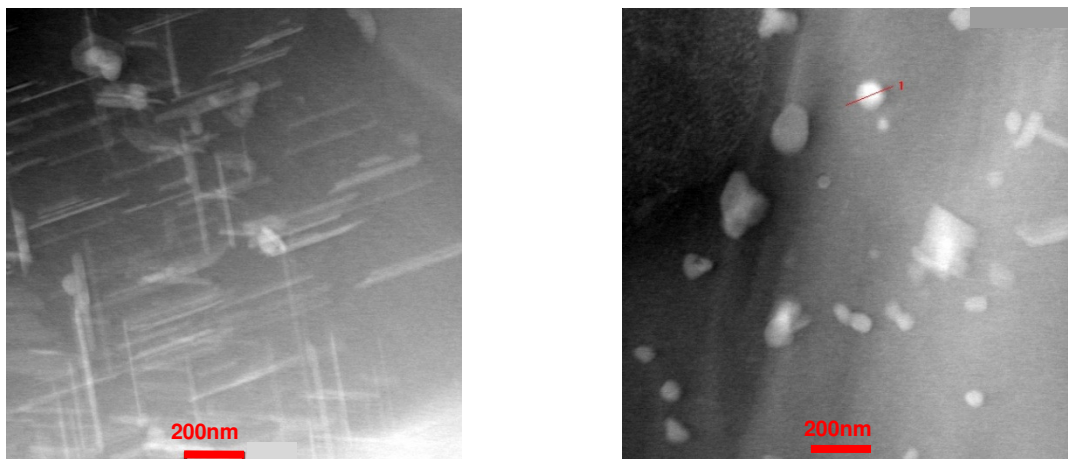


**Figure 4.44** a) WB 2124/SiC/25p<5µm in T4S condition with 1 hour overaging and b) WB 2124/SiC/25p<20µm after 30 hours of creep exposure time

### 4.1.4  Electron Backscatter Diffraction Technique (EBSD)

Figure 4.45 shows the unreinforced 2124 alloy after extrusion and after the T4S heat treatment of a) without BM and b) with BM as well as c) the unreinforced BM 6061 alloy after extrusion and after the T4S heat treatment. A refinement of the grain size due to the process of BM is evident. The unreinforced matrix without BM shows many elongated big grains (up to 150µm) as well as small ones and subgrains (3-7µm). The same matrix produced with BM shows much less of the elongated big grains (up to 100µm) resulting in mainly small ones (1-3µm). The unreinforced BM 6061 matrix

alloy shows no grains longer than 50µm. Mainly, this material shows grains in the size range 2-5µm and they seem to be more aligned in the direction of extrusion than those in the BM 2124 alloy where the grains tend to be more rounded.

The initial grain size of the PRMs is given in Figure 4.46. The black areas either indicate SiC particles, the shadows around the SiC particles or poorly indexed grains. The grain size in T4S condition of WB 2124/SiC/25p<5µm can be seen in Figure 4.46 a), whereas Figure 4.46 b) reveals the initial grain size of WB 6061/SiC/25p<5µm in T4S condition. Compared with the BM 2124/SiC/25p<5µm shown in Figure 4.46 c) the WB PRMs tend to have slightly bigger grains. The elongated big grains tend to disappear due to the presence of SiC particles resulting in mainly small grains. All the analysis of the grain size was conducted in longitudinal direction. The effect of mechanical alloying and the corresponding refinement of the microstructure and the resulting effect on the mechanical properties is discussed by several authors [91, 92, 93, 94] in the last decades. A slight decrease of the grain size in the BM PRMs (1-3µm) compared with the WB PRMs (3-5µm) was found in the present study.

c)
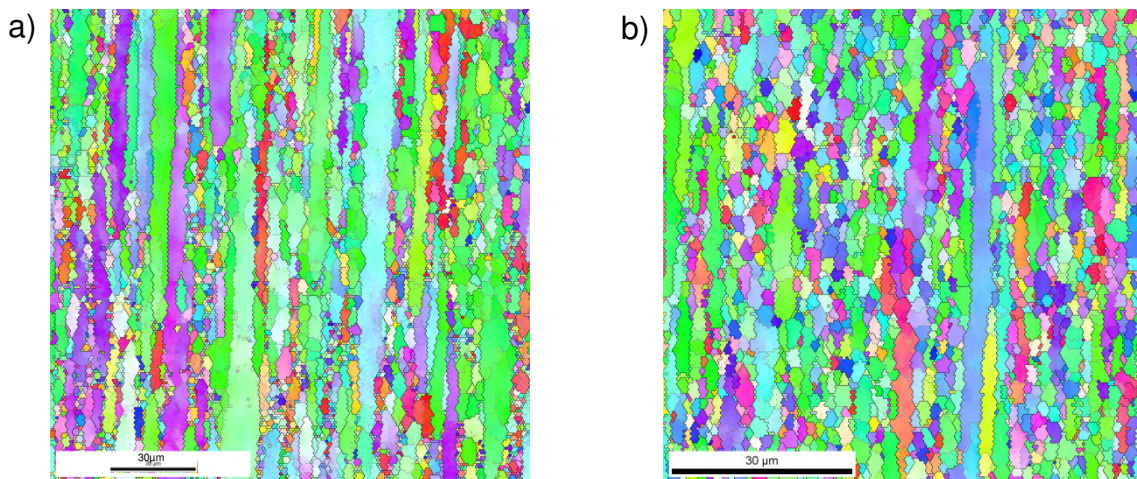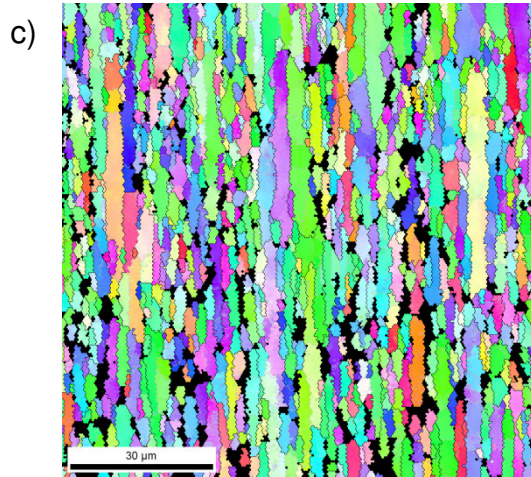


**Figure 4.45** Initial grain size of unreinforced 2124 alloy after extrusion at 450 °C followed by a heat treatment T4S of a) without BM and b) with BM and c) BM 6061 T4S
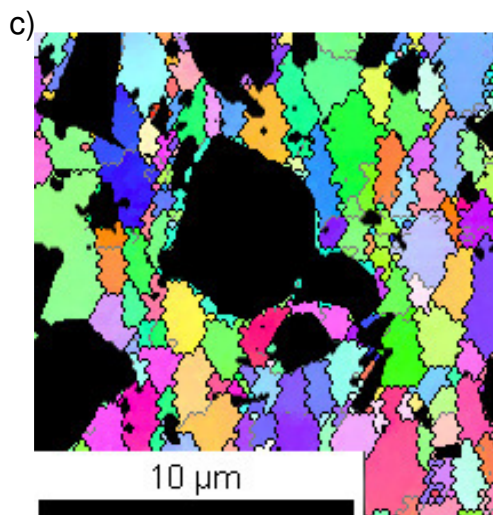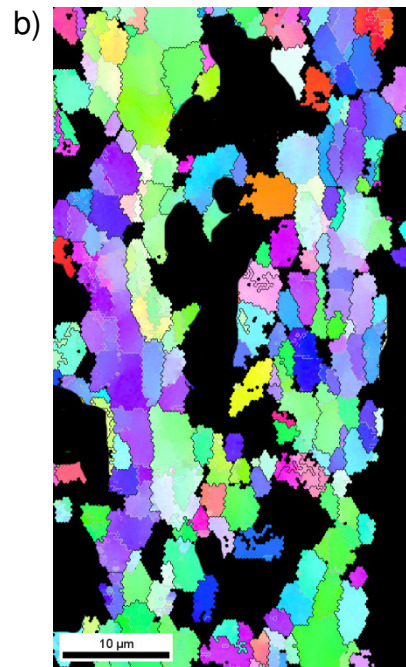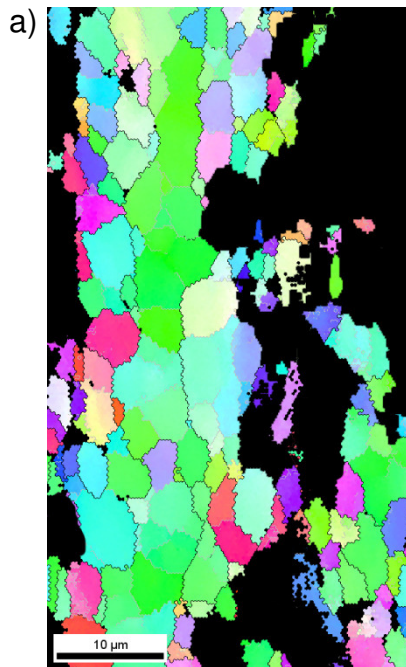
a)



b)



c)



**Figure 4.46** Initial grain size of the PRMs: a) WB 2124/SiC/25p<5µm, b) WB 6061/SiC/25p<5µm c) BM 2124/SiC/25p<5µm

## 4.2 Dynamical Mechanical Analysis (DMA)

Up to four tests were carried out for each material. Only one test was conducted for each WB PRM due to a shortage of material. That is why there could be an error within the measurement of the WB PRMs the Young´s Moduli of which are slightly (3%) higher than those of the BM PRMs. The reinforcement phase added to the introduced 2124 and 6061 alloys causes an increase of the Young´s Modulus of about 60% and 40%, respectively, in the whole tested temperature range. The DMA results for a temperature range from 30 °C to 295 °C are given in Table 4.3. Additionally, the obtained curves of the Young´s modulus in this temperature range are given in Figure 4.47.

The results show a faster decrease of the Young´s Modulus with temperature for all the 6061 materials than for the 2124 materials. The unreinforced matrix as well as the particle reinforced 6061 alloys result in a decrease of the Young´s Modulus by about 25% between 30 °C and 300 °C. This decrease is only about 18% for all the 2124 materials. These results are summarized in Table 4.4.

The results of the DMA tests of the unreinforced 2124 matrices both with and without BM are very close. The unreinforced 6061 matrix shows a Young´s Modulus which is in quite good accordance to the unreinforced 2124 matrix at lower temperatures. The higher the temperature raises the bigger the difference between 2124 and 6061 unreinforced matrices because of a faster decrease of Young´s Modulus of 6061 at higher temperatures.

For the BM PRMs with the different SiC particle sizes it can be observed that there are no differences in the resulting temperature dependence of the E-Modulus.

In case for the WB PRMs with 2124 matrix, the bigger reinforcing particles yield slightly smaller (8%) Youngs Modulus. All in all, it can be concluded that the presence of SiC particles within the matrices lead to an increase of the Young´s Modulus. Regarding the different alloying routes and the different SiC particle sizes there should no difference be manifested at all.

| Material | | Temperature [°C] | | | |
|---|---|---|---|---|---|
| | | **30** | **100** | **200** | **295** |
| | | **Youngs Modulus [GPa]** | | | |
| **AA2124/SiC/25p/<5µm/BM** | 566_01 | 116 | 113 | 106 | 95 |
| | 566_02 | 115 | 112 | 106 | 96 |
| | 572_01 | 118 | 115 | 109 | 98 |
| | 572_02 | 119 | 115 | 110 | k.a. |
| | | **117 ± 2** | **114 ± 2** | **108 ± 2** | **96 ± 1** |
| **AA2124/SiC/25p/<10µm/BM** | 567_01 | 119 | 116 | 110 | 100 |
| | 567_02 | 118 | 115 | 110 | 99 |
| | 573_01 | 120 | 116 | 111 | 100 |
| | 573_02 | 116 | 113 | 107 | 97 |
| | | **118 ± 2** | **115 ± 1** | **110 ± 2** | **99 ± 1** |
| **AA2124/SiC/25p/<20µm/BM** | 568_01 | 112 | 109 | 102 | 91 |
| | 568_03 | 112 | 109 | 104 | 93 |
| | 574_01 | 114 | 111 | 107 | 96 |
| | 574_02 | 117 | 114 | 109 | 98 |
| | | **114 ± 2** | **111 ± 3** | **106 ± 3** | **95 ± 3** |
| **AA2124/4h BM** | 576_01 | 73 | 71 | 66 | 60 |
| | 576_02 | 75 | 72 | 68 | 61 |
| | 577_01 | 70 | 68 | 63 | 57 |
| | 577_02 | 72 | 71 | 67 | 59 |
| | | **73 ± 2** | **71 ± 2** | **66 ± 2** | **59 ± 2** |
| **AA2124/as rec.** | 570_01 | 73 | 71 | 67 | 61 |
| | 570_02 | 73 | 70 | 66 | 61 |
| | 571_01 | 76 | 74 | 69 | 64 |
| | 571_02 | 76 | 73 | 69 | 65 |
| | | **75 ± 1** | **72 ± 1** | **68 ± 1** | **63 ± 2** |
| **AA6061/4h BM** | 637_01 | 76 | 72 | 64 | 55 |
| | 637_02 | 74 | 71 | 64 | 56 |
| | | **75 ± 1** | **72 ± 1** | **64 ± 0** | **56 ± 1** |
| **AA6061/SiC/25p/<5µm/WB** | 638_01 | 102 | 99 | 89 | 78 |
| | 638_02 | 108 | 104 | 93 | 82 |
| | | **105 ± 3** | **102 ± 2** | **91 ± 2** | **80 ± 2** |
| **AA6061/SiC/25p/<20µm/WB** | 632_01 | 110 | 106 | 95 | 82 |
| | | **110** | **106** | **95** | **82** |
| **AA2124/SiC/25p/<5µm/WB** | 639_01 | 124 | 122 | 115 | 103 |
| | | **124** | **122** | **115** | **103** |
| **AA2124/SiC/25p/<20µm/WB** | 633_01 | 116 | 114 | 107 | 94 |
| | | **116** | **114** | **107** | **94** |

**Table 4.3** Results of Young´s Modulus measurements of all the introduced materials

| Material | [%] |
|---|---|
| AA2124/SiC/25p/<5µm/BM | 17 |
| AA2124/SiC/25p/<10µm/BM | 16 |
| AA2124/SiC/25p/<20µm/BM | 17 |
| AA2124/4h BM | 18 |
| AA2124/as rec. | 16 |
| AA6061/4h BM | 26 |
| AA6061/SiC/25p/<5µm/WB | 24 |
| AA6061/SiC/25p/<20µm/WB | 26 |
| AA2124/SiC/25p/<5µm/WB | 17 |
| AA2124/SiC/25p/<20µm/WB | 19 |

**Table 4.4** Decrease of value of Young´s Modulus during heating up to 300°C of all the materials
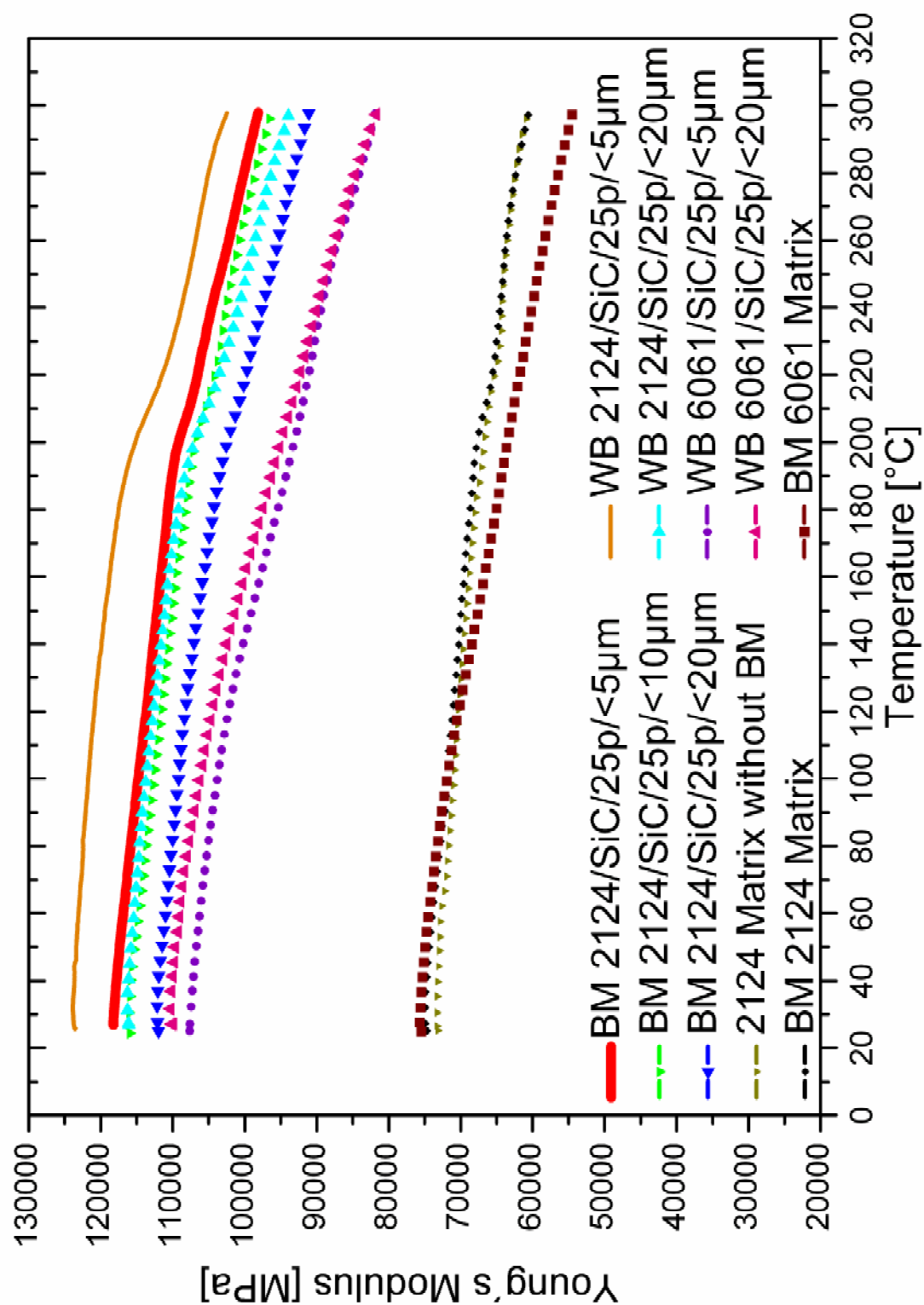
**Figure 4.47** Curves of Young´s Modulus as a function of temperature of all the introduced materials

## 4.3  High Temperature (HT) Tensile Tests

HT tensile tests were conducted at 300 °C in air atmosphere in order to investigate the high temperature strength of the unreinforced matrices and PRMs. All the resulting curves of the tests are given in Figure 4.48. The results of $R_{p0.2}$, $\sigma_{max}$ and strain failure are summarized in Table 4.5. The 2124 material has good strength and ductility, with total elongation exceeding 30% at 300 °C in the case of the 2124 without BM and reaching almost 40% total elongation in the case of the 2124 which was subjected to BM. The unreinforced 2124 alloy shows a high temperature strength about 60% higher than that of the unreinforced 6061 alloy. The strengthening behaviour and the strain to failure was studied frequently during the last decades by means of hot tensile tests [61, 91, 95, 96, 97].

The BM PRMs show the biggest high temperature strength and this increases the smaller the initial particle size combined with decreasing ductility. There is little increase in $R_{p0.2}$ and $R_m$ and no strain hardening occurs. The same tendency is observed for the WB PRMs. It can be seen that the WB PRMs with the smaller reinforcing particles also result in better high temperature strength than those with the bigger reinforcing particles. The ductility of 2124/SiC/25p<5µm is higher than that of the PRM with bigger particles. Lower strength and less ductility is observed as well for the 6061 matrix compared with 2124.

The BM PRMs result in a significantly higher HT strength than the corresponding unreinforced matrix, while the WB PRMs<20µm show almost the same high temperature strength as the unreinforced matrix but with a significant loss of ductility. This is observed for both the WB 2124 PRMs as well as for the WB 6061 PRMs. The strains to failure of the unreinforced matrices exceed those of the PRMs about 2 to 3 times. The addition of SiC particles increases the strength but decreases the strain to failure as softening rate is increasing. For the BM PRMs the strain to failure is going to be third and for the WB PRMs it is going to be the half. This effect is obtained for both, the BM and the WB PRMs. There is also an effect of the SiC particle size on $R_{p0.2}$ and $\sigma_{max}$. This means that with decreasing the added SiC particle size the strengthening properties increases. This can be clearly seen by comparing the results of hot tensile tests of all the PRMs. Among all the tested materials the PRMs

prepared by BM show the highest $R_{p0.2}$ value. A clear ranking is obtained which can be attributed to the particle size and to the interparticle distances, respectively. This means the smaller the particles the smaller the interparticle distances and the higher the value for $R_{p0.2}$. Among the WB materials the same ranking can be seen. The WB PRMs with the smaller particles show higher $R_{p0.2}$ than WB PRMs with bigger particles. Those WB PRMs with the bigger particles (<20µm) show almost the same UTS than the unreinforced matrix. This means, that the UTS value cannot be increased by adding SiC particles with sizes of <20µm.

The same behaviour can be observed for the 6061 PRMs and the corresponding unreinforced alloy but with 40% reduced values of $R_{p0.2}$ compared to the 2124 matrix and PRMs. This means that the WB PRM with 6061 matrix with bigger SiC particles show the same $R_{p0.2}$ as the 6061 matrix. The failure strain for WB PRM is about 50% less than that of the corresponding unreinforced matrix alloy. Again the WB PRMs with 6061 with the smaller SiC particles obtain clearly higher $R_{p0.2}$ than the one with bigger SiC and the unreinforced 6061.

| Material | Sample | $Rp_{0,2}$ [N/mm²] | | $\sigma_{max}$ [N/mm²] | | $Rp_{0,2}/\sigma_{max}$ | A [%] | |
|---|---|---|---|---|---|---|---|---|
| AA2124/SiC/25p/<5µm/BM | 566_2 | 123 | | 129 | | **0.96** | 10 | |
| | 572 | 122 | **123 ± 1** | 127 | **128 ± 1** | | 9 | **10 ± 1** |
| AA2124/SiC/25p/<10µm/BM | 567 | 119 | | 122 | | **0.97** | 13 | |
| | 567_2 | 117 | **118 ± 1** | 122 | **122 ± 0** | | 12 | **12 ± 1** |
| AA2124/SiC/25p/<20µm/BM | 568 | 114 | | 117 | | **0.97** | 13 | |
| | 568_2 | 113 | **113 ± 1** | 116 | **116 ± 1** | | 13 | **13 ± 0** |
| AA2124/SiC/25p/<5µm/WB | 643a | 100 | | 108 | | **0.91** | 9 | |
| | 643b | 97 | **99 ± 2** | 110 | **109 ± 1** | | 12 | **10 ± 2** |
| AA2124/SiC/25p/<20µm/WB | 642a | 93 | | 97 | | **0.94** | 8 | |
| | 642b | 86 | **89 ± 3** | 93 | **95 ± 2** | | 10 | **9 ± 1** |
| AA2124 Matrix as rec. | 570 | 92 | | 92 | | **0.99** | 31 | |
| | 571 | 89 | **90 ± 2** | 89 | **91 ± 2** | | 32 | **31 ± 1** |
| AA2124 Matrix 4h BM | 576 | 95 | | 95 | | **0.99** | 37 | |
| | 577 | 90 | **92 ± 2** | 91 | **93 ± 2** | | 42 | **39 ± 2** |
| AA6061/SiC/25p/<5µm/WB | 641a | 67 | | 71 | | **0.94** | 12 | |
| | 641b | 66 | **66 ± 1** | 70 | **70 ± 1** | | 11 | **11 ± 1** |
| AA6061/SiC/25p/<20µm/WB | 636a | 57 | | 60 | | **0.95** | 14 | |
| | 636b | 54 | **56 ± 2** | 57 | **59 ± 1** | | 10 | **12 ± 2** |
| AA6061 Matrix 4h BM | 640a | 58 | | 58 | | **0.98** | 28 | |
| | 640b | 57 | **57 ± 1** | 57 | **58 ± 1** | | 27 | **27 ± 1** |

**Table 4.5** Results of all the conducted high temperature tensile tests at 300 °C
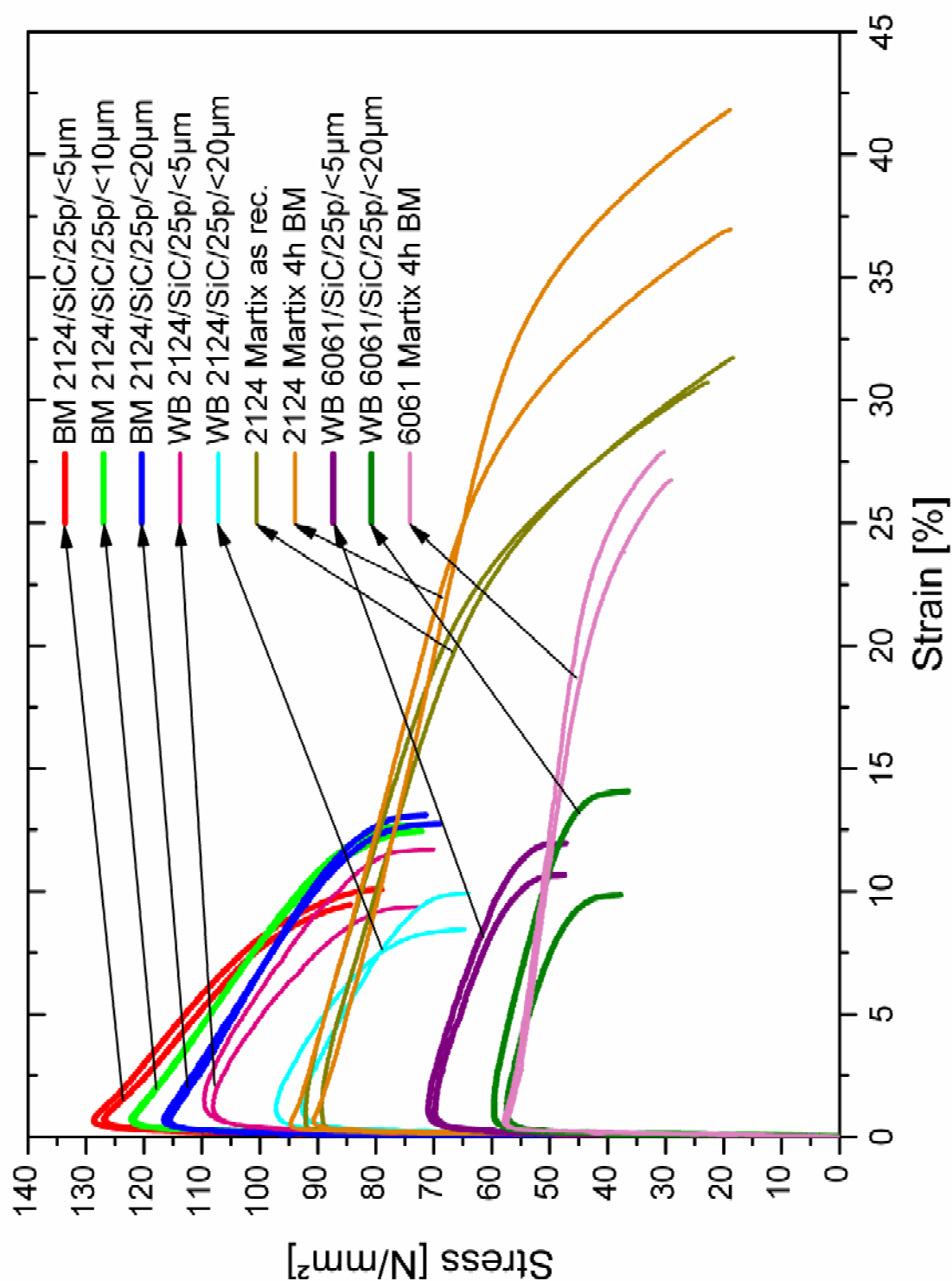
**Figure 4.48** Results of HT tensile tests at 300°C of all the introduced materials in T4S condition

## 4.4 Nano Hardness Measurements

Nano hardness measurements were carried out in order to see if there is a difference in the hardness of the matrix due to the blending route of the PRMs.

The matrix without BM and the matrix subjected to BM as well as the 2124 BM PRMs and the 2124 WB PRMs were tested in the directions longitudinal and perpendicular to extrusion. It was found that there is no difference in the nano hardness between these directions. Therefore the results were combined as shown in Figure 4.49. The nano hardness increases in both the BM PRMs as well as in the WB PRMs compared to the unreinforced matrix whereas the WB <20µm PRM is very close to the unreinforced matrix. No differences were found between the matrix subjected to 4 hours BM and without BM. This means that the process of BM itself does not influence the hardness of the unreinforced alloy. Considerable differences were obtained between the BM and the WB PRMs. Here, the sub-µm SiC particles introduced during BM result in an increase of the nano-hardness for the BM PRMs. The absence of small SiC particles in the regions between large SiC particles results in a lower nano hardness. The PRMs with the biggest SiC particles (<20µm) show a lower nano hardness than those with the smaller initial SiC particle sizes (<10µm and <5µm) for both types of PRMs.
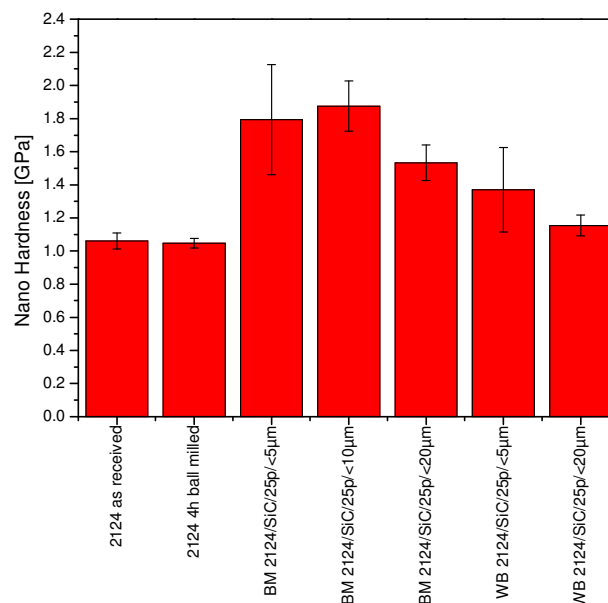


**Figure 4.49** Nano hardness of the unreinforced 2124 matrices and the 2124 WB and BM PRMs

### 4.4.1 Brinell hardness after Creep Exposure Time

The results in Figure 4.50 show a decrease of the Brinell hardness HB between the T4 and T4S conditions. After a few hours more at 300°C the HB remains constant during creep exposure. This means that there is no further overaging effect. Figure 4.50 a) shows the results of hardness measurement of BM 2124/SiC/<5μm. The HB at 4200 hours exposure time is the same than after 8000 hours exposure time. Figure 4.50 b) shows the results of WB 2124/SiC/<5μm. The HB at 16 hours exposure time is the same as after 300 hours exposure time what emphasises the above mentioned statement. Again it can be seen that no effect of further overaging is evident in any alloy during exposure times >3 hours according to the results of the unreinforced matrix without BM shown in c).

Figure 4.51 shows the results of all the Brinell hardness measurements compared with the time to the power of 1/3. Assuming diffusion controlled ripening of spherical precipitates [98] at constant temperature, this plot indicates relatively fast overaging.

c)



d)



e)
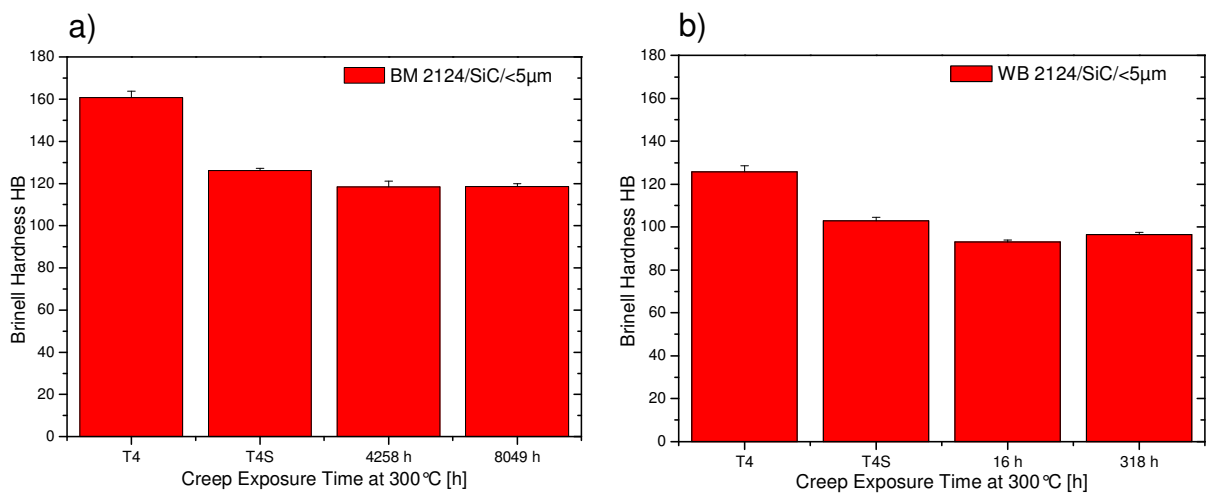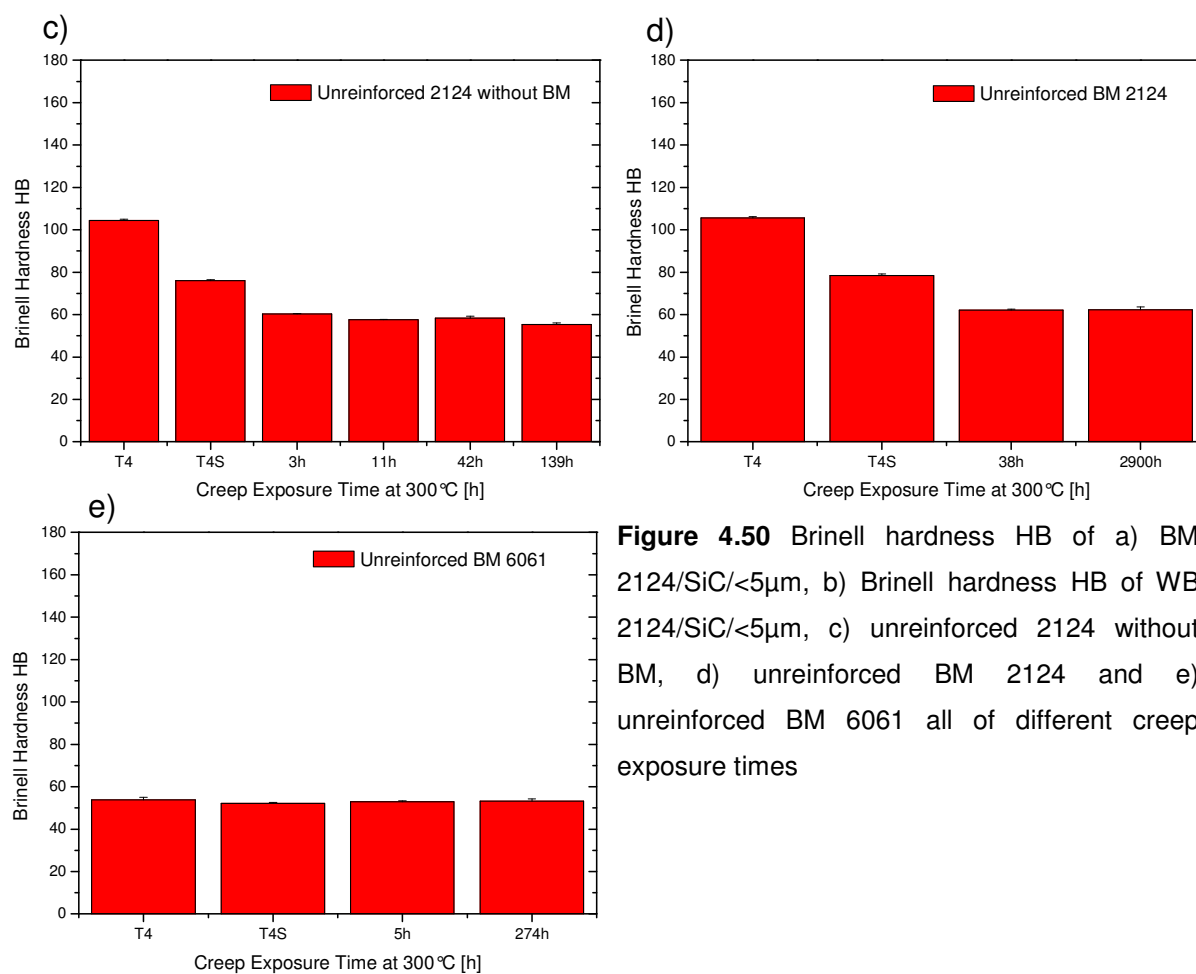


**Figure 4.50** Brinell hardness HB of a) BM 2124/SiC/<5µm, b) Brinell hardness HB of WB 2124/SiC/<5µm, c) unreinforced 2124 without BM, d) unreinforced BM 2124 and e) unreinforced BM 6061 all of different creep exposure times
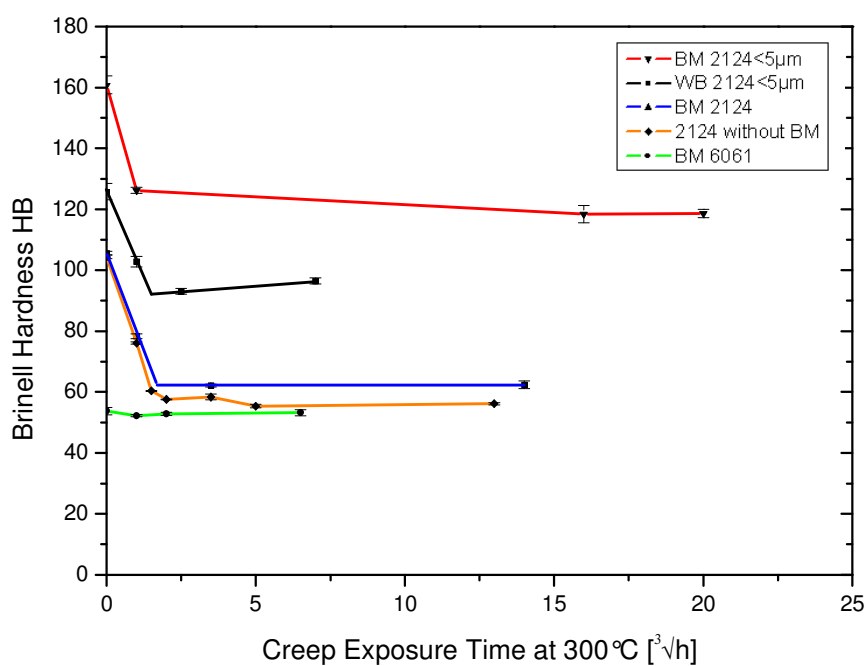


**Figure 4.51** Comparison of the Brinell hardness HB over $^3\sqrt{}$time

## 4.5  Isothermal Tensile Creep Experiments

All the strain $\varepsilon$ vs. time t and strain rate $\dot{\varepsilon}$ vs. time t curves obtained during the isothermal creep tests are presented in the Appendix. In the appendix the nomenclature for each isothermal tensile creep test conducted at each tensile load, the minimum creep rate and the total exposure time at each tensile load can be found.

Figure 4.52 a) presents typical creep curves of WB 2124/SiC/25p<20µm, WB 2124/SiC/25p<5µm, unreinforced 2124 and BM 2124/SiC/25p<20µm at a load of 40MPa. The curves exhibit the typical three stage creep behaviour which consist of an instantaneous elongation followed by decelerating primary creep, a linear portion designated as secondary creep stage and finally accelerated (tertiary stage) creep followed by fracture [42]. The derivation of these curves gives the corresponding creep rates as shown in Figure 4.52 b).

In cases with expanded secondary creep stage the load was increased as it can be seen in Figure 4.52 for the BM 2124/SiC/25p<20µm which reached the resolution limit of the strain rate of 10-10/s with 40MPa load, when the other samples were already broken.

Figure 4.53 shows $\dot{\varepsilon}_{stat}$ vs. $\varepsilon$ of a) the unreinforced 2124 matrix without BM, b) the BM 2124/SiC/25p/<5µm, c) BM 2124/SiC/25p/<20µm and d) WB 2124/SiC/25p/<5µm to make sure that the stationary creep rate used for further analyses is actually stationary with respect to time and strain.
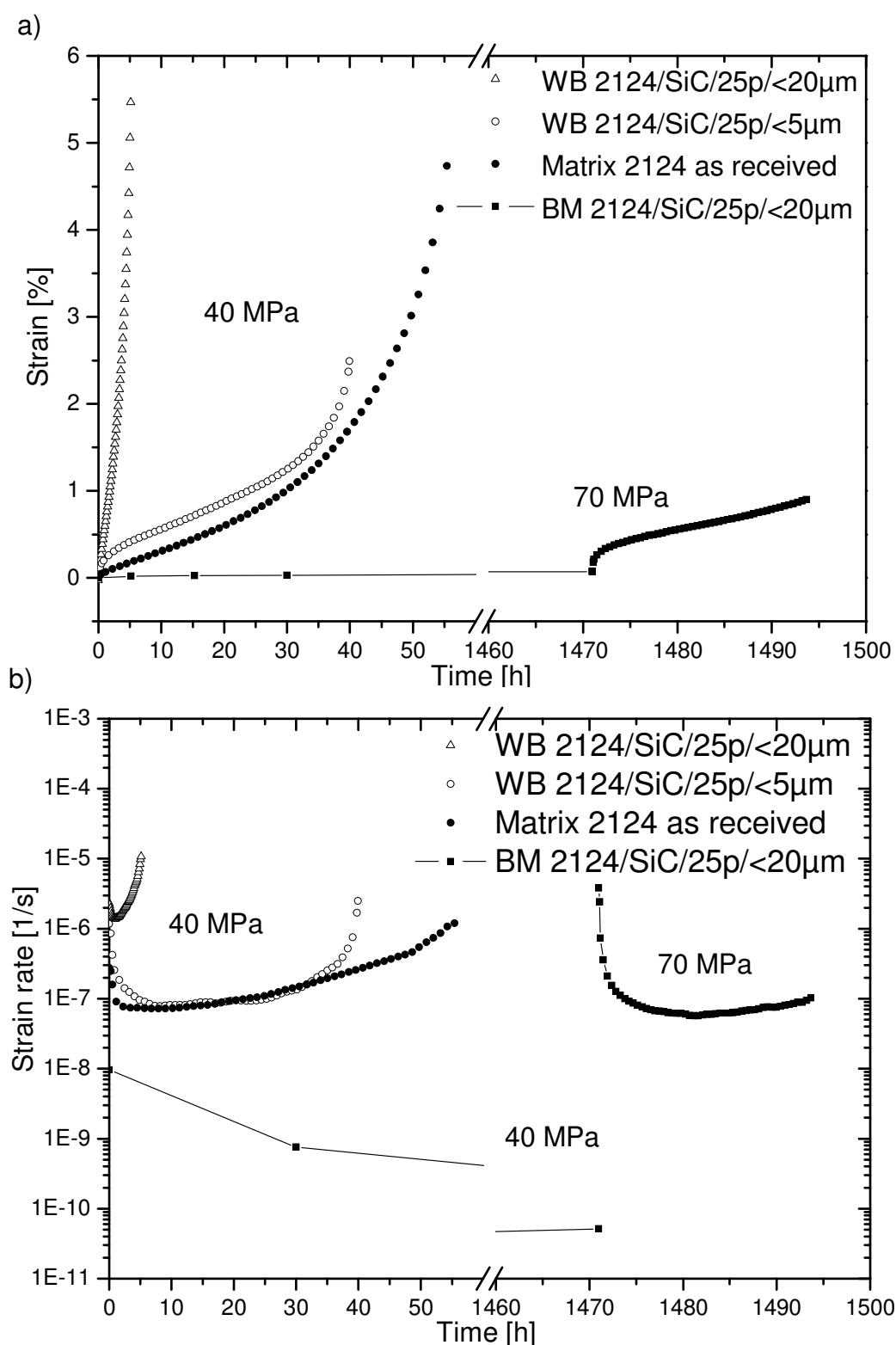
**Figure 4.52** a) Examples of creep curves ε vs. t and b) the corresponding creep rates $\dot{\varepsilon}$ vs. t – the load was changed from 40MPa to 70MPa for BM 2124/SiC/25p<20μm after 1471h
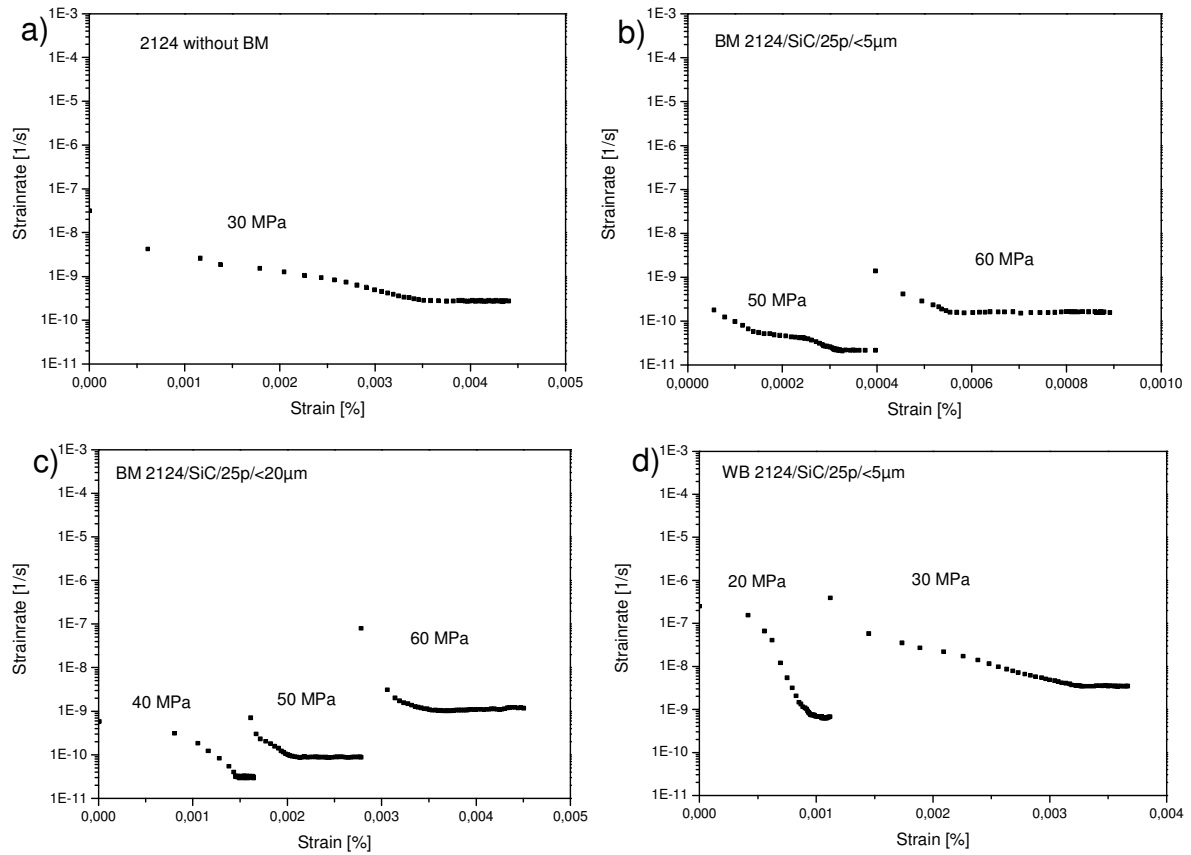
**Figure 4.53** $\dot{\varepsilon}_{stat}$ vs. $\varepsilon$ of a) the unreinforced 2124 matrix without BM, b) the BM 2124/SiC/25p/<5µm, c) BM 2124/SiC/25p/<20µm and d) WB 2124/SiC/25p/<5µm

The stationary creep rates of all the investigated materials are collected as a function of the applied stress $\sigma_A$ for the unreinforced matrices and the WB PRMs in Figure 4.54 and for the unreinforced 2124 matrices and the BM PRMs in Figure 4.55.

According to Figure 4.54 the <5µm SiC particles show no reinforcing effect for both the 2124 as well as the 6061 matrix for the WB PRMs. The minimum creep rate of WB 2124/SiC/25p<5µm and of WB 6061/SiC/25p<5µm is in the range of the corresponding unreinforced matrices. The n values represent dislocation creep only at $\sigma_A \leq$ 30MPa. There is a detrimental effect of the <20µm SiC particles for the WB PRMs yielding high creep exponents in the whole stress range. This shows that the creep resistance decreases with particle size for the WB PRMs.

As shown in Figure 4.55 the 2124 alloy subjected to 4 hours BM results in a better creep resistance (half the stationary creep rate) than the same alloy without BM. This

effect is increased for the PRMs prepared by BM. Here it can be seen that the BM PRMs reveal a decrease of the stationary creep rate of about 1-2 orders of magnitude for loads between 30 to 35MPa and of about 3-4 orders of magnitude for loads ≥ 35MPa. No significant differences in the creep resistance were found regarding the initial particle sizes for these materials.

Table 4.6 shows the summary of all the resulting values for the creep exponent n for all the studied materials. The creep exponent for the unreinforced 2124 matrix with and without BM is about 2 for applied tensile loads ranging from 15 to 30MPa and increases sharply up to about 16 for higher applied tensile loads. Very similar values of the creep exponent n were obtained for the BM PRMs. Here it was found that the values for n results in about 2 for tensile loads ranging from 30 to 50MPa and about 15 for tensile loads from 50 to 70MPa. As the corresponding unreinforced matrices give similar values for the creep exponent n it can be concluded that the same mechanism is responsible for creep of these materials.
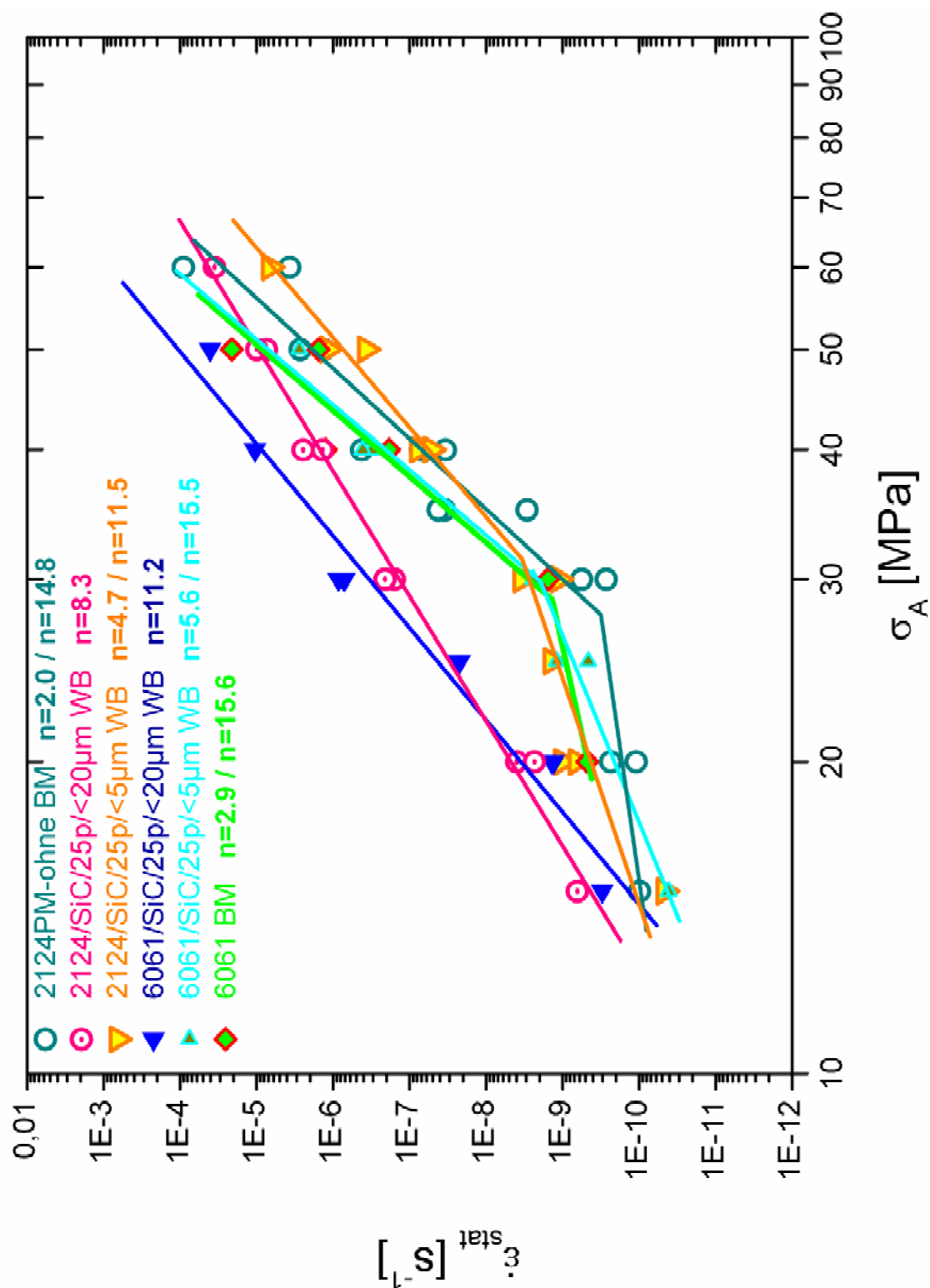
**Figure 4.54** Summary of all the minimum creep rates of the unreinforced matrices and the WB PRMs
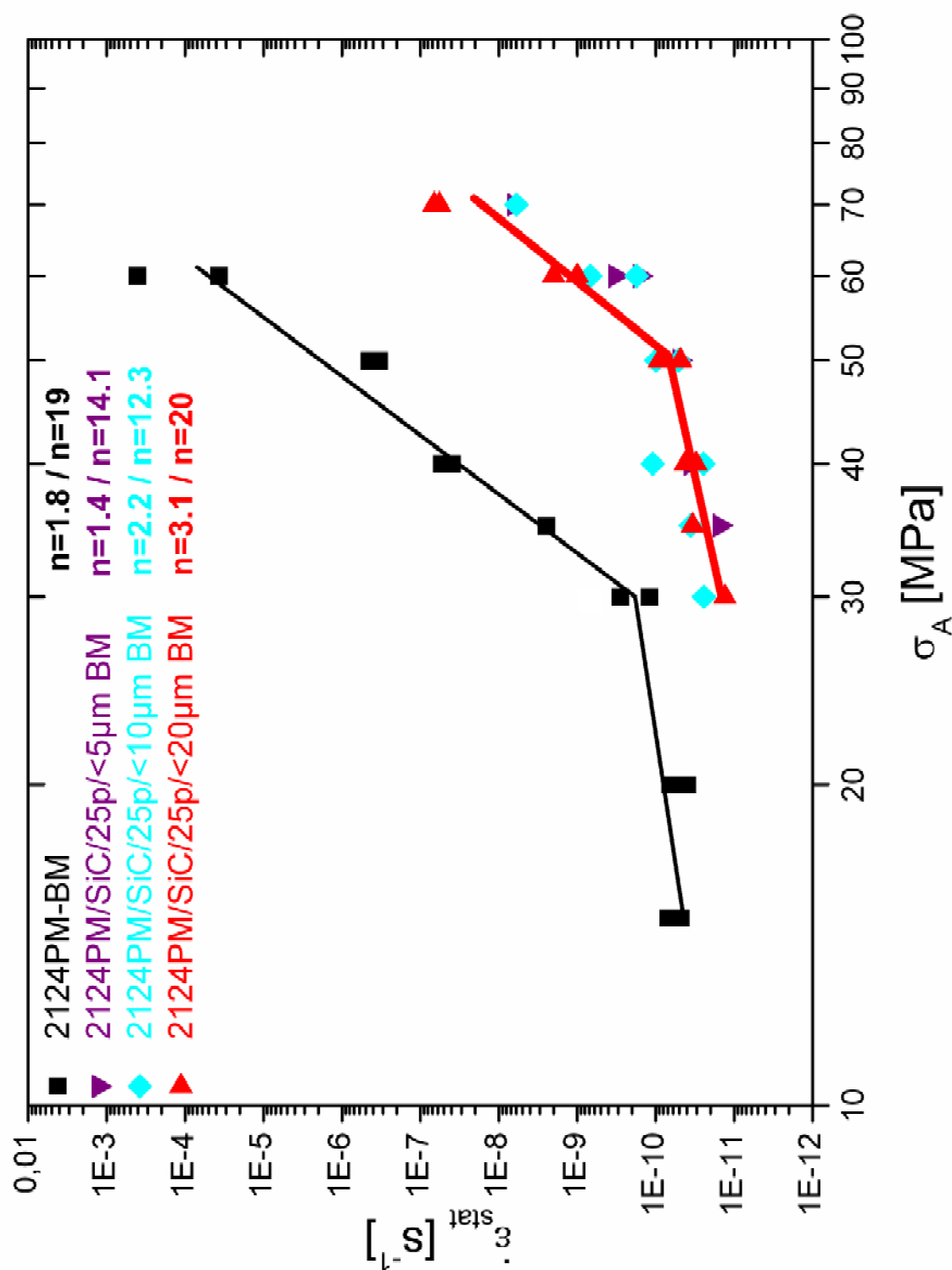
**Figure 4.55** Summary of all the minimum creep rates of the unreinforced matrix and the BM PRMs

| Material | Creep exponent n +/- 0.5 | | | | |
| | Range of load [MPa] | | | | |
| | 15-30 | 30-60 | 15-60 | 30-50 | 50-70 |
|---|---|---|---|---|---|
| Matrix 2124 BM | 1.8 | 15.6 | | | |
| Matrix 2124 without BM | 2.0 | 14.8 | | | |
| 2124/SiC/25p/<5µm BM | | | | 2.0 | 15.0 |
| 2124/SiC/25p/<10µm BM | | | | 2.0 | 15.0 |
| 2124/SiC/25p/<20µm BM | | | | 2.0 | 15.0 |
| Matrix 6061 BM | 2.9 | 15.6 | | | |
| 2124/SiC/25p/<5µm WB | 4.7 | 11.5 | | | |
| 2124/SiC/25p/<20µm WB | | | 8.3 | | |
| 6061/SiC/25p/<5µm WB | 5.6 | 15.5 | | | |
| 6061/SiC/25p/<20µm WB | | | 11.2 | | |

**Table 4.6** Summary of the values of the creep exponent n for all the investigated materials and all applied tensile loads

### 4.5.1 Fractography

The fractographic analysis in this section was carried out for fractured samples from the HT tensile tests and for fractured tensile creep samples with the loading history shown in Table 4.7:

| Sample | History of tensile load [MPa] | Total creep exposure time [h] | $A_u$ [%] |
|---|---|---|---|
| a) WB 2124/SiC/25p<5µm | 20 => 30 => 60 | 318 | 0.35 |
| b) WB 2124/SiC/25p<20µm | 20 => 30 | 205 | 0.75 |
| c) BM 2124/SiC/25p<5µm | 50 => 60 | 4901 | 0.25 |
| d) BM 2124/SiC/25p<20µm | 40 => 50 => 60 => 70 | 7480 | 0.75 |
| e) WB 6061/SiC/25p<5µm | 25 => 40 | 228 | 3.2 |
| f) WB 6061/SiC/25p<20µm | 15 => 30 | 267 | 5.6 |
| g) Unreinforced matrix 2124 with 4 hours BM | 50 | 0.5 | 6 |
| h) Unreinforced matrix 6061 with 4 hours BM | 20 => 40 | 4169 | 7 |

**Table 4.7** History of loads of the creep samples used for fractographic analysis

Images of the fractured creep samples, listed in Table 4.7, are shown in Figure 4.56. It is seen that there is a considerable necking in the unreinforced alloys 2124 as well as 6061 what results in a large elongation to fracture. However, both the WB as well as the BM PRMs do not show necking and therefore the elongation at fracture is remarkable smaller.

Figure 4.57 shows the fracture areas of the creep samples of a) WB 2124/SiC/25p<20µm, c) BM 2124/SiC/25p<20µm and e) unreinforced matrix with 4 hours BM investigated by means of SEM. As it can be seen in Figure 4.57 a) for the WB PRMs decohesion at the particle-matrix interface takes place at interfaces perpendicular to external stress. The same effect is seen in the Figure 4.57 b) BM PRMs. The fracture surface of the WB samples passes more through the matrix than that of the BM samples, where many particles create the surface. The unreinforced matrix (Figure 4.57 c)) shows also considerable creep pores.

The fracture surfaces of HT tensile test samples of a) WB 2124/SiC/25p<5µm, b) WB 2124/SiC/25p<20µm, c) BM 2124/SiC/25p<5µm, d) BM 2124/SiC/25p<20µm, e) WB 6061/SiC/25p<5µm, f) WB 6061/SiC/25p<20µm, g) unreinforced matrix 2124 with 4 hours BM and h) unreinforced matrix 6061 with 4 hours BM are shown in Figure 4.58. The fracture surfaces corresponding to the images in Figure 4.56 of broken creep samples of a) WB 2124/SiC/25p<5µm, b) WB 2124/SiC/25p<20µm, c) BM 2124/SiC/25p<5µm, d) BM 2124/SiC/25p<20µm , e) WB 6061/SiC/25p<5µm, f) WB 6061/SiC/25p<20µm, g) unreinforced matrix 2124 with 4 hours BM and h) unreinforced matrix 6061 with 4 hours BM are shown in Figure 4.59.

The macroscopic observation of the broken samples reveals a considerable necking before fracture in case of the unreinforced alloys 2124 as well as 6061 for both the samples from HT tensile test and fractured creep samples. The PRMs do not show necking neither after tensile fracture nor after creep fracture. This is a result of the loss of ductility due to the introduction of the reinforcing ceramic phase.

For all the fracture surfaces shown in Figure 4.58 and Figure 4.59 for the unreinforced matrices as well as for the PRMs the images show the occurrence of dimples in the Al-matrix but with considerable differences. The dimples in the fractured creep samples (Figure 4.59) somehow seem to be more regular, but with bimodal size distribution, compared to the broken samples from the hot tensile tests (Figure 4.58). The PRMs reinforced with the smaller particles (Figure 4.58 a) and c) and Figure 4.59 a) and c)) reveal much smaller dimples due to the smaller SiC particle size. In both cases, tensile (Figure 4.58) and creep (Figure 4.59) fracture the unreinforced matrix show much deeper dimples than the PRMs. No broken particles could be observed in crept PRM samples.
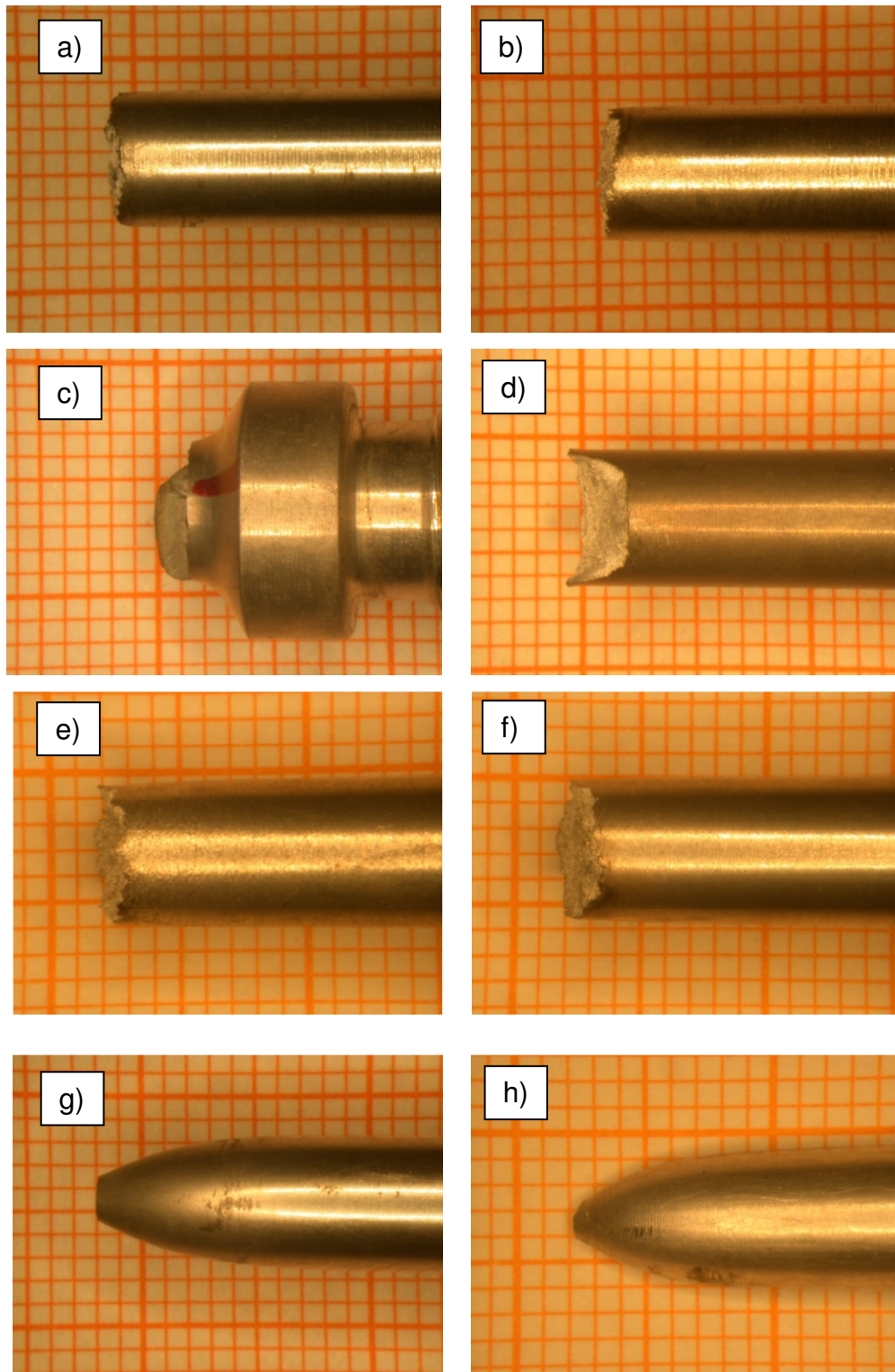
**Figure 4.56** Images of the fractured creep samples of a) WB 2124/SiC/25p<5µm, b) WB 2124/SiC/ 25p/ <20µm, c) BM 2124/SiC/25p<5µm, d) BM 2124/SiC/25p<20µm, e) WB 6061/SiC/25p<5µm, f) WB 6061/SiC/25p<20µm, g) unreinforced matrix 2124 with 4 hours BM and h) unreinforced matrix 6061 with 4 hours BM
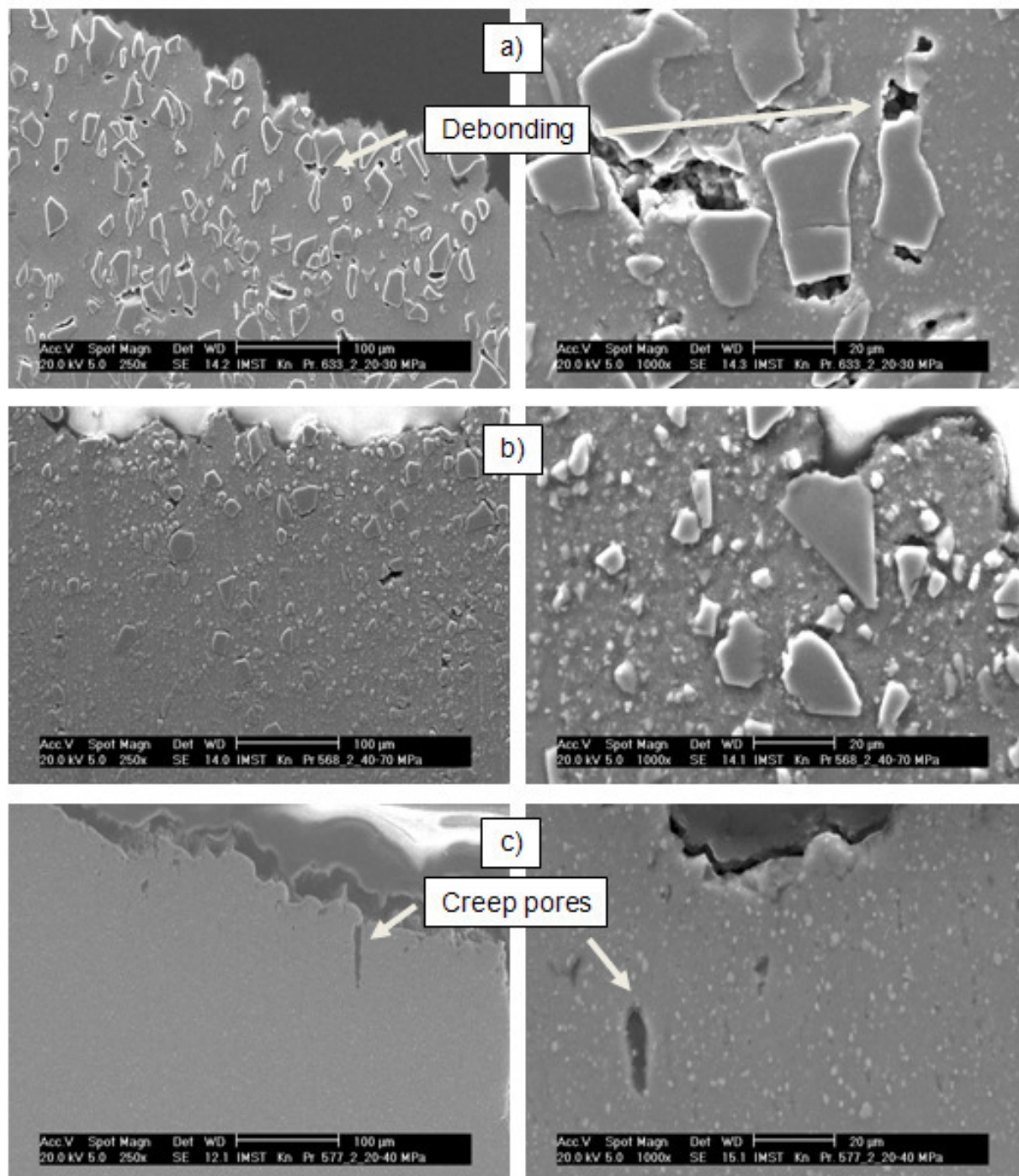
**Figure 4.57** Images of the longitudinal section of fracture areas of fractured creep samples of a) WB 2124/SiC/25p<20µm (**Figure 4.56** b)), b) BM 2124/SiC/25p<20µm (**Figure 4.56** d)) and c) unreinforced matrix with 4 hours BM (**Figure 4.56** e))
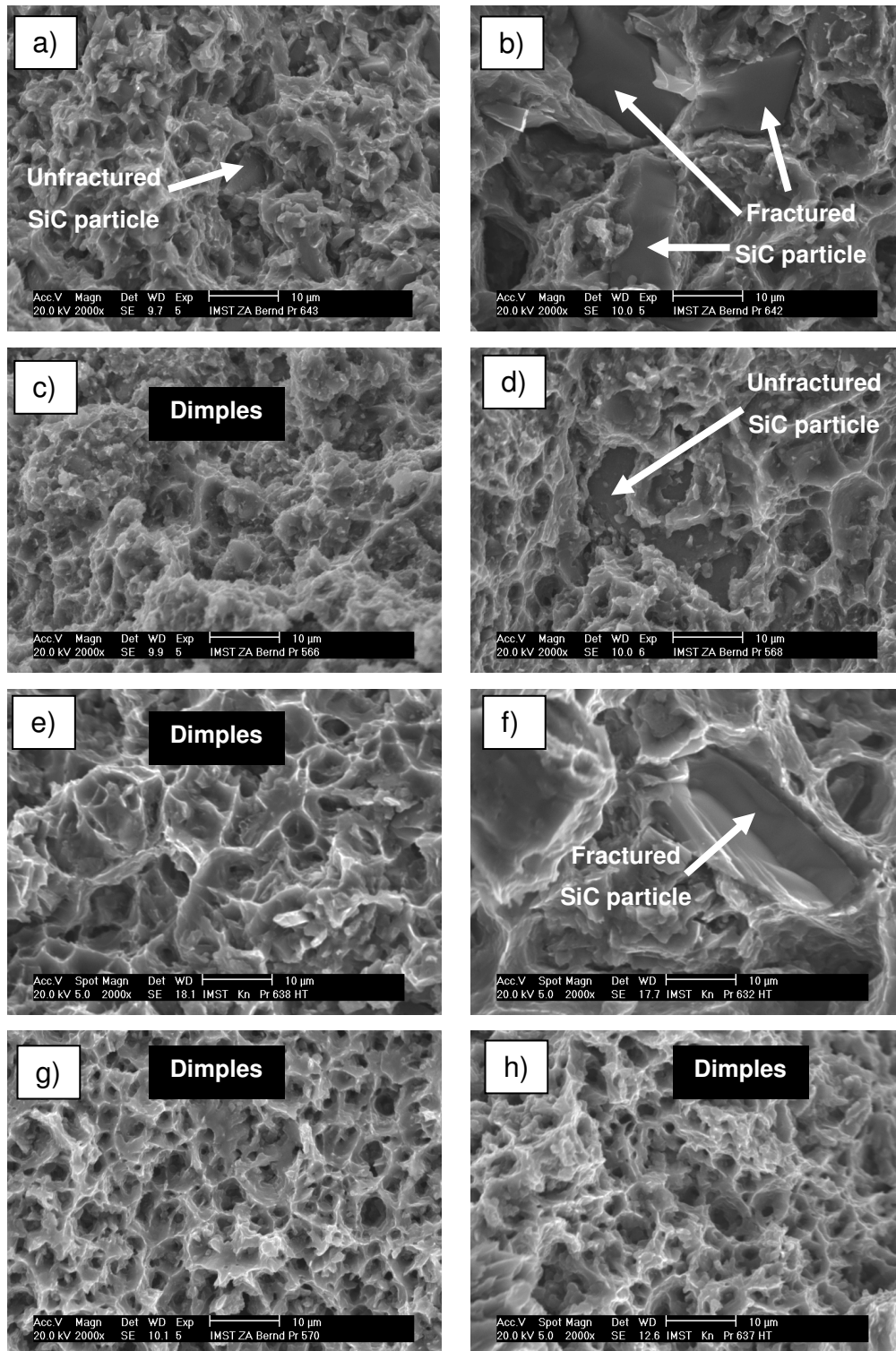
**Figure 4.58** Images of the fracture surfaces of HT tensile test samples of a) WB 2124/SiC/25p<5μm, b) WB 2124/SiC/25p<20μm, c) BM 2124/SiC/25p<5μm, d) BM 2124/SiC/25p<20μm, e) WB 6061/SiC/25p<5μm, f) WB 6061/SiC/25p<20μm, g) unreinforced matrix 2124 with 4 hours BM and h) unreinforced matrix 6061 with 4 hours BM
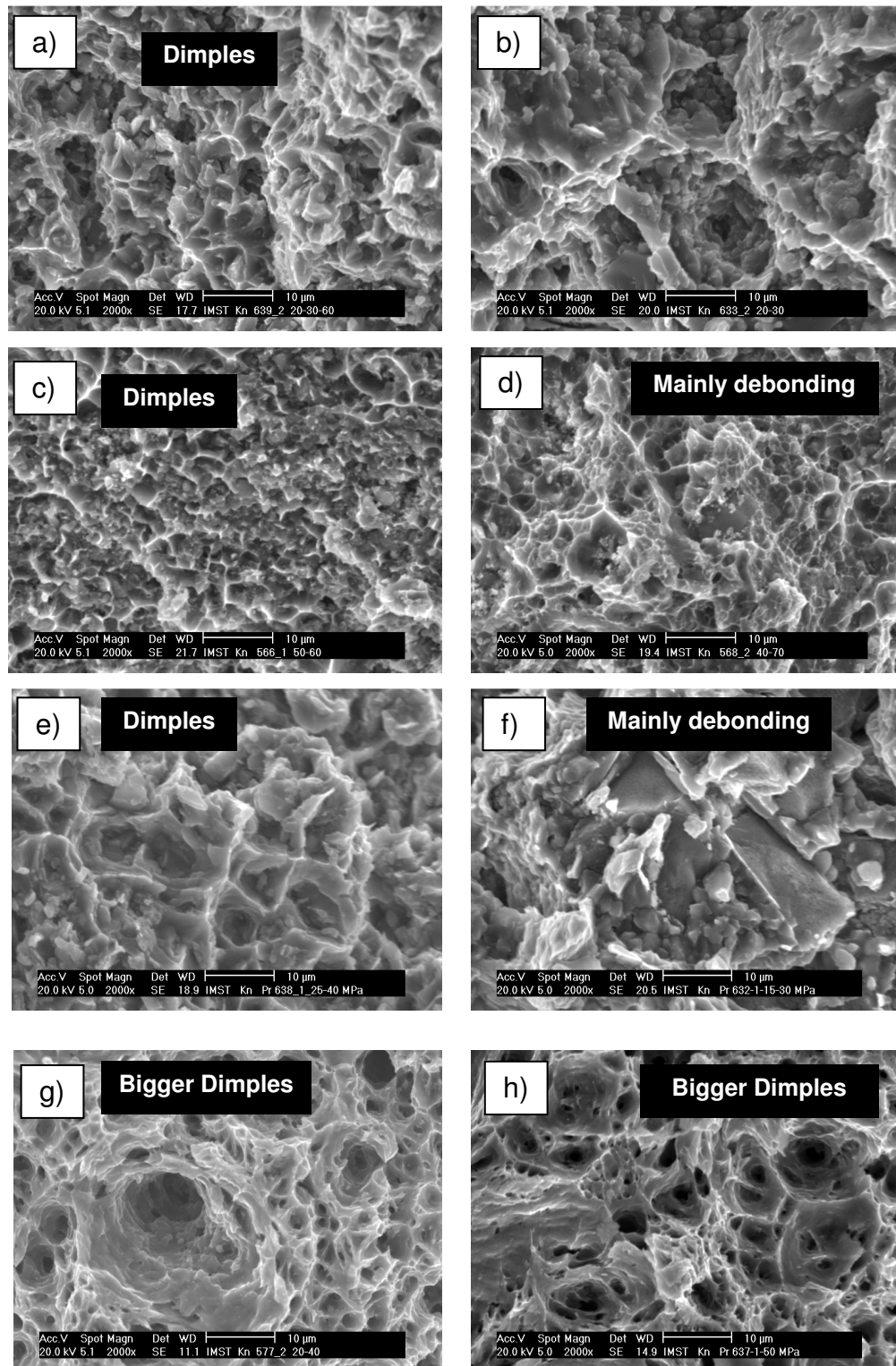
**Figure 4.59** Images of the fracture surfaces of fractured creep samples of a) WB 2124/SiC/25p<5µm, b) WB 2124/SiC/25p/ <20µm, c) BM 2124/SiC/25p<5µm, d) BM 2124/SiC/25p<20µm, e) WB 6061/SiC/25p<5µm, f) WB 6061/SiC/25p<20µm, g) unreinforced matrix 2124 with 4 hours BM and h) unreinforced matrix 6061 with 4 hours BM

# 5 Interpretation and Discussion

## 5.1 Microstructures

The mixing methods in the present study lead to the result that in case of WB PRMs the particles are not broken, but remain with their initial size and elongated shape having more pointed corners than the particles which were subjected to BM. The process of BM breaks the SiC particles according to chapter "state of the art" obtaining smaller and more equi-axed shapes as it can be seen in the appendix of chapter "results".

Liu et al compared PRMs processed by means of mechanical alloying on the one hand and by means of mechanical mixing on the other hand [92, 99]. According to the above mentioned results they found that particles with sharper edges could be seen clearly in those powders that were mechanically mixed. However, with mechanically alloying, the powders, especially the SiC particles, appear to be more rounded, and it is more difficult to find particles that have sharp edges. During mechanical alloying the number of large-size SiC particles was found to decrease giving rise to a composite with finer particles than that in the as-mixed condition.

### 5.1.1 The unreinforced matrix

In order to study the effect of the BM, the unreinforced matrix was extruded with and without BM. The unreinforced matrix which was extruded without prior subjection to BM shows a considerable cleaner mircostructure than the unreinforced matrix which was subjected to BM. In the BM matrix network-like oxide structures as well as various kinds of intermetallic phases were identified.

The 2124 alloy system has a multiphase structure consisting of $(Mn,Fe)_3SiAl_{12}$, $Mg_2Si$, $CuAl_2$, $Al_2CuMg$ and occasionally $(Fe,Mn)Al_3$ or $(Mn,Fe)Al_6$. Heating to 300 °C dissolves much of the copper and magnesium leaving only some bigger $Al_2CuMg$ and perhaps $CuAl_2$ precipitates. Most of the iron containing phase undergo

transformation to $Al_7Cu_2Fe$. Simultaneously, manganese is precipitated from solid solution as $Cu_2Mn_3Al_{20}$ dispersoid [79].

The 6061 alloy system is formulated to make use of the solubility of $Mg_2Si$ and thereby utilize precipitation hardening. If slowly cooled, precipitating occurs [79]. If there is no manganese or chromium present, the iron-rich phases are $Fe_3SiAl_{12}$, $Fe_2Si_2Al_9$, or a mixture of the two, depending on the proportions of silicon and iron. Manganese and chromium stabilize $(Fe,Mn,Cr)_3SiAl_{12}$.

### 5.1.2 The ball milled (BM) PRMs

In the BM PRMs, it was found that the SiC particles are fractured, resulting in more rounded particles and interparticle spaces filled with sub-µm particles. This gives a multimodal particle size distribution. The mean SiC particle area and the percentiles do not differ considerably for the different particle sizes, but are significantly smaller than for all WB PRMs. The SiC median of the particle size is markedly reduced for the case of the BM composites. BM results in a reduction of about 50% and of about 70% of the particle mean size for the <5µm and <20µm PRMs, respectively. The volume fraction of SiC particles larger than 5µm remains below 2vol% for all BM composites. There is hardly any difference in the particle distribution with respect to the extrusion direction.

The distribution of SiC particles <1µm of both BM 2124/SiC/25p<5µm as well as for BM 2124/SiC/25p<20µm was found to be very close to each other. The broken SiC appears in the size class of 0.1µm and are somewhat clustered with interparticle distances of the same range.

The presence of different kinds of sub-µm particles in the size range of 0.05µm-0.3µm is evident. Mg-rich oxides appear at the SiC-particle-matrix interface. Oxide structures located at the SiC particle interfaces were found connecting SiC particles. Additional CuMn-rich as well as Cu-rich particles were found in the microstructure of the BM PRMs. The dispersoids with heavy elements appear evenly distributed in BSE images. They are in between the SiC particles in the size class of 0.1µm but less frequent with an interparticle distance in the range of 0.5µm. These kind of

multiphase structures with oxides are a distinctive characteristic of the studied BM PRMs. Altogether the number density of dispersoids is by 1-2 magnitudes higher than in WB PRMs.

### 5.1.3  The wet blended (WB) PRMs

Fracture of particles is avoided during wet blending resulting in a monomodal particle size distribution with a few 1µm size SiC particles. Most of the SiC particles remain with their initial size, are more angular than in the BM case and have sharp edges. All PRMs exhibit some elongated particle-free zones which are generated during the hot extrusion process. An alignment of the SiC particles in the direction of extrusion is evident in the WB-PRMs. This alignment is not observed in the materials prepared by BM due to the more spherical shape of the fractured particles.

These results reveal considerable differences between the WB PRMs with particles <5µm and the WB PRMs with particles <20µm. The mean particle area is about 10µm² in case of the particles <5µm and 2 to 3 times bigger in case of the particles <20µm. The WB PRMs <5µm contain about 4vol% of particles bigger than 19.6µm² while in the WB PRMs <20µm remain about 9.5vol% of SiC particles >19.6µm².

No sub-µm SiC particles were observed in the WB materials. Various sub-µm particles are evident between the SiC particles.

It was found that a smaller amount of sub-µm particles is present in the WB material resulting in a "cleaner" microstructure than for the BM material. Mainly Fe, Mn, Cu-aluminides of 0.1-0.3µm diameter were identified with interparticle spaces of about 1µm. $Al_2Cu$ platelets (<0.5µm) can be observed as well in BSE images and are confirmed by TEM, which are difficult to distinguish in BM PRM from other dispersoids.

Chapter: Interpretation and Discussion

## 5.2  Isothermal Tensile Creep

The BM PRMs show the highest creep resistance among all introduced and hereby studied materials. The stationary creep rate of the BM PRMs is about one order of magnitude lower than that of the BM 2124 unreinforced matrix in the lower applied stress region. This difference increases up to 4 orders of magnitude for the higher applied stresses region. The stationary creep rate of the WB PRMs prepared with <5µm SiC particles is more or less the same as for the corresponding unreinforced alloys. The creep resistance of the <20µm SiC WB PRMs is considerably smaller than that of the unreinforced matrices. The larger particle size resulting from WB is responsible for this behaviour [9, 100, 101]. Sharp edges are eliminated during high-energy mixing producing more spherical reinforcement morphology. The BM process reduces the reinforcement size resulting in sub-µm particles, as it can be seen in the images shown in the appendix. The sub-µm particles act as dispersoids which reduce the creep rate by pinning dislocations even at thermally activated motion [73].

### 5.2.1  Creep of the unreinforced 2124 and 6061 alloys

The results of all the unreinforced 2124 matrices are compared in Figure 5.1 as stationary creep rate, $\dot{\varepsilon}_{stat}$, vs. the applied stress, $\sigma_A$. The deducted n values are distinguished for the low and the high stress region. The results obtained in the present investigations are compared with previous results obtained for the same unreinforced alloys produced by different routes: conventional rolled 2024 and powder forged AMC 2124 [102].

Figure 5.2 presents the results of the isothermal tensile creep tests of the unreinforced 6061 alloy produced by PM and compared with a result of earlier studies of material produced by ingot metallurgy (IM) [87]. Again the PM produced alloy show in the low stress region a little higher creep resistance than the IM produced alloy, for which the stress exponent increases significantly at stresses ≥ 40MPa.

For both the BM 2124 and BM 6061 the dependence of the stationary creep rates with the applied tensile loads show two regions: the low stress region ranging up to 30MPa and the high stress region ranging from 30MPa up to 60MPa. The creep exponent obtained in the low stress region is about 2 for the 2124 matrices what indicates grain boundary sliding as the dominating creep mechanism as it was reported by Lüthy et al [47] and for the 6061 alloy it is about 3 what means that viscous drag is the dominating creep mechanism. The creep behaviour of the IM 6061 alloy show also n=2.2 for lower stresses what also corresponds to grain boundary sliding, as it was described elsewhere [22, 87].

The PM BM 2124 alloy compared with the same alloy produced without BM leads to a slightly higher creep resistance. This behaviour can be attributed to the higher oxygen fraction and the higher amount of intermetallic phases what rises from BM. The PM BM 2124 alloy shows a higher creep resistance in the lower stress region than the conventionally produced IM alloys and the AMC material. This behaviour is reversed in the high stress region where the PM BM alloys result in a higher stationary creep rate than the others.

The unreinforced PM 2124 with and without BM alloy shows higher creep resistance than the unreinforced BM 6061 for all the tested loads. The oxygen fraction for the 2124 BM material is about 3-4 times higher than for the alloy without BM (see Table 3.5). This indicates the presence of more oxides acting as dispersoids in the BM matrix than for the 2124 matrix without BM. This difference does not influence the creep resistance essentially. But there is a significant difference between the AMC and the here described PM 2124 matrix alloy. The powder size class and the mixing of AMC material are not known.

In both PM alloys the creep exponent increases sharply in the higher stress region above 30MPa reaching values about 15 to 19.

This behaviour may indicate the presence of a threshold stress, $\sigma_{th}$, for creep, which can be calculated in Figure 5.3. The calculation of the threshold stress, $\sigma_{th}$, for a certain load range always needs an assumption of the dominating creep mechanism in this region either it is diffusion creep (n=1), viscous drag (n=3) or dislocation climbing (n=5). Scaling by $\dot{\varepsilon}^{\frac{1}{n}}_{stat}$ vs. the applied stress, $\sigma_A$, and calculating the

correlation coefficient leads to the result of the actually predominating creep mechanism.

The data of the high stress region were calculated by assuming n=1, n=3 and n=5 by a scale $\dot{\varepsilon}^{\frac{1}{n}}_{stat}$, vs. the applied stress, $\sigma_A$. It was found that the value for the correlation coefficient gives the best fitting by assuming the dominating creep mechanism for this region is dislocation climb with a corresponding n=5 [22]. The resulting threshold stress for the introduced unreinforced PM materials is $\sigma_{th}$= 27±2MPa except the 6061 IM which has a significantly reduced $\sigma_{th}$= 15MPa. The obtained results of the threshold stresses of all the unreinforced matrices are compared in Table 5.1.
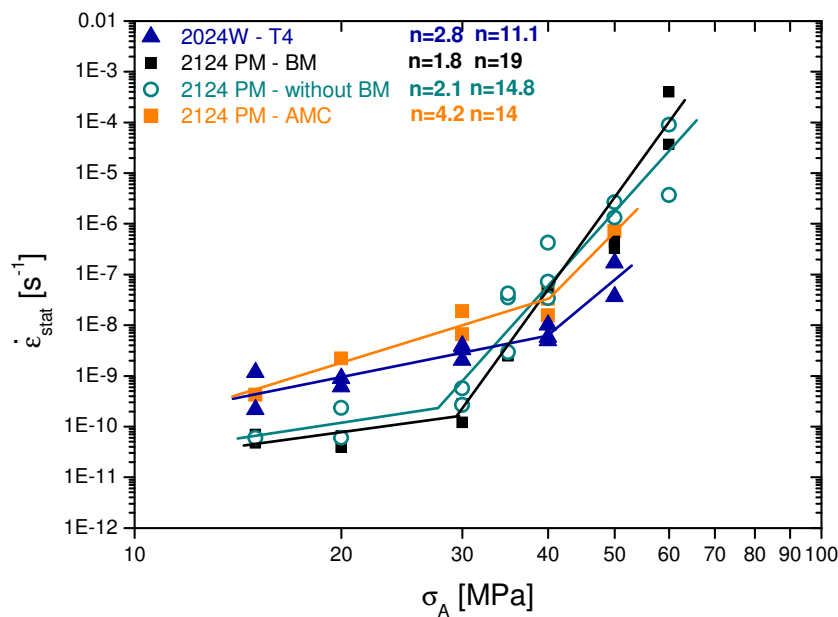


**Figure 5.1** Results of the isothermal tensile creep tests of the unreinforced 2124 alloys produced by PM and IM indicating the deducted n exponents for the low and high stress range.
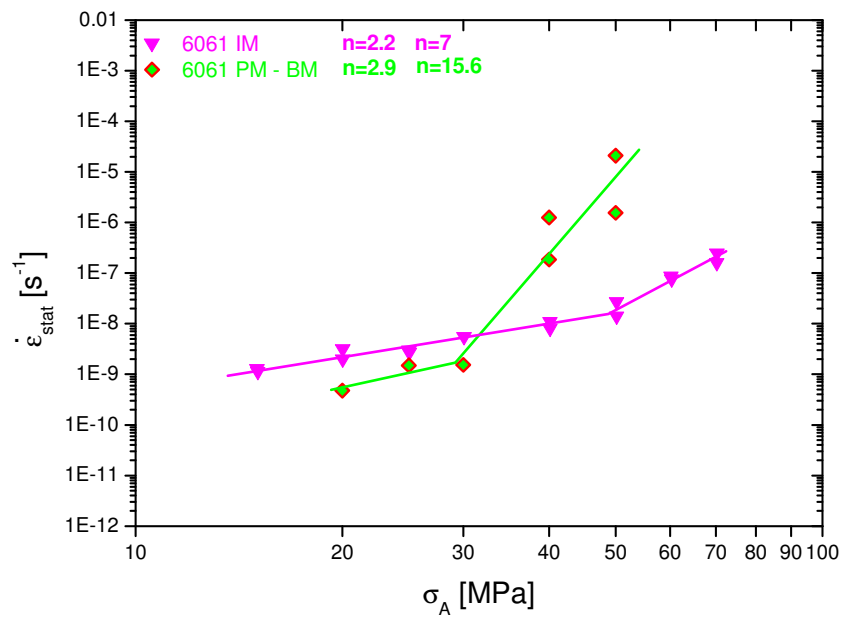
**Figure 5.2** Results of the isothermal tensile creep tests of the unreinforced 6061 alloy produced by PM and IM indicating the deducted n exponents for the low and high stress range.
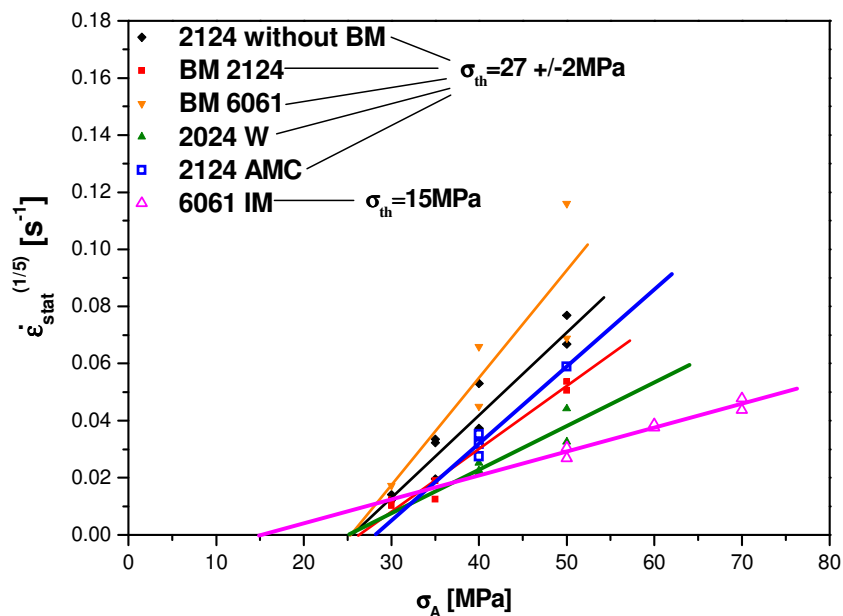


**Figure 5.3** Calculated threshold stress of the unreinforced PM 2124 and 6061 for n=5

| | $n_1$ | $\sigma_A \leq$ [MPa] | $n_2$ | $\sigma_{th}$ [MPa] |
|---|---|---|---|---|
| 2024 W | 3 | 40 | 11 | 25 |
| 2124 AMC | 4 | 40 | 14 | 28 |
| 2124 PM without BM | 2 | 30 | 15 | 25 |
| 2124 PM BM | 2 | 30 | 19 | 26 |
| 6061 IM | 2 | 50 | 7 | 15 |
| 6061 PM BM | 3 | 30 | 16 | 25 |

**Table 5.1** Calculated threshold stresses for the unreinforced matrices (n=5)

### 5.2.2 Creep of the WB particle reinforced 2124 and 6061 alloys

The results of the isothermal tensile creep tests of the WB 2124/SiC/25p<5µm and <20µm are presented in Figure 5.4 as the stationary creep rate, $\dot{\varepsilon}_{stat}$, vs. the applied stress, $\sigma_A$. Similarly to unreinforced 2124 alloy (without BM is taken as reference) the WB 2124/SiC/25p<5µm reveals two regions of creep behaviour. The low stress region ranges from 15 up to 30MPa, whereas the high stress region ranges from 30 up to 60MPa. The WB 2124/SiC/25p<20µm exhibit no change of the dominating creep mechanism over the entire load range at all.

The results of the isothermal tensile creep tests of the WB 6061/SiC/25p<5µm and <20µm are presented in Figure 5.5 as the stationary creep rate, $\dot{\varepsilon}_{stat}$, vs. the applied stress, $\sigma_A$. The WB 6061/SiC/25p<5µm also reveals two regions of creep behaviour. The low stress region ranges from 15 up to 30MPa, whereas the high stress region ranges from 30 up to 60MPa. This is very similar to the unreinforced BM matrices. Again the WB 6061/SiC/25p<20µm reveal the same dominating creep mechanism in the whole load range.

The results of all the WB PRMs and the corresponding unreinforced alloys are shown in Figure 5.6. For the WB 2124/SiC/25p<5µm and the WB 6061/SiC/25p<5µm the values of the creep exponent n is 4.7 and 5.6, respectively. These values of n refer to dislocation climbing as the dominating creep mechanism for $\sigma_A$=15-30MPa [68, 73].

Similarly to the unreinforced matrices, the WB PRMs <5µm show also a change of the creep exponent n at $\sigma_A$=30MPa. The creep exponent n in the high stress region reaches values of 11.5 and 15.5 for the WB reinforced 2124 and the reinforced as well as the unreinforced 6061 alloys, respectively.

For the WB PRMs <20µm there is no change in the creep exponent over the entire range of applied tensile loads. The WB PRMs <20µm show a weaker creep resistance for all the tested applied tensile loads with a creep exponent n of 8.3 and 11.2 between 15 and 60MPa.

The existence of a threshold stress, $\sigma_{th}$, for creep due to the increase of n in the high stress region for these materials is suggested and calculated in Figure 5.7. The data of the high stress region were calculated by assuming n=1, n=3 and n=5 by a scale $\dot{\varepsilon}^{\frac{1}{n}}_{stat}$, vs. the applied stress, $\sigma_A$. It was found that the value for the correlation coefficient gives the best fitting by assuming the dominating creep mechanism for this region is dislocation climb with a corresponding n=5. The WB 2124 and 6061 PRMs with the biggest particles obtain the lowest threshold stress ($\sigma_{th}$=14±1MPa). The WB 2124 and 6061 PRMs with the smaller SiC particles as well as the unreinforced PM alloys obtain a threshold stress of $\sigma_{th}$=25±1MPa. Table 5.2 lists all the results of calculated threshold stresses for the WB PRMs.
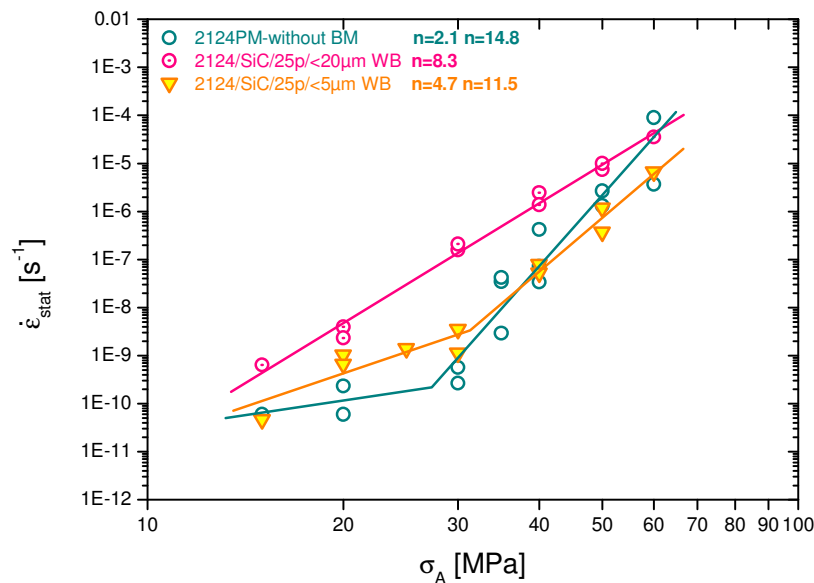


**Figure 5.4** Results of the isothermal tensile creep tests of the WB 2124/SiC/25p<5µm and <20µm
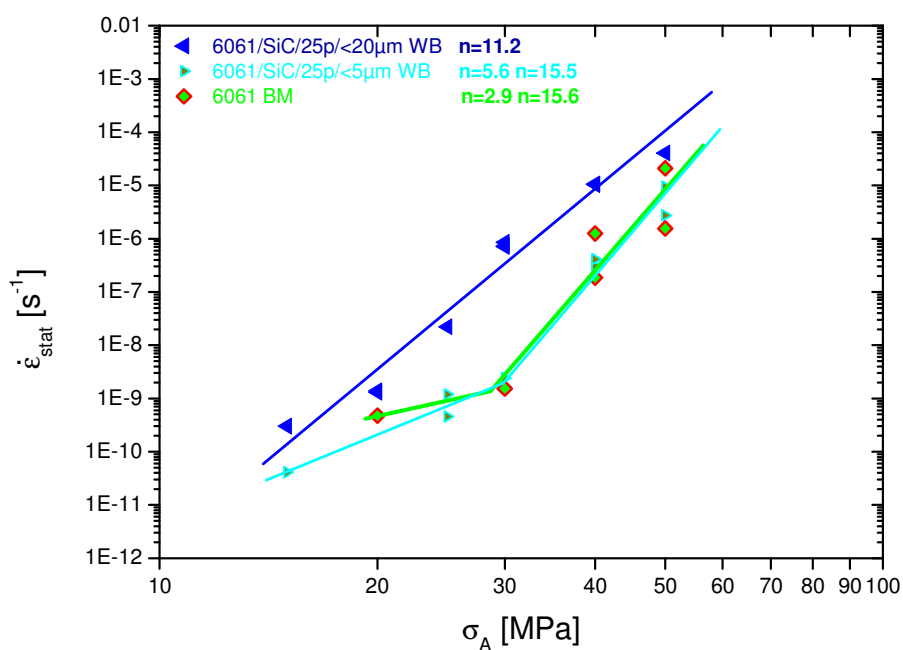
**Figure 5.5** Results of the isothermal tensile creep tests of the WB 6061/SiC/25p<5µm and <20µm
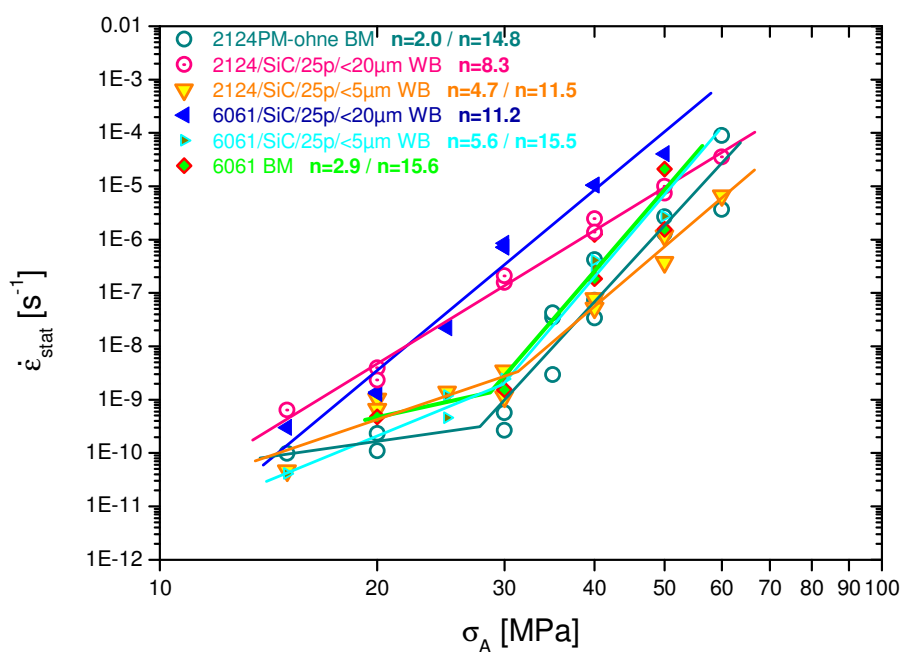


**Figure 5.6** Results of the isothermal tensile creep tests of the all the WB PRMs
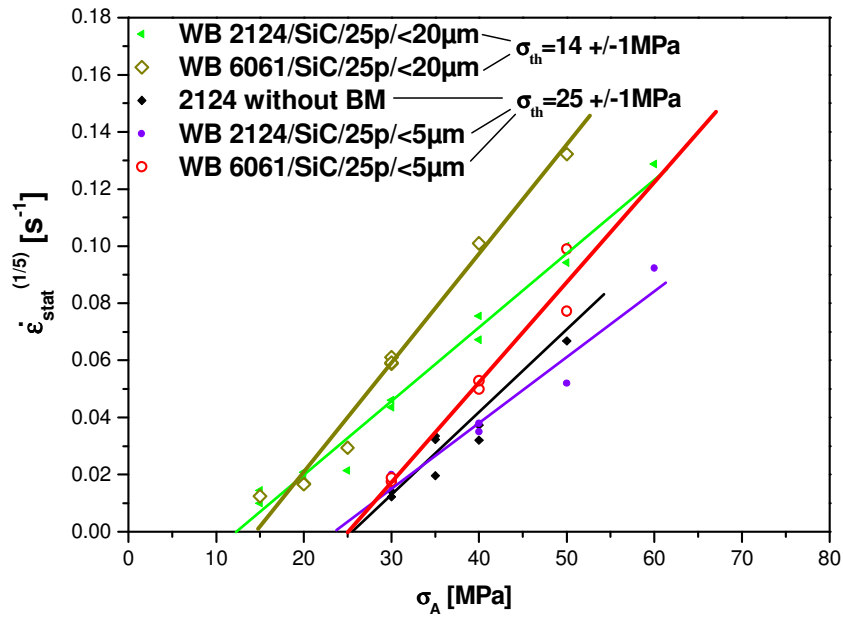
**Figure 5.7** Calculated threshold stress of WB PRMs

|  | $n_1$ | $\sigma_A \leq$ [MPa] | $n_2$ | $\sigma_{th}$ [MPa] |
|---|---|---|---|---|
| WB 2124/SiC/25p<5µm | 5 | 30 | 12 | 25 |
| WB 6061/SiC/25p<5µm | 5 | 30 | 16 | 25 |
| WB 2124/SiC/25p<20µm | 8 | - | - | 12 |
| WB 6061/SiC/25p<20µm | 11 | - | - | 15 |

**Table 5.2** Calculated threshold stresses for the WB PRMs (n=5)

## 5.2.3   Creep of the BM particle reinforced 2124 PRM

Figure 5.8 shows the results of the isothermal tensile creep experiments for the unreinforced 2124 alloy and the 2124 PRMs produced by BM with initial particle sizes of <5µm, <10µm and <20µm as well as the WB 2124 PRM <5µm. The BM PRMs

show up to 4 orders of magnitude lower stationary creep rate than the corresponding unreinforced matrix what appears independent of the initial particle sizes.

The creep of the BM PRMs shows again two regions of applied stresses with change of the resulting creep exponent: the low stress region from 30-50MPa and the high stress region from 50-70MPa. Since the results for the BM PRMs in the low stress region are similar for the different initial SiC sizes they can be combined and a mean stress exponent can be estimated. This gives n=2.2±0.7 what indicates grain boundary sliding as the dominating creep mechanism. Experimentally, the strain rate dropped to the limit of measurement accuracy, but was reproducibly observed for relatively long periods (1000-8000h) justifying a stationary creep condition. For applied loads above 50MPa the combined apparent creep exponent goes from 14 to 20. As the values of the creep exponent n for the unreinforced 2124 matrix for the low stress regime as well as for the high stress regime are very close to those for the BM PRMs, it can be assumed that the dominating creep mechanisms in the unreinforced alloy are the same as in the BM PRMs.

The 4 hours of BM fractures the SiC particles down to the sub µm-scale and produces a more refined microstructure as it can be seen by TEM investigations. The interparticle spacing is reduced resulting in more effective obstacles for the dislocation climb [103].

Figure 4.43 and Figure 4.44 show TEM images of BM 2124/SiC/25p<5µm a) in T4S condition with 1 hour overaging and b) after 8000 hours of creep exposure time as well as WB 2124/SiC/25p<5µm in T4S condition with 1 hour overaging and b) WB 2124/SiC/25p<20µm after 30 hours of creep exposure time, respectively. It can be seen that the $Al_2Cu$ precipitates change their shape during creep exposure what could be a possible explanation for the increase of the creep exponent n after certain duration. Nevertheless, in measuring the hardness after the same exposure times no effect was found what indicates no athermal weakening of the material after long time creep exposure.

The resulting threshold stresses for the BM PRMs together with those from the corresponding WB PRMs as well as the unreinforced matrices are given in Figure 5.9 and listed in Table 5.3. The threshold stress for the BM PRMs reaches up to about $\sigma_{th}$=40±5MPa. It can be analysed that with increasing the reinforcing particle size the

Chapter: Interpretation and Discussion

values for the threshold stress decrease. Going from the WB PRM <20µm with the lowest creep resistance and the biggest particles via the WB PRM <5µm and the unreinforced matrices to the BM PRMs with the highest creep resistance and the smallest particles, the resulting threshold stress for creep rises from 12MPa to 40MPa. The bigger the reinforcing particles in the WB PRMs the more they act as dislocation sources and additionally those materials do not contain as much precipitations and intermetallic phases acting as dispersoids, whereas the sub-µm particles present in the BM material act as dispersoids and additionally do not contain big SiC particles (>5µm).
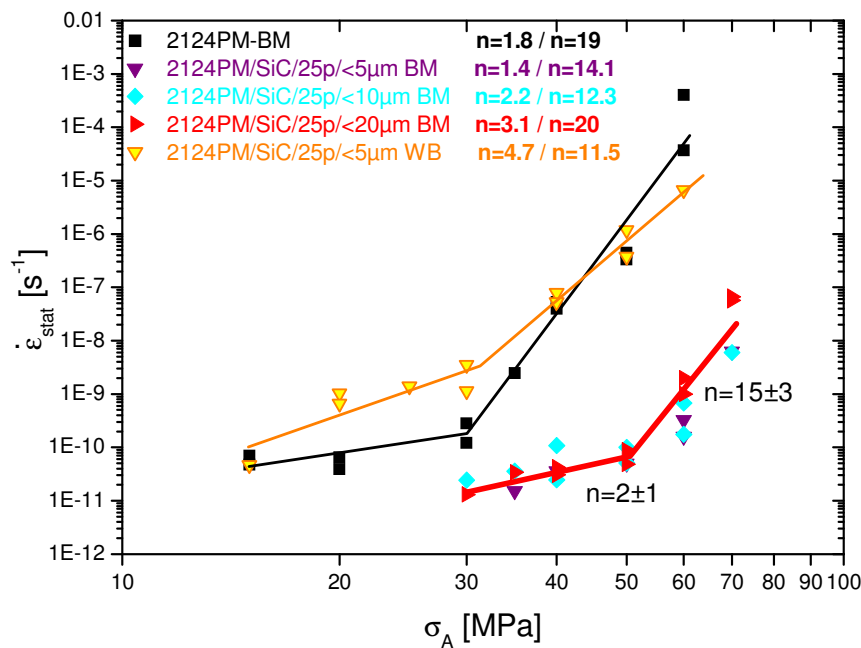


**Figure 5.8** Results of the isothermal tensile creep tests of the unreinforced 2124 alloy and particle reinforced produced by BM indicating the deducted n exponents for the low and high stress range.
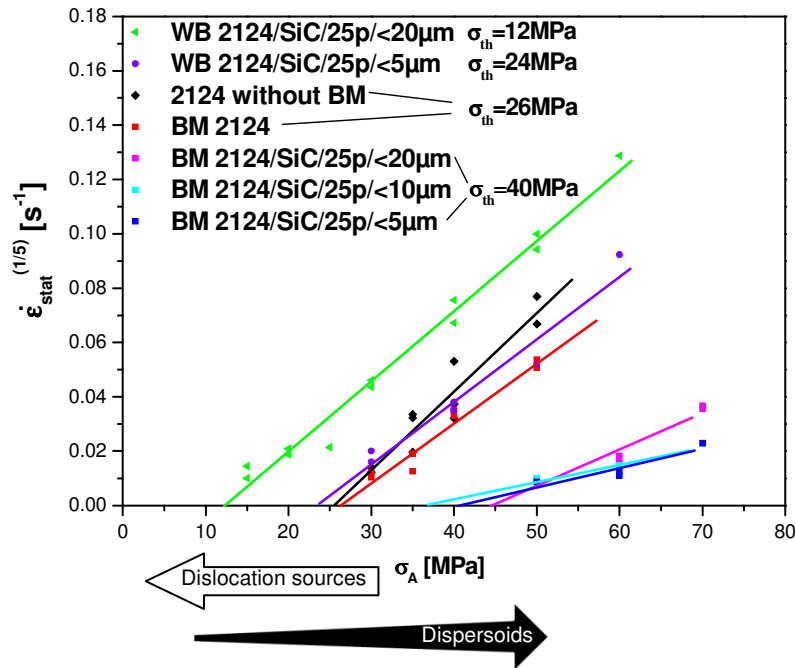
**Figure 5.9** Calculation of the values for threshold stress of the BM PRMs, the WB PRMs and the unreinforced matrices

| | $n_1$ | $\sigma_A \leq$ [MPa] | $n_2$ | $\sigma_{th}$ [MPa] |
|---|---|---|---|---|
| BM 2124/SiC/25p<5µm | 1.4 | 50 | 14 | 40 |
| BM 2124/SiC/25p<10µm | 2.2 | 50 | 12 | 35 |
| BM 2124/SiC/25p<20µm | 3.1 | 50 | 20 | 45 |

**Table 5.3** Calculated threshold stresses for the BM PRMs (n=5)

### 5.2.4 Comparison of the creep mechanisms

The results of the creep tests for the BM PRMs, the unreinforced matrices and the WB PRMs <5µm exhibit a significant increase of the slope of the $\dot{\varepsilon}_{stat}$ against $\sigma_A$ curves in the high stress region. This change in the slope takes place at 50MPa for the BM PRMs, whereas in the other materials mentioned above this change appears at 30MPa. Above this change the slope increases sharply achieving values of n

between 14 and 18. Both WB 2124/SiC/25p<20µm as well as WB 6061/SiC/25p<20µm give values of n ≈ 10 in the whole stress range.

These large n values may suggest the appearance of a threshold stress creep behaviour as it is reported for dispersion strengthened alloys [10, 16, 69]. This behaviour is proposed to be related to particle back stresses due to the presence of sub-µm particles such as oxides, intermetallic particles and fragments of SiC particles as it was shown in chapter "Results".

The presence of SiC particles in the BM PRMs results in enhancing the creep resistance of the matrix alloy over the entire range of strain rate measured. Adding SiC particles <5µm to the matrix alloy and mixing it by WB results in no significant enhancement of the creep resistance or even in a weakening of the matrix. The <20µm SiC particles mixed by WB cause an increase of the creep rate compared to the unreinforced alloys what indicates that the strengthening effect by particles is lost. This could happen due to the occurrence of interfacial debonding in case of the WB materials.

In the low stress region grain boundary sliding is replaced by dislocation climb at an increased rate of dislocation generation. There is still a threshold stress effective, but significantly smaller than for the dispersion strengthened BM material.

As the values of the creep exponent, n, are similar for the BM PRMs and for the unreinforced 2124 it can be assumed that the creep mechanism is the same in these materials. Below the change of the creep exponent, n, the value for n is about 2 for the unreinforced 2124 alloy and for the BM PRMs. This suggests that the dominating creep mechanism for these applied stresses (<30MPa for the unreinforced 2124 alloy and <50MPa for the BM PRMs, respectively) is grain boundary sliding. On the other hand, the values for the creep exponent, n, are similar for the WB PRM<5µm and for the unreinforced 6061 alloy what leads to the assumption that for these materials the dominating creep mechanism is also the same. In these materials the resulting creep exponent is about n=5 what means dislocation climbing is the dominating creep mechanism. The values for the creep exponent, n, are similar for the WB PRMs<20µm and are >8. All the values for the creep exponent after a certain applied stress are even bigger than 10 indicating different levels of threshold stresses.

## 5.3  Short term Strength

Hardness was measured of BM PRM <5µm, WB PRM <5µm as well as from all the corresponding unreinforced matrices in T4 and T4S condition and after certain creep exposure time. There is a loss of hardness going from T4 condition to T4S condition. Shortly after T4S condition there is a further loss of hardness obtained. After 3 hours of overaging at 300 °C no effect of overaging on the hardness is evident (see Figure 4.50 and Figure 4.51). Confirming the results of the HT tensile tests and of the creep tests the addition of SiC particles to the Al alloys lead to an increase of the hardness. This hardening behaviour is attributed to the higher dislocation density resulting from the SiC particles. The BM materials show the biggest hardness values among all the investigated materials due to the high content of dispersoids followed by the WB PRMs. There is a slight decrease of hardness after a couple of hours of exposure to 300 °C but then after further exposure there is no change in hardness. This is attributed to the changing age hardening efficiency.

According to [92] the results of the hardness measurements do not show an increase in hardness of the WB materials while there is an increase of hardness in the BM material. This also is due to the distribution of dispersoids [91]. Liu et al [92] found that there is essentially no change in microhardness after mechanical mixing compared to the as-received powders. However, the mechanical-alloying process leads to an increase in microhardness, and this increases with increasing milling time, reaching saturation after 10 hours of ball milling. Further ball milling did not lead to any useful increase in the microhardness of the powder mixture. Anyhow after extrusion the strain hardening during milling is certainly recovered.

Preparing by BM give additional rise to the UTS due to the presence of broken sub-µm and the increased oxide and intermetallic content whereas the WB PRMs with less oxide content and without broken SiC result in a much less UTS value. This means, that the route of preparing materials has a strong influence on the UTS. Among the BM PRMs those with the smallest SiC particles obtain the highest value of UTS. The same was observed for the WB PRMs. The smaller the particles are the higher are the values of the UTS. The addition of the reinforcing phase leads to a loss of ductility (see Figure 4.48).

The effect of the size of the SiC particles can be attributed to the role of the interparticle distances. Same amount of particles but bigger particles leads to bigger interparticle spaces and in this way it causes dislocations to move easier because of the absence of obstacles. Additionally the bigger particles in the WB PRMs with much more sharp edges act as dislocation sources.

According to [95] the increase in strength of composites compared to the unreinforced alloys has been attributed to several mechanisms. Load transfer from the matrix to the reinforcement is accordingly a significant contributor to composite strengthening. Reinforcement particles impede dislocation motion and lead to dislocation pileups at particle-matrix interfaces. This effect is most pronounced in composites with extremely fine reinforcement particles with sizes below 1µm, as in the present BM material is the case. In T4 condition coherent precipitate combinations in the Al matrix are present, and are sheared by dislocations. While the precipitates are deformable, the SiC particles are non-deformable, acting as obstacles to dislocation motion and refining the slip length in the matrix. A combination of non-deformable particles in a matrix of shearable precipitates can result in a beneficial change in the deformation mechanisms [95].

According to the results of Shen et al [104] a clear increase in elastic modulus, over the unreinforced alloy, was observed with the addition of SiC. In the composite containing large SiC particles the yield strength and the ultimate tensile strength were significantly lower compared the composite with small particles. This can be attributed to the higher propensity of particle fracture of the bigger particles. This phenomenon and its influence are degrading the composite mechanical properties.

## 5.4  Damage

The fracture images shown in chapter "Results" show the appearance of dimples in all the investigated materials but with considerable differences. Due to the two different processing routes of the PRMs the particles in case of the BM PRMs are broken and reach down to the µm-scale while this is not the case for the WB PRMs where the particles remain with bigger size (e.g. sharp edged, with cracks). These differences in the particle lead to different behaviour in fracture.

Investigations of the fracture surfaces gives differences of the fracture HT tensile tests compared with the fractured creep samples. Analysis were conducted with the BM PRMs <5µm and <20µm, the WB PRMs <5µm and <20µm as well as all the corresponding unreinforced matrices 2124 and 6061. The macroscopic images of all the fractured samples showed considerable necking of the unreinforced alloy samples, whereas no necking is observed at the PRMs in all cases. This means that the ductility due to the addition of SiC particles, regardless what blending method was conducted, is much decreased for both the 2124 as well as for the 6061 alloys (see Figure 4.56). Creep pores observed in the unreinforced matrix are found what leads to the fracture of the sample (Figure 4.57). Fracture of SiC particles is evident as well as decohesion of the SiC-matrix. These mainly occurs at the HT tensile tests accompanied with formation of dimples and from all the materials the WB PRMs show the most particle fracture due to the bigger particles (Figure 4.58). Observations of the fractured surfaces from the tensile creep tests show the formation of smaller dimples and almost no particle fracture but more interface debonding (Figure 4.59).

Observations of the fracture surfaces using SEM conducted by Lu et al [99, 63] revealed three types of fracture modes, namely, fracture of the SiC particles, fracture due to the coalescence of micro-viods in the matrix material and fracture due to debonding between the matrix and the SiC particles. They reported that fracture due to debonding was observed to dominate. This could be due to the weak matrix/SiC interface and the concentration of porosity at the interface of the materials. Cracks were initiated at the interface by decohesion and these give rise to the final fracture

of the test samples. The tendency of debonding was also observed to increase with mechanical alloying time.

They observed that agglomeration of sharp edged SiC particulates in the matrix of specimen without BM can be easily seen [61, 91]. Large dimples can be seen in the Al matrix due to the ductility of the matrix material and the relatively large powder particle size. The dispersion of the reinforcement in the matrix was not attained. The fracture surface analyses suggests that fracture was due mainly to the cluster of SiC particles and/or debonding at the matrix particle interfaces in conventional blending and at shorter duration of BM where a uniform distribution of SiC particles had not been achieved. Generally, in particulate reinforced materials microvoid coalescence is the predominant fracture mode. The stages of microvoid coalescence consist of void nucleation, growth, and coalescence. The void nucleation process can be influenced by a variety of factors including the total volume fraction and the local volume fraction of the particulates, the matrix deformation characteristics and the interfacial bond strength [91]. Crack propagation is mainly transverse to the external stress direction.

# 6 Conclusions

The PRMs with the smallest SiC particles show the highest creep resistance and the highest $R_{p0.2}$ and $\sigma_{max}$ values among the all the studied materials. Those are attributed to the increased number of sub-µm particle size and the resulting smaller interparticle spacing due to BM.

## 6.1 The blending Methods and resulting microstructures

Due to the processing routes of the investigated materials the reinforcing SiC particles result in quite different morphologies. A comparable view of the microstructures due to different blending methods is given in Table 6.1.

On the one hand the SiC particles are fractured during BM causing the formation of sub-µm particles. This results in a particle size distribution with absence of particles >5µm for all the BM composites. On the other hand, the WB materials show a bimodal particle size distribution with only a few broken 1µm particles. All the images exhibit some elongated particle free zones which result from the hot extrusion of bigger matrix powder grains. An alignment of the SiC particles in direction of extrusion is evident in the materials mixed by WB. This alignment is not observed in the materials prepared by BM due to the more spherical shape of the broken particles.

A refinement of the grain size due to the process of BM is evident. The unreinforced matrix without BM obtains many elongated big grains (up to 150µm) as well as mainly considerable smaller ones (3-7µm). The unreinforced BM 2124 shows much less of the elongated big grains (only up to 100µm) resulting in mainly small ones (1-3µm). The unreinforced BM 6061 shows no grains longer than 50µm. This material mainly has grains in the size range 2-5µm and they seem to be more aligned to the direction of extrusion than those in the BM 2124 alloy where the grains tend to be more rounded. The mentioned elongated big grains in the unreinforced matrices tend to disappear in the PRMs due to the presence of SiC particles resulting in mainly small grains. The effect of mechanical alloying and the corresponding refinement of

the microstructure and the resulting effect on the mechanical properties is discussed by several authors [105, 106, 107, 108] in the last decades. A slight decrease of the grain size in the BM PRMs (1-3µm) compared with the WB PRMs (3-5µm) was found in the present study.

| | Unreinforced Matrix | | | WB PRM 2124 & 6061 | | BM PRM 2124 | | |
|---|---|---|---|---|---|---|---|---|
| | 2124 | | 6061 BM | <5µm | <20µm | <5µm | <10µm | <20µm |
| | With-out BM | BM | | | | | | |
| SiC particles | - | | - | 2.2-4.4µm | 1.6-7.3µm | 1.6-2.9µm | 1.3-2.9µm | 1.3-2.6µm |
| | | | | Sharp edges, alignment and fracture by extrusion, small fraction of ~1µm particles | | Essentially independent of initial size, rounded, fractured by BM (few>5µm), high number density of fragments (sub-µm) | | |
| Intermetallic dispersoids | - | - | - | Fe, Mn, Si aluminides | | Fe, Mn, Si, Cu Smaller and more aluminides | | |
| Oxide dispersoids | Due to extrusion | Due to BM and extrusion | Due to BM and extrusion | Due to extrusion | | Oxides near SiC arised mainly by BM | | |
| Precipitates | $Al_2Cu$, $Al_2CuMg$ | | $Mg_2Si$ | $Al_2Cu$ in 2124 $Mg_2Si$ in 6061 | | $Al_2Cu$, $Al_2CuMg$, $Cu_2Mn_3Al_{20}$ but difficult to distinguish | | |
| Grain size | Many elongated grains mainly 3-7µm up to 150µm | Less elongated grains, Smaller mainly 1-3µm up to 100µm | No grains >50µm mainly 3-7µm | No elongated grains due to SiC 3-5µm | - | No elongated grains due to SiC 1-3µm | - | - |

**Table 6.1** Summarizing view of the resulting microstructures due to different blending routes

The unreinforced 2124 matrix extruded without BM show a cleaner microstructure and a less content of oxygen than the BM. The unreinforced 2124 matrix extruded with prior subjecting to four hours BM shows much more intermetallic phases, a higher oxygen fraction due to BM and as well a higher amount of dispersoids.

The SiC particles are not fractured during blending route but during extrusion process. This also leads to decreased particle sizes compared to the initial SiC powder but they remain much bigger in size compared to the BM PRMs. The SiC particles in the WB PRMs show sharp edges and a slightly alignment in direction of extrusion. The PRMs prepared by wet blending show less than the half of the oxygen content and additionally very large SiC particles are present. This leads to the result of having the least creep resistance of all the tested materials when SiC particles <20µm are the utilized phase resulting in 10% particles >5µm.

A resulting multimodal SiC particle distribution in the BM PRMs is evident due to the fracture of SiC during BM and extrusion. The fractured sub-µm SiC particles can be found (<2vol%) as well as bigger SiC particles but all are smaller than 5µm. The SiC particles can be described as more rounded with no sharp edges and decreased in the size compared to the initial SiC powder. The measurements of oxygen fraction of BM PRMs revealed the highest oxygen fraction in the PRMs. Much more dispersoids <1µm are evident.

## 6.2  Isothermal Tensile Creep

### 6.2.1  The unreinforced matrices

All the unreinforced matrices, the 2124 without BM, BM 2124 and BM 6061 together with the WB PRMs <5µm show a two-region creep behaviour: the low stress region of an applied tensile load ranging from 15-30MPa and the high stress region of an applied tensile load from 30-60MPa.

The unreinforced 2124 alloy was tested with and without subjecting to BM what leads to the result that the matrix prepared with BM prior to extrusion show a little higher creep resistance among all the tested unreinforced alloys. This comes from the higher oxygen fraction as well as from the higher amount of intermetallic phases and inclusions as it was observed by means of TEM investigations.

The creep exponent n in the low stress region for the unreinforced PM 2124 alloy is about 2. This indicates grain boundary sliding as the dominating creep mechanism as it was reported by Lüthy et al [47]. The slightly higher creep rate of the PM 2124 without BM than that of the BM version corresponds to the different grain size of approximately 5µm and 3µm, respectively. For the 6061 alloy it is about 3 what means that viscous drag is the dominating creep mechanism.

The creep resistance of the unreinforced 2124 and 6061 matrices produced by powder metallurgy is about one order of magnitude higher than that of those produced by ingot metallurgy. It is reported to be the powder metallurgy route due to the larger oxygen content what provides some dispersion strengthening.

In the high stress region ($\geq$ 30MPa for the PM BM 2124 and without BM, PM BM 6061 and $\geq$ 40MPa for 2024W and 2124AMC and $\geq$ 50MPa for 6061IM) the increasing values of n could indicate the evidence of a threshold stress for creep. In the unreinforced matrices the threshold stress is $\sigma_{th}$=26±2MPa except for the 6061IM with a $\sigma_{th}$=15MPa.

### 6.2.2 The WB PRMs

During wet blending the SiC particles keep their initial size and are being fractured only during extrusion. This leads to the absence of sub-µm SiC particles and the presence of bigger particles compared to the BM PRMs. The quantitative analysis of the SiC particle sizes is shown in Table 4.1. The WB PRMs reinforced with initial particle sizes <5µm contain a volume fraction of about 4vol% of particles which are bigger than 5µm, whereas the WB PRMs with initial SiC particles <20µm result in a total volume fraction of about 10vol% of particles which are bigger than 5µm.

The amount of dispersoids in the WB PRMs is much smaller than in the BM PRMs what means on the one hand that due to the bigger SiC particles more sources for dislocations and on the other hand less obstacles for dislocation motion are present what leads to a detrimental effect. Oxide dispersoids only result from the extrusion process since during mixing the Al particles are not fractured.

For the WB PRMs <5µm the values of the creep exponent n is about 5. These values of n refer to dislocation climbing as the dominating creep mechanism for $\sigma_A$=15-30MPa [68, 73]. The WB PRMs <5µm show a change of the creep exponent n at $\sigma_A$=30MPa. The creep exponent n reaches values of >11 for the WB PRMs <5µm in the high stress region. Therefore a threshold stress is suggested which reaches values of $\sigma_{th}$=25±1MPa for the WB 2124 and 6061 <5µm similar to the unreinforced PM 6061 and all 2xxx samples.

For the WB PRMs <20µm there is obviously no change in the creep exponent over the entire range of applied tensile loads. The WB PRMs <20µm show a weaker creep resistance for all the tested applied tensile loads with a creep exponent n of 8.3 and 11.2 between 15 and 60MPa, respectively. This also could indicate the existence of a threshold stress for creep for this material in the entire range of applied loads which is $\sigma_{th}$=14±1MPa for the WB 2124 and 6061 <20µm similar to IM 6061.

These results suggest that there is a critical SiC particle size and volume fraction for which the particles will act as a reinforcing phase or as dislocation sources. 4vol% of SiC particles bigger than 5µm, as it is the case for an initial particle size <5µm, have very small effect on the creep resistance of the WB PRMs. On the other hand,

10vol% of SiC particles bigger than 5µm as obtained for the WB PRMs with an initial particle size of <20µm are detrimental for the creep resistance of the alloy.

### 6.2.3  The BM PRMs

There are no remarkable differences in particle size distribution between the three BM PRMs regarding the value for the percentiles P25-P75, as this range contains 50vol% of all the added SiC particles. The volume fraction of SiC particles bigger than 5µm is 0.6vol% for the BM PRM <5µm and 2vol% for BM PRM <10µm and <20µm.

Additionally the content of oxygen in the BM PRMs (see Table 3.5) is 3 times bigger than in the unreinforced BM matrix suggesting a higher amount of oxides. Another consequence of BM is that during the blending process continuously new matrix surfaces are formed due to repeated fracturing. In this way the oxygen fraction is increased sharply. The oxygen fractured from the surfaces of the Al particles due to BM and extrusion act as obstacles for dislocation movements and these dispersoids increases the creep resistance.

The creep of the BM PRMs shows two regions of applied stresses with change of the resulting creep exponent: the low stress region from 30-50MPa and the high stress region from 50-70MPa. This gives a low stress region creep exponent of $n=2.2\pm0.7$ what indicates the grain boundary sliding as the dominating creep mechanism. The high stress region creep exponent rises up to 14 to 20. In the high stress region there may be a threshold stress for creep of $\sigma_{th}=40\pm5$MPa significantly higher than for the other materials.

The 4 hours of BM fractures the SiC particles down to the sub µm-scale and produces a more refined microstructure as it can be seen by TEM investigations. The interparticle spacing is reduced by one magnitude resulting in more effective obstacles for the dislocation climb. Also the Fe fraction from the container and balls may enrich the powder giving rise to the dislocation obstacles.

Dispersion strengthened composites show very high values of apparent creep exponent. This suggests that the creep behaviour of such composites may be

explained in terms of the existence of a threshold stress for creep. The origin and the characteristics of the threshold stress are still controversial [9, 100]. During the last decades several researchers investigated the creep behaviour of discontinuously-reinforced aluminium-based composites. It is well-established that the presence of a dispersion of fine (~100nm or less) insoluble particles in a metal can raise the creep resistance substantially, even when constituting only a small overall volume fraction (<1vol%).

There is considerable evidence for the presence of a threshold stress in the high temperature creep of ball milled metal matrix composites where the threshold stress is defined as a lower limiting stress below which no measurable strain rate can be achieved.

Figure 5.9 presents the threshold stresses from all the introduced materials. The threshold stress for the BM PRMs reaches $\sigma_{th}=40MPa$. With increasing the reinforcing particle size the values for the threshold stress decreases. Going from the WB PRM <20µm with the lowest creep resistance and the biggest particles via the WB PRM <5µm and the unreinforced matrices to the BM PRMs with the highest creep resistance and the smallest particles rises the resulting threshold stress for creep from 12MPa to 40MPa.

## 6.3  Dispersion Strengthening versus Particle Softening

All the PRMs produced by BM show a better creep resistance independent of the introduced SiC particle size compared with those PRMs produced by WB. This is the result of the broken SiC-particles of sizes <1µm yielding smaller particles and in smaller interparticle distances. The application of BM as a blending route produces dispersoids acting as dislocation obstacles. Although the increase in interface areas of refined microstructure accelerates diffusion creep, the dispersion strengthening prevails as was reported by several studies [83, 109]. The threshold stress of about 40MPa can be estimated.

A critical particle size can be introduced below which the SiC particles act as reinforcing phase, whereas bigger particles have a detrimental effect on the mechanical properties with respect to the increasing interparticle spacing with increasing particle size at a constant volume fraction of SiC [8, 9].

The WB PRMs with particle size <5µm containing a small fraction of SiC particles (≈4%) bigger than 5µm show approximately the same creep resistance as the unreinforced matrices. Dislocation climb is dominating at external stress >30MPa where a threshold stress of about 25MPa is estimated which is more or less the same as in unreinforced 2xxx samples as well as in the AMC 2124. Thus it can be concluded that overaged precipitates produce such a back stress. Diffusion creep becomes dominating below 30MPa.

Whereas 10vol% (more than 1/3 of the particles in WB PRMs <20µm) of particles bigger than 5µm lead to a weakening of the creep resistance. The threshold stress becomes only half of the unreinforced matrix. Dislocation climb is the dominating creep mechanism already at external stresses ≥ 15MPa. This means that there is a critical maximum particle size for strengthening as dislocation climb obstacles as well as a critical volume fraction of particles bigger than 5µm which increase the creep rate at the studied creep exposure. The bigger the volume fraction of the big particles is the weaker is the creep resistance because those act as dislocation sources [6, 7].

A list of selected studies is given in Table 6.2 in order to classify whether the reinforcement of PRMs has a detrimental effect or an increasing effect of the creep resistance.

| Decrease of creep resistance due to particles | Increase of creep resistance due to particles |
|---|---|
| J.W. Luster, M. Thumann, R. Baumann, Mechanical Properties of Aluminium Alloy 6061-Al2O3 Composites, Materials Science and Technology 9, 1993, 10, 853-862 | J. Čadek, S. J. Zhu, K. Milička, Creep behaviour of ODS aluminium reinforced by silicon carbide particulates: ODS Al–30SiCp composite Materials Science and Engineering A, Vol 248, 1998, 65-72 |
| J.D. Lord, B. Roebuck, P. Pitcher, Effect of Thermal Cycling and Thermal Exposure on the Mechanical Properties of Particulate Reinforced PRMs, C. In Visconti, Proc. Of the 8th European Conference on Composite Materials, Neapel, Italien, 1998 | S. J. Zhu, L. M. Peng, Q. Zhou, K. Kuchařová, J. Čadek, Creep behaviour of aluminium strengthened by fine aluminium carbide particles and reinforced by silicon carbide particulates — DS Al–SiC/Al4C3 composites, Materials Science and Engineering A, Vol 282, 2000, 273-284 |
| C. Broeckmann, Kriechen partikelverstärkter metallischer Werkstoffe, Fortschritt-Berichte VDI, Institut für Werkstoffe Lehrstuhl für Werkstofftechnik, Ruhr-Universität Bochum, Reihe 5, Nr. 612 | M. Furukawa, J. Wang, Z. Horita, M. Nemoto, Y. Ma, T.G. Langdon, An Investigation of Strain Hardening and Creep in an Al-6061/ Al2O3 Metal Matrix Composite, Metallurgical and Materials Transactions A 26A, 1995, 3, 633-639 |
| A. Whitehouse, T. Clyne, Effects of Reinforcement Content and Shape on Cavitation and Failure in Metal-Matrix Composites, Composites, 24, 1993, 256-261 | I.A. Ibrahim, F.A. Mohamed, E.J. Lavernia, Particulate Reinforced Metal Matrix Composites – a Review, Journal of Materials Science 26, 1991, 1137-1156 |
| A. Whitehouse, T. Clyne, Cavity Formation During Tensile Straining of Particulate and short Fibre metal matrix composites, Acta Metallurgica Materialia, 41(6), 1993, 1701-1711 | Y. Li, T.G. Langdon, A Comparison of the Creep Properties of an Al-6092 Composite and the Unreinforced Matrix Alloy, Metallurgical and Materials Transactions A 29A, 1998, 10, 2523-2531 |
| Zedalis MS, Bryant JD, Gilman PS, Das SK. JOM 1991;8:29–31 | Y. Li, F.A. Mohamed, An Investigation of Creep Behaviour in an SiC-2124 Al Composite, Acta Materialia 45, 1997, 11, 4775-4785 |
| | H. Winand, A. Whitehouse, P. Whiters, An investigation of the isothermal creep response of Al-based composites by neutron diffraction, Materials Science and Engineering, A284, 2000, 103-113 |
| | S. Tjong, Z. Ma, High-temperature creep behavior of powder-metallurgy alluminium reinforced with SiC particles of various sizes, Composites Science and Technology, 59, 1999, 1117-1125 |
| | Krajewski PE, Jones JW, Allison JE. Metall Trans A 1995;26: 3107–18 |
| | Z. Y. Ma, S. C. Tjong, The high-temperature creep behaviour of 2124 aluminium alloys with and without particulate and SiC-whisker reinforcement, Composites Science and Technology, Vol 59, 1999, 737-747 |

**Table 6.2** Classification of selected studies regarding their results of particle reinforcement

# 7 Further Work

Preparing materials with SiC particle sizes of <5μm or <20μm with different particle volume fraction (5vol%, 10vol%, 15vol%) in order to determine the role played by the volume fraction on the creep resistance of PM PRMs. The results are needed to be compared with those from the present work from the BM 2124/SiC/25p<5μm and BM 2124/SiC/25p<20μm material, to identify a critical volume fraction, below which the strengthening vanishes.

Quantitative TEM analysis with respect to dispersoids (size, number density, phase) to quantify the efficiency of the distribution of dispersoids.

Milling of SiC powder in the utilized ball milling device for a period of 4 hours should be carried out. The fine fraction (<1μm) of the milled SiC powder should then be mixed with the alloy eliminating the particle fraction >1μm. Volume powder fractions 1-5% of dispersoids are to be investigated.

The volume fraction of bigger particles of 10-20% would provide increased specific stiffness and room temperature strength, but reduced ductility. Knowledge-based material design can be applied compromising the properties serving best for specific applications.

# 8 References

[1] http://PRM-assess.tuwien.ac.at

[2] U. Kainer, Metal Matrix Composites, Wiley-VCH, 2003

[3] A. Evans, C. San Marchi, A. Mortensen, Metal Matrix Composites in Industry, TA481.E93, 2003

[4] AMS, Metals Handbook, Ninth Edition, Volume 7, Powder Metallurgy, 1990

[5] R.S. Mishra, A.B. Pandey, Y.R. Mahajan, Steady state creep behaviour of Silicon carbide particulate reinforced aluminium composites, Acta metall. mater., Vol. 40, No. 8, 1992, 2045-2052

[6] A. Whitehouse, T. Clyne, Effects of Reinforcement Content and Shape on Cavitation and Failure in Metal-Matrix Composites, Composites, 24, 1993, 256-261

[7] A. Whitehouse, T. Clyne, Cavity Formation During Tensile Straining of Particulate and short Fibre metal matrix composites, Acta Metallurgica Materialia, 41(6), 1993, 1701-1711

[8] H. Winand, A. Whitehouse, P. Whiters, An investigation of the isothermal creep response of Al-based composites by neutron diffraction, Materials Science and Engineering, A284, 2000, 103-113

[9] S. Tjong, Z. Ma, High-temperature creep behavior of powder-metallurgy alluminium reinforced with SiC particles of various sizes, Composites Science and Technology, 59, 1999, 1117-1125

[10] G. Gonzalez-Doncel, O. D. Sherby, High temperature creep behaviour of metal matrix aluminium-SiC composites, Acta metal. Mater., Vol. 41, No. 10, 1993, 2797-2805

[11] Y. Li, T. Langdon, Creep Behavior of an Al-6061 metal matrix composite reinforced with alumina particulates, Acta mater. Vol 45, No. 11, 1997, 4797-4806

[12] J. Cadek, M. Pahutova, V. Sustek, Creep behaviour of a 2124 Al alloy reinforced by 20 vol.% SiC, Materials Science and Engineering A246, 1998, 252-264

[13] Y. Li, T. Langdon, Fundamental Aspects of Creep in Metal Matrix Composites, Metallurgical and Materials Transactions, Vol. 30A, 1999, 315-324

[14] G. Requena, H.P. Degischer, Effects of particle reinforcement on creep behaviour of AlSi1MgCu, Z. Metallkd. 96, 2005, 7

[15] R. Fernandez, G. Gonzalez-Doncel, Threshold stress and load partitioning during creep of metal matrix composites, Acta Materialia 56, 2008, 2549-2562

[16] T.W. Clyne, P.J. Withers, An Introduction to Metal Matrix Composites, Cambridge University Press 1993

[17] N. Chawla, K.K. Chawla, Metal Matrix Composites, Springer Science + Business Media, Inc., 2006

[18] H.P. Degischer, P. Prader, H. Kilian, Defekte in stranggepreßtem, teilchenverstärktem Aluminium und die Streuung der Eigenschaften, DVM_Bericht 518 Bauteilversagen durch Mikrodefekte, 1998, 135-140

[19] M. Pech-Canul, R. Katz, M. Makhlouf, Optimum conditions for pressureless infiltration of SiCp performs by aluminium alloys, Journal of Materials Processing Technology, 108, 1, 2000, 68-77

[20] A. Mortensen, V. Michaud, M. Flemings, Pressure-Infiltration Processing of Reinforced Aluminium, JOM, 1993, 36-43

[21] T. Srivatsan, T. Sudarshant, E. Laverniaj, Processing of Discontinuously Reinforced Metal Matrix Composites by Rapid Solidification, Progress in Materials Science, 39, 1995, 317-409

[22] A. Kelly, C. Zweben, Comprehensive Composite Materials, Vol. 3, Metal Matrix Composites, Ed. T.W. Clyne, Elsevier, 2000

[23] H. Dudek, R. Leucht, Titanium Matrix Composites, in Advanced Aerospace Materials, Ed by H. Buhl, Springer Verlag, Berlin, 1992, 124-139

[24] W.S. Miller, F.J. Humphreys, Strengthening Mechanisms in Metal Matrix Composites, 1990

[25] M.F. Ashby, D.R.H. Jones, Engineering Materials 1, 1996

[26] W. Schatt, K.-P. Wieters, Pulvermetallurgie, Technologien und Werkstoffe, VDI-Verlag GmbH, Düsseldorf, 1994

[27] R.K. McGeary, Mechanical Packing of Spherical Particles, J. Am. Ceramic Soc., Vol. 44, 1961, 513

[28] P.E. Evans, R.S. Millman, The Vibratory Packing of Powders, in Perspectives in Powder Metallurgy, Vol. 2, H.H. Hausner, K.H. Roll, P.K. Johnson, Plenum Press, New York, 1967, 237-251

[29] M.Y. Balshin, Theory of Compacting, Vestnik Metalloprom., Vol. 18, 1938, 137-147

[30] R.W. Heckel, An Analysis of Powder Compaction Phenomena, Trans. AIME, Vol. 221, 1961, 1001-1008

[31] L.F. Hammond, E.G. Schwartz, The Effect of Die Rotation on the Compaction of Metal Powders, Int. J. Powder Metall., Vol. 6 (No. 1), 1970, 25-36

[32] A. Broese van Groenou, Pressing of Ceramic Powders, A Review of Recent Work, Powder Metall. Int., Vol. 10, 1978, 206-211

[33] R.I. Davies, S. Elwakil, Comparison of Slow Speed, High Speed and Multiple Compaction in Ferrous Powders, Proceedings of 17th Machine Tool Design and Research Conference, sponsored by University of Birmingham, Vol. 3, 1976, 483-488

[34] R.M. Rusnak, Energy Relationship in High Velocity Compacting of Copper Powder, Int. J. Powder Metall., Vol. 12 (No. 2), 1976, 91-99

[35] G. Shatalova, N.S. Gorbunov, V.I. Likhman, Physicochemical Principles of Vibratory Compacting, in Perspectives in Powder Metallurgy, Vol. 2, H.H. Hausner, P.K. Johnson, K.H. Roll, Ed. Plenum Press, New York, 1967, 1-206

[36] E.Y. Gutmanas, Cold Sintering Under High Pressure-Mechanism and Application, Powder Metall. Int., Vol. 15, 1983, 129-132

[37] P. Loewenstein, L.R. Aronin, A.L. Geary, Hot Extrusion of Metal Powders, in Powder Metallurgy, W.Leszynski, Ed., New York, 1961, 563-583

[38] R.S. Busk, T.E. Leontis, The Extrusion of Powdered Magnesium Alloys, Trans. AIME., Vol. 188, 1950, 297-306

[39] R.S. Busk, The Pellet Metallurgy of Magnesium, Light Metals, Vol. 23, 1960, 197-200

[40] J.P. Lyle, W.C. Cebulak, Fabrication of High Strength Aluminium Products from Powder, in Powder Metallurgy for High-Performance Applications, J.J. Burke, V. Weiss, Ed., Syracuse, 1972, 231-254

[41] A.S. Bufferd, Complex Superalloy Shapes, in Powder Metallurgy for High-Performance Applications, J.J. Burke, V. Weiss, Ed., Syracuse, 1972, 303-316

[42] F.R.N. Nabarro, H.L. de Villiers, The Physics of Creep, Taylor&Francis Ltd, 1995

[43] R. Bürgel, Handbuch Hochtemperatur-Werkstofftechnik, Grundlagen, Werkstoffbeanspruchungen, Hochtemperaturlegierungen, Vieweg Technik, 1998

[44] J.J. Skrzypek, Plasticity and creep, Theory, Examples and Problems, 2000

[45] W. Blum, P. Eisenlohr, Dislocation mechanics of creep, Material Science and Engineering A, 2009

[46] F.A. Mohamed, T.G. Langdon, The transition from Dislocation Climb to Viscous Glide in Creep of Solid Solution Alloys, Acta Metallurgica 22, 1974, 779-788

[47] H. Lüthy, R.A. White, O.D. Sherby, Grain Boundary Sliding and Deformation Mechanism Maps, Materials Science and Engineering 39, 1979, 211-216

[48] R.A. White, Ph.D. Dissertation, Department of Materials Science and Engineering, Stanford University, Stanford, Calif., March 1978

[49] H.J.Frost, M.F.Ashby, Deformation Mechanism Maps-The Plasticity and Creep of Metals and Ceramics, Pergamon, Oxford, 1982

[50] B. Nix, B. Ilschner, Machanisms Controlling Creep of Single Phase Metals and Alloys, In: P. Haasen, V. Gerold, G. Kostorz: Int. Conf. Strength of Metals and Alloys, ICSMA 5, Aachen, 1979, 1503-1530

[51] R. Lagneborg, in Ispra Seminar on Creep of Engineering Materials and Structures, G. Bernasconi, G. Piatti, Applied Science Publishers Ltd., Varese, 1978, 1-34

[52] C. Broeckmann, Kriechen partikelverstärkter metallischer Werkstoffe, Fortschritt-Berichte VDI, Institut für Werkstoffe Lehrstuhl für Werkstofftechnik, Ruhr-Universität Bochum, Reihe 5, Nr. 612, 2001

[53] Y. Li, T.G. Langton, Creep behavior of a Reinforced Al-7005 Alloy: Implications of the Creep Process in Metal Matrix Composites, Acta Materialia 46, 1998, 4, 1143-1155

[54] Y. Ma, K. Xia, J.L. Mihelich, T.G. Langton, Creep Behavior in an Aluminum Composite Containing Alumina Microspheres, T. In Chandra, A.K. Dhingra, Proc. Of "Advanced Composites", , TMS-AIME, Warrendale, USA, 1993, 1177-1180

[55] J.W. Luster, M. Thumann, R. Baumann, Mechanical Properties of Aluminium Alloy 6061- Al2O3 Composites, Materials Science and Technology 9, 1993, 10, 853-862

[56] J.D. Lord, B. Roebuck, P. Pitcher, Effect of Thermal Cycling and Thermal Exposure on the Mechanical Properties of Particulate Reinforced PRMs, C. In

Visconti, Proc. Of the 8th European Conference on Composite Materials, Neapel, Italien, 1998

[57] M. Furukawa, J. Wang, Z. Horita, M. Nemoto, Y. Ma, T.G. Langdon, An Investigation of Strain Hardening and Creep in an Al-6061/ Al2O3 Metal Matrix Composite, Metallurgical and Materials Transactions A 26A, 1995, 3, 633-639

[58] I.A. Ibrahim, F.A. Mohamed, E.J. Lavernia, Particulate Reinforced Metal Matrix Composites – a Review, Journal of Materials Science 26, 1991, 1137-1156

[59] Y. Li, T.G. Langdon, A Comparison of the Creep Properties of an Al-6092 Composite and the Unreinforced Matrix Alloy, Metallurgical and Materials Transactions A 29A, 1998, 10, 2523-2531

[60] Y. Li, F.A. Mohamed, An Investigation of Creep Behaviour in an SiC-2124 Al Composite, Acta Materialia 45, 1997, 11, 4775-4785

[61] S. Qin, C. Chen, G. Zhang, W. Wang, Z. Wang, The effect of particle shape on ductility of SiCp reinforced 6061 Al matrix composites, Materials Science and Engineering A 272, 2004, 363-370

[62] S.G. Song, N. Shi, G.T. Gray, J.A. Roberts, Metall. Mater. Trans. A 27A, 1996, 3739

[63] J.E. Spotwart, D.B. Miracle, The influence of reinforcement morphology on the tensile response of 6061/SiC/25p discontinuously-reinforced aluminium, Materials Science and Engineering A357, 2003, 111-123

[64] D. Hull, Introduction to Dislocations, Pergamon Press Ltd., 1968

[65] X.J. Xin, G.S. Daehn, R.H. Wagoner, Modeling the Generation, Equilibrium, and emission of Dislocations at elastically misfitted Particles, Acta mater. Vol. 46, No. 17, 1998, 6131-6144

[66] S.P. Deshmukh, R.S. Mishra, K.L. Kendig, Creep behaviour and threshold stress of an extruded Al-6Mg-2Sc-1Zr alloy, Materials Science and Engineering A381, 2004, 381-385

[67] Z. Lin, Y. Li, F.A. Mohamed, Creep and substructure in 5 vol.% SiC-2124 Al composite, Materials Science and Engineering A332, 2002, 330-342

[68] J. Cadek, M. Pahutova, V. Sustek, Creep behaviour of a 2124 Al alloy reinforced by 20 vol.% SiC, Materials Science and Engineering A246, 1998, 252-264

[69] K.T. Park, F.A. Mohamed, Creep strengthening in a discontinuous SiC-Al Composite, Metallurgical and Materials Transactions, Vol. 26A, 1995, 3119-3129

[70] L. Kloc, S. Spigarelli, E. Cerri, E. Evangelista, T. Langdon, Creep behaviour of an aluminum 2024 alloy produced by powder metallurgy, Acta mater. Vol. 45, No. 2, 1997, 529-540

[71] J. Cadek, H. Oikawa, V. Sustek, Threshold creep behaviour of discontinuous aluminium and aluminium alloy matrix composites: an overview, Materials Science and Engineering A 190, 1995, 9-23

[72] Y. Li, T. Langdon, A Simple Procedure for Estimating Threshold Stresses in the Creep of Metal Matrix Composites, Scripta Materialia, Vol. 36, No. 12, 1997, 1457-1460

[73] J. Cadek, S.J. Zhu, K. Milicka, Creep behaviour of ODS aluminium reinforced by silicon carbide particulates: ODS Al-30SiCp composite, Materials Science and Engineering A248, 1998, 65-72

[74] K.T. Park, E.J. Lavernia, F.A. Mohamed, High-temperature deformation of 6061 Al, Acta metal. Mater., Vol. 42, No. 3, 1994, 667-678

[75] F.A. Mohamed, Correlation between creep behaviour in Al-based solid solution alloys and powder metallurgy Al alloys, Materials Science and Engineering A245, 1998, 242-256

[76] Y. Li, S.R. Nutt, F.A. Mohamed, An investigation of creep and substructure formation in 2124 Al, Acta mater., Vol. 45, No. 6, 1997, 2607-2620

[77] A.B. Pandey, R.S. Mishra, Y.R. Mahajan, Acta Metall. Mater., 1992, 40, 2045-2052

[78] H.M.A. Winand, Ph.D. Thesis, University of Cambridge, 1996

[79] ASM Aluminium and Aluminium Alloys, 1994

[80] Chemical analyses by AMAG rolling GmbH, Nr. 026932/TP/08, 2008, http://www.amag.at/

[81] http://www.alpoco.co.uk, Alpoco, Aluminium Powder Company, United Kingdom, 2006

[82] http://www.esk-sic.de/

[83] J.B. Fogagnolo, Effect of mechanical alloying on the morphology, microstructure and properties of aluminium matrix composite powders, Materials Science and Engineering A342, 2003, 131-143

[84] http://www.ustem.tuwien.ac.at/

[85] http://en.wikipedia.org/wiki/Nanoindentation

[86] http://www.microphotonics.com/nanoindentationtester.htm

[87] G. Requena, Dissertation TU - Vienna, 2004

[88] http://www.micro-epsilon.de/de-de/

[89] http://www.hbm.de/

[90] http://www.gerhard-rauch.at/

[91] L. Lu, M.O. Lai, C.W. Ng, Enhanced mechanical properties of Al based metal matrix composite prepared using mechanical alloying, Materials Science and Engineering A252, 1998, 203-211

[92] Y.B. Liu, J.K.M. Kwok, S.C. Lim, L. Lu, M.O.Lai, Fabrication of an Al-4,5Cu/15SiC composites: I Processing using mechanical alloying, Journal of Materials Processing Technology, 37, 1993, 441-451

[93] N. Zhao, P. Nash, X. Yang, The effect of mechanical alloying on SiC distribution and the properties of 6061 aluminum composite, Journal of Materials Processing Technology 170, 2005, 586-592

[94] Z. Xiao, Z. Li, M. Fang, S. Xiong, Effect of processing of mechanical alloying and powder metallurgy on microstructure and properties of Cu-Al-Ni-Mn alloy, Materials Science and Engineering A488, 2008, 266-272

[95] E. Martin, A. Forn, R. Nogue, Strain hardening behaviour and temperature effect on Al-2124/SiCp, Journal of Materials Processing Technology 143-144, 2003, 1-4

[96] Y.-L. Shen, N. Chawla, On the correlation between hardness and tensile strength in particle reinforced metal matrix composites, Materials Science and Engineering A 297, 2001, 44-47

[97] Y.-L. Shen, E. Fishencord, N. Chawla, Correlating macrohardness and tensile behaviour in discontinuously reinforced metal matrix composites, Scripta mater. 42, 2000, 427-432

[98] P. Haasen, Physikalische Metallkunde, Springer Verlag, 1994

[99] L. Lu, J.K.M. Kwok, M.O.Lai, Y.B. Liu, S.C. Lim, Fabrication of an Al-4,5Cu/15SiC composites: II Effects of the processing parameters on the fracture properties, Journal of Materials Processing Technology, 37, 1993, 453-462

[100] Z. Lin, S.L. Chan, F.A. Mohamed, Effect of nano-scale particles on the creep behaviour of 2014 Al, Materials Science and Engineering A 394, 2005, 103-111

[101] S.J. Zhu, L.M. Peng, Q. Zhou, Z.Y. Ma, K. Kucharova, J. Cadek, Creep behaviour of aluminium strengthened by fine aluminium carbide particles and reinforced by silicon carbide particulates DS Al-SiC/Al4C3 composites, Materials Science and Engineering A282, 2000, 273-284

[102] V. Mutafov, H.P. Degischer, Kriechuntersuchungen an AlCu4 Legierungen mit und ohne Partikelverstärkung, Insitut für Werkstoffwissenschaft und Werkstofftechnologie, 2005

[103] R. Fernandez, G. Gonzalez-Doncel, Creep behaviour of ingot and powder metallurgy 6061Al, Lournal of Alloys and Compounds 440, 2007, 158-167

[104] Y.-L. Shen, J.J. Williams, G. Piotrowski, N. Chawla, Y.L. Guo, Correlation between tensile and indentation behaviour or particle-reinforced metal matrix composites: an experimental and numerical study, Acta mater. 49, 2001, 3219-3229

[105] L. Lu, M.O. Lai, C.W. Ng, Enhanced mechanical properties of Al based metal matrix composite prepared using mechanical alloying, Materials Science and Engineering A252, 1998, 203-211

[106] Y.B. Liu, J.K.M. Kwok, S.C. Lim, L. Lu, M.O.Lai, Fabrication of an Al-4,5Cu/15SiC composites: I Processing using mechanical alloying, Journal of Materials Processing Technology, 37, 1993, 441-451

[107] N. Zhao, P. Nash, X. Yang, The effect of mechanical alloying on SiC distribution and the properties of 6061 aluminum composite, Journal of Materials Processing Technology 170, 2005, 586-592

[108] Z. Xiao, Z. Li, M. Fang, S. Xiong, Effect of processing of mechanical alloying and powder metallurgy on microstructure and properties of Cu-Al-Ni-Mn alloy, Materials Science and Engineering A488, 2008, 266-272

[109] E. Arzt, R. Behr, E. Göhring, P. Grahle, Dispersion strengthening of intermetallics, Materials Science and Engineering A234-236, 1997, 22-29

# 9 Appendix

## 9.1 Extrusion data sheets

EXTRUSION Nº 571     FECHA: 17/03/06

USUARIO: BERND / JAVI

MATERIAL: 2124 as rec.

Masa lata (g).............
Masa polvo (g)..........
Diámetro lata / compacto (mm)...
Longitud lata / compacto (mm)... 200

Vel. ext. (mm/s)..... 18 (0.4)

Lubricante....................

Vel. papel (mm/min)....... 3.0

δ∞ (g/cm³)...............
δ/δ∞......................

Desgasificación...
(tiempo/temp.)

R extrusión........... 14
Diá. matriz (mm)...... 11,8

T tocho (ºC)....... 450
Tiempo....................

T contenedor (ºC)....
T horno matriz (ºC)...

T ambiente (ºC)..... 25
Tmáx. matriz (ºC)..... 455

P dens. (N/mm²).............
P máxima (N/mm²)..... 507 682
P final (N/mm²)...............

---

EXTRUSION Nº 572     FECHA: 21/3/06

USUARIO: Bernd

MATERIAL: 2124 / SiC <5 MA4

Masa lata (g).............
Masa polvo (g)..........
Diámetro lata / compacto (mm)... 40
Longitud lata / compacto (mm)... 200

Vel. ext. (mm/s)..... 0,4 (18)

Lubricante....................

Vel. papel (mm/min)....... 30

δ∞ (g/cm³)...............
δ/δ∞......................

Desgasificación...
(tiempo/temp.)

R extrusión........... 14
Diá. matriz (mm)...... 11,8

T tocho (ºC)....... 450
Tiempo........... 15'

T contenedor (ºC).... 450
T horno matriz (ºC)... 560

T ambiente (ºC)..... 19
Tmáx. matriz (ºC)..... 459

P dens. (N/mm²)............. 630
P máxima (N/mm²).....
P final (N/mm²)...............

---

EXTRUSION Nº 573     FECHA: 21/3/06

USUARIO: Bernd

MATERIAL: 2124 / SiC < 10 μm black 4h MA

Masa lata (g).............
Masa polvo (g)..........
Diámetro lata / compacto (mm)... 40
Longitud lata / compacto (mm)... 200

Vel. ext. (mm/s)..... 0,4 (18)

Lubricante....................

Vel. papel (mm/min)....... 30

δ∞ (g/cm³)...............
δ/δ∞......................

Desgasificación...
(tiempo/temp.)

R extrusión........... 14
Diá. matriz (mm)...... 11,8

T tocho (ºC)....... 450
Tiempo........... 15

T contenedor (ºC).... 550
T horno matriz (ºC)... 560

T ambiente (ºC)..... 23
Tmáx. matriz (ºC)..... 444

P dens. (N/mm²).............
P máxima (N/mm²)..... 665
P final (N/mm²)...............

---

EXTRUSION Nº 574     FECHA: 21/3/06

USUARIO: Bernd

MATERIAL: 2124 / SiC < 20 μm 4h MA

Masa lata (g).............
Masa polvo (g)..........
Diámetro lata / compacto (mm)... 40
Longitud lata / compacto (mm)... 200

Vel. ext. (mm/s)..... 0,4 (18)

Lubricante....................

Vel. papel (mm/min)....... 3.0

δ∞ (g/cm³)...............
δ/δ∞......................

Desgasificación...
(tiempo/temp.)

R extrusión........... 14
Diá. matriz (mm)...... 11,8

T tocho (ºC)....... 450
Tiempo........... 30

T contenedor (ºC).... 450
T horno matriz (ºC)... 560

T ambiente (ºC)..... 24
Tmáx. matriz (ºC)..... 446

P dens. (N/mm²).............
P máxima (N/mm²)..... 630
P final (N/mm²)...............

**EXTRUSION Nº** 576     **FECHA:** 21/3/06

**USUARIO:** Bernd

**MATERIAL:** 2124    4h BM

Masa lata (g)............
Masa polvo (g)............
Diámetro lata / compacto (mm)... 40
Longitud lata / compacto (mm)... 200

**Vel. ext. (mm/s)**... 0,4 (A8)

Lubricante....................

Vel. papel (mm/min)...... 30

δ∞ (g/cm³)................
δ/δ∞....................

**Desgasificación**.... ‾
(tiempo/temp.)

P dens. (N/mm²)............
**P máxima (N/mm²)**..... 630
P final (N/mm²)............

**R extrusión**........ 14
Diá. matriz (mm)..... 11,8

**T tocho (°C)**..... 450
Tiempo............ 215

T contenedor (°C)... 450
T horno matriz (°C)... 560

T ambiente (°C)..... 26
**Tmáx. matriz (°C)** 449

---

**EXTRUSION Nº** 577     **FECHA:** 21/3/06

**USUARIO:** Bernd

**MATERIAL:** 2124    4h MA

Masa lata (g)............
Masa polvo (g)............
Diámetro lata / compacto (mm)... 40
Longitud lata / compacto (mm)... 200

**Vel. ext. (mm/s)**... 0,4 (A8)

Lubricante....................

Vel. papel (mm/min)...... 30

δ∞ (g/cm³)................
δ/δ∞....................

**Desgasificación**.... ‾
(tiempo/temp.)

P dens. (N/mm²)............
**P máxima (N/mm²)**..... 595
P final (N/mm²)............

**R extrusión**........ 14
Diá. matriz (mm)..... 11,8

**T tocho (°C)**..... 450
Tiempo............ 215

T contenedor (°C)... 450
T horno matriz (°C)... 560

T ambiente (°C)..... 25
**Tmáx. matriz (°C)** 503

---

**EXTRUSION Nº** 632     **FECHA:** 3/7/07

**USUARIO:** Bernd

**MATERIAL:** 6061 / SC <20µ (200g)

Masa lata (g)............
Masa polvo (g)............
Diámetro lata / compacto (mm)... 40
Longitud lata / compacto (mm)... 200

**Vel. ext. (mm/s)**... 0,4 (A8)

Lubricante....................

Vel. papel (mm/min)........

δ∞ (g/cm³)................
δ/δ∞....................

**Desgasificación**...
(tiempo/temp.)

P dens. (N/mm²)............
**P máxima (N/mm²)**..... 714
P final (N/mm²)............

**R extrusión**........ 14
Diá. matriz (mm)..... 11,8

captura : 18

pasta :

**T tocho (°C)**..... 450
Tiempo............ 15'

T contenedor (°C)... 450
T horno matriz (°C)... 580

T ambiente (°C)... 33
**Tmáx. matriz (°C)** 448

---

**EXTRUSION Nº** 633     **FECHA:** 3/7/07

**USUARIO:** Bernd

**MATERIAL:** 2124 / S.C <20µm (200g)

Masa lata (g)............
Masa polvo (g)............
Diámetro lata / compacto (mm)... 40
Longitud lata / compacto (mm)... 200

**Vel. ext. (mm/s)**... 0,4 (A8)

Lubricante....................

Vel. papel (mm/min)........

δ∞ (g/cm³)................
δ/δ∞....................

**Desgasificación**...
(tiempo/temp.)

P dens. (N/mm²)............
**P máxima (N/mm²)**..... 684
P final (N/mm²)............

**R extrusión**........ 14
Diá. matriz (mm)..... 11,8

captura : 20

pasta :

**T tocho (°C)**..... 450
Tiempo............ 15'

T contenedor (°C)... 450
T horno matriz (°C)... 580

T ambiente (°C)... 34
**Tmáx. matriz (°C)** 438

```
        ENSAYO      DE      EXTRUSION      N°      636
636


_____

        IDENTIFICACION DEL ENSAYO _____

    Ensayo N°  : 636
    Fecha      : Thursday, September 20, 2007
    Usuario    : Bernd
    Material   : 6061/<20mic – 200g


    Datos De Identificación Complementarios:

      Temp ambiente 25°C – velocidad manual 0.4 mm/s


    PARAMETROS CONTROLADOS _____

    Velocidad:  0.00 mm/s

    PARAMETROS PRINCIPALES _____

    Temperatura Tocho     : 450 °C
    Temperatura Contenedor : 450 °C
    Temperatura Horno Matriz: 550 °C
    Relación de Extrusión  : 14
    Diámetro Matriz        : 11,8 mm

    PARAMETROS GENERALES _____

    Diámetro Tocho                40 mm
    Longitud Tocho               150 mm
    Tiempo                     15 min s
    Desgasificación               S/N
    Masa                         200 g

    RESUMEN DE RESULTADOS _____


    Captura  TaIni  TmIni   P máxima    T@Pmax  Notas

       27  26 °C  600 °C   684.00 MPa  0104 °C

    INCIDENCIAS / OBSERVACIONES _____

    El termopar no baja de 72°C, a partir de ahí mide bien.
```

```
        ENSAYO      DE      EXTRUSION      N°      637
637


_____

        IDENTIFICACION DEL ENSAYO _____

    Ensayo N°  : 637
    Fecha      : Thursday, September 20, 2007
    Usuario    : Bernd
    Material   : 6061 4h bm


    Datos De Identificación Complementarios:


    PARAMETROS CONTROLADOS _____

    Velocidad:  0.00 mm/s

    PARAMETROS PRINCIPALES _____

    Temperatura Tocho     : 450 °C
    Temperatura Contenedor : 450 °C
    Temperatura Horno Matriz: 550 °C
    Relación de Extrusión  : 14
    Diámetro Matriz        : 11,8 mm

    PARAMETROS GENERALES _____

    Diámetro Tocho                40 mm
    Longitud Tocho               200 mm
    Tiempo                     15 min s
    Desgasificación               S/N
    Masa                         200 g

    RESUMEN DE RESULTADOS _____


    Captura  TaIni  TmIni   P máxima    T@Pmax  Notas

       28  26 °C  600 °C   633.54 MPa  0446 °C   La Tamb y
Tinicio están mal: Tamb: 30°C y Tini: 447°C

    INCIDENCIAS / OBSERVACIONES _____

    El termopar no baja de 72°C, a partir de ahí mide bien
Temperatura ambiente: 30°C Velocidad 0.4mm/s (A8) Sale mal la temperatura
inicial, que fue de472°C
```

```
        ENSAYO      DE      EXTRUSION      N°      638
638


_____

        IDENTIFICACION DEL ENSAYO _____

    Ensayo N°  : 638
    Fecha      : Thursday, September 20, 2007
    Usuario    : Bernd
    Material   : 6061 <5mic 100g


    Datos De Identificación Complementarios:


    PARAMETROS CONTROLADOS _____

    Velocidad:  0.4 mm/s

    PARAMETROS PRINCIPALES _____

    Temperatura Tocho     : 450 °C
    Temperatura Contenedor : 450 °C
    Temperatura Horno Matriz: 550 °C
    Relación de Extrusión  : 14
    Diámetro Matriz        : 11,8 mm

    PARAMETROS GENERALES _____

    Diámetro Tocho                40 mm
    Longitud Tocho               150 mm
    Tiempo                       150 s
    Desgasificación             N S/N
    Masa                         200 g

    RESUMEN DE RESULTADOS _____


    Captura  TaIni  TmIni   P máxima    T@Pmax  Notas

       29  26 °C  600 °C   637.67 MPa  0457 °C

    INCIDENCIAS / OBSERVACIONES _____

    Igual que la anterior y además no funciona el ratón del
ordenador uso el de José Luis,TAmb 32°C y TInicio 470°C
```

```
        ENSAYO      DE      EXTRUSION      N°      639
639


_____

        IDENTIFICACION DEL ENSAYO _____

    Ensayo N°  : 639
    Fecha      : Thursday, September 20, 2007
    Usuario    : Bernd
    Material   : 2124 <5mic 100g


    Datos De Identificación Complementarios:


    PARAMETROS CONTROLADOS _____

    Velocidad:  0.4 mm/s

    PARAMETROS PRINCIPALES _____

    Temperatura Tocho     : 450 °C
    Temperatura Contenedor : 450 °C
    Temperatura Horno Matriz: 550 °C
    Relación de Extrusión  : 14
    Diámetro Matriz        : 11,8 mm

    PARAMETROS GENERALES _____

    Diámetro Tocho                40 mm
    Longitud Tocho               150 mm
    Tiempo                       150 s
    Desgasificación             N S/N
    Masa                           g

    RESUMEN DE RESULTADOS _____


    Captura  TaIni  TmIni   P máxima    T@Pmax  Notas

       30

    INCIDENCIAS / OBSERVACIONES _____

    Igual que la anterior uso el ratón de José Luis,
TAmb 33°C y TInicio 460°C PMáx 750MPa y T: 421°C
```

```
EXTRUSION N° 640
_____


        Fecha      : Friday, October 19, 2007
        Usuario    : Bernd
        Material   : Al6061

        ball milled 4 horas


        PARAMETROS CONTROLADOS _____

        Velocidad:  0.40 mm/s

        PARAMETROS PRINCIPALES _____

        Temperatura Tocho       :    450 °C
        Temperatura Contenedor  :    450 °C
        Temperatura Horno Matriz:    550 °C
        Relación de Extrusión   :     14
        Diámetro Matriz         :    11.8 mm

        OTROS PARAMETROS _____

        Diámetro Tocho          :     40 mm
        Longitud Tocho          :    150 mm
        Tiempo                  :     15 min
        Desgasificación         :        S/N
        Masa                    :         g


        RESUMEN DE RESULTADOS _____

        P máxima  TdePmáx  Ttocho    Tamb    Tini Captura

        600 MPa   440 °C   450 °C    18 °C    473 °C      34


        INCIDENCIAS / OBSERVACIONES _____
```

```
EXTRUSION N° 641
_____


        Fecha      : Friday, October 19, 2007
        Usuario    : Bernd
        Material   : 6061/SiC

        < 5 mic – 100g


        PARAMETROS CONTROLADOS _____

        Velocidad:  0.40 mm/s

        PARAMETROS PRINCIPALES _____

        Temperatura Tocho       :    450 °C
        Temperatura Contenedor  :    450 °C
        Temperatura Horno Matriz:    550 °C
        Relación de Extrusión   :     14
        Diámetro Matriz         :    11.8 mm

        OTROS PARAMETROS _____

        Diámetro Tocho          :     40 mm
        Longitud Tocho          :    150 mm
        Tiempo                  :     15 min
        Desgasificación         :        S/N
        Masa                    :         g


        RESUMEN DE RESULTADOS _____

        P máxima  TdePmáx  Ttocho    Tamb    Tini Captura

        660 MPa   441 °C   450 °C    25 °C    467 °C      36


        INCIDENCIAS / OBSERVACIONES _____
```

```
EXTRUSION N° 642
_____


        Fecha      : Friday, October 19, 2007
        Usuario    : Bernd
        Material   : 2124/SiC

        < 20 mic – 200g


        PARAMETROS CONTROLADOS _____

        Velocidad:  0.40 mm/s

        PARAMETROS PRINCIPALES _____

        Temperatura Tocho       :    450 °C
        Temperatura Contenedor  :    450 °C
        Temperatura Horno Matriz:    550 °C
        Relación de Extrusión   :     14
        Diámetro Matriz         :    11.8 mm

        OTROS PARAMETROS _____

        Diámetro Tocho          :     40 mm
        Longitud Tocho          :    150 mm
        Tiempo                  :     15 min
        Desgasificación         :        S/N
        Masa                    :         g


        RESUMEN DE RESULTADOS _____

        P máxima  TdePmáx  Ttocho    Tamb    Tini Captura

        680 MPa   447 °C   450 °C    23 °C    469 °C      44


        INCIDENCIAS / OBSERVACIONES _____
```

```
EXTRUSION N° 643
_____


        Fecha      : Friday, October 19, 2007
        Usuario    : Bernd
        Material   : 2124/SiC

        < 5 mic – 100g


        PARAMETROS CONTROLADOS _____

        Velocidad:  0.40 mm/s

        PARAMETROS PRINCIPALES _____

        Temperatura Tocho       :    450 °C
        Temperatura Contenedor  :    450 °C
        Temperatura Horno Matriz:    550 °C
        Relación de Extrusión   :     14
        Diámetro Matriz         :    11.8 mm

        OTROS PARAMETROS _____

        Diámetro Tocho          :     40 mm
        Longitud Tocho          :    150 mm
        Tiempo                  :     15 min
        Desgasificación         :        S/N
        Masa                    :         g


        RESUMEN DE RESULTADOS _____

        P máxima  TdePmáx  Ttocho    Tamb    Tini Captura

        758 MPa   447 °C   450 °C    31 °C    470 °C      48


        INCIDENCIAS / OBSERVACIONES _____
```

## 9.2 Metallographics
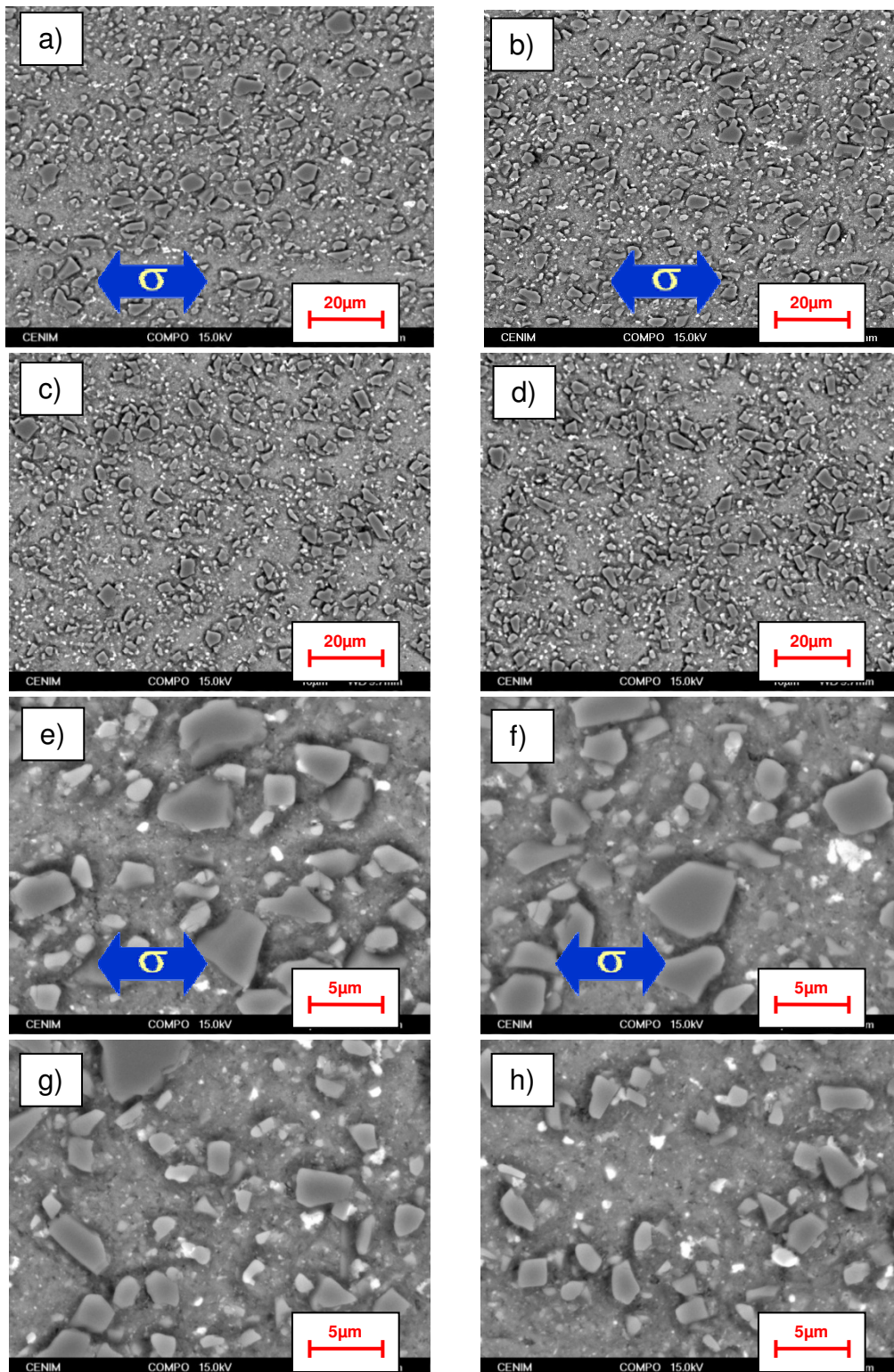


**Figure 9.1** BSE micrographs of BM 2124/SiC/25p<5µm in a), b), e), f) longitudinal and c), d), g), h) perpendicular direction of extrusion
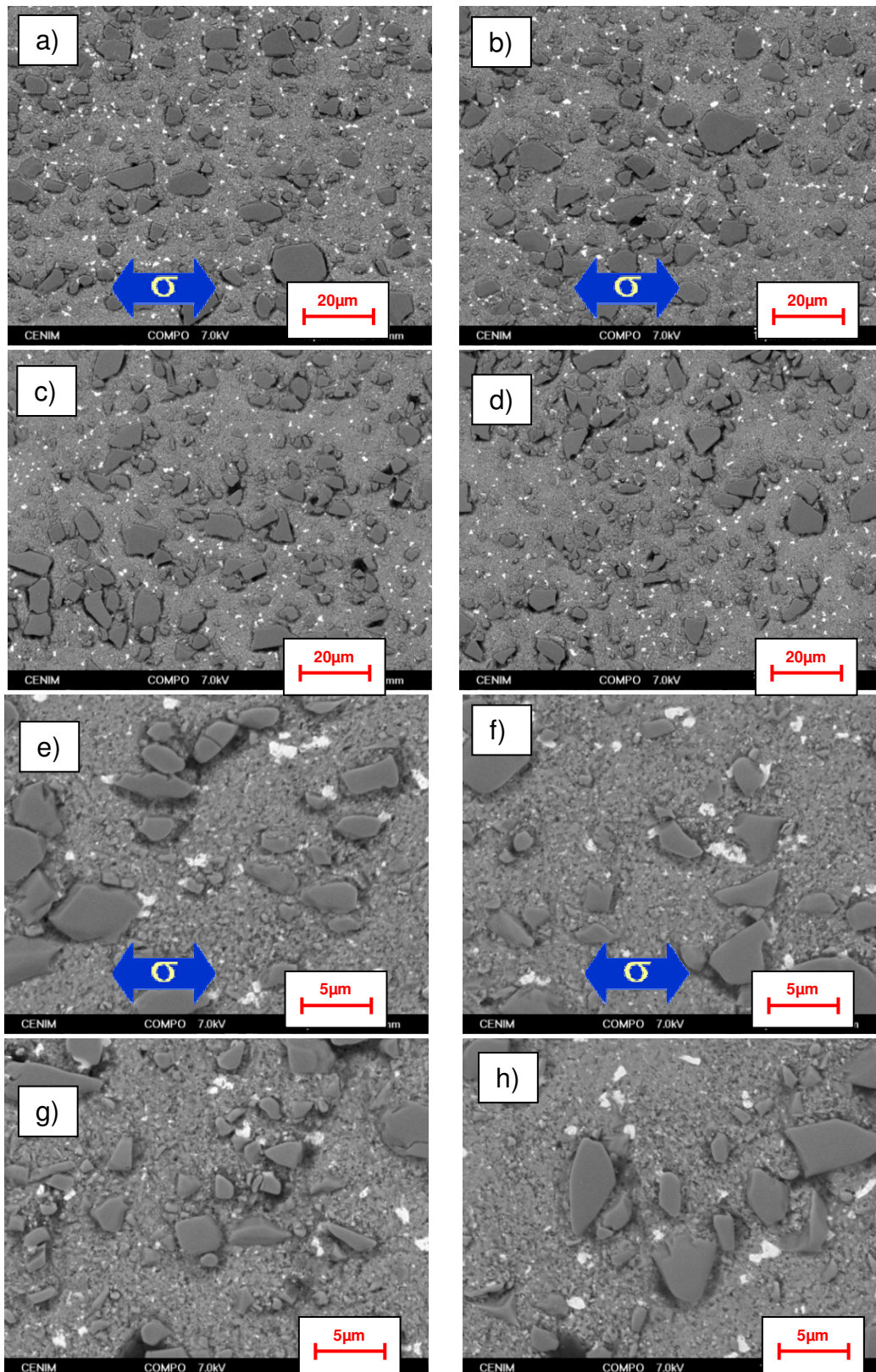
**Figure 9.2** BSE micrographs of BM 2124/SiC/25p<10µm in a), b), e), f) longitudinal and c), d), g), h) perpendicular direction of extrusion
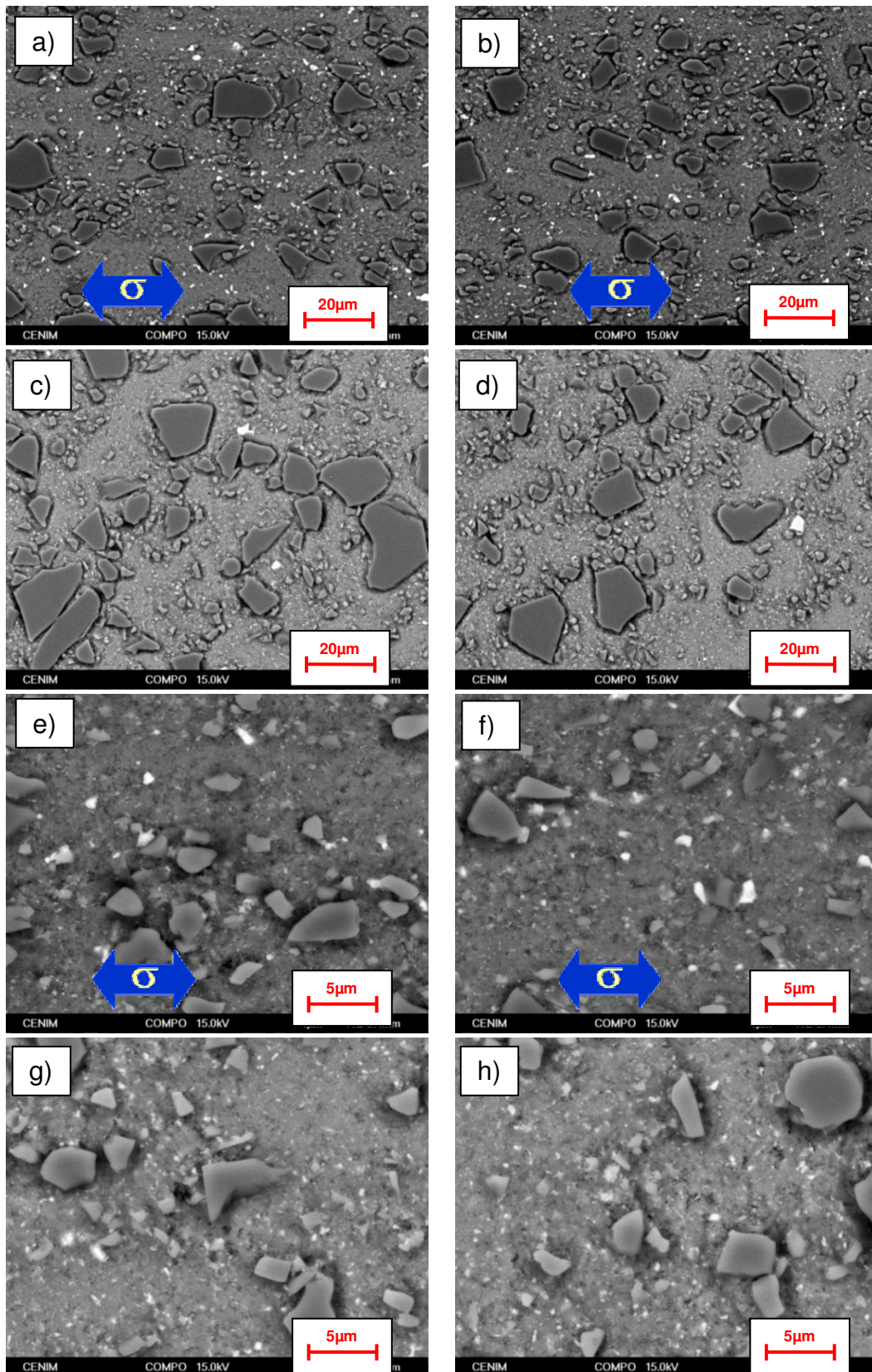
**Figure 9.3** BSE micrographs of BM 2124/SiC/25p<20µm in a), b), e), f) longitudinal and c), d), g), h) perpendicular direction of extrusion
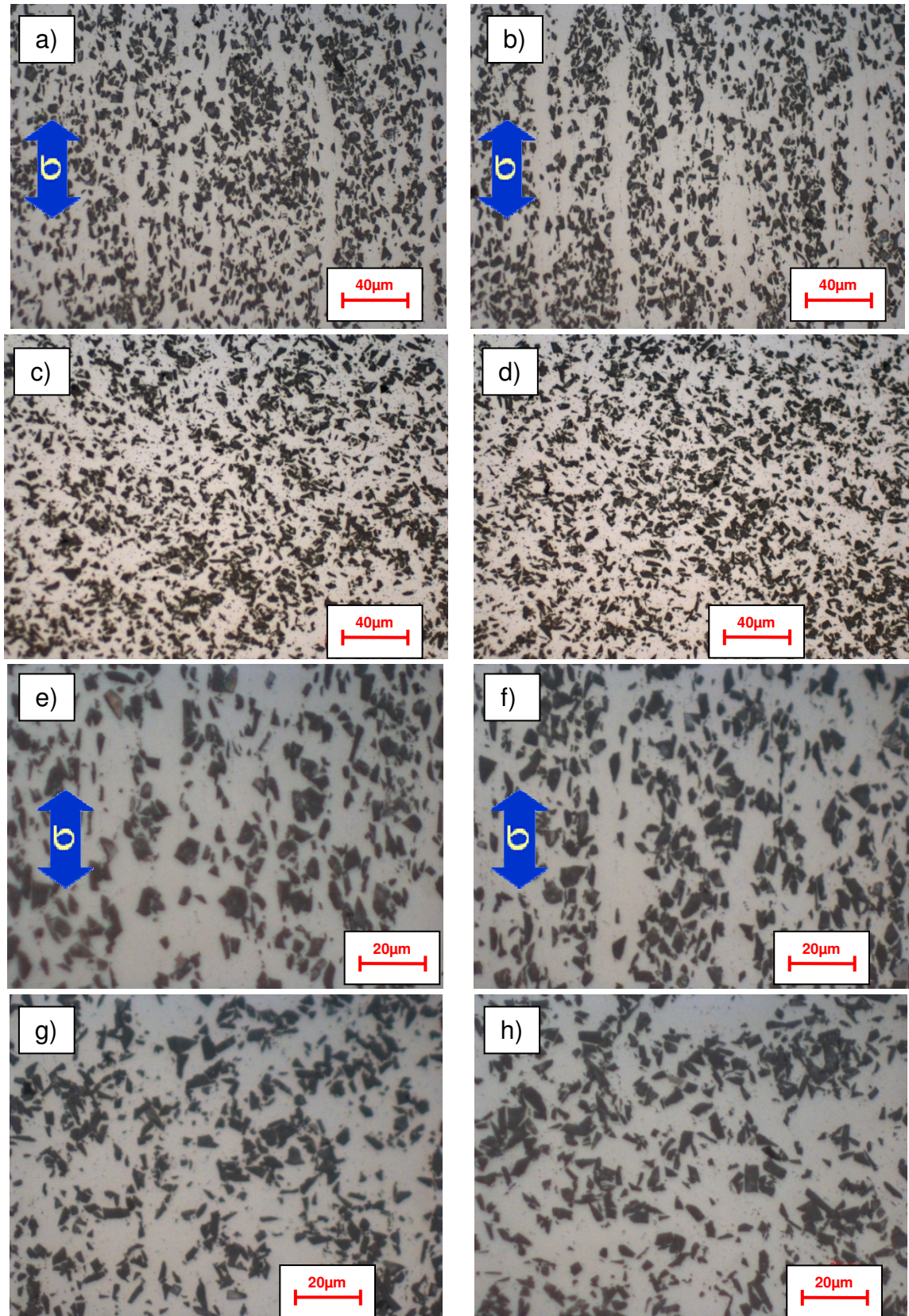
**Figure 9.4** LOM Micrographs of WB 2124/SiC/25p<5µm in a), b), e), f) longitudinal and c), d), g), h) perpendicular direction of extrusion
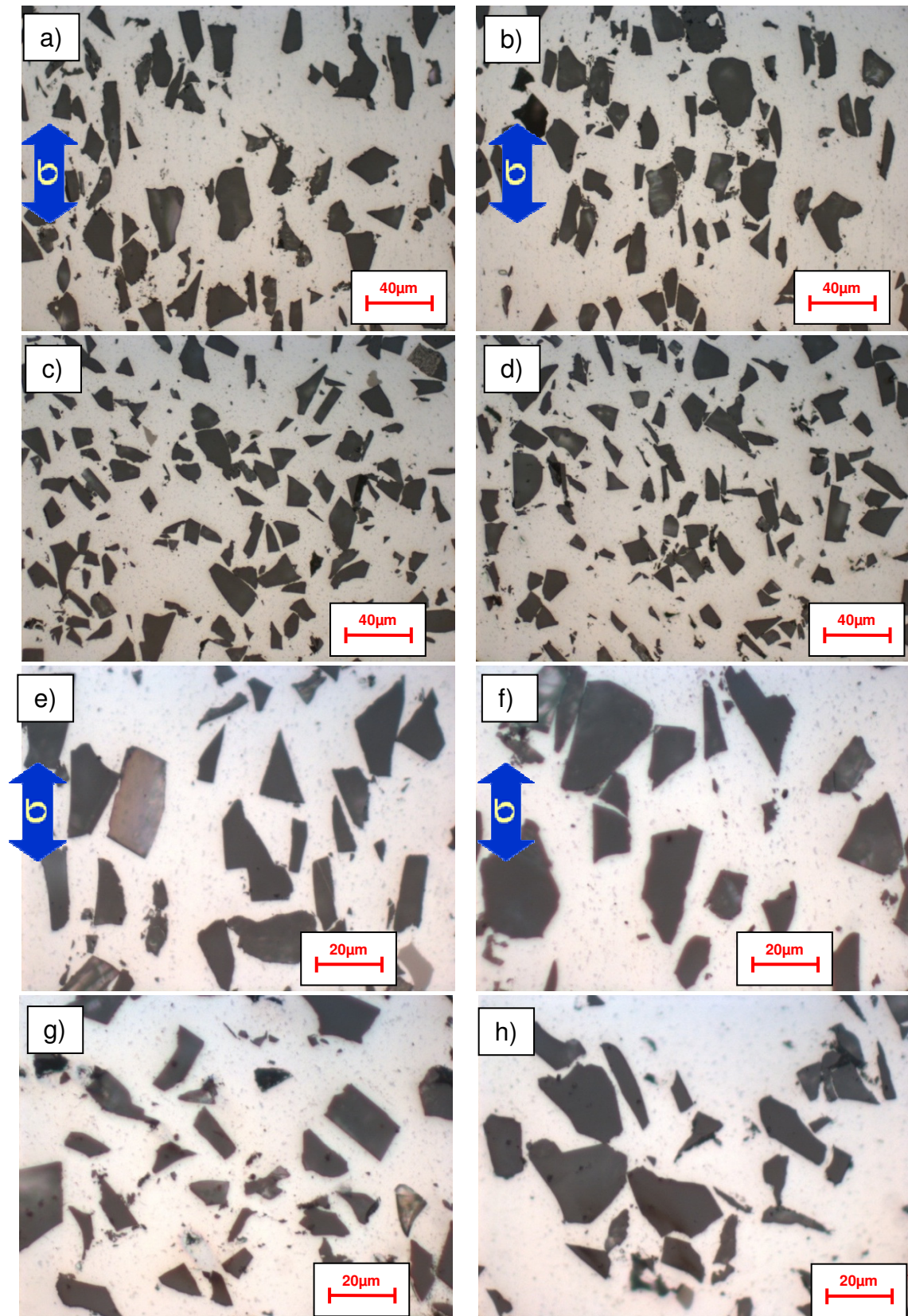
**Figure 9.5** LOM Micrographs of WB 2124/SiC/25p<20µm in a), b), e), f) longitudinal and c), d), g), h) perpendicular direction of extrusion
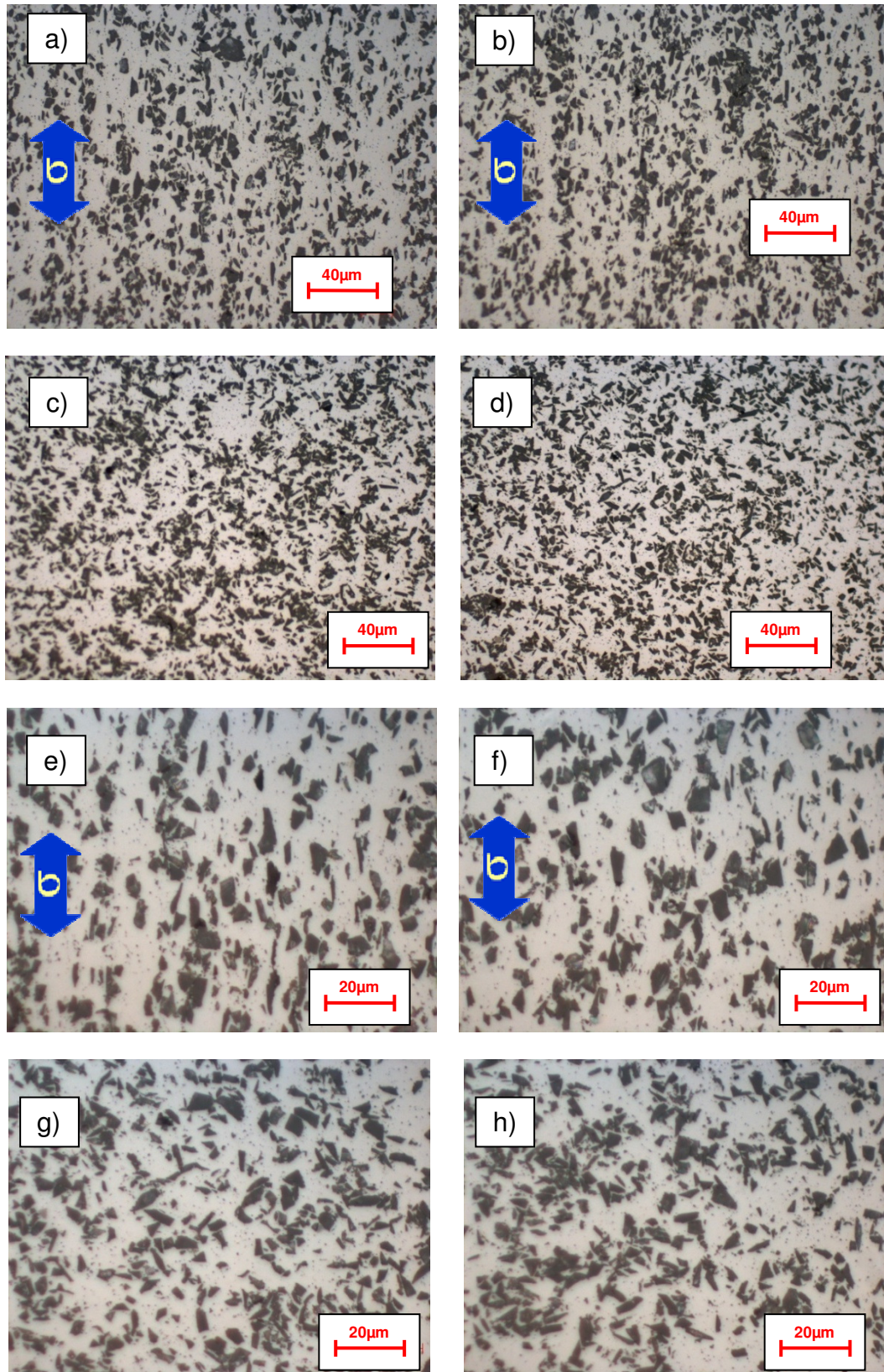
**Figure 9.6** LOM Micrographs of WB 6061/SiC/25p<5μm in a), b), e), f) longitudinal and c), d), g), h) perpendicular direction of extrusion
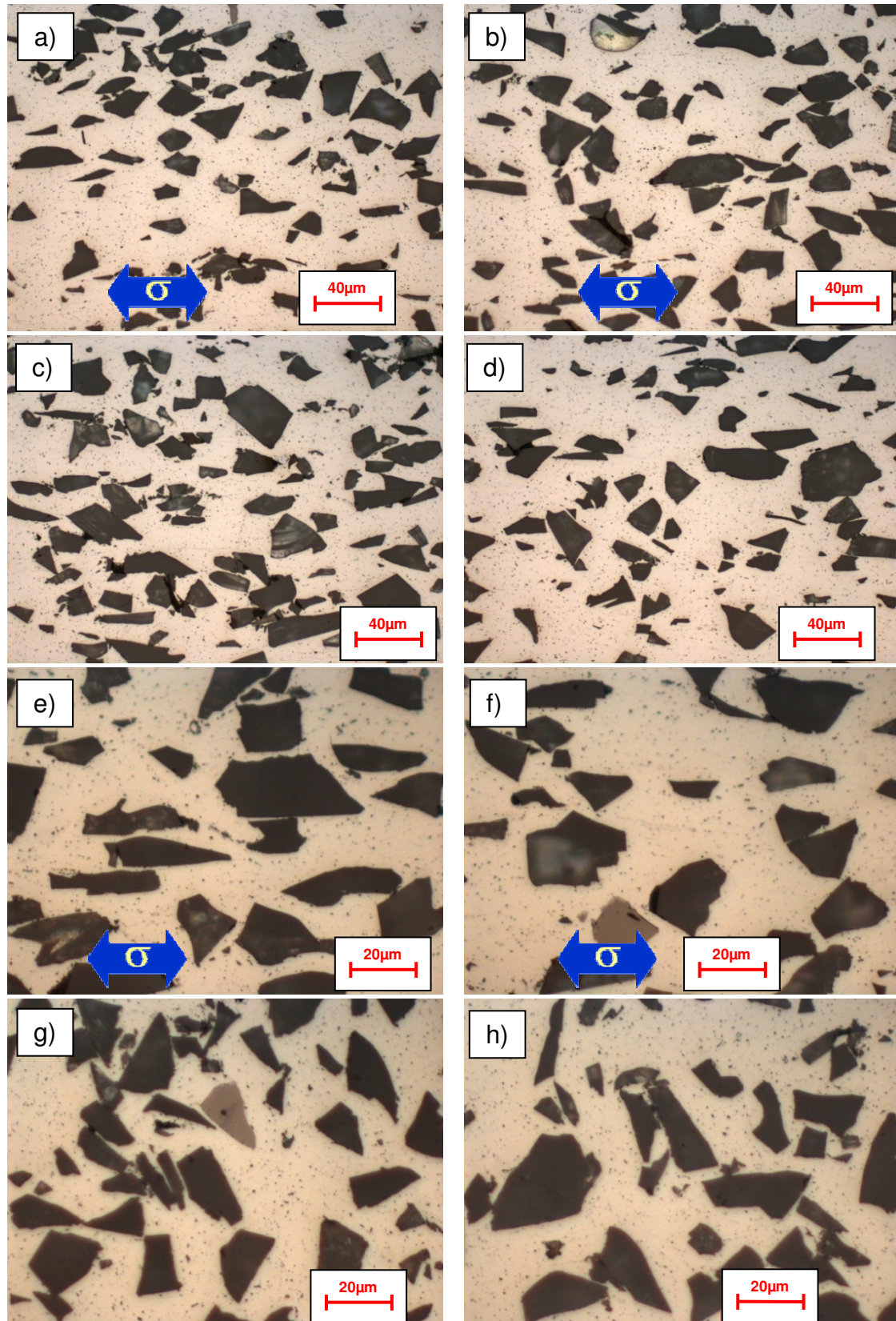
**Figure 9.7** LOM Micrographs of WB 6061/SiC/25p<20μm in a), b), e), f) longitudinal and c), d), g), h) perpendicular direction of extrusion
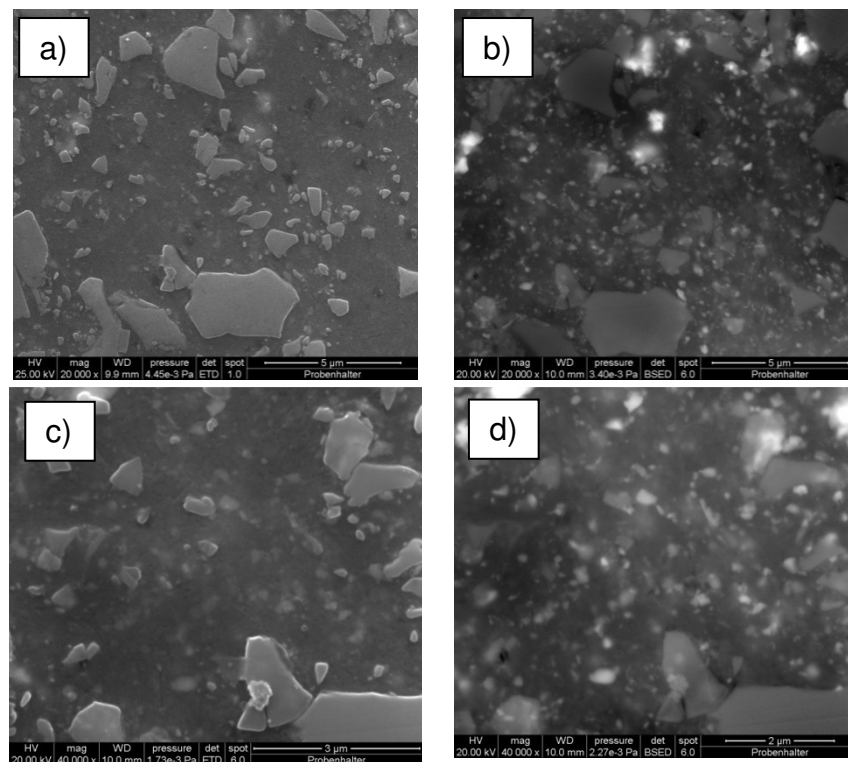
**Figure 9.8** FEG-SEM images of BM 2124/SiC/25p<5µm a), c) SE and b), d) BSE in perpendicular direction to extrusion
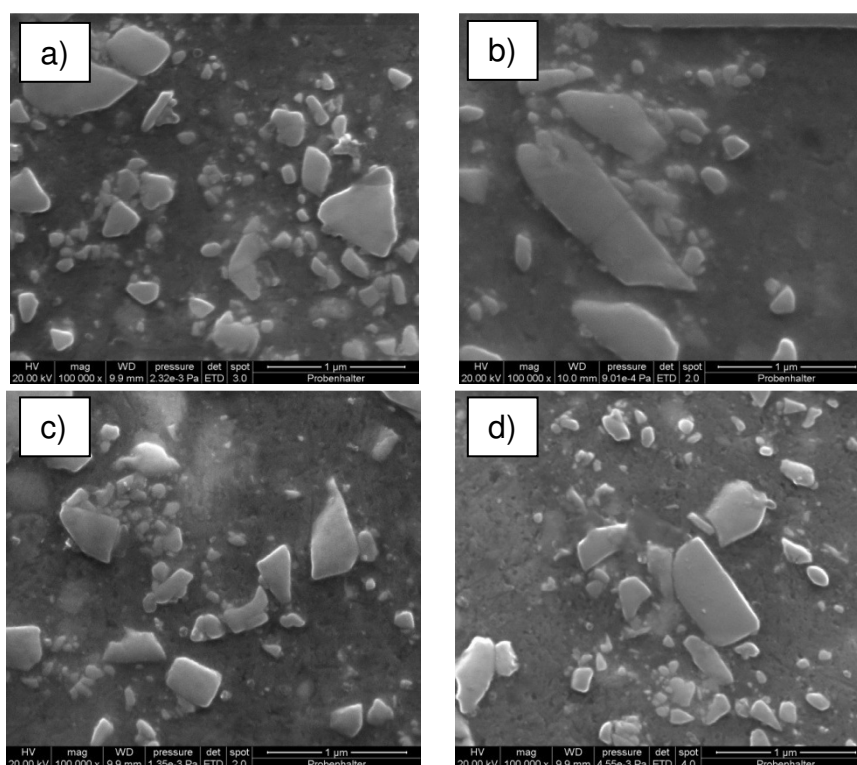


**Figure 9.9** FEG-SEM SE images of BM 2124/SiC/25p<5µm in perpendicular direction to extrusion
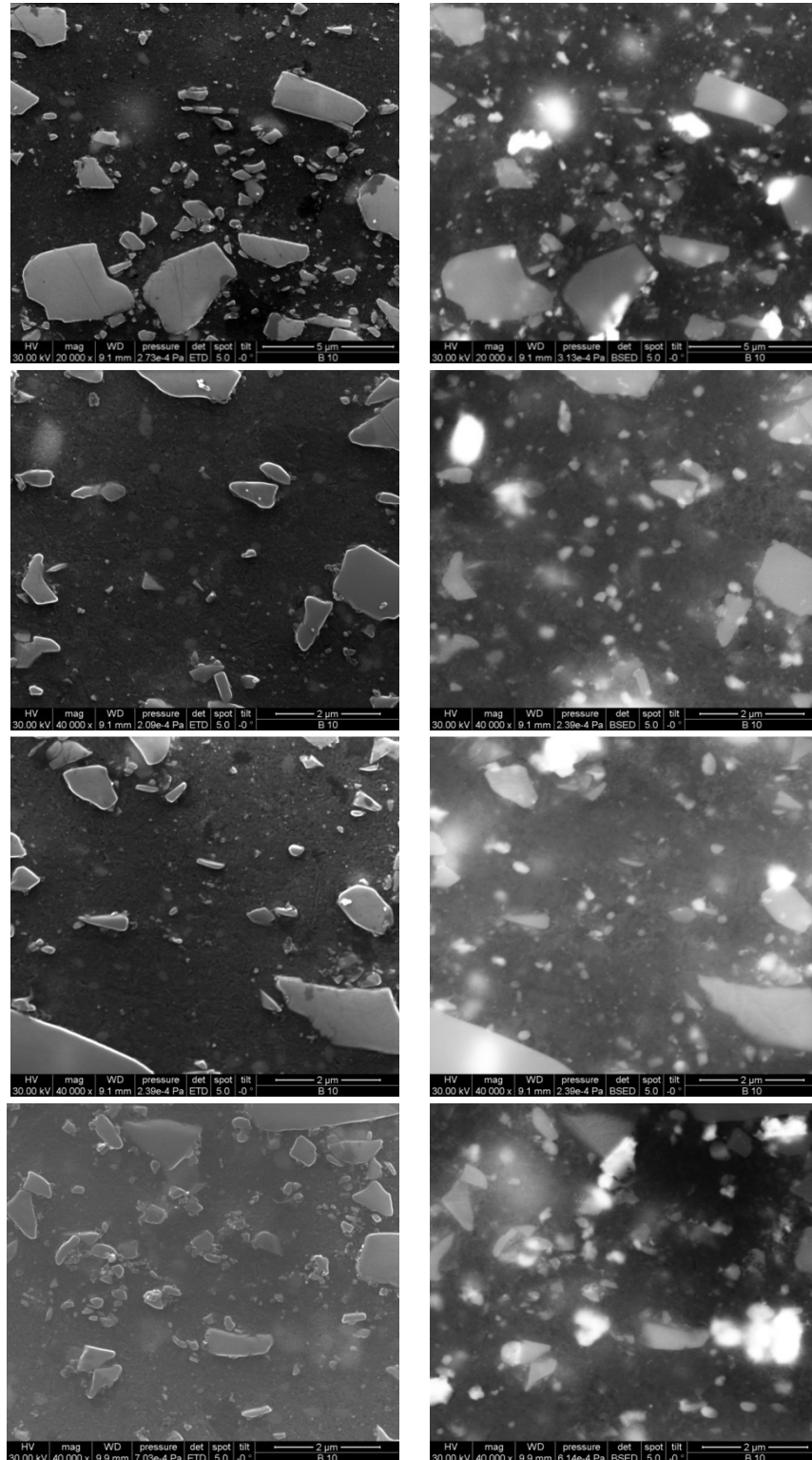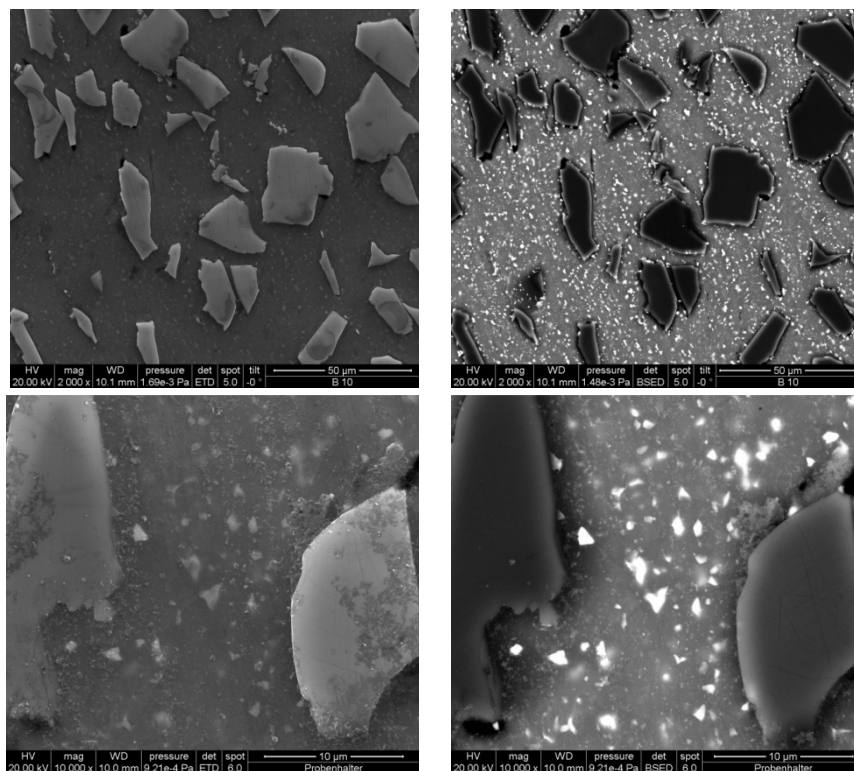
**Figure 9.10** FEG-SEM images of WB 2124/SiC/25p<20µm left column SE and right column BSE in perpendicular direction to extrusion
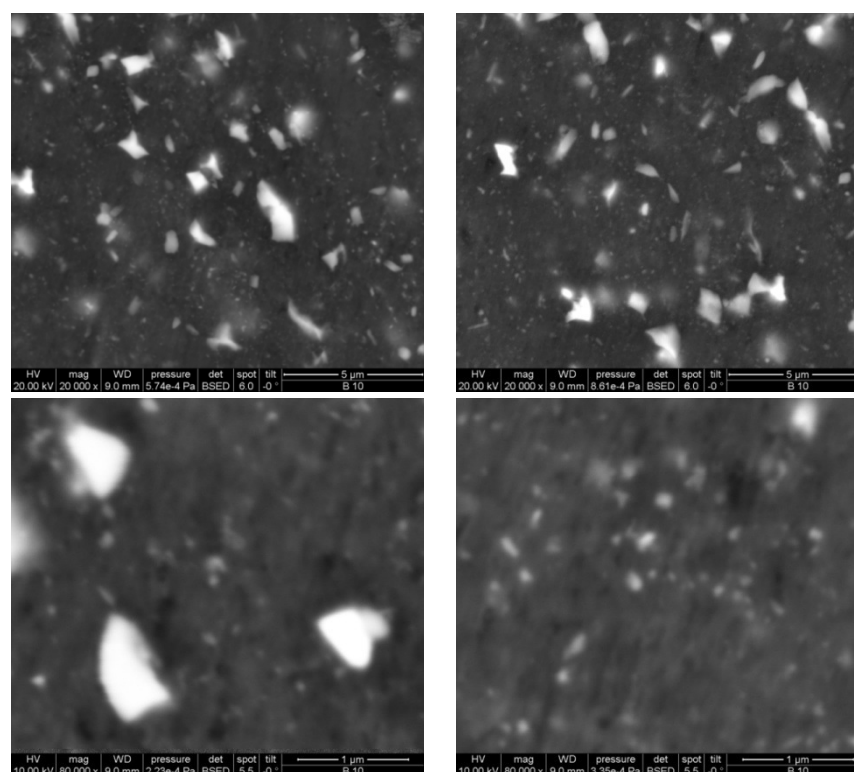


**Figure 9.11** FEG-SEM images of WB 2124/SiC/25p<20µm in perpendicular direction to extrusion

## 9.3 Creep curves

a)



b)



c)



d)



e)



f)

g)



h)
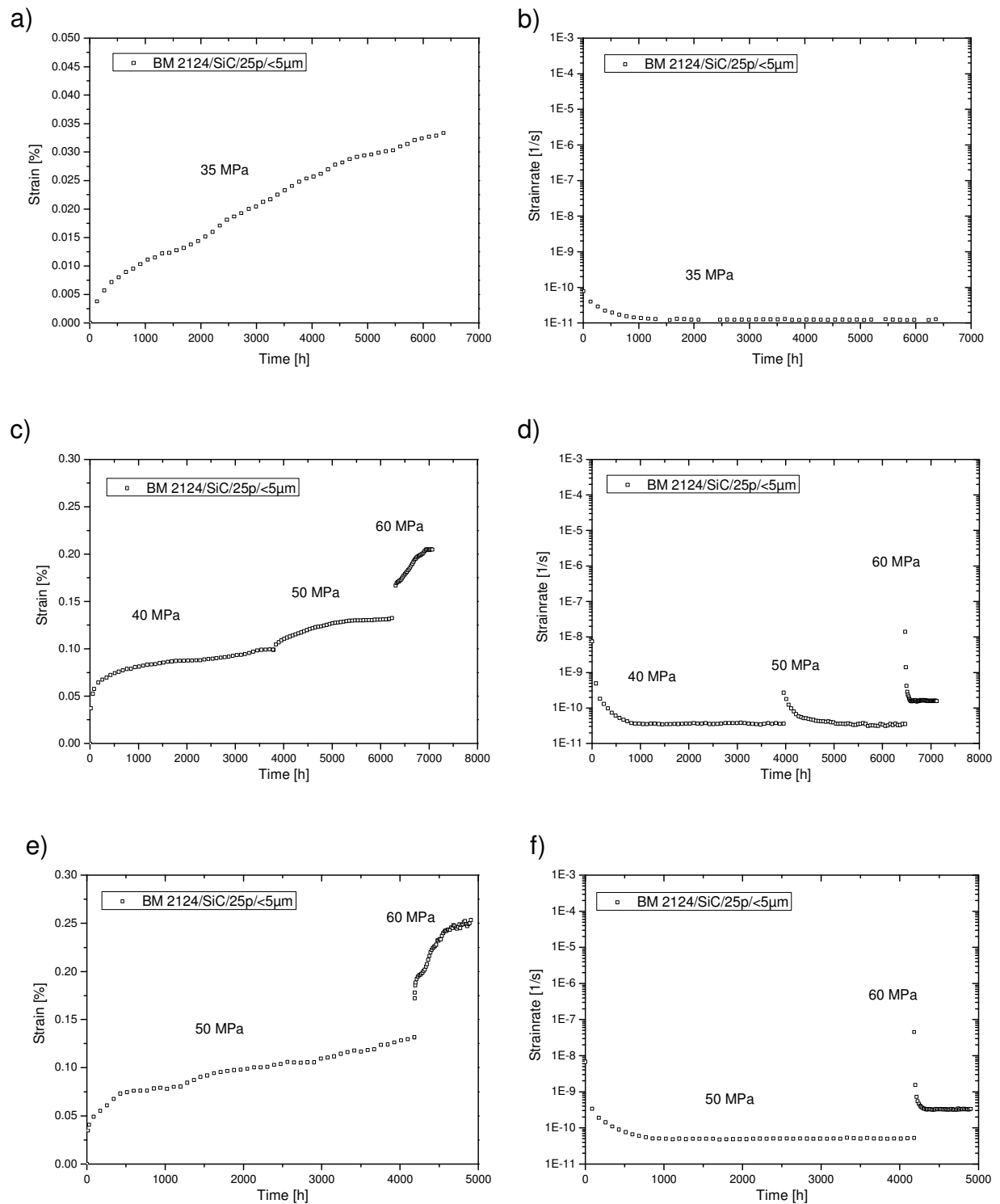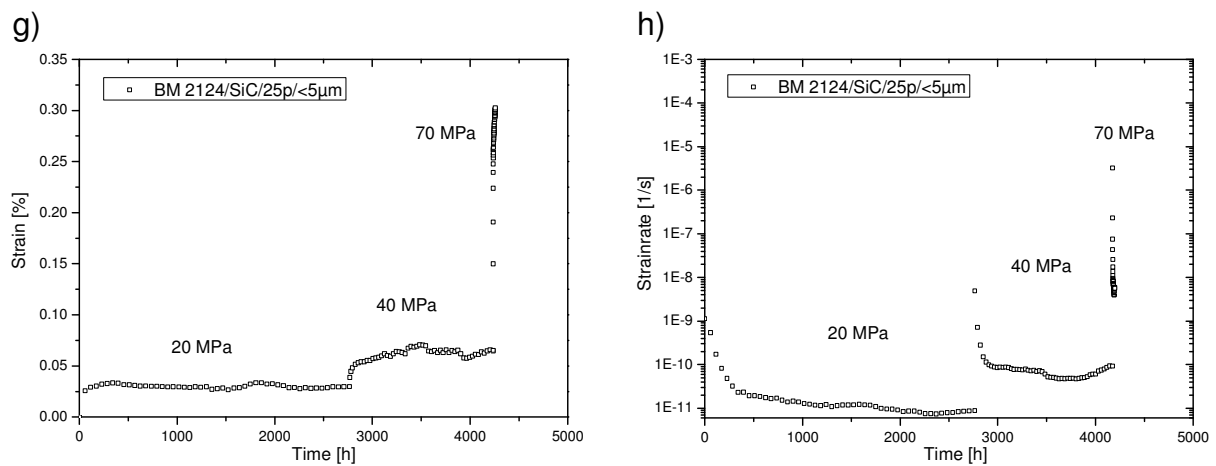


**Figure 9.12 a)-h)** Curves of $\varepsilon$ vs. t and $\dot{\varepsilon}$ vs. t of BM 2124/SiC/25p<5μm obtained during the creep tests

a)



b)



c)



d)

e)



f)



g)



h)
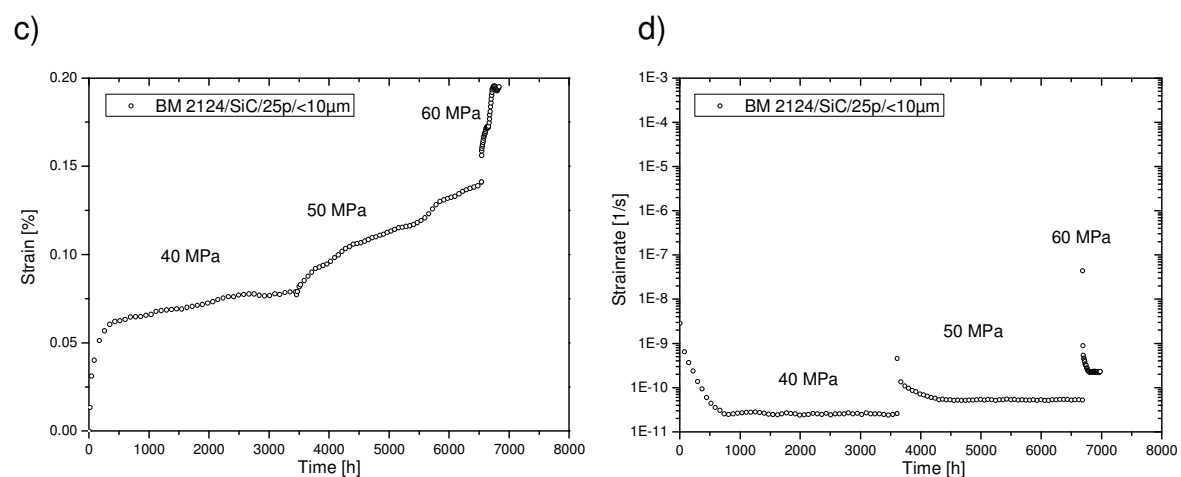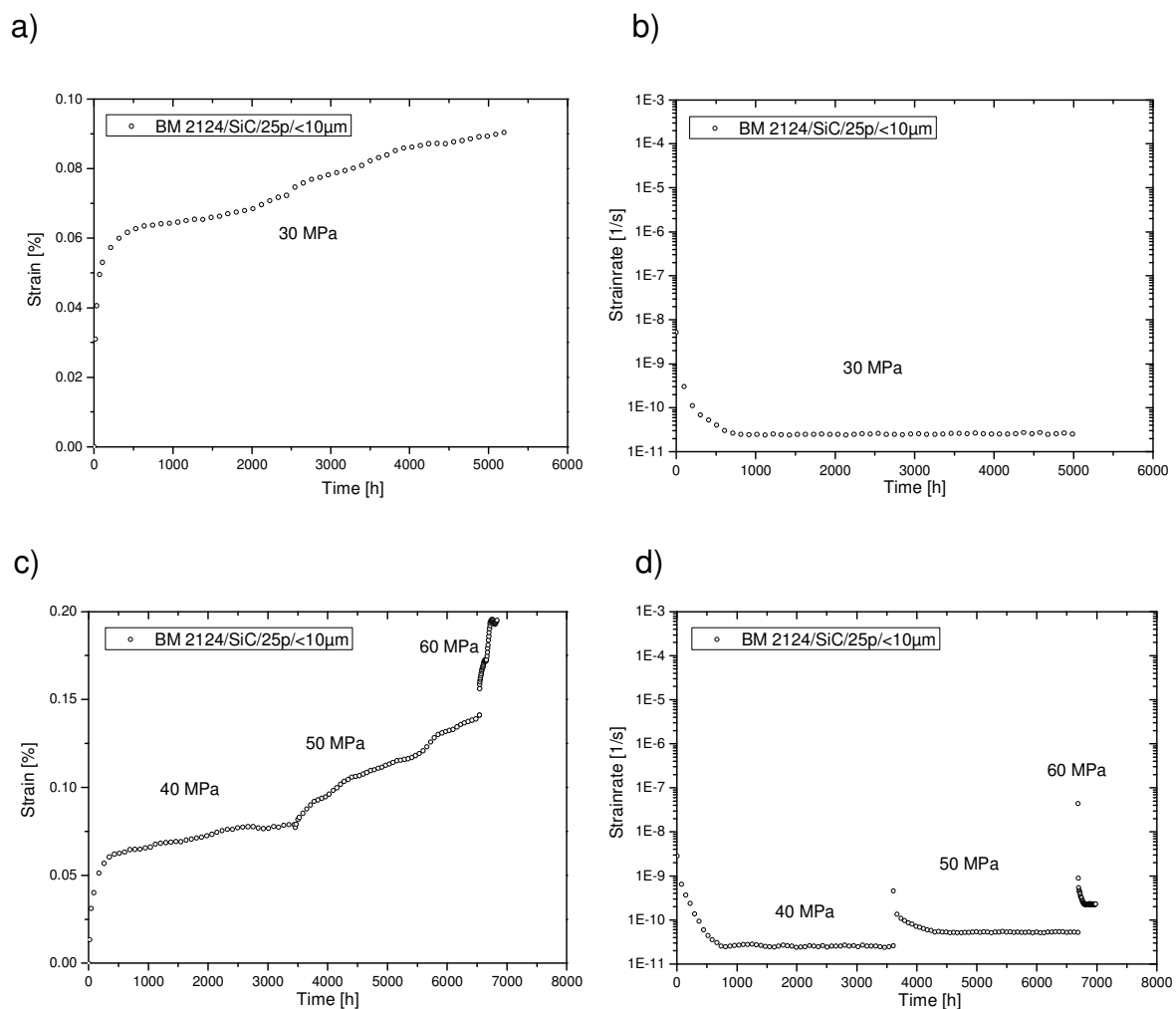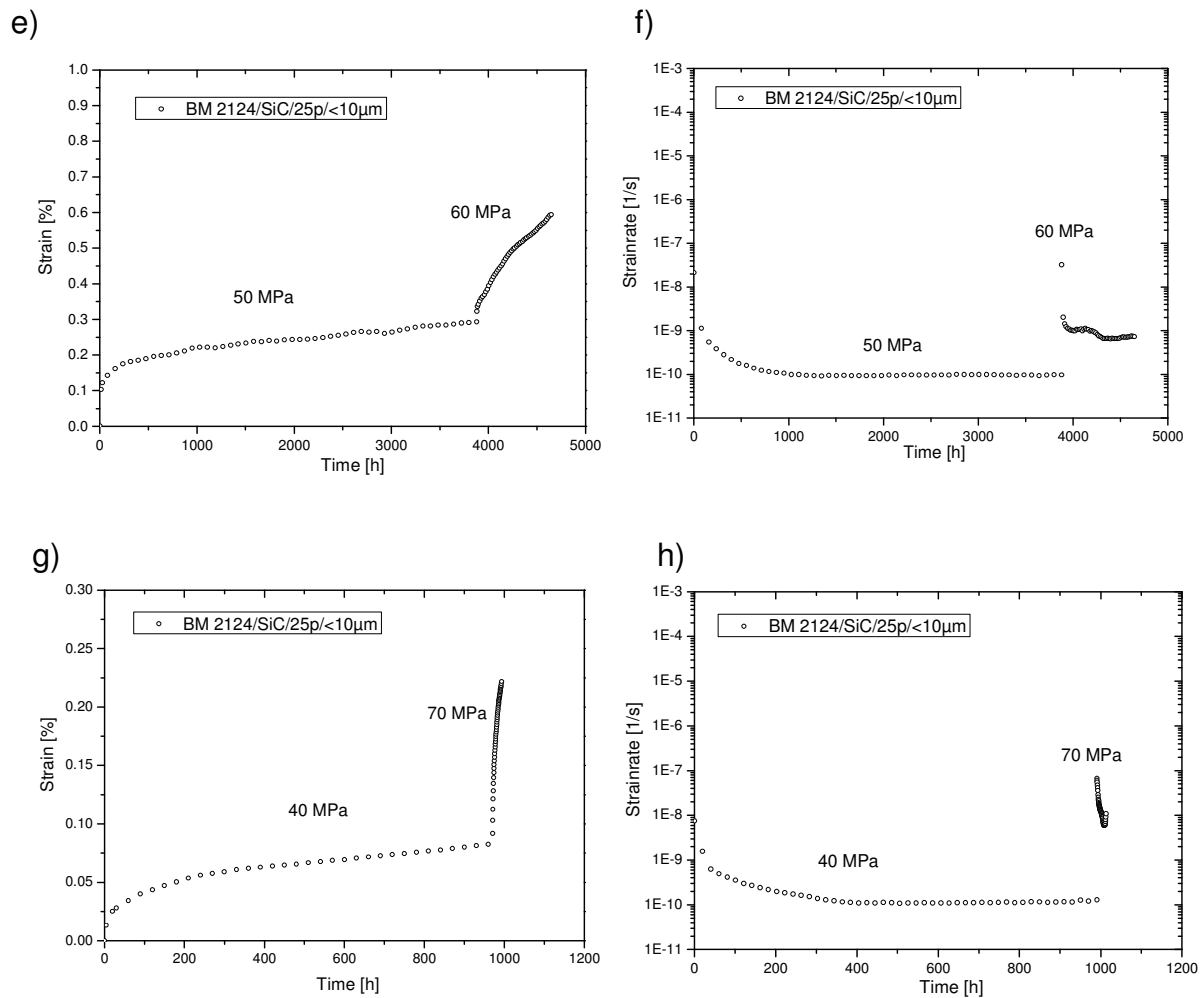


**Figure 9.13 a)-h)** Curves of $\varepsilon$ vs. t and $\dot{\varepsilon}$ vs. t of BM 2124/SiC/25p<10µm obtained during the creep tests

a)



b)

c)



d)



e)



f)



g)



h)
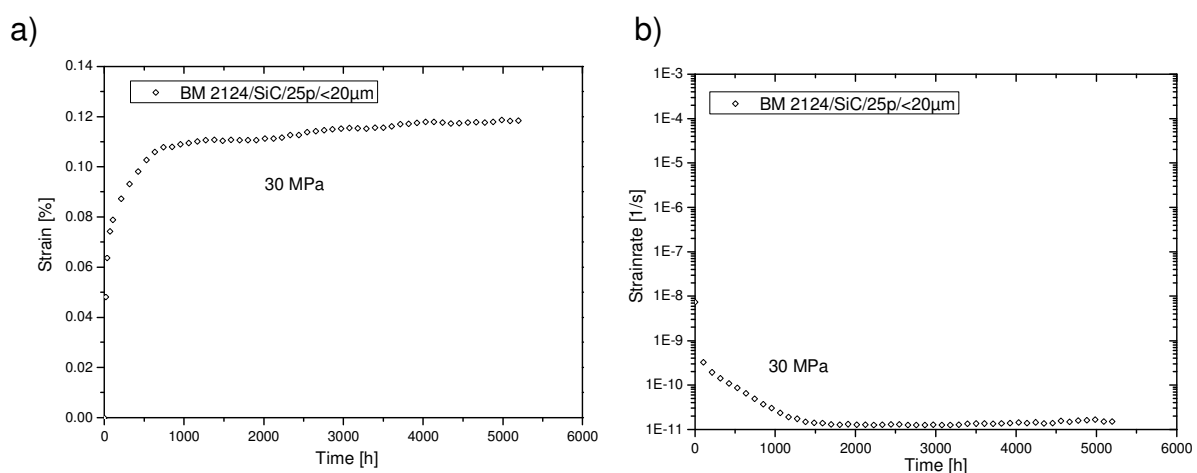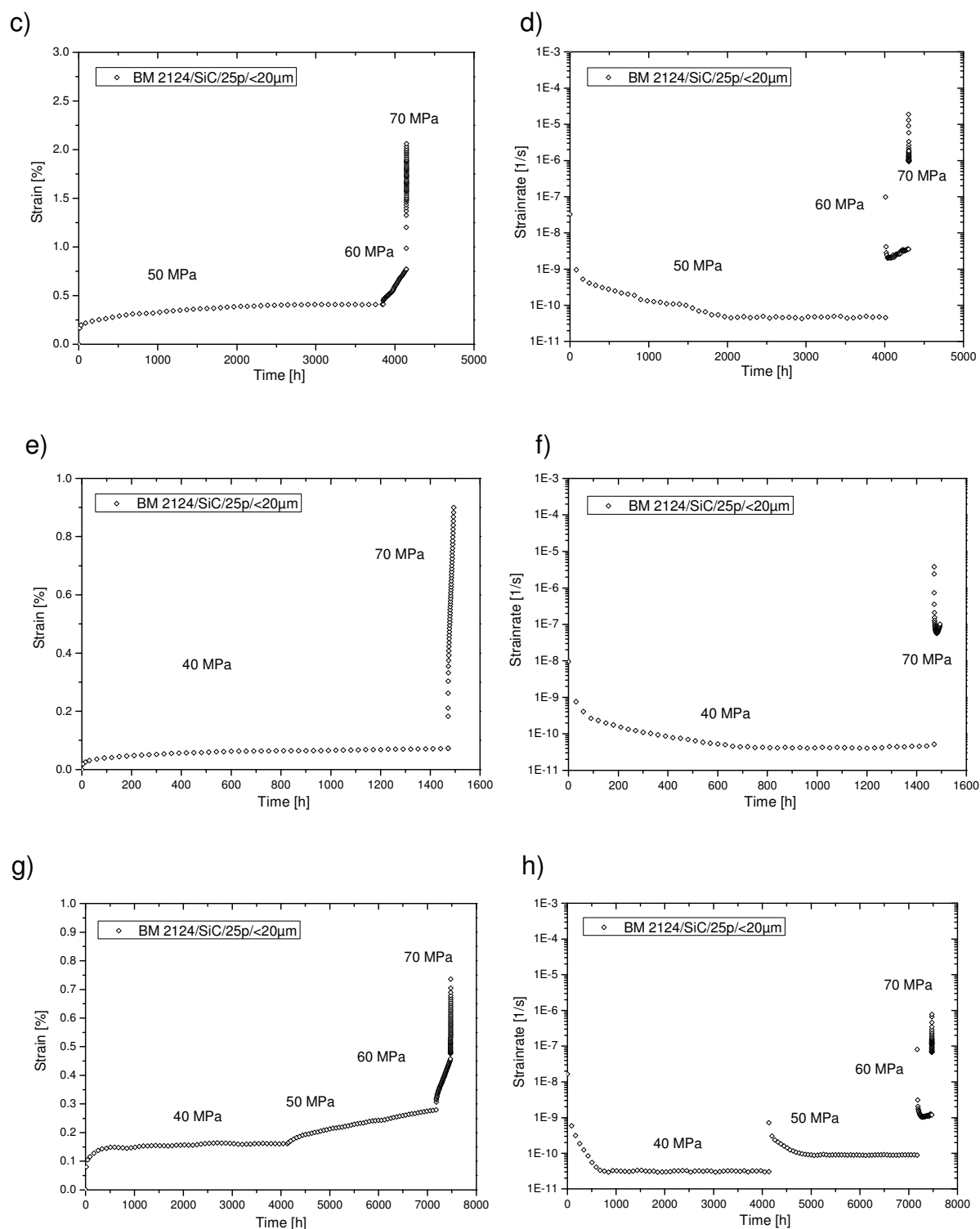


**Figure 9.14 a)-h)** Curves of $\varepsilon$ vs. t and $\dot{\varepsilon}$ vs. t of BM 2124/SiC/25p<20µm obtained during the creep tests
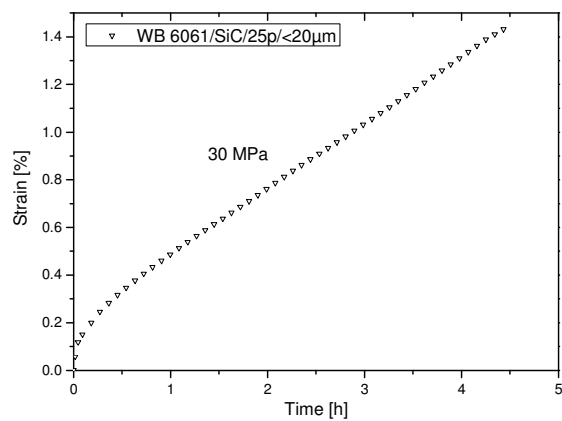
a)



b)



c)



d)



e)



f)

g)



h)



i)



j)



k)



l)

m)



n)



o)



p)



q)



r)

s)



t)



u)



v)



w)



x)

y)



z)
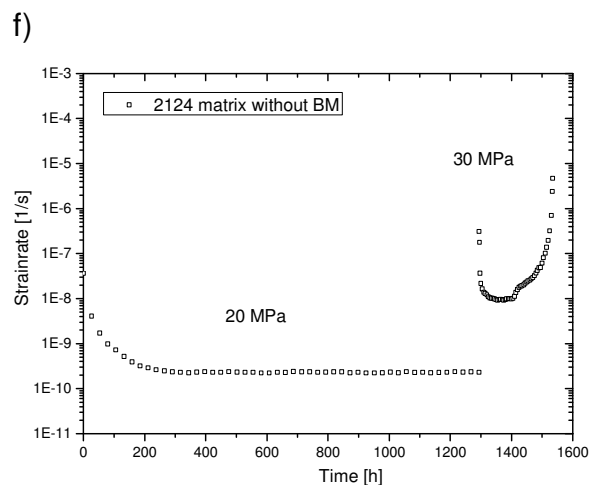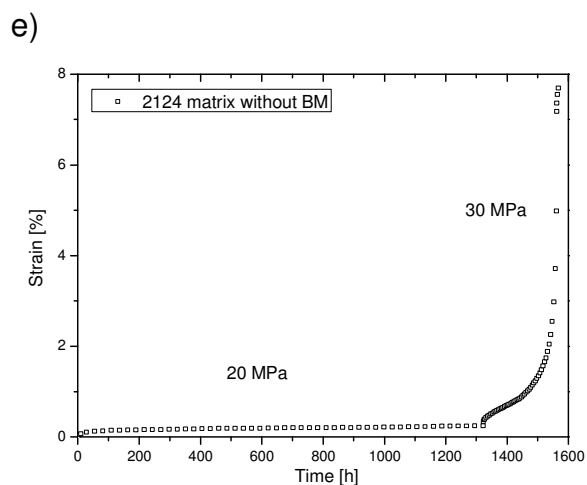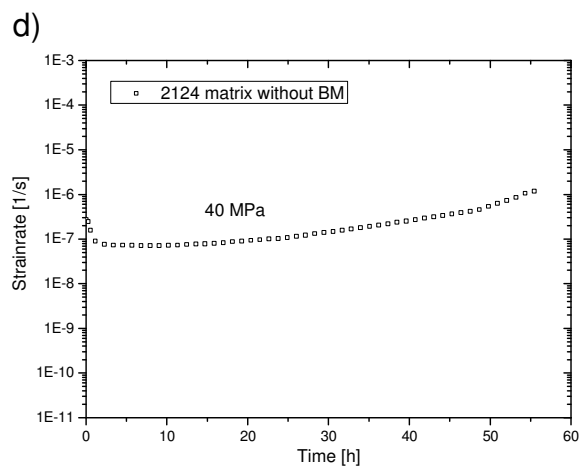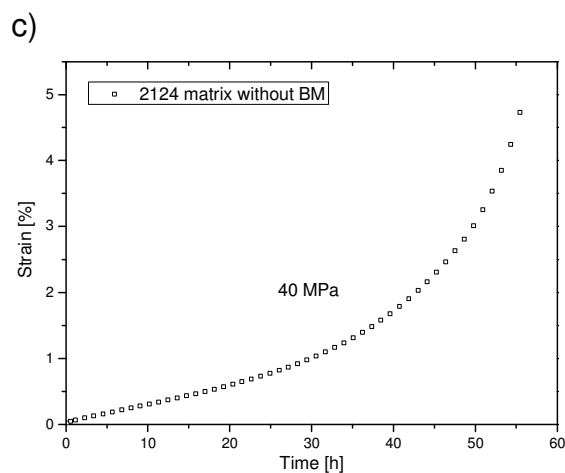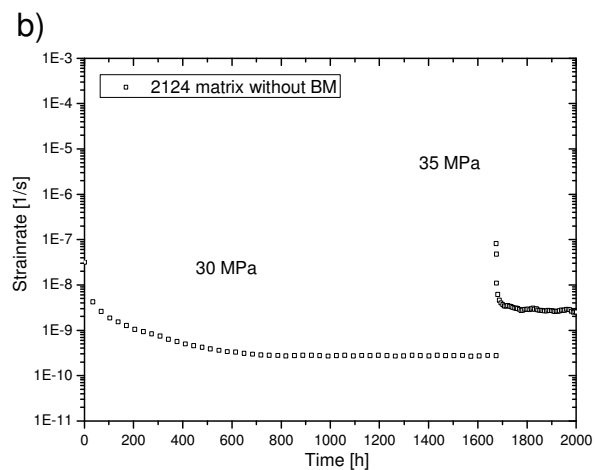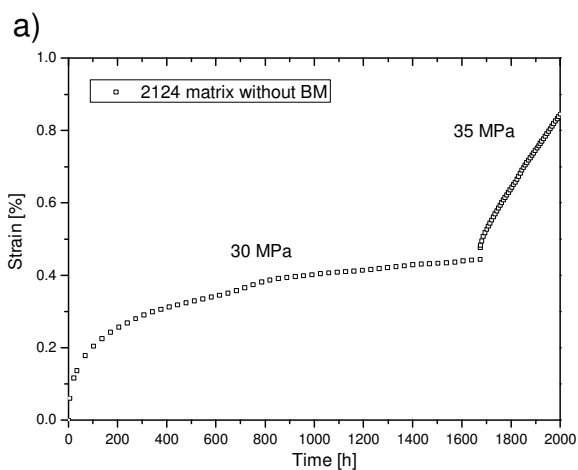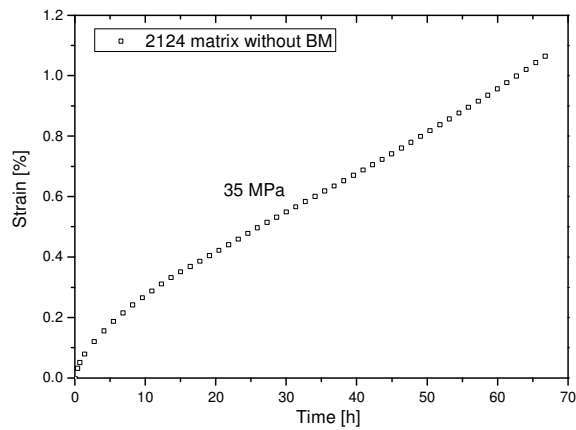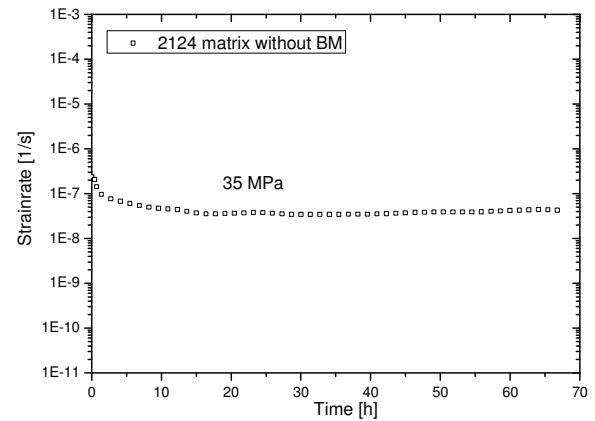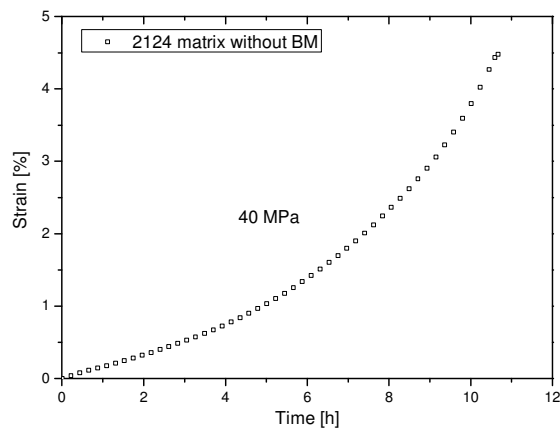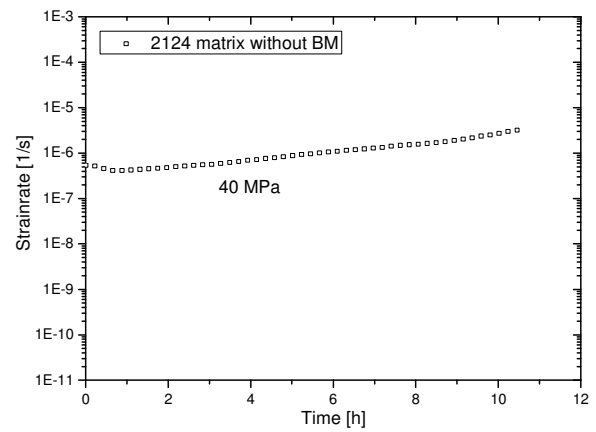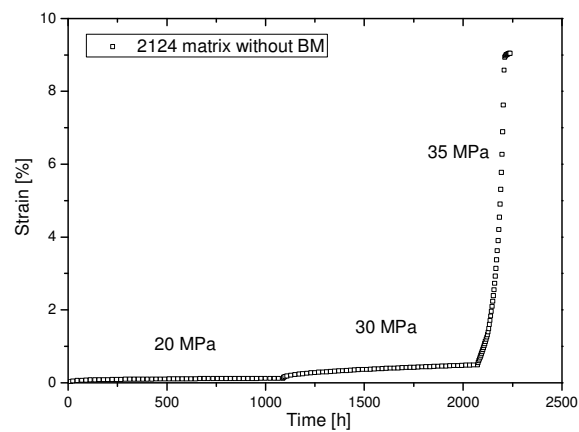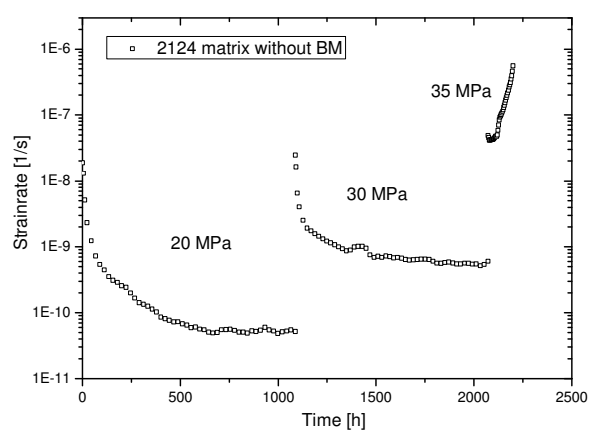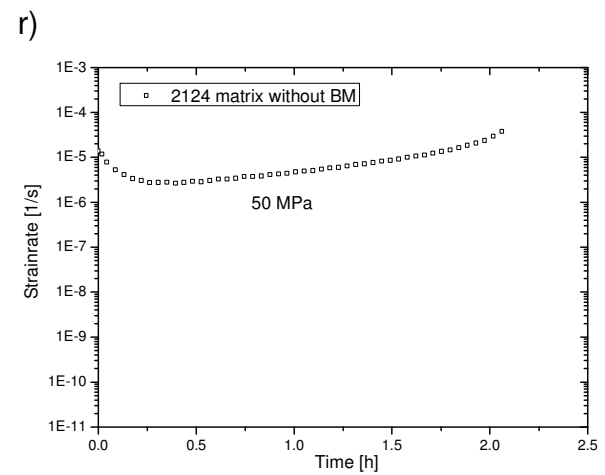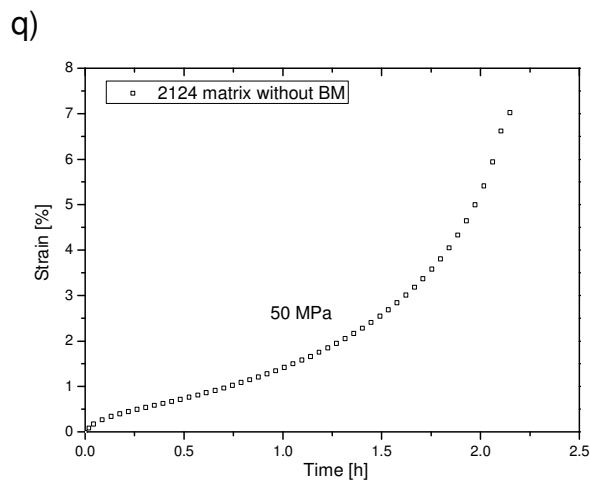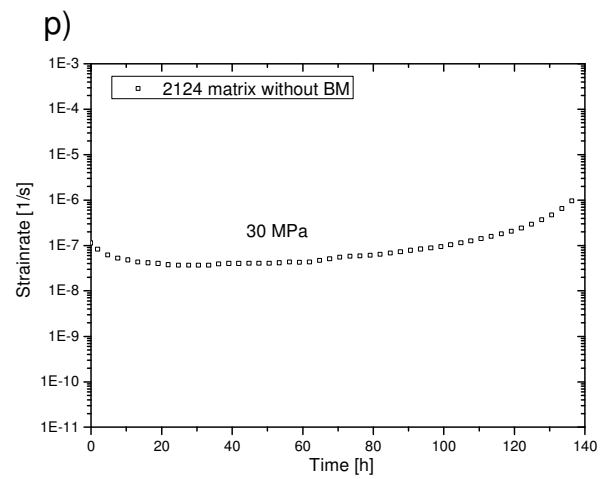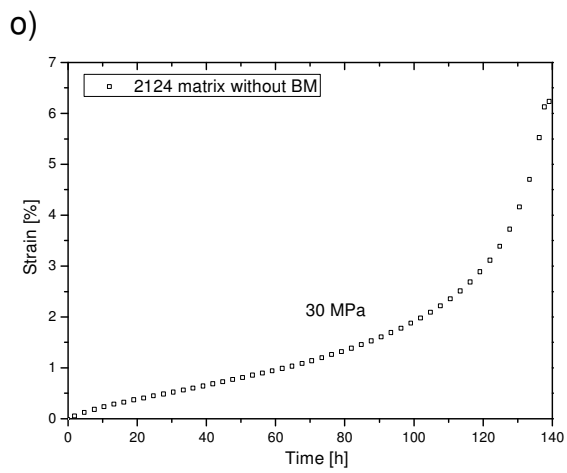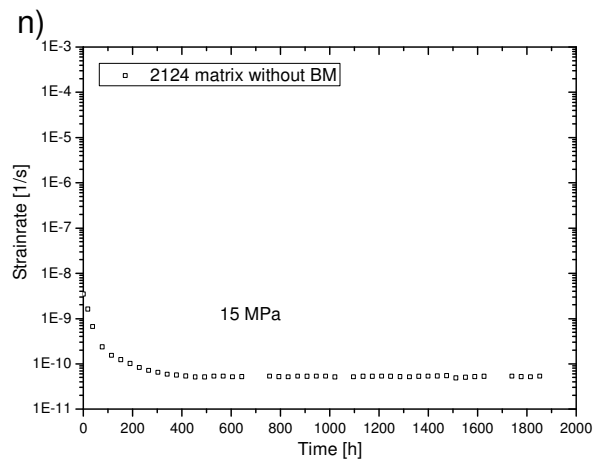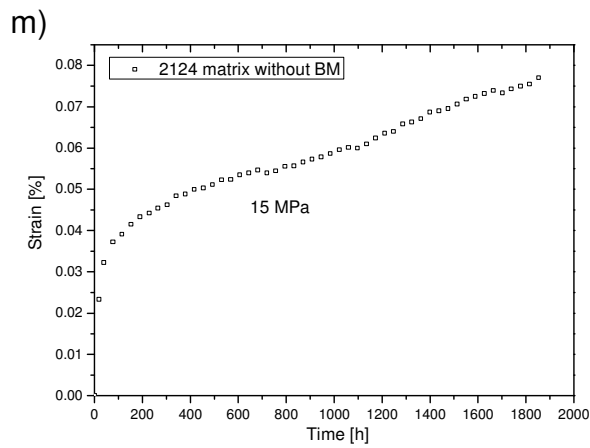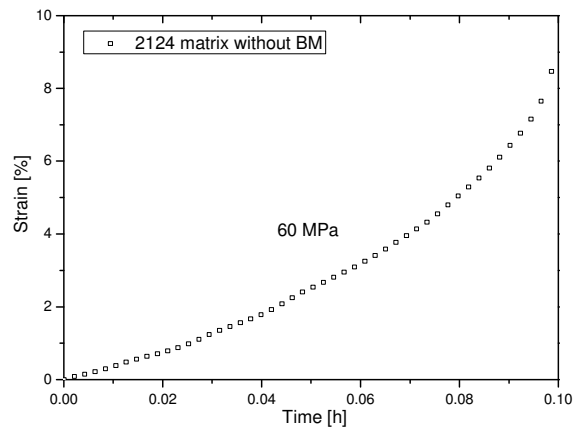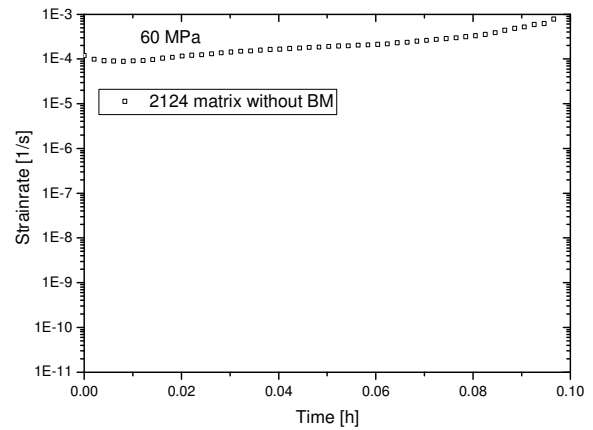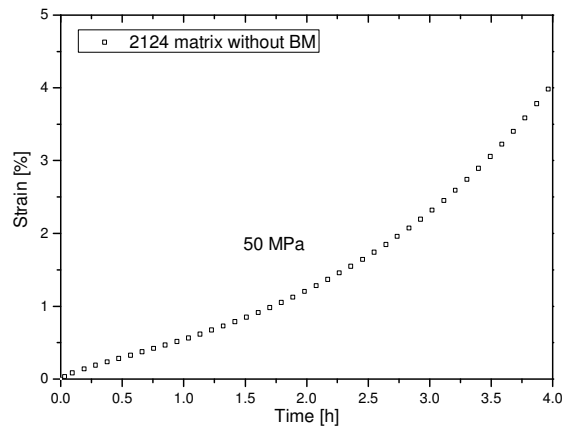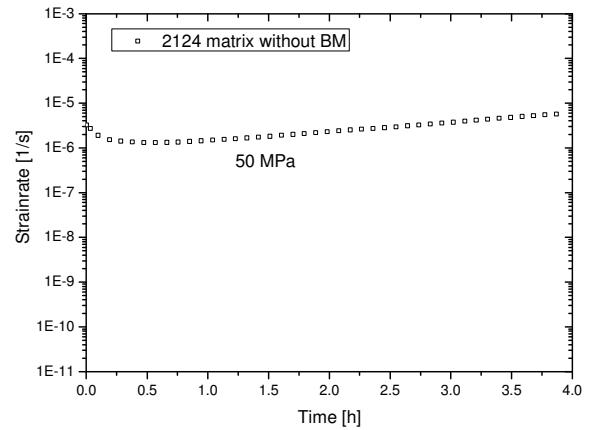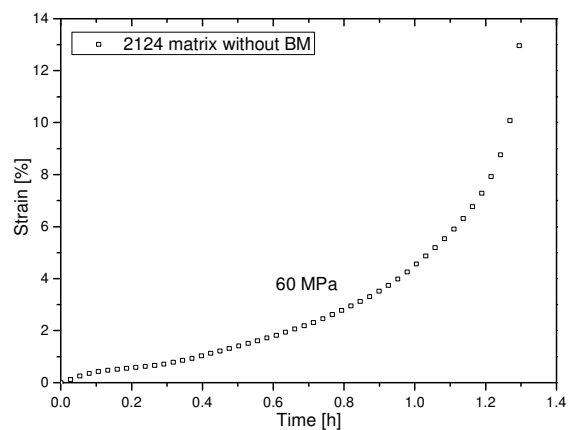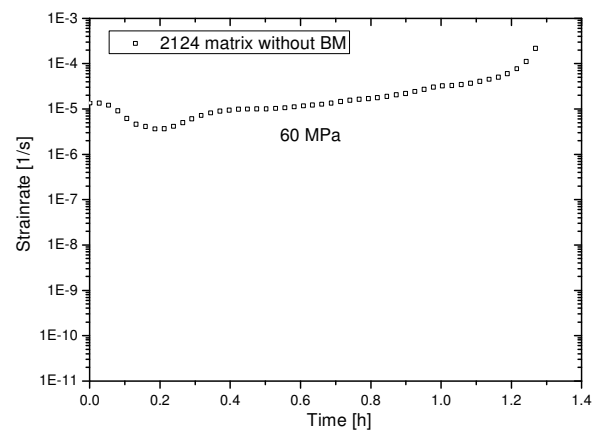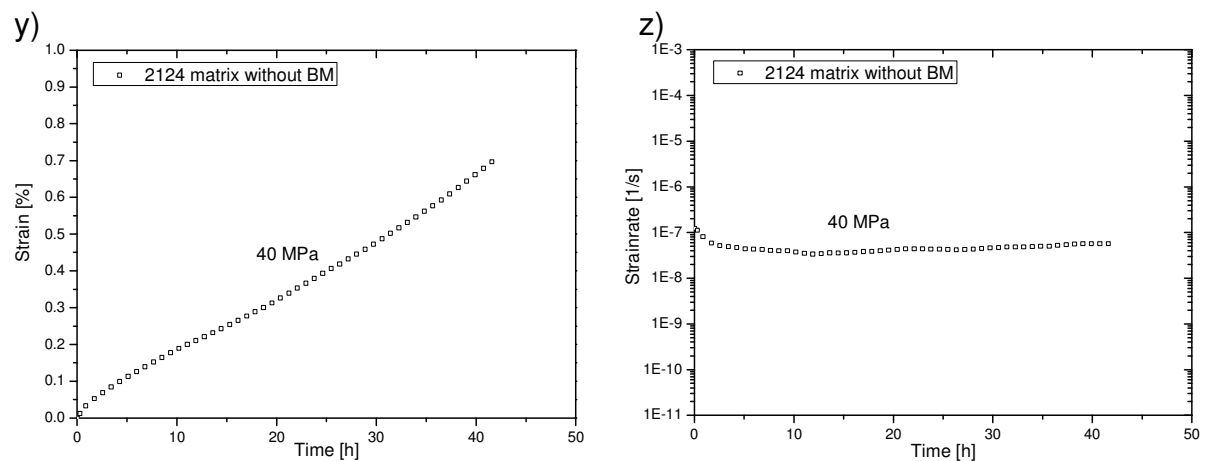


**Figure 9.15 a)-z)** Curves of $\varepsilon$ vs. t and $\dot{\varepsilon}$ vs. t of 2124 matrix without BM obtained during the creep tests

a)



b)



c)



d)

e)



f)



g)



h)



i)



j)

k)



l)



m)



n)



o)



p)

q)



r)



s)



t)
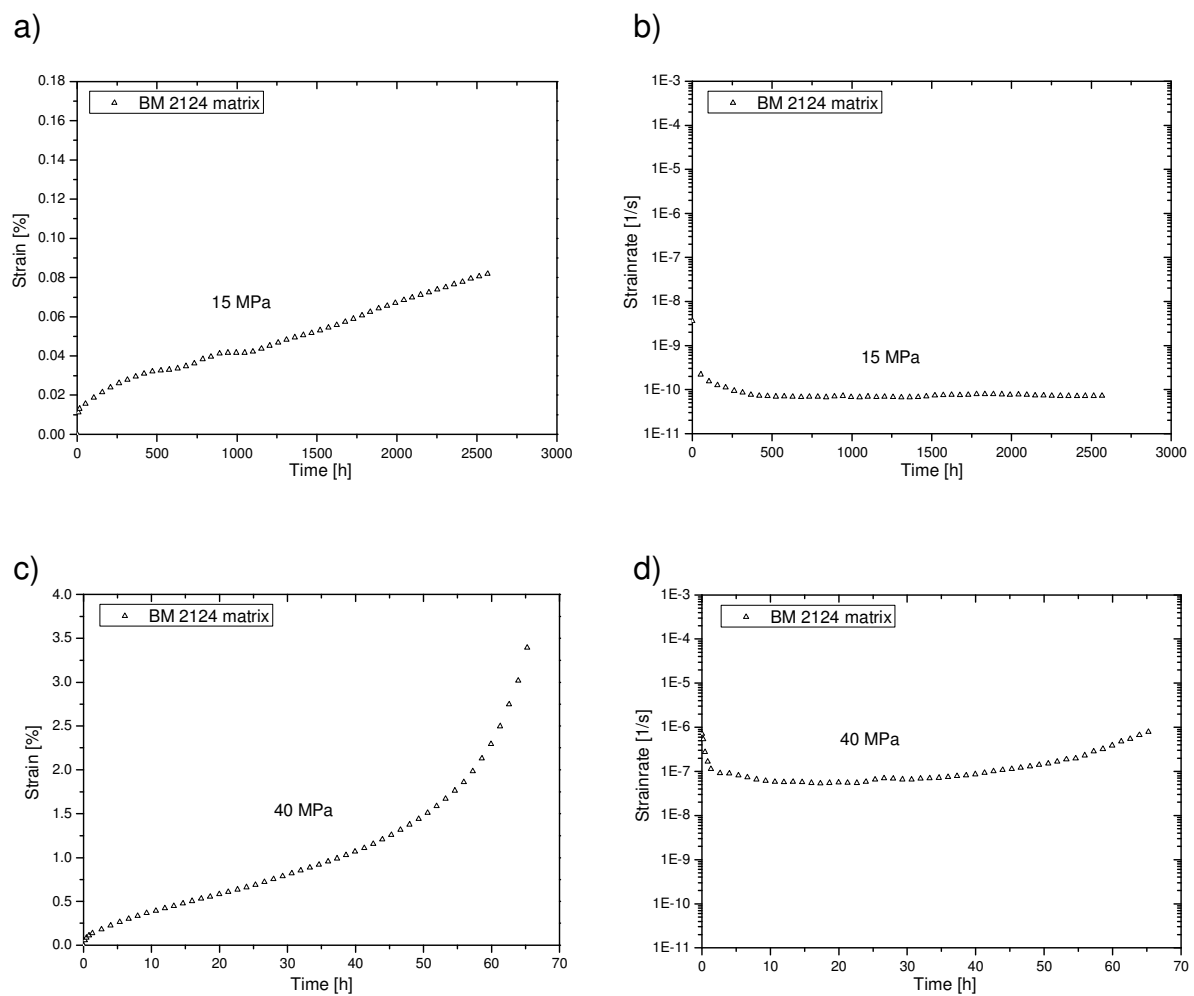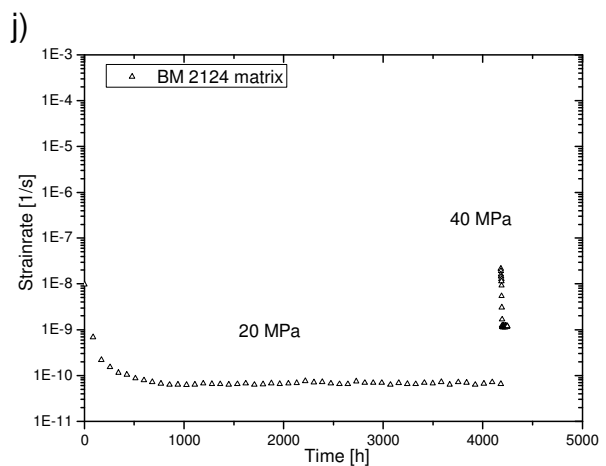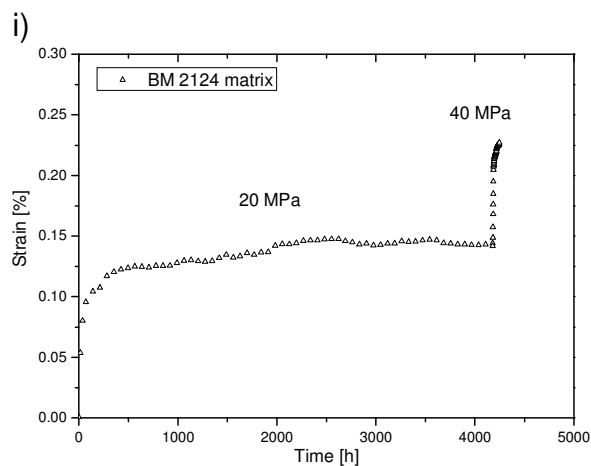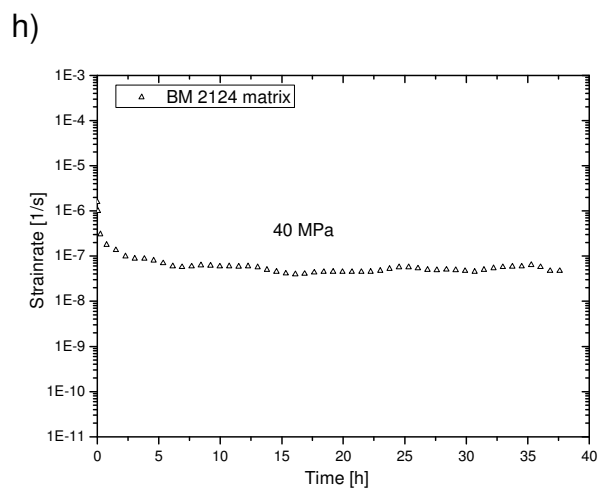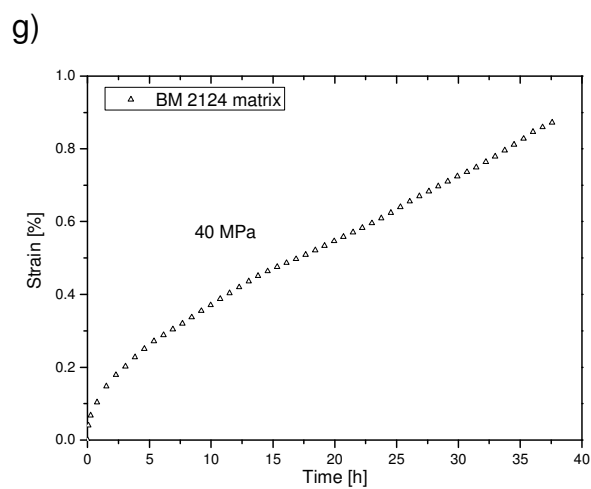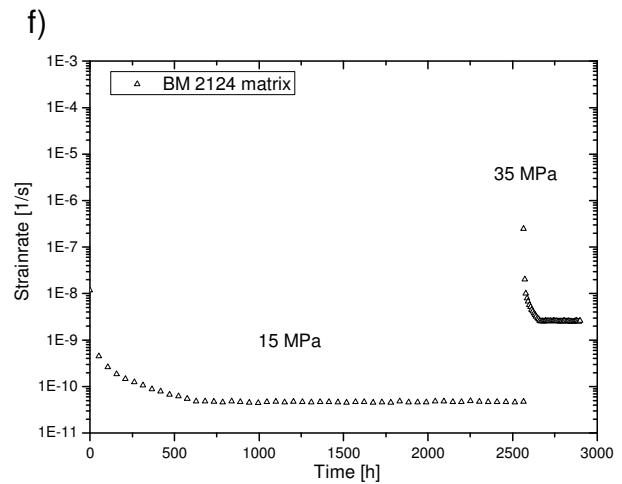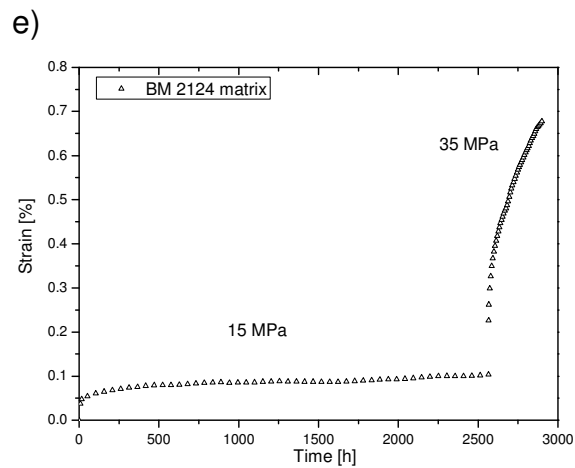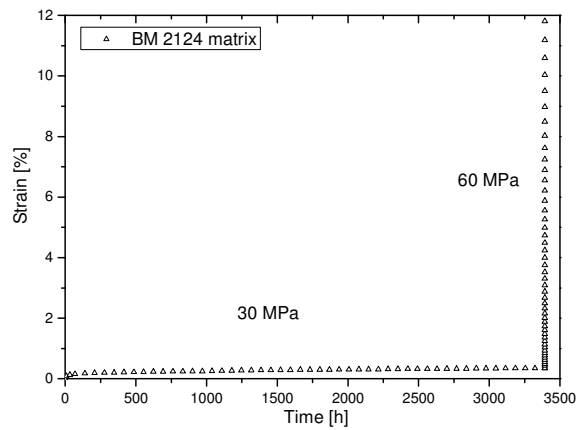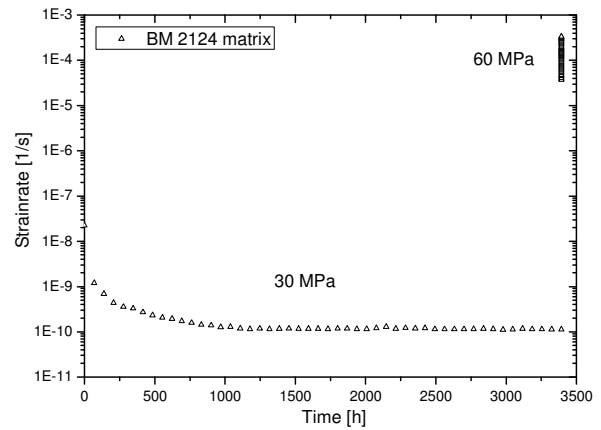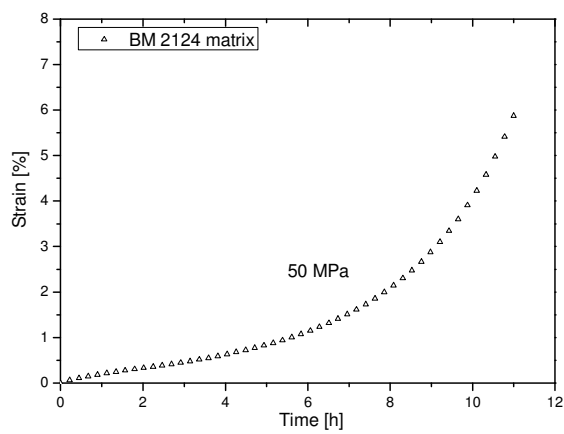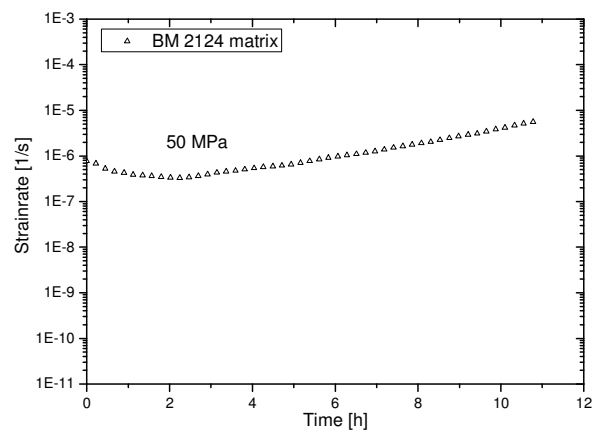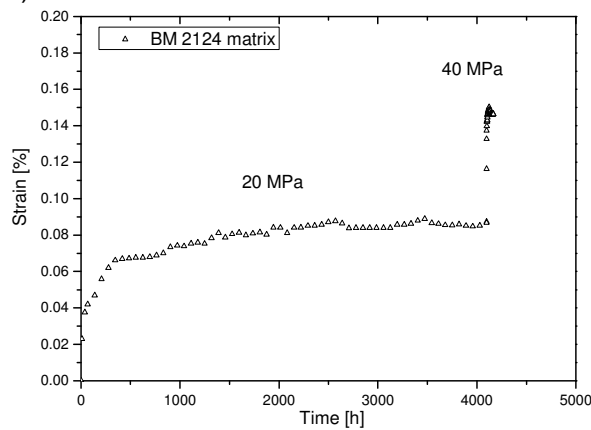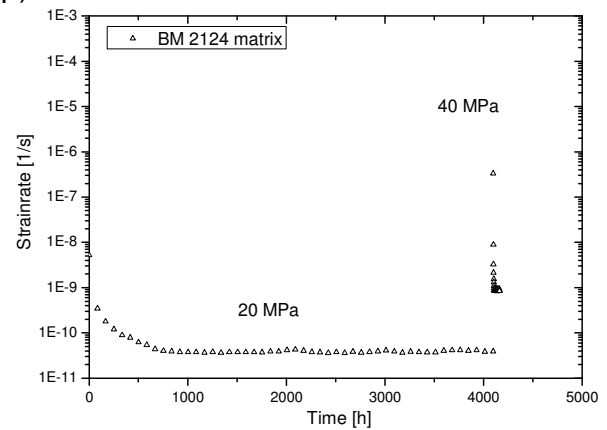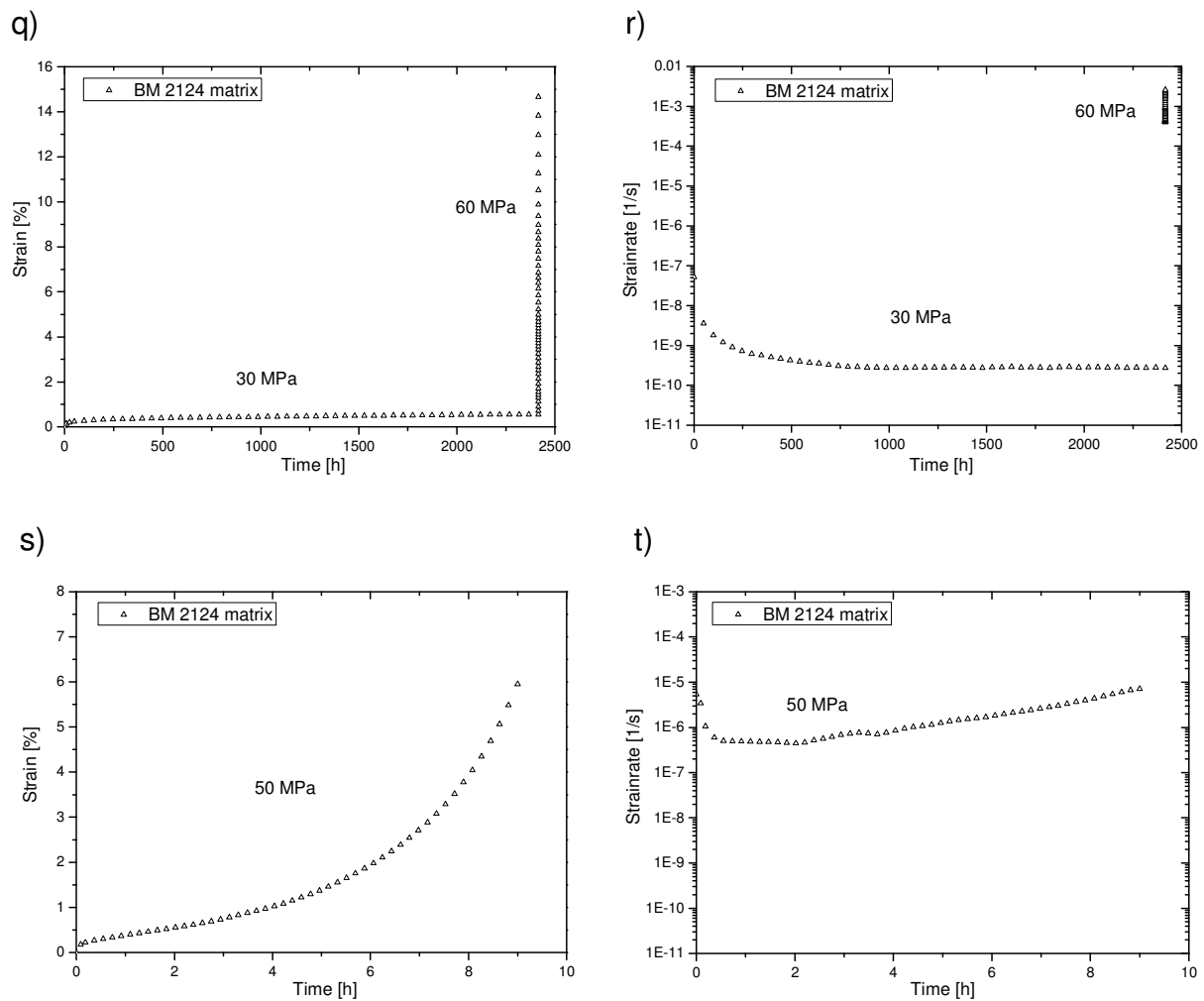


**Figure 9.16 a)-t)** Curves of $\varepsilon$ vs. t and $\dot{\varepsilon}$ vs. t of BM 2124 matrix obtained during the creep tests

a)



b)

c)



d)



e)



f)



g)



h)

i)



j)



k)



l)



m)



n)

o)



p)
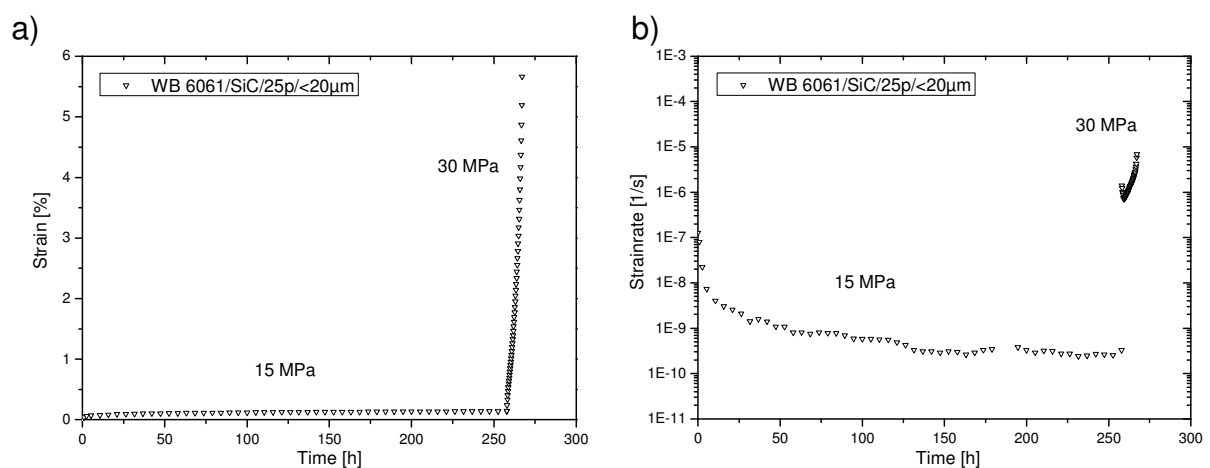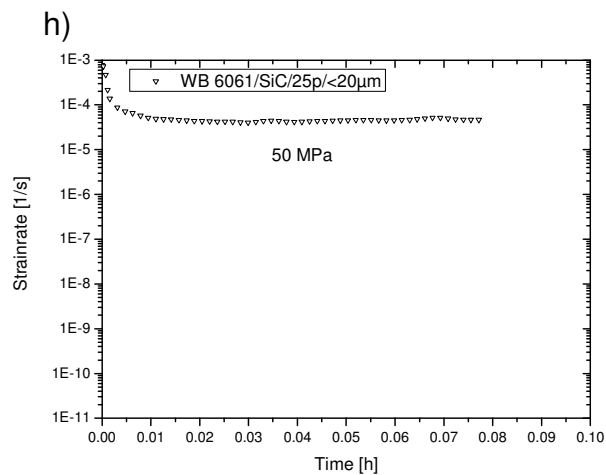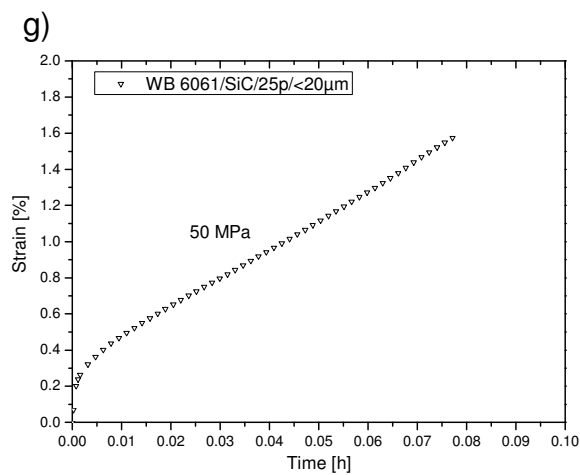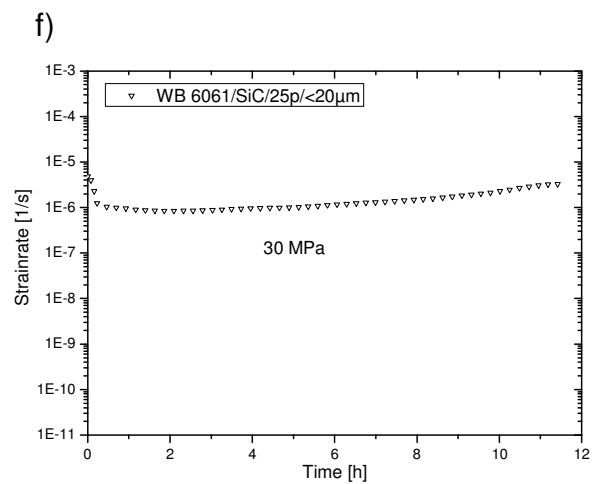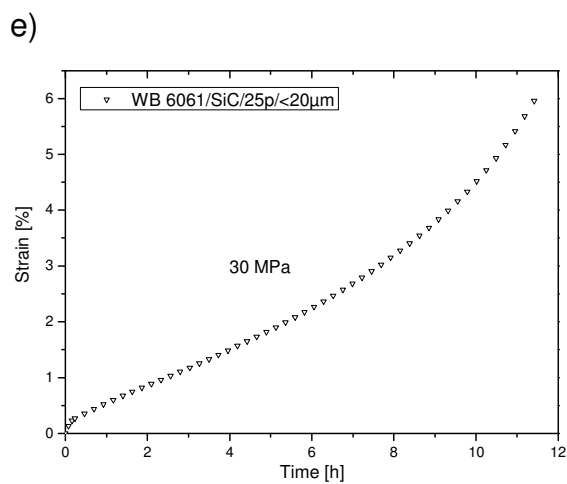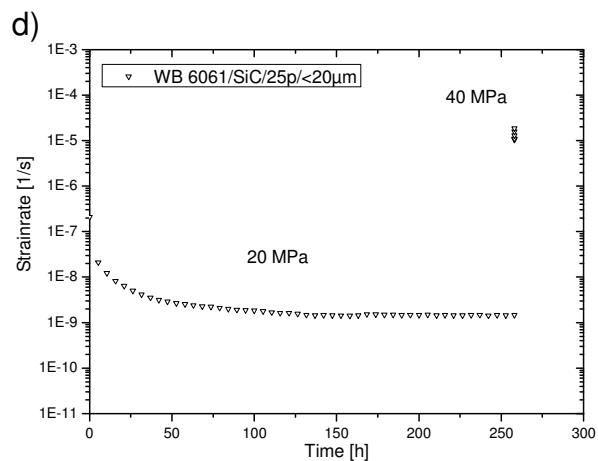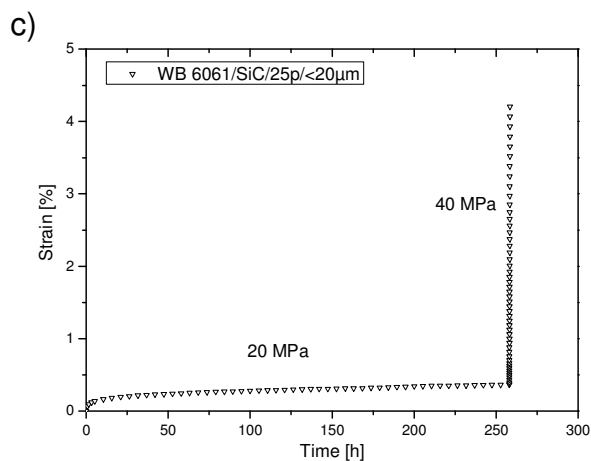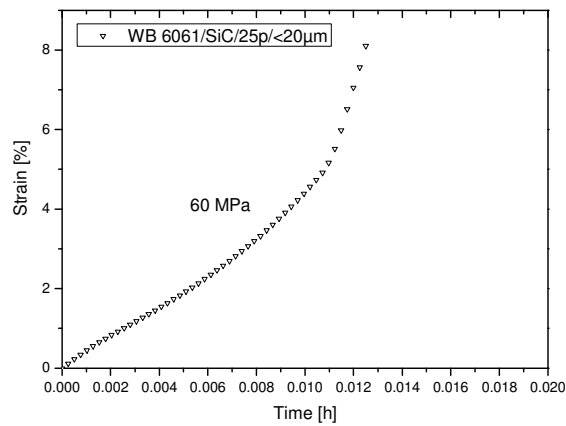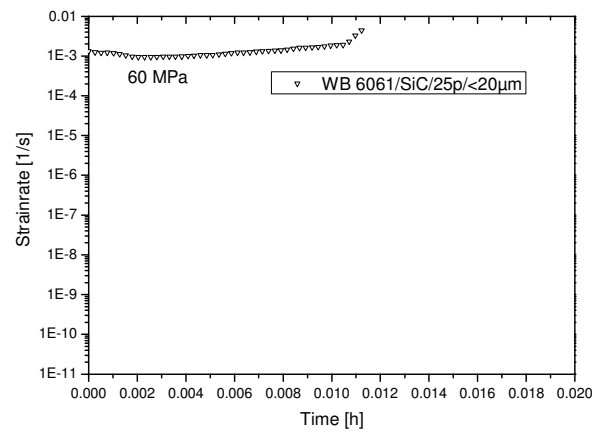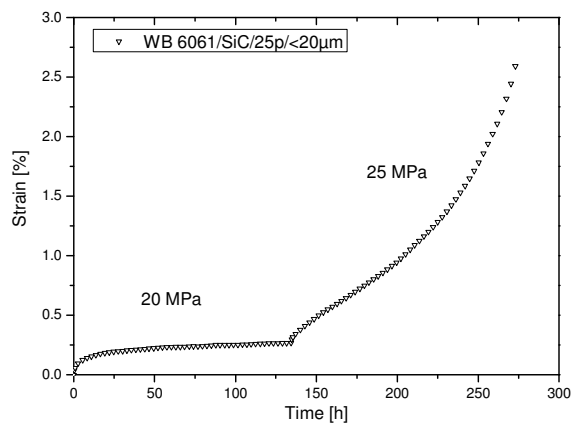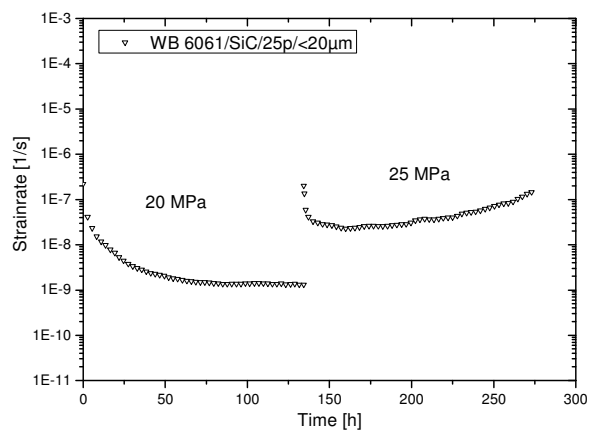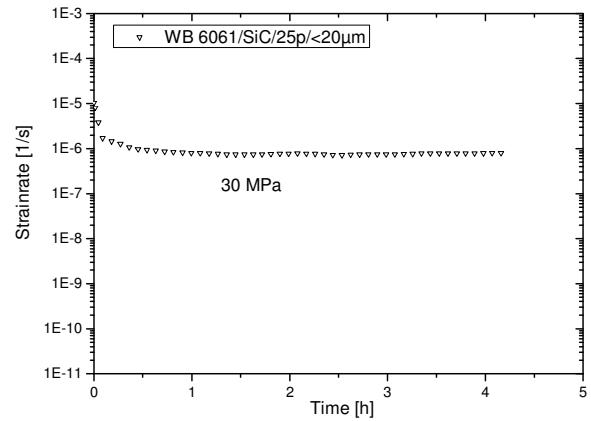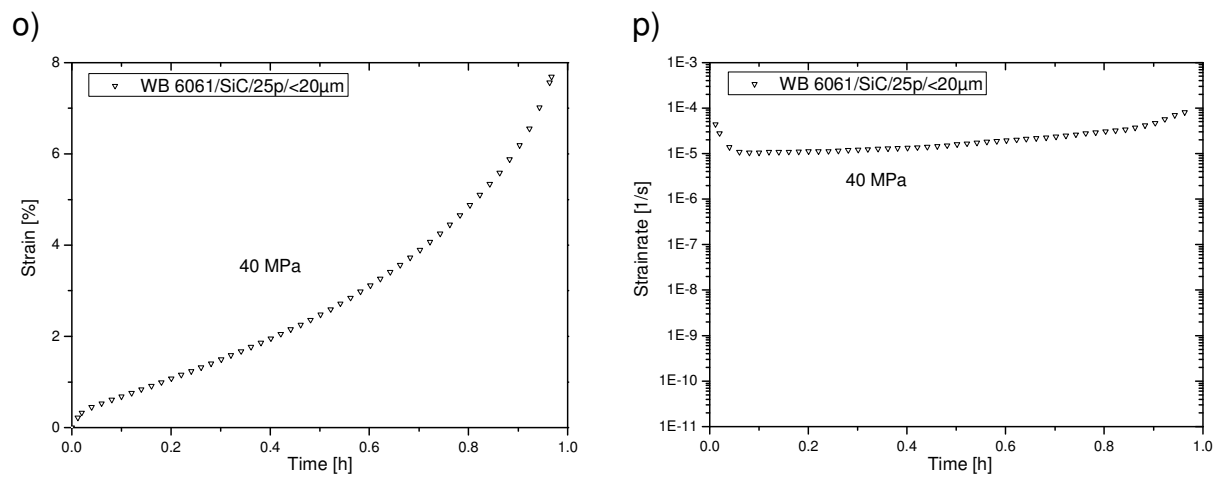


**Figure 9.17 a)-p)** Curves of $\varepsilon$ vs. t and $\dot{\varepsilon}$ vs. t of WB 6061/SiC/25p<20µm obtained during the creep tests

a)



b)



c)



d)

e)



f)



e)



f)



g)



h)

i)



j)



k)



l)



m)



n)

o)



p)



q)



r)
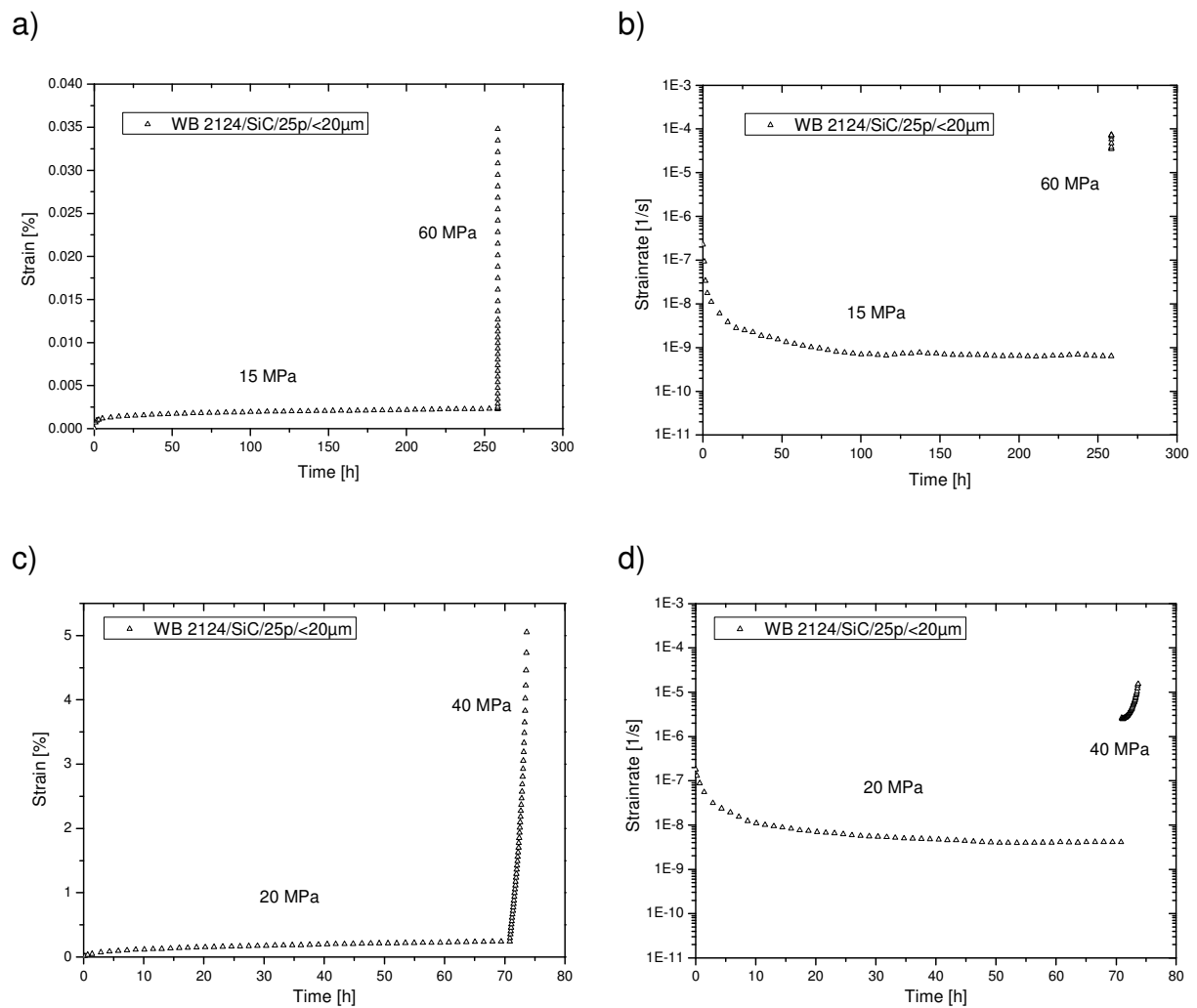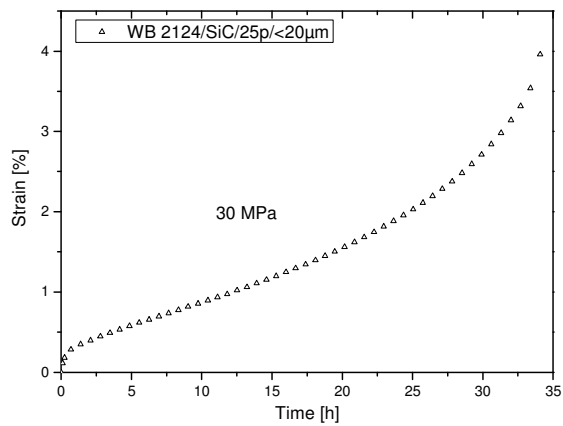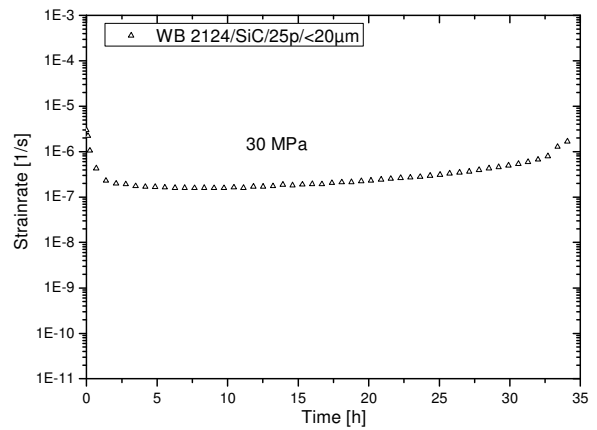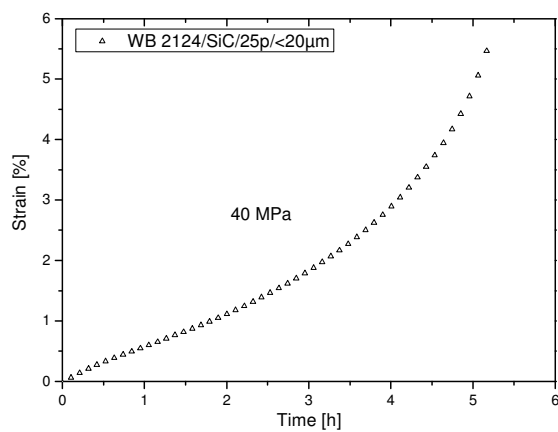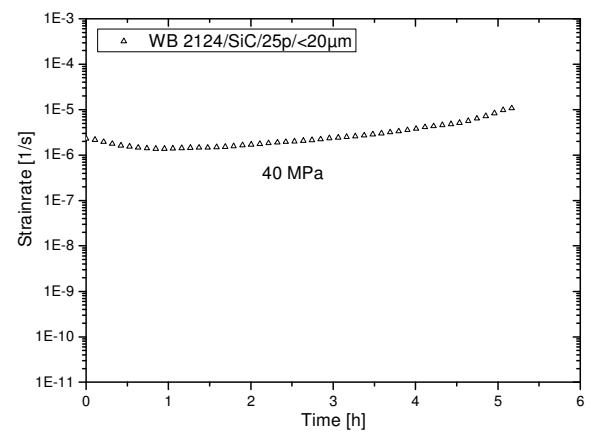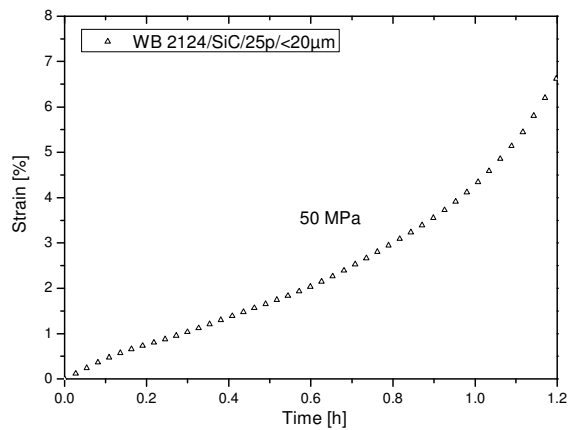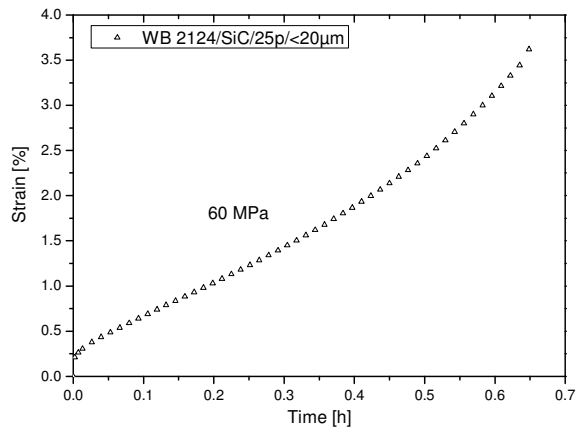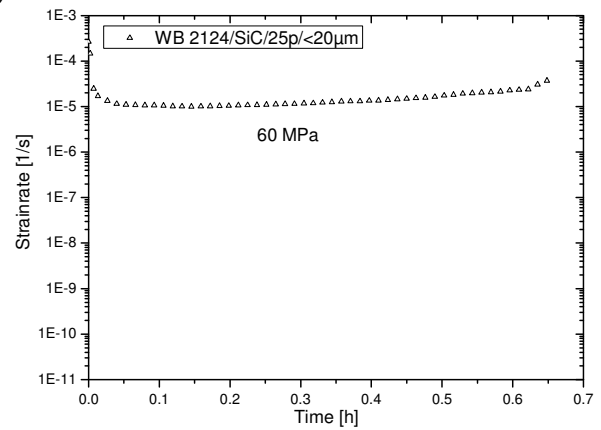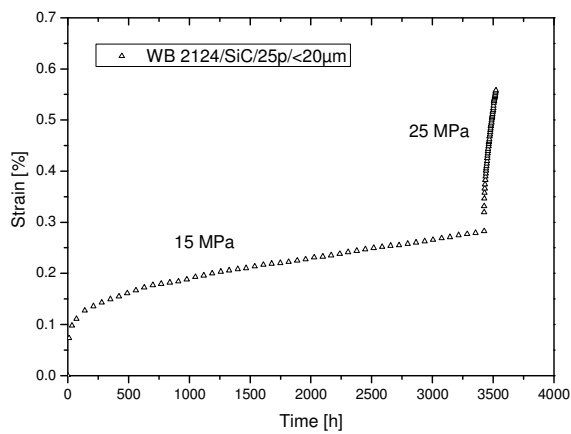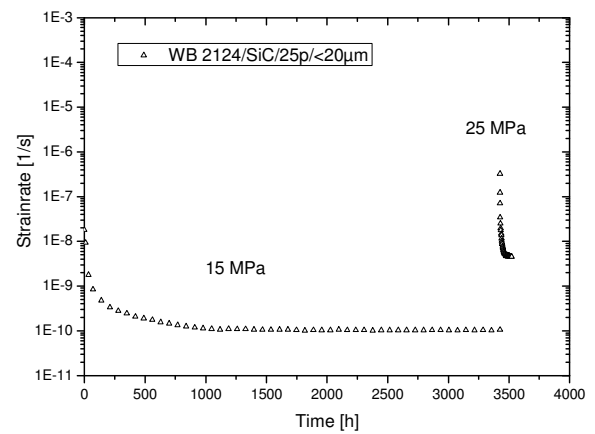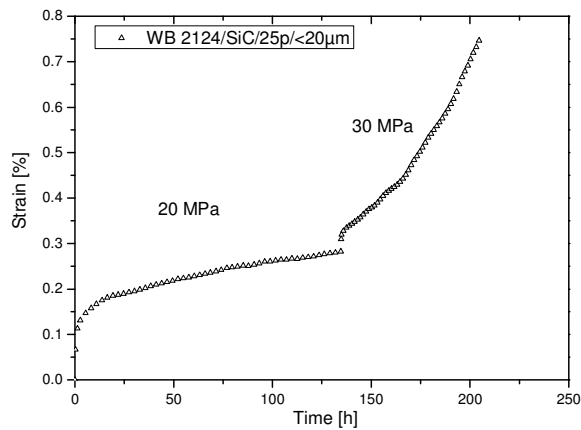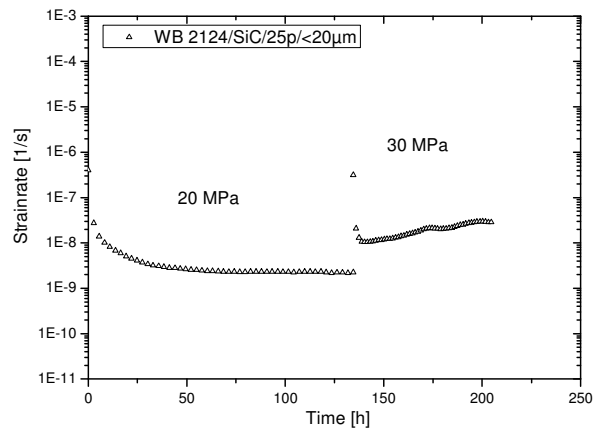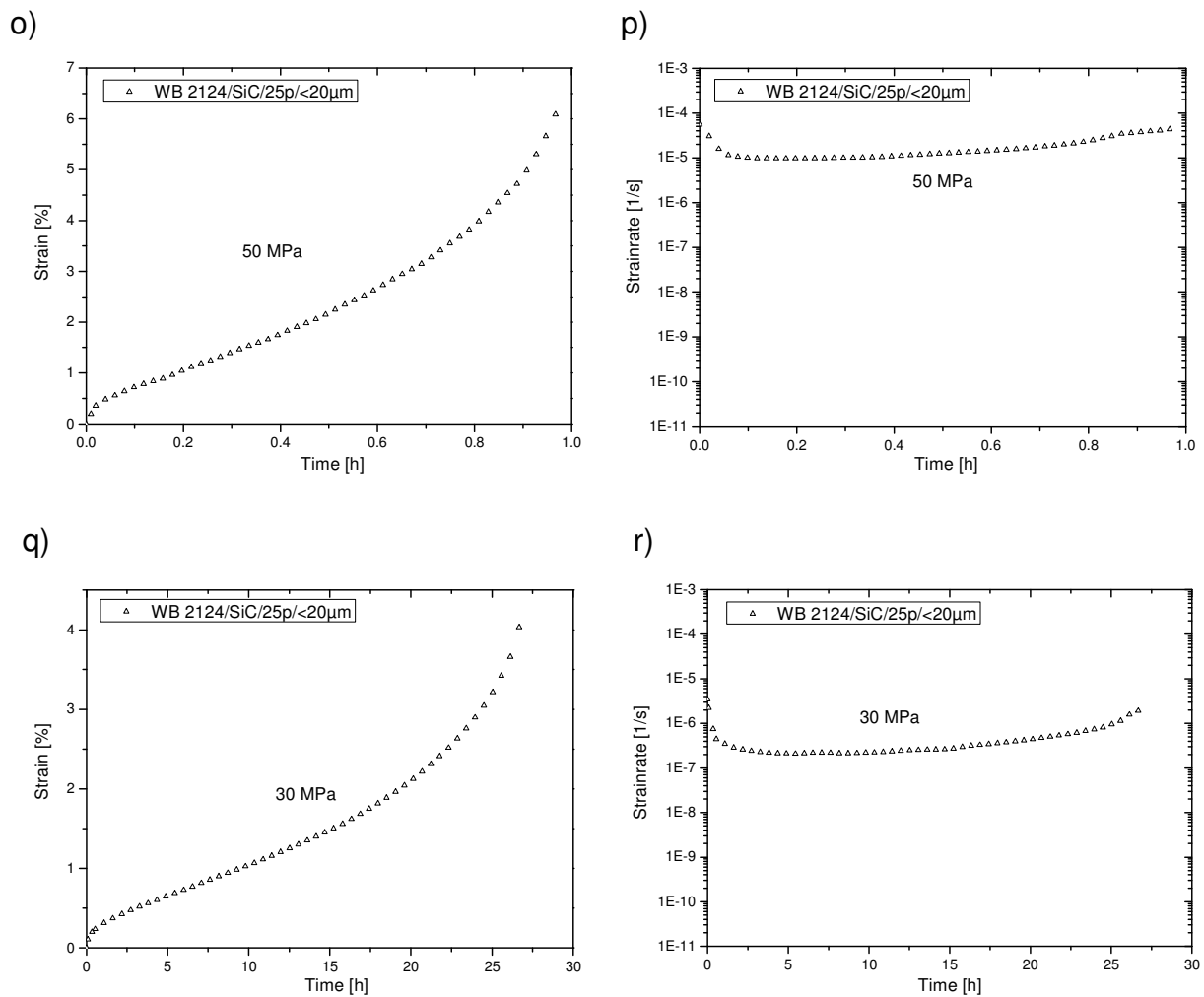


**Figure 9.18 a)-r)** Curves of $\varepsilon$ vs. t and $\dot{\varepsilon}$ vs. t of WB 2124/SiC/25p<20μm obtained during the creep tests

a)



b)

c)



d)



e)



f)



g)



h)

i)



j)



k)



l)



m)



n)

o)



p)



q)



r)
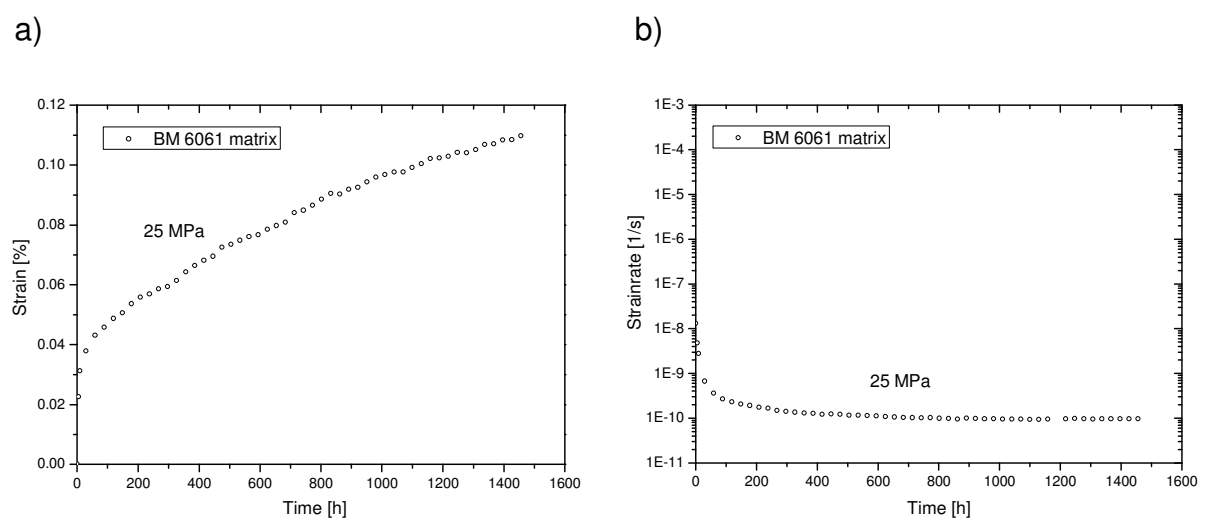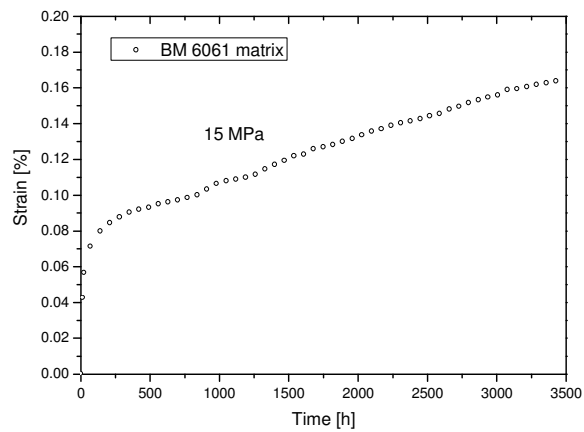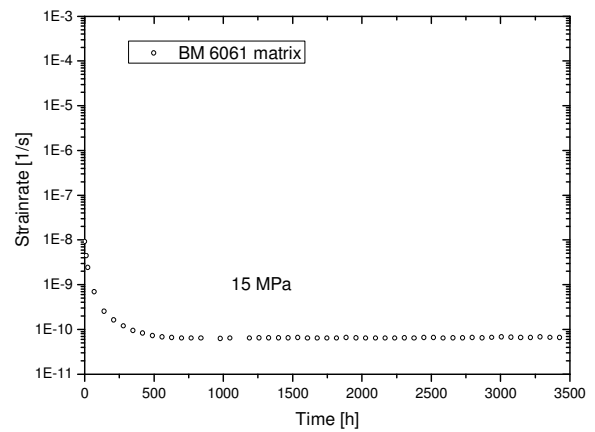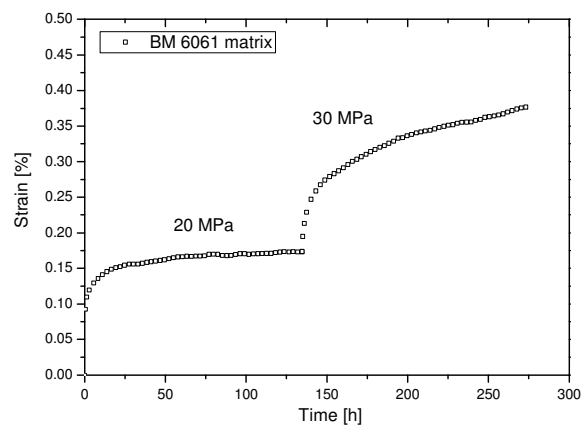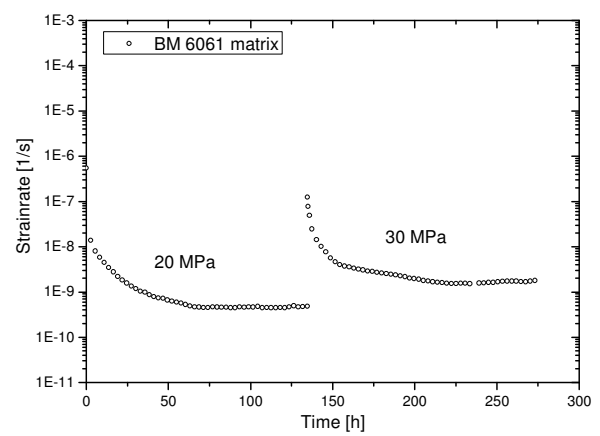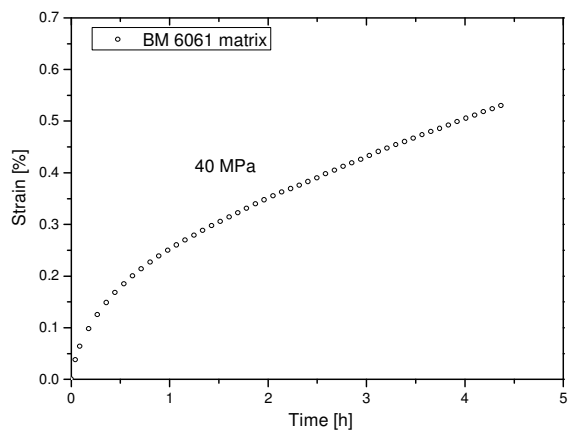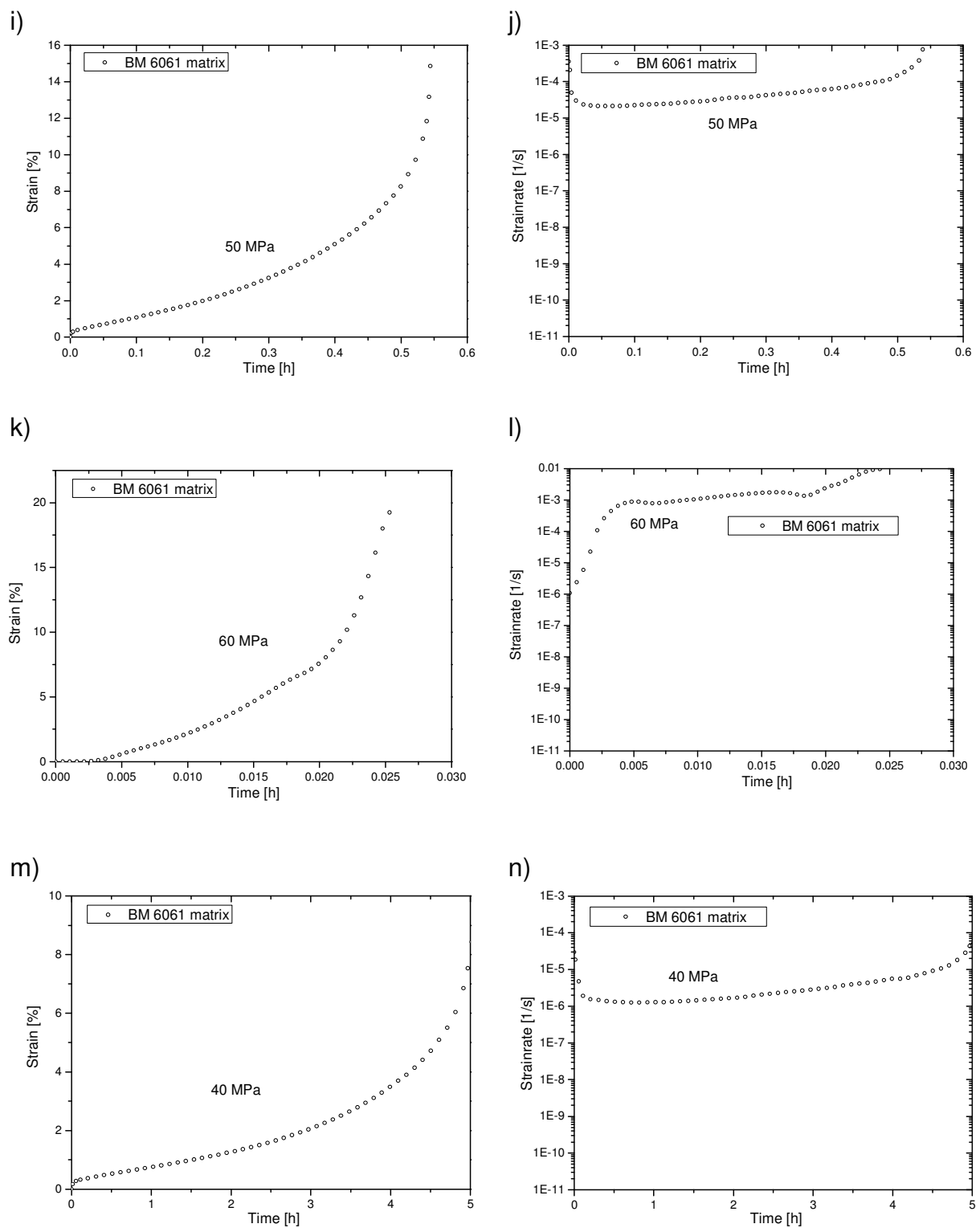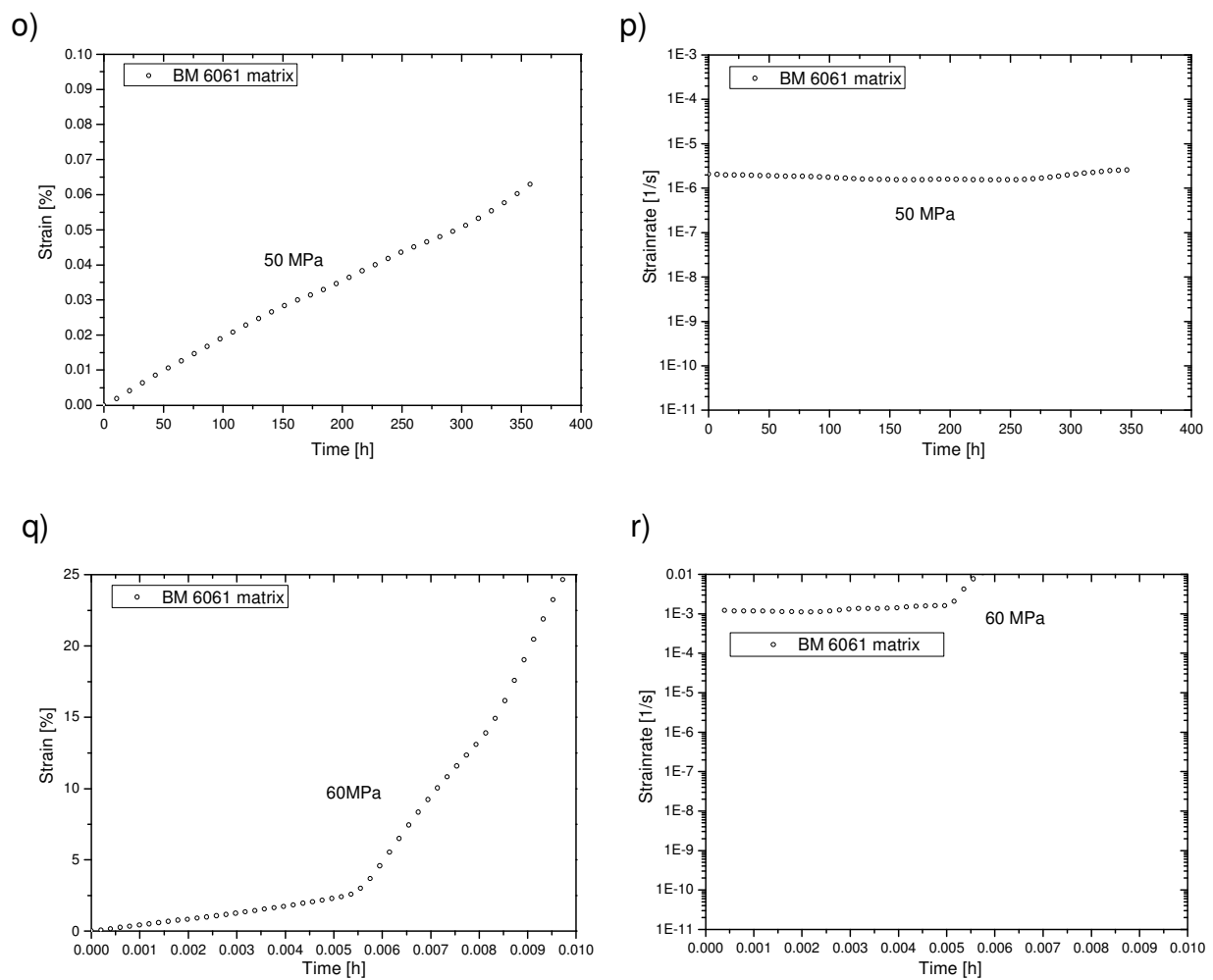


**Figure 9.19 a)-r)** Curves of $\varepsilon$ vs. t and $\dot{\varepsilon}$ vs. t of BM 6061 matrix obtained during the creep tests

a)



b)

c)



d)



e)



f)



g)



h)

i)



j)



k)



l)
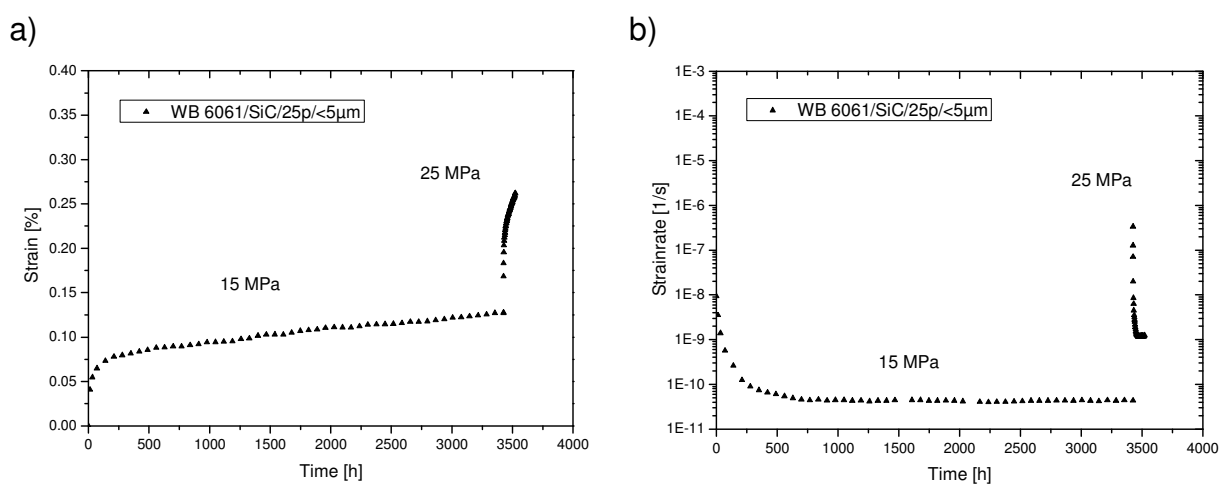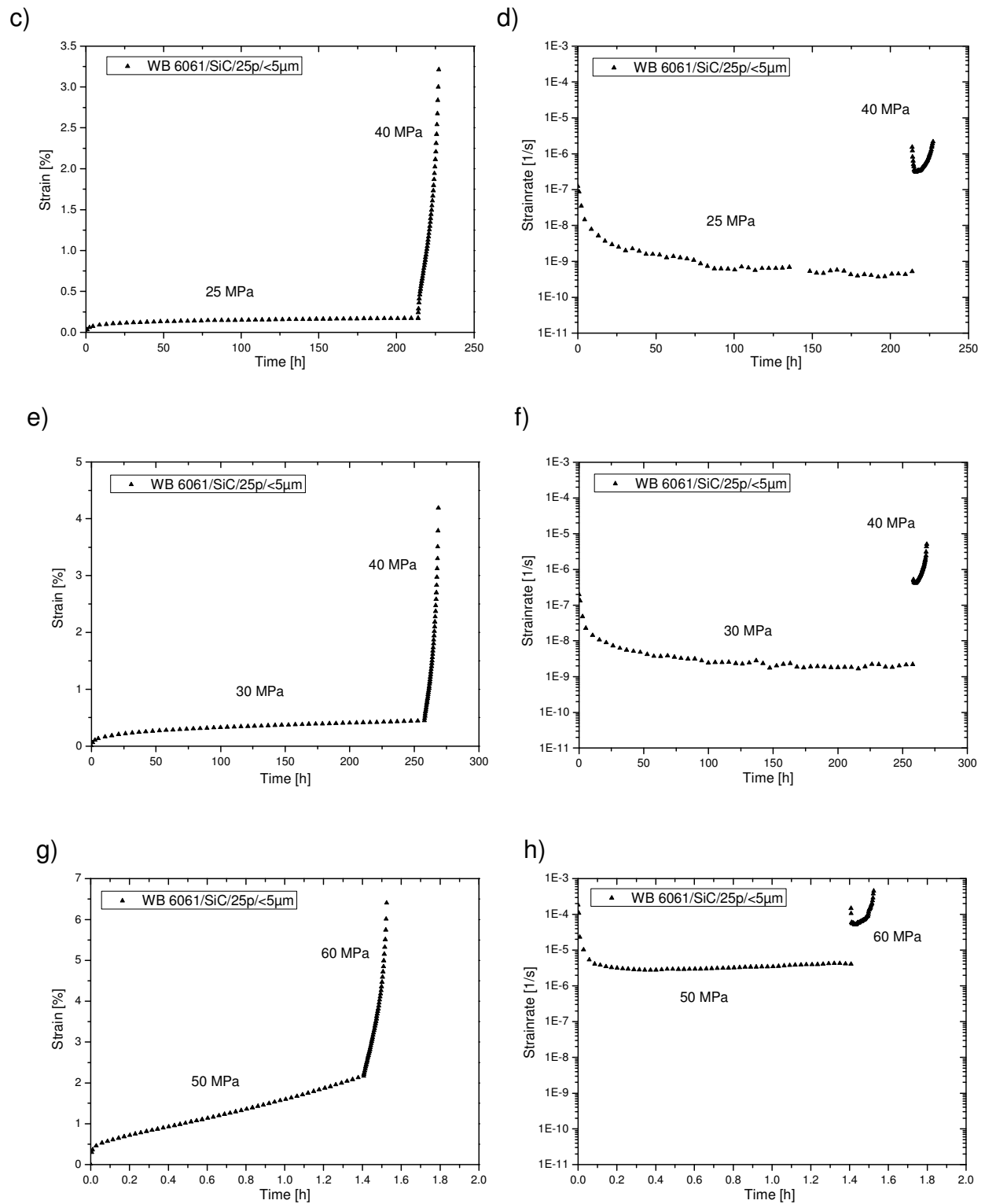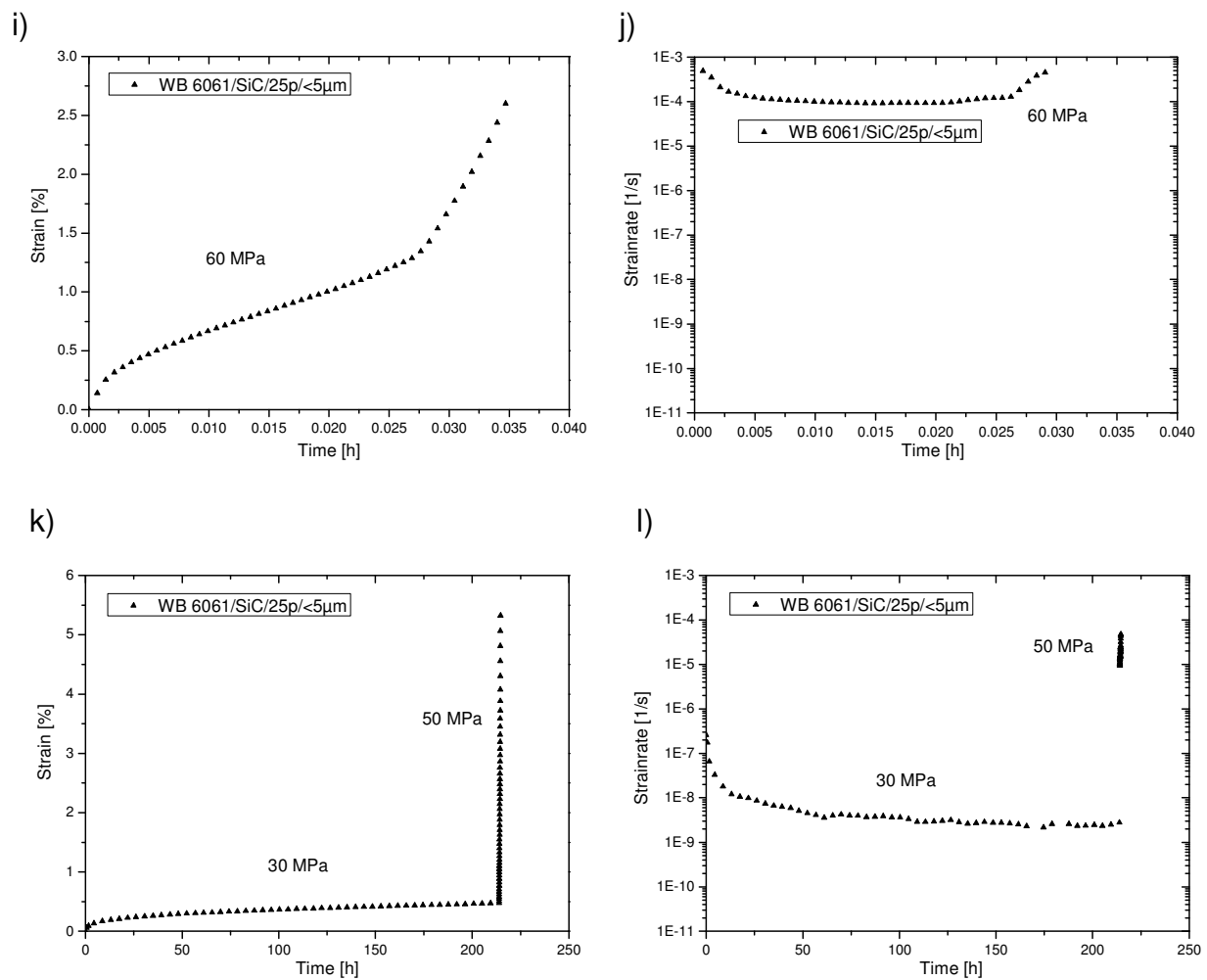


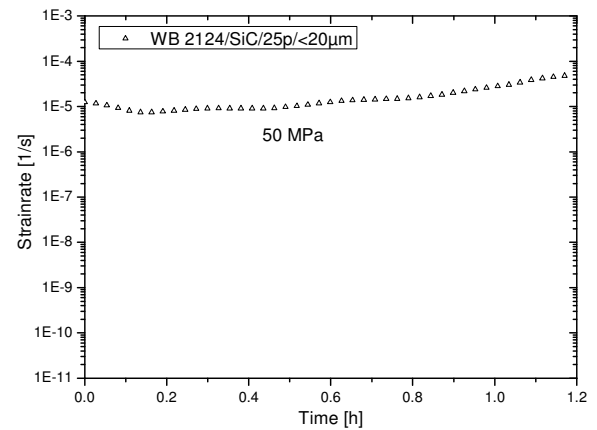**Figure 9.20 a)-l)** Curves of $\varepsilon$ vs. t and $\dot{\varepsilon}$ vs. t of WB 6061/SiC/25p<5µm obtained during the creep tests

a)



b)

c)



d)



e)



f)



g)



h)

i)



j)



k)



l)
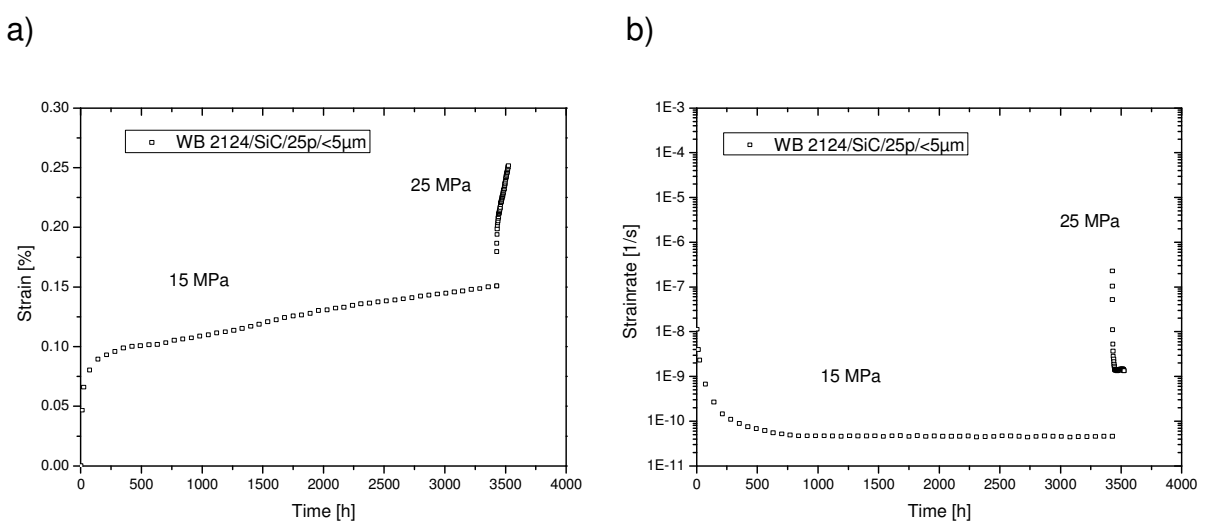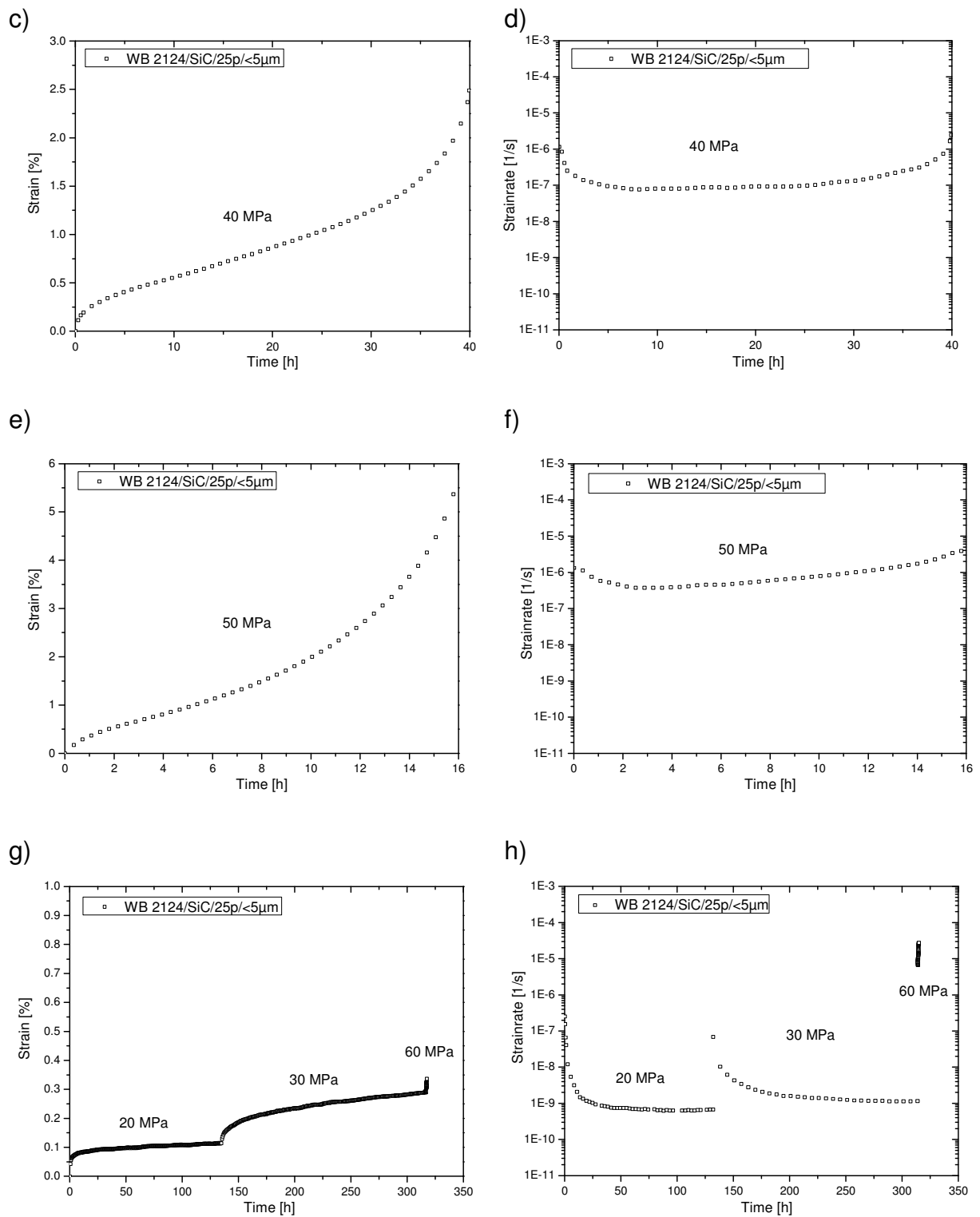


**Figure 9.21 a)-l)** Curves of $\varepsilon$ vs. t and $\dot{\varepsilon}$ vs. t of WB 2124/SiC/25p<5µm obtained during the creep tests

## 9.4 Results of creep tests

Min. strainrate at Load [MPa]

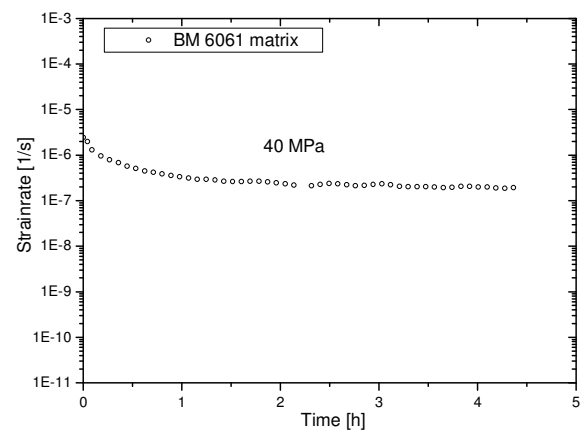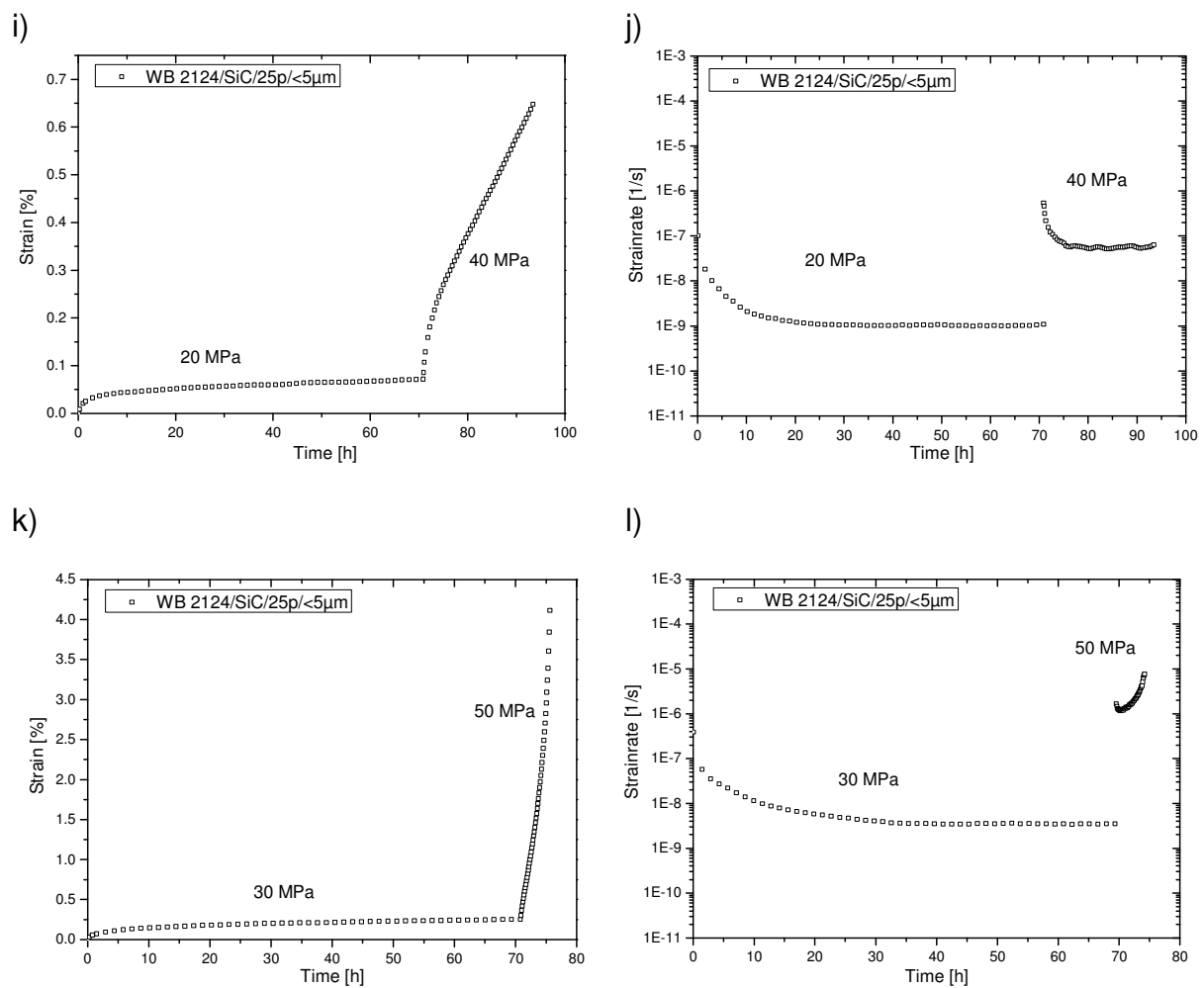| Sample | 15 | 20 | 25 | 30 | 35 | 40 | 50 | 60 | 70 | $t_{exp/load}$ [h] | $t_{exp}$ [h] |
|---|---|---|---|---|---|---|---|---|---|---|---|
| **2124 matrix as received** | | | | | | | | | | | |
| 571_1_15 | 9,85E-11 | | | | | | | | | 1852 | 1852 |
| 570_2_20-30 | | 2,35E-10 | | | | | | | | 1321 | |
| | | | | 9,41E-09 | | | | | | 247 | 1568 |
| 570_3_20-30-35 | | 1,09E-10 | | | | | | | | 1087 | |
| | | | | 5,64E-10 | | | | | | 986 | |
| | | | | | 4,22E-08 | | | | | 139 | 2212 |
| 571_1_30 | | | | 3,71E-08 | | | | | | 139 | 139 |
| 570_1_30-35 | | | | 2,69E-10 | | | | | | 1674 | |
| | | | | | 2,93E-09 | | | | | 334 | 2008 |
| 570_2_35 | | | | | 3,50E-08 | | | | | 67 | 67 |
| 570_1_40 | | | | | | 7,22E-08 | | | | 55 | 55 |
| 570_2_40 | | | | | | 4,21E-07 | | | | 11 | 11 |
| 571_3_40 | | | | | | 3,40E-08 | | | | 42 | 42 |
| 571_1_50 | | | | | | | 2,69E-06 | | | 3 | 3 |
| 571_2_50 | | | | | | | 1,33E-06 | | | 5 | 5 |
| 571_1_60 | | | | | | | | 9,03E-05 | | 0,1 | 0,1 |
| 571_2_60 | | | | | | | | 3,70E-06 | | 1,3 | 1,3 |
| **2124 matrix 4h ball milling** | | | | | | | | | | | |
| 576_1_15-35 | 6,94E-11 | | | | | | | | | 2567 | |
| | | | | | 3,06E-10 | | | | | 334 | 2901 |
| 576_2_15-35 | 4,76E-11 | | | | | | | | | 2566 | |
| | | | | | 2,47E-09 | | | | | 334 | 2900 |
| 577_1_20-40 | | 6,53E-11 | | | | | | | | 4181 | |
| | | | | | | 1,23E-09 | | | | 77 | 4258 |
| 577_2_20-40 | | 3,91E-11 | | | | | | | | 4100 | |
| | | | | | | 8,32E-10 | | | | 69 | 4169 |
| 577_1_30-60 | | | | 1,20E-10 | | | | | | 3393 | |
| | | | | | | | | 3,68E-05 | | 0,2 | 3393,2 |
| 577_2_30-60 | | | | 2,81E-10 | | | | | | 2420 | |
| | | | | | | | | 4,02E-04 | | 0,1 | 2420,1 |
| 576_1_40 | | | | | | 5,32E-08 | | | | 65,3 | 65,3 |
| 576_2_40 | | | | | | 3,94E-08 | | | | 38 | 38 |
| 577_1_50 | | | | | | | 3,33E-07 | | | 11 | 11 |
| 577_2_50 | | | | | | | 4,45E-07 | | | 9 | 9 |
| **2124 / SiC / 25p / <5µm** | | | | | | | | | | | |
| 566_1_20-35 | | k.e. | | | | | | | | 4700 | |
| | | | | | 1,10E-11 | | | | | 6400 | 11100 |
| 566_1_40-50-60 | | | | | | 3,57E-11 | | | | 4126 | |
| | | | | | | | 2,22E-11 | | | 2859 | |
| | | | | | | | | 1,60E-10 | | 1064 | 8049 |
| 566_1_50-60 | | | | | | | 4,98E-11 | | | 4182 | |
| | | | | | | | | 3,27E-10 | | 719 | 4901 |
| 566_2_20-40-70 | | k.e. | | | | | | | | 2764 | |
| | | | | | | 9,05E-11 | | | | 1471 | |
| | | | | | | | | | 6,35E-09 | 23 | 4258 |
| **2124 / SiC / 25p / <10µm** | | | | | | | | | | | |
| 567_2_20-40-70 | | k.e. | | | | | | | | 1000 | |
| | | | | | | 1,09E-10 | | | | 1471 | |
| | | | | | | | | | 5,97E-09 | 22 | 2493 |
| 567_1_40-50-60 | | | | | | 2,47E-11 | | | | 4213 | |
| | | | | | | | 5,12E-11 | | | 3079 | |
| | | | | | | | | 1,75E-10 | | 294 | 7586 |
| 567_1_50-60 | | | | | | | 9,94E-11 | | | 3881 | |
| | | | | | | | | 6,81E-10 | | 768 | 4649 |
| 567_1_30 | | | | 2,44E-11 | | | | | | 5197 | 5197 |
| 567_3_20-35 | | | | | | | | | | | |
| **2124 / SiC / 25p / <20µm** | | | | | | | | | | | |
| 568_2_40-50-60-70 | | | | | | 3,06E-11 | | | | 4133 | |
| | | | | | | | 8,91E-11 | | | 3047 | |
| | | | | | | | | 1,28E-09 | | 294 | |
| | | | | | | | | | 6,69E-08 | 6 | 7480 |
| 568_1_50-60-70 | | | | | | | 4,83E-11 | | | 4182 | |
| | | | | | | | | 3,02E-09 | | 294 | |
| | | | | | | | | | 9,74E-07 | 2 | 4478 |
| 568_2_20-40-70 | | k.e. | | | | | | | | 2764 | |
| | | | | | | 4,20E-11 | | | | 1471 | |
| | | | | | | | | | 5,71E-08 | 23 | 4258 |
| 568_1_30 | | | | 1,31E-11 | | | | | | 5197 | 5197 |

| Sample | Min. strainrate at Load [MPa] | | | | | | | | | $t_{exp/load}$ [h] | $t_{exp}$ [h] |
|---|---|---|---|---|---|---|---|---|---|---|---|
| | 15 | 20 | 25 | 30 | 35 | 40 | 50 | 60 | 70 | | |
| **6061 / SiC / 25p / <20µm Wet Blending** | | | | | | | | | | | |
| 632_1_15-30 | 3,00E-10 | | | | | | | | | 257 | |
| | | | | 7,10E-07 | | | | | | 10 | 267 |
| 632_2_20-25 | | 1,31E-09 | | | | | | | | 135 | |
| | | | 2,20E-08 | | | | | | | 139 | 274 |
| 632_1_20-40 | | 1,39E-09 | | | | | | | | 258 | |
| | | | | | | 1,05E-05 | | | | 0,5 | 258,5 |
| 632_1_30 | | | | 8,48E-07 | | | | | | 12 | 12 |
| 632_2_30 | | | | 7,23E-07 | | | | | | 5 | 5 |
| 632_2_40 | | | | | | 1,05E-05 | | | | 1 | 1 |
| 632_1_50 | | | | | | | 4,04E-05 | | | 0,08 | 0,08 |
| 632_1_60 | | | | | | | | 9,47E-04 | | 0,02 | 0,02 |
| **6061 / SiC / 25p / <5µm Wet Blending** | | | | | | | | | | | |
| 638_1_15-25 | 4,10E-11 | | | | | | | | | 3444 | |
| | | | 1,20E-09 | | | | | | | 98 | 3542 |
| 638_1_25-40 | | | 4,60E-10 | | | | | | | 214 | |
| | | | | | | 3,20E-07 | | | | 14 | 228 |
| 638_1_30-40 | | | | 1,68E-09 | | | | | | 258 | |
| | | | | | | 4,12E-07 | | | | 11 | 269 |
| 638_1_50-60 | | | | | | | 2,76E-06 | | | 2 | |
| | | | | | | | 5,15E-05 | | | 0,12 | 2,12 |
| 638_1_60 | | | | | | | 9,18E-05 | | | 0,04 | 0,04 |
| **2124 / SiC / 25p / <20µm Wet Blending** | | | | | | | | | | | |
| 633_1_15-60 | 6,40E-10 | | | | | | | | | 258 | |
| | | | | | | | 3,00E-04 | | | 0,3 | 258,3 |
| 633_2_15-25 | 1,00E-10 | | | | | | | | | 3472 | |
| | | | 4,50E-09 | | | | | | | 97 | 3569 |
| 633_1_20-40 | | 3,97E-09 | | | | | | | | 71 | |
| | | | | | | 2,47E-06 | | | | 3 | 74 |
| 633_2_20-30 | | 2,34E-09 | | | | | | | | 135 | |
| | | | | 8,49E-09 | | | | | | 70 | 205 |
| 633_1_30 | | | | 1,58E-07 | | | | | | 34 | 34 |
| 633_1_40 | | | | | | 1,37E-06 | | | | 5 | 5 |
| 633_1_50 | | | | | | | 7,42E-06 | | | 2 | 2 |
| 633_2_50 | | | | | | | 9,96E-06 | | | 1 | 1 |
| 633_1_60 | | | | | | | | 9,98E-06 | | 0,6 | 0,6 |
| 633_3_30 | | | | 2,09E-07 | | | | | | 27 | 27 |
| **2124 / SiC / 25p / <5µm Wet Blending** | | | | | | | | | | | |
| 639_1_15-25 | 4,70E-11 | | | | | | | | | 3444 | |
| | | | 1,40E-09 | | | | | | | 98 | 3542 |
| 639_2_20-30-60 | | 6,57E-10 | | | | | | | | 135 | |
| | | | | 1,16E-09 | | | | | | 182 | |
| | | | | | | | | 6,70E-06 | | 1 | 318 |
| 643_1_20-40 | | 1,03E-09 | | | | | | | | 71 | |
| | | | | | | 5,24E-08 | | | | 23 | 94 |
| 643_1_30-50 | | | | 3,48E-09 | | | | | | 71 | |
| | | | | | | | 1,18E-06 | | | 5 | 76 |
| 639_1_40 | | | | | | 7,80E-08 | | | | 40 | 40 |
| 639_1_50 | | | | | | | 3,74E-07 | | | 18 | 18 |
| **6061 matrix 4h ball milling** | | | | | | | | | | | |
| 637_1_15-25 | k.e. | | | | | | | | | 4167 | |
| | | | 9,20E-11 | | | | | | | 1472 | 5639 |
| 637_2_15 | 6,50E-11 | | | | | | | | | 3431 | 3431 |
| 637_1_20-30 | | 4,77E-10 | | | | | | | | 135 | |
| | | | | 1,55E-09 | | | | | | 139 | 274 |
| 637_1_40 | | | | | | 1,86E-07 | | | | 4,5 | 4,5 |
| 637_2_40 | | | | | | 1,25E-06 | | | | 5 | 5 |
| 637_1_50 | | | | | | | 2,11E-05 | | | 0,5 | 0,5 |
| 637_2_50 | | | | | | | 1,60E-06 | | | 0,2 | 0,2 |
| 637_1_60 | | | | | | | | 7,78E-04 | | 0,03 | 0,03 |
| 637_2_60 | | | | | | | | 0,00111 | | 0,01 | 0,01 |

**Table 9.1** Results of the conducted isothermal tensile creep tests for all the studied materials

# Lebenslauf

| | |
|---|---|
| Name | **BAUER Bernd, Dipl.-Ing.** |
| Adresse | Zur Spinnerin 33/27 |
| | 1100 Wien |
| Geburtstag | 05.01.1979 |
| Geburtsort | Eisenstadt/Bgld. |
| Familienstand | ledig |
| Telefon | 0699 / 10 71 94 40 |
| e-Mail | bauer_bernd@gmx.net |
| Arbeitsadresse | TU-Wien, Institut für Werkstoffkunde und Werkstofftechnologie |
| | Karlsplatz 13 |
| | 1040 Wien |
| Telefon | 01 / 58801 308 13 |

## Schulische Bildung

| | |
|---|---|
| 1985-1989 | Volksschule Mattersburg |
| 1989-1993 | Gymnasium Mattersburg |
| 1993-1998 | Höhere Technische Bundeslehranstalt Eisenstadt für Allgemeinen Maschinenbau |
| | Matura am 20.06.1998 mit gutem Erfolg |

## Präsenzdienst

| | |
|---|---|
| 07/1998-03/1999 | Präsenzdienst in Oberwart |

# Universitäre Bildung

1999-2004          Wirtschaftsingenieurwesen-Maschinenbau an der Technischen Universität Wien
Diplomprüfung am 28.09.2004 mit ausgezeichnetem Erfolg
Thema: Vergleich und kritische Bewertung von Kraftfahrzeugeinstufungen im Hinblick auf Umweltfreundlichkeit

02/2005 – 07/2005 Assistent am Institut für Fertigungstechnik/Labor für Produktionstechnik an der Technischen Universität Wien

03/2004-2009       Soziologie an den Universitäten Wien und Linz
Thema: Todesstrafe

09/2005-03/2009    Doktoratsstudium am Institut für Werkstoffkunde und Werkstoffwissenschaft an der Technischen Universität Wien
Thema: Verbesserung der Kriecheigenschaften mit unterschiedlichen Größen von SiC-Verstärkungspartikel

08/2008            Ausbildung zur Psychotherapie

Wien, 19.03.2009